



VYSOKÉ UČENÍ TECHNICKÉ V BRNĚ
BRNO UNIVERSITY OF TECHNOLOGY



FAKULTA STROJNÍHO INŽENÝRSTVÍ
ENERGETICKÝ ÚSTAV

FACULTY OF MECHANICAL ENGINEERING
ENERGY INSTITUTE

STUDY OF THE DISSIPATION IN SPIRALING VORTICAL STRUCTURES

STUDY OF THE DISSIPATION IN SPIRALING VORTICAL STRUCTURES

DIZERTAČNÍ PRÁCE
DOCTORAL THESIS

AUTOR PRÁCE
AUTHOR

Ing. David Štefan

VEDOUCÍ PRÁCE
SUPERVISOR

doc. Ing. Pavel Rudolf, Ph.D.

BRNO 2015

ABSTRACT

This work deals with study of swirling flows where the spiral vortical structure appears. The main relation is to flow seen in the draft tube cone of hydraulic turbines operated out of the design point (i.e. best efficiency point). In this cases large coherent vortex structure (vortex rope) appears and consequently high pressure pulsations are propagated to the whole machine system leading to possible restriction of turbine operation. This flow features are consequence of flow instability called vortex breakdown in case of Francis turbine operated at part load (flow rate lower than optimal one).

The present study is carried out using simplified device of swirl generator in order to access similar flow conditions as can be found in real hydraulic turbines. Both the dynamic and dissipation effect of spiral vortex breakdown are investigated.

The first part of thesis deals with spiral form of vortex breakdown. The experimentally measured velocity profiles (LDA) and wall static pressures are correlated with numerical simulations carried out using open-source CFD package OpenFOAM 2.2.2. The high speed camera recording of cavitating vortex core is used to obtain image ensemble for further post-processing. The dissipation effect of spiral vortex structure is in detail discussed based on computed flow fields.

The second part of thesis is dedicated to the application of POD decomposition to the study of spatio-temporal features of spiral vortex dynamics. Firstly the POD is applied to the both the experimentally obtained image ensemble of cavitating vortex and numerically computed static pressure fields. Secondly the comprehensive analysis of spiral vortex mitigation effect by the axial water jet is analyzed. The collaborative study employing the swirl generator apparatus designed by the researchers from Politehnica University of Timisoara in Romania is performed and changes in spatio-temporal vortex dynamic are studied. In this study the numerical data (in a form of three-dimensional pressure and velocity fields) are obtained using commercial CFD software ANSYS Fluent R14.

Keywords: dissipation, swirling flow, coherent structure, spiral vortex, vortex rope, vortex breakdown, diffuser, draft tube, cavitation, pressure pulsations, POD, OpenFOAM, LDA.

Klíčová slova: disipace, vířivé proudění, koherentní struktura, spirální vír, vírový cop, rozpad víru, difuzor, sací trouba, kavitace, tlakové pulzace, POD, OpenFOAM, LDA.

BIBLIOGRAPHIC CITATION

ŠTEFAN, D. *Study of the dissipation in spiraling vortical structures*. Brno: Vysoké Učení Technické v Brně, Fakulta strojního inženýrství, 2015. 176s. Vedoucí práce doc. Ing. Pavel Rudolf, Ph.D.

STATEMENT OF THE THESIS ORIGINALITY

I honestly declare that this thesis *Study of the dissipation in spiraling vortical structures* was written only by me under the professional leadership of my supervisor.

Ing. David ŠTEFAN

ACKNOWLEDGEMENTS

Here I would like to thank all people who supported and helped me during my postgraduate study resulting to this thesis.

First of all I would like to thank whole my family, namely to my mother Hana and father Dalibor who supported my whole study life. The big lovely thanks are for my girlfriend Tereza who spent with me plenty of time when I had to work instead of relaxing with her and for her big support.

The huge thank for supervising of my postgraduate work is dedicated to doc. Ing. Pavel Rudolf, Ph.D., who professionally led me through tough academic work and patiently revised this thesis. The experimental measurements could not be performed without big help of laboratory staff. Namely I would like to thank to Ing. Martin Hudec for his help with measuring apparatus and recording software, Mr. Jan Bauer and Mr. Bronislav Kusý for their help to build up the experimental circuit and doc. Ing. Vladimír Habán, Ph.D. for his useful troubleshooting comments.

The LDA measurements were performed in collaboration with Ing. Pavel Zubík, Ph.D from the Faculty of Civil Engineering, Brno University of Technology.

During my post-graduate study I spent two months internship at University of Stuttgart (August – September 2012) and three months at Politehnica University of Timisoara (October – December 2012). From University of Stuttgart I would like to thank to Dr.-Ing. Albert Ruprecht for hosting me at their institute and thank to local doctoral students for friendly atmosphere. From Politehnica University of Timisoara the huge thanks are to professor Romeo Susan-Resiga and Sebastian Muntean, Ph.D for their particular help with my thesis and for great collaboration leading to the joint journal paper. I have to thank also to other local academic staff and Ph.D. students (which are now my friends) for kind atmosphere.

Finally I would like to thank all other staff and Ph.D. students from our department for friendly atmosphere.

This work is an output of research and scientific activities of NETME Centre, regional R&D centre built with the financial support from the Operational Programme Research and Development for Innovations within the project NETME Centre (New Technologies for Mechanical Engineering), Reg. No. CZ.1.05/2.1.00/01.0002 and, in the follow-up sustainability stage, supported through NETME CENTRE PLUS (LO1202) by financial means from the Ministry of Education, Youth and Sports under the „National Sustainability Programme I“.

CONTENT

1	INTRODUCTION.....	10
1.1	Vortex breakdown in the field of hydraulic turbines.....	10
1.2	Draft tube flow	12
2	MOTIVATION AND SCOPE OF THE PRESENT WORK	16
3	THEORY AND APPLIED METHODS.....	18
3.1	LASER DOPPLER ANEMOMETRY (LDA).....	18
3.1.1	<i>Principle</i>	18
3.1.2	<i>Determination of the sign of the flow direction</i>	20
3.1.3	<i>Two- and three-component measurements</i>	20
3.2	Computatioanal fluids dynamics (CFD).....	21
3.2.1	<i>Reynolds Averaged Navier-Stokes (RANS)</i>	21
3.3	Proper orthogonal decomposition (POD)	22
3.4	Energetic assessment	24
4	TEST CASES.....	26
4.1	Swirl generator apparatus designed at Brno university of technology (“BUT”)	26
4.2	Swirl generator apparatus designed at “Politehnica” University of Timisoara (“UPT”) ..	27
PART I - INVESTIGATION OF SWIRLING FLOW GENERATED BY THE “BUT” SWIRL GENERATOR.....		
5	EXPERIMENTAL MEASUREMENTS	30
5.1	Measuring equipments and uncertainties.....	31
5.1.1	<i>Measuring uncertainties</i>	31
6	VELOCITY MEASUREMENTS IN THE CONICAL DIFFUSER.....	33
6.1	Velocity unsteadiness	36
7	UNSTEADY PRESSURE PULSATIONS.....	37
7.1	Mean static pressure	38
7.2	Unsteady pressure pulsations	40
7.3	Distinguishing between synchronous and asynchronous pressure pulsations arising from the spiral vortex dynamic	42
7.3.1	<i>Asynchronous pressure pulsations</i>	43
7.3.2	<i>Synchronous pressure pulsations</i>	45
8	COMPARISON OF PRESSURE AND VELOCITY FIELDS DYNAMIC	46
9	HIGH SPEED CAMERA RECORDING OF THE CAVITATING VORTEX	48
9.1	Time evolution of the spiral vortex	49

9.2	Estimation of the cavitation vapor fraction.....	50
9.3	Spatial representation of the time-averaged cavitating vortex.....	52
10	INVESTIGATION OF FREQUENCY DECREASE OF ASYNCHRONOUS PRESSURE PULSATIONS ALONG THE DIFFUSER CONE.....	58
11	CFD CALCULATION USING OPEN-SOURCE SOFTWARE OPENFOAM [68].....	60
11.1	Solver theory	60
11.1.1	<i>Numerical schemes</i>	60
11.1.2	<i>Time schemes</i>	60
11.1.3	<i>Gradient schemes</i>	61
11.1.4	<i>Divergence schemes</i>	61
11.1.5	<i>Laplacian schemes</i>	61
11.1.6	<i>Interpolation schemes</i>	62
11.1.7	<i>Surface normal gradient schemes</i>	62
11.1.8	<i>Flux calculation</i>	62
11.1.9	<i>Solution and algorithm control</i>	62
11.1.10	<i>PISO and SIMPLE algorithm</i>	63
11.1.11	<i>Solution under-relaxation</i>	64
11.2	Computational domain	65
11.3	NUMERICAL SOLUTION of “BUT” swirl generator	66
11.4	RESULTS OF NUMERICAL SIMULATIONS	68
11.4.1	<i>Computed pressure fields</i>	70
11.4.2	<i>Computed velocity fields</i>	71
11.4.3	<i>Estimation of the swirl number S_r along the diffuser length</i>	74
12	COMPARISON OF EXPERIMENTAL MEASUREMENTS AND NUMERICAL RESULTS	76
12.1	Comparison of pressure results	76
12.1.1	<i>Mean static pressure field</i>	76
12.1.2	<i>Unsteady pressure pulsations</i>	78
12.1.3	<i>Time evolution of numerically computed spiral vortex</i>	79
12.2	Comparison of velocity results.....	80
13	ENERGY DISSIPATION IN THE DOWNSTREAM PART OF THE DIFFUSER	84
13.1	Unsteady evolution of energy dissipation.....	84
13.2	Steady evolution of energy dissipation.....	88
13.2.1	<i>Dissipation function</i>	90
14	CONCLUSIONS OF PART I.....	93
	PART II POD ANALYSIS	96
15	APPLICATION OF POD TO THE SWIRLING FLOW WITH THE SPIRAL VORTEX STRUCTURE	97
15.1	Assigning of modes to the mode Pair	97

16	POD ANALYSIS OF “BUT” SWIRL GENERATOR.....	100
16.1	POD of cavitating vortex structure.....	100
16.2	POD of numericalLy computed pressure fields	106
16.2.1	<i>Comparison of numerically and experimentally decomposed flow fields.....</i>	<i>112</i>
16.2.2	<i>POD of numerically computed field in the cross-sectional planes.....</i>	<i>113</i>
16.3	Conclusion of POD analysis of “BUT” swirl generator.....	118
17	POD ANALYSIS OF “UPT” SWIRL GENERATOR WITH THE AXIAL WATER INJECTION	120
17.1	Numerical set-up	121
17.2	POD of pressure and velocity fields in the conical diffuser	124
17.3	Decelerated swirling flow with the vortex rope	125
17.3.1	<i>POD modes of axial velocity field</i>	<i>126</i>
17.3.2	<i>POD modes of tangential velocity field</i>	<i>127</i>
17.3.3	<i>POD modes of radial velocity field.....</i>	<i>129</i>
17.4	POD modes of static pressure field	130
17.4.1	<i>Backward reconstruction of static pressure field.....</i>	<i>132</i>
17.5	Decelerated swirling flows with the axial water injection.....	133
17.5.1	<i>2% jet discharge</i>	<i>138</i>
17.5.2	<i>5% jet discharge</i>	<i>140</i>
17.5.3	<i>8%, 11% and 14% jet discharges</i>	<i>142</i>
17.5.4	<i>Backward reconstruction in cases of the axial water injection.....</i>	<i>144</i>
17.5.5	<i>Robustness of POD technique</i>	<i>147</i>
17.6	Conclusions of POD analysis of “UPT” swirl genrator	149
18	GLOBAL CONCLUSIONS	152
	LITERATURE.....	155
	NOMENCLATURE	164
	ABBREVIATIONS	165
	LIST OF PUBLICATIONS.....	167
	AUTHOR’S CV.....	169
	APPENDIX 1	170
	APPENDIX 2	174



The small eddies are almost numberless, and large things are rotated only by large eddies and not by small ones, and small things are turned by both small eddies and large.

Leonardo da Vinci (April 15, 1452 – May 2, 1519)

1 INTRODUCTION

The control of energy distribution and electricity production are in last several years considerably influenced by the electricity produced from the renewable sources highly depending on changes in weather conditions i.e. solar power plants and wind power plants. The pump storage hydro power plants (PSHPP) are proved to be effective for reduction of voltage and frequency fluctuations in whole power distribution grid. The control ability of PSHPP is connected with operation of a turbine in an extended area of flow rates Q quite far from the best efficiency point (BEP). Unfortunately, operation of the Francis turbine with a constant pitch of turbine runner (mainly used for the PSHPP) at partial discharge (off-design conditions where the flow rate $Q < Q_{BEP}$) or overload (off-design conditions where the flow rate $Q > Q_{BEP}$) is connected with occurrence of highly swirling flow at the inlet of the draft tube (outlet diffuser downstream of turbine runner) with a formation of so called vortex rope, see Figure 1. The vortex rope evolution correlates with a vortex breakdown and leads to the high pressure fluctuations in the draft tube [23], [112]. This draft tube surge propagates pressure pulsations into whole hydraulic system eventually leading to the runner blades breakdown [27] and may cause power swing phenomena at the electric generator [11]. Moreover, when the frequency of the pressure pulsations generated by the vortex rope rotation corresponds with a natural frequency of machine unit, it can enforce restrictions of turbine operation [23].

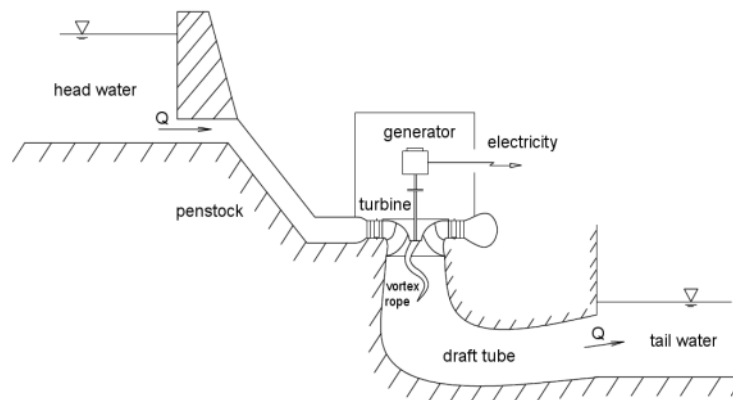


Figure 1 Schematic cross section of hydraulic power plant

1.1 VORTEX BREAKDOWN IN THE FIELD OF HYDRAULIC TURBINES

In many cases of industrial fluid flows the flow instability called vortex breakdown occurs as a consequence of mechanisms in decelerated swirling flow. The vortex breakdown can be found in several forms related to the character of particular flow. Nevertheless, many forms of the vortex breakdown are not relevant to the industrial applications, e.g. bubble form of the vortex breakdown in low-Re flows. In case of hydraulic turbines with constant pitch of the runner, the high Reynolds number spiral form of the vortex breakdown appears, when the turbine is operated at part load $Q < Q_{BEP}$. In Novak's thesis [62], concerned on the high Re flow in pipes and diffusers, the mechanism of the spiral breakdown is described as a rapid axial deceleration towards what appears to be a stagnation point. Then after an abrupt kink, the dye filament (used for flow visualization) expands outwards into helix and after one or

two windings of the spiral, the filament breaks up into the large scale unsteadiness and turbulence. Results agreed with Brücker's [12] notion, that the spiral mode is one of the basic forms of vortex breakdown.

Despite the large database [46], covering investigations of the vortex breakdown during the last forty five years and extensive theoretical, experimental and computational research, we still lack deeper understanding of all influences on origin of this phenomena and their direct relations to the vortex rope properties (instability trigger, frequency of the precessing motion, helix shape, pressure amplitudes, etc.) [80]. Some important features of the vortex breakdown related to the flow in the draft tube can be mentioned; the vortex breakdown is asymmetric and time dependent, precessing vortex core is developed and laid in between the boundary of main flow and recirculation region [46], i.e. in the mixing layer developed between the opposing flow streams. The spiral form of the vortex breakdown can be interpreted as a nonlinear global mode originating at the convective/absolute instability transition point of the axisymmetrical vortex breakdown bubble [28], [113].

Susan-Resiga et al. [100] concluded that the most significant case of the vortex breakdown in conical diffusers is a high Re spiral shape with central quasi stagnant region. They concluded, that the vortex breakdown in conical diffusers is a mechanism for limiting the increase in the swirl number

$$S_n = \frac{\int v_{ax} v_{tan} r dS}{R \int v_{ax}^2 dS} \quad (1.1)$$

and it occurs once the axial flux of circumferential moment of momentum is large enough with respect to the axial flux of axial momentum. This conclusion can be very useful when we are able to act on flow and keep the swirl number at the limit value, so that the breakdown cannot be formed. Nevertheless, in a case of Francis turbine with the constant pitch of the runner (in contrary to Kaplan type, where the runner blades can be controlled to achieve convenient flow angles) this can be achieved only by an external intervention on the flow in the draft tube. In following section the problem of the spiral vortex breakdown (so called spiral vortex rope or helical vortex in case of the draft tube flow) is described, as well as summary of recent research investigations is presented. Important note is, that besides the spiral form of the vortex breakdown for the part load turbine operation, the cylindrical vortex rope (vapor and air filled void) may appear below the runner during the full load operation, i.e. $Q > Q_{BEP}$ [40], [21], [11]. When the static pressure in the vortex core decreases under the value of saturated vapor the cavitating vortex core occurs and can be easily visible as is shown in Figure 2.

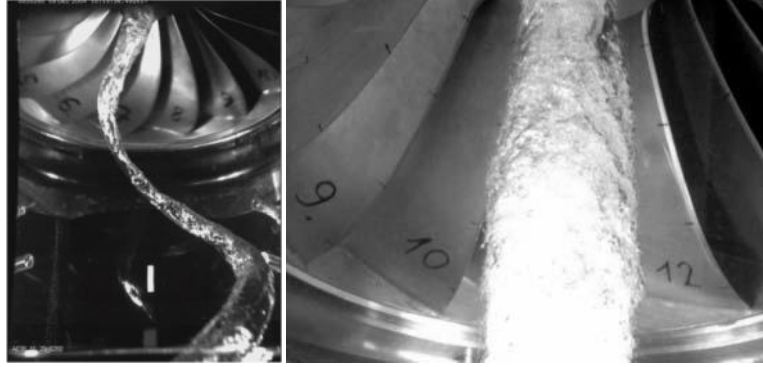


Figure 2 Vortex rope in the draft tube of Francis hydraulic turbine at part load (left) and full load (right) [41]

1.2 DRAFT TUBE FLOW

The hydraulic turbines with a constant pitch of the runner are designed for operation in a narrow range close to the optimal conditions. While the turbine discharge is decreased a high residual swirl (as a result of the mismatch between the swirl generated by the guide vanes and the angular momentum extracted by the turbine runner) enters the draft tube inlet [24].

The swirl orientation at the draft tube inlet is determined by the velocity triangle at the runner exit. Due to constant pitch of Francis turbine runner the blade angle β defined between circumferential velocity u and relative velocity w remains constant when the flow rate is changed. When the discharge decreases (described by the magnitude of meridional velocity v_m) and runner speed ΩR stays unchanged the magnitude of circumferential velocity u is same as in the BEP operating point, thus the orientation of the residual swirl v_u (described by the circumferential component of the absolute velocity v) entering draft tube is in same direction as the runner rotation, left velocity triangle in Figure 3. On the other hand for discharges higher than BEP the orientation of the residual swirl v_u is opposite than the runner rotation, right velocity triangle in Figure 3.

The appearance of the vortex rope is in correlation with the strength of the swirl at the runner outlet [37]. However, the small residual swirl at the outlet of the turbine runner has positive effect in avoiding flow separation due to opening angle of the draft tube [26].

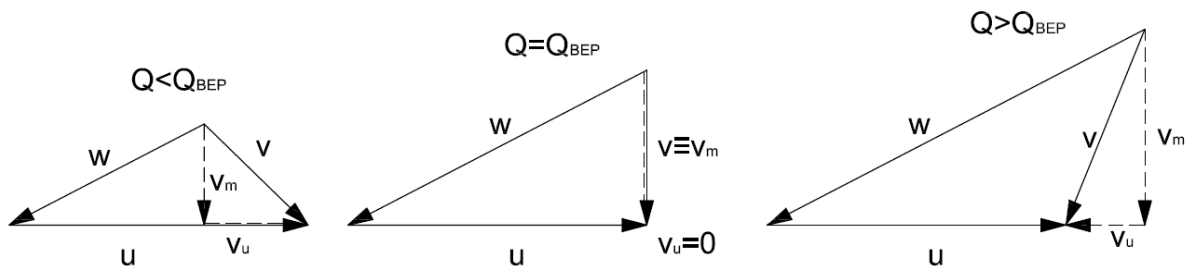


Figure 3 Velocity triangles at the draft tube inlet from left: partial load, BEP and full load

When the turbine discharge is further decreased an unsteady helical vortex breakdown develops in the draft tube cone. If the value of static pressure in the vortex core drops enough,

the water is evaporated and vortex core is visible due to the cavitation.¹ Besides its significant unsteady behavior causing flow instabilities and pressure fluctuations the vortex breakdown phenomenon causes increase in hydraulic losses, thus decreases overall turbine efficiency. Above mentioned conditions are usually called the draft tube surge and lead to an unwanted restriction of the whole turbine operation [69]. As a consequence intensive investigation in the draft tube flow was established in the last two decades.

For example a large research project FLINDT (Flow Investigation in Draft Tubes) with its relatively large amount of experimental data base describing a wide range of operating points of the Francis turbine scale model was conducted at EPFL Lausanne [3]. Recently the experimental data base of the FLINDT project was employed for various theoretical [95], [100], [97], experimental [31] and computational [15] investigations of the swirling flow in the draft tubes.

Ciocan, Iliescu et al. [14], [31] performed complex PIV measurements in the draft tube cone of the Francis turbine model in order to cover lack of experimental data for the draft tube swirling flow with the vortex rope occurrence and study the vortex rope shape behavior. They also used experimental data for the vortex rope reconstruction by the parametrical model for the vortex helix. They showed difficulty in analysis of the flow field in a region of the vortex rope boundary, where measurements are affected due to uncertainty and cavitating vortex reflection of the laser sheet. It was confirmed that the frequency of the vortex rope precession is decreasing when the value of σ (cavitating number) decreases.

$$\sigma = \frac{p_1 - p_v}{1/2 \rho v_{ref}^2} \quad (1.2)$$

where p_1 is upstream static pressure, p_v is vapour pressure, ρ density and v_{ref} is reference velocity.

Susan-Resiga et al. [95] exploited experimental data of LDV measurements at the draft tube inlet in the neighborhood of BEP (i.e. +/- 10% from the best efficiency turbine discharge) in order to develop analytical representation of the swirling flow, with the turbine discharge as an independent parameter. They found that investigated mean swirling flow can be accurately represented as a superposition of three distinct vortices (rigid body rotation and various Batchelor vortices). Presented theory was then used for the flow analysis at the runner outlet to show critical swirl configuration causing the sudden drop in the draft tube efficiency.

This model was further enhanced by Tridon et al. [107], who presented new formulation for radial velocity component in order to catch the blade-wakes influence on the velocity profile and bring better agreement with the experimental data. The magnitude of radial velocity component at the runner exit is usually small and uncertainties relatively large, thus the component of radial velocity is rarely recorded. As can be seen from previous analysis [95], the swirling flow consists from two dominant velocity components (axial and circumferential), however for the numerical simulation where the boundary conditions play

¹ Cavitation is the formation of vapor cavities in a liquid (i.e. "bubbles" or "voids"). It usually occurs when a liquid is subjected to rapid changes of pressure that cause the formation of cavities where the pressure is lower than saturated vapor pressure. When subjected to higher pressure, the voids implode and can generate an intense shockwave.

important role, the fully defined inlet boundary condition composed from the axial, radial and circumferential velocity components can significantly enhance results accuracy. Moreover, neglecting the radial velocity can lead to the spurious flow detachment at the wall and alters the results in the discharge cone of the draft tube [13]. Pochylý et al. [73] presented stability analysis of swirling flow showing the strong sensitivity of the cavitating vortex rope formation to the inlet velocity field. They showed that not only velocity components themselves, but also their derivatives in the radial and axial directions play crucial role in generation of the flow instability. Influence of geometrical boundary conditions was shown on case of diffuser, where the adverse pressure gradient supports origin of the backflow and triggers the flow instability [70].

Kuibin et al. [42] presented mathematical model enabling to compute swirling flow at the runner outlet. With two given integral quantities (discharge coefficient and dimensionless flux of moment of momentum) describing the turbine operating point and radial profile of swirl-free velocity (corresponds to the runner blade design at the trailing edge), they were able to solve constrained variation problem for computation of axial and circumferential velocity profiles at the runner outlet corresponding with the FLINDT turbine operated at 70% of the BEP discharge.

This innovative approach using swirl-free velocity for Francis turbine design was further used for analysis of swirling flow for the wide operating range of the turbine [97]. The swirl-free velocity is an axial velocity corresponding to the operating regime when the absolute circumferential velocity v_u at the runner trailing edge is vanished. The main advantage of this approach is that the swirl-free velocity remains unchanged for various operating points because it directly depends on the trailing edge geometry of the runner. It enables to predict the runner design with minimal tendency to produce instability of the flow during off-design operation. The applicability of mathematical model was verified against experimental data obtained within FLINDT project phase 1 [3] (flow rate within +/- 10% of BEP) and phase 2 [15] (low discharge). Numerical results showed ability to correctly capture the swirling flow evolution as the turbine discharge varies.

Since the methodology using swirl-free velocity is determined from the basic Euler equation, several simplified assumptions were made (steady, axisymmetric, parallel flow of an inviscid and incompressible fluid). Consequently the flow features associated with the viscous effects, such as the runner hub wake, three-dimensional effects and inter-blade vortices, cannot be captured within the simplified assumptions of this model. Therefore this approach is suitable only for early stage of the turbine design optimization.

Later the model of swirl-free velocity was applied on experimental data of Francis GAMM turbine by Ciocan et al. [16] in order to verify the model accuracy for three different flow rates (part load, optimal and full load). The computed velocity profiles were in a very good agreement with the experimental results, however the discrepancy of viscous effect in runner crown wake region are presented due to limitation of inviscid model.

Kirschner and Ruprecht [37] presented detailed investigation of model pump turbine operated during two part load, two full load and BEP specific discharges. They showed variable behaviour (pressure fluctuations, spatial shape and rotation direction) of the vortex structure when the discharge is changed. Only for operating point of 72% of BEP specific

discharge the vortex rope shows nearly steady movement corresponding to the constant frequency of pressure pulsations. The PIV measurements of velocity field in a longitudinal section of the draft tube with tracking of the vortex core position were presented for five operating points. They showed that pressure fluctuations have much higher amplitudes when keeping specific speed n_{11} constant and changing the specific discharge Q_{11} contrary to case when the keeping specific discharge Q_{11} constant and changing the specific speed n_{11} . In this case the vortex rope structure should be unchanged for the full range of Thoma cavitating numbers. Thus the measurements of velocity field could be done for non-cavitating regimes.

The part load (70 – 90% of Q_{BEP}) is one of the most common regimes of the Francis turbine operation. The self-excited pressures pulsations corresponding to 25 – 35% of the runner rotation frequency are induced by the spiral vortex. These pulsations have two components; the first is given by rotation of asymmetrical pressure field (asynchronous pulsations) and the second is given by the pulsation of whole water column (synchronous pulsation) [74]. At upper partial load the low frequency of the vortex rope is often accompanied by an additional phenomenon with higher frequency (which is not multiple of the dominant lower frequencies), documented especially for the high specific speed turbine models [23]. The possible source of these frequencies can arise due to precession movement of the cavitating vortex rope with an elliptical cross-section [82], [74]. Nevertheless, contrary to pulsations induced by the precession frequency, this component exists only when the cavitation occurs. The corkscrew partial load vortex is fairly robust flow pattern and rotates very uniformly and regularly. However at the limit of its range of occurrence, it may become intermittent with temporary prevalence of other flow patterns (e.g. twin vortex rope). As a consequence the vortex collapse with sharp pressure shock occurs during a transition between different flows [23].

2 MOTIVATION AND SCOPE OF THE PRESENT WORK

As was mentioned in the introduction especially in section 1.2, despite the large amount of research concerns with the decelerated flow in the draft tube of hydraulic turbines where the precessing vortex rope appears, many related phenomena are not fully clarified and described, e.g. main trigger causing flow instability leading to the vortex rope formation.

Besides the deeper understanding of the vortex rope phenomena developed during past decades, methodology to suppress this undesired flow features for turbomachinery is still sought and remains an object of interest. For these reasons a passive as well as an active (in form of external energy source) control methods for the vortex rope mitigation were introduced [106]. The passive control methods include fins mounted on the draft tube cone [60], [52], extension cones mounted on the runner crown [109], [75] or J-grooves [43], [44]. On the other hand, the active control methods include air injections either downstream (through the runner cone) or upstream (through the wicket gates trailing edge) of the runner [106], [70], tangential water jets at the discharge cone wall [39], axial water jet injection along the axis [102] and two-phase air-water jet injection along the axis [38].

Two ways of the draft tube flow investigations can be chosen. The first one utilizes full turbine model and can be used to provide clearly specified flow conditions of the draft tube flow for full range of operating points and a specific runner geometry. Nevertheless this approach is very demanding on financial sources and available facilities. Therefore the second way with the simplified swirl generator apparatus was employed. Basically the swirl generator is used to imitate flow conditions similar to ones in the draft tube cone of the Francis turbine.

The base of this thesis investigates flow behind two different swirl generator apparatus. While the first one (“BUT” swirl generator) was designed at our department the second one (“UPT” swirl generator) is outcome of the research of the hydraulic group from the Politehnica University of Timisoara in Romania. The detailed description of both swirl generators is presented in section 4 . Consequently this thesis is later divided into two main parts, each of them devoted to study of the flow produced by the particular generator.

In the first part the comprehensive experimental and numerical investigation of swirling flow is carried out using the “BUT” swirl generator apparatus. Both the energy and dynamical aspects of the resulting swirling flow with the spiral vortical structure are accessed using the methods summarized in section 3 and aims to bring a new findings and summaries to the field of spiral vortex breakdown.

In the second part the POD technique described in section 3.3 is applied to both “BUT” swirl generator and “UPT” swirl generator in order to assess the energy-dynamical description of these decelerated flows based on the spatio-temporal information extracted by the POD technique.

It is POD which allows better understanding of the flow behavior. For example strong advantage of POD applied on 2D or 3D flow fields in comparison with FFT obtained from the signal in the discrete points is that POD provides complete spatial representation of modes besides only temporal view obtained by FFT. This brings new view for research of decelerated swirling flows. In last several years the POD technique started to be widely used for full range of applications. The medical application of POD for transient turbulent flow over one cardiac cycle is presented in [29]. The civil engineering application of POD for

turbulent flow inside a street canyon was investigated in [36]. The applications of POD analysis to extract the vortex shedding in the near wake of cylinder are presented in [66] and [71]. Several studies are concerned with turbulent jets [50] and swirling jets undergoing vortex breakdown [63], [64].

The utilization of POD in the field of turbomachinery is relatively new and was first introduced by our department [77], [78], [83]. One of the outcomes of this thesis is comprehensive utilization of POD for the study of the swirling flows where the spiral vortical structure appears. Moreover in case of the “UPT swirl generator” the results of POD analysis presented in section 17 are used to study possible ways to control and mitigate the vortex rope development in the draft tube of real hydraulic turbines and enhance overall turbine efficiency and operation reliability. The active control method in a form of axial water jet injection along the diffuser axis is utilized.

The POD analysis of “UPT” swirl generator is consequence of the collaborative work established during my internship at Politehnica University of Timisoara in 2012.

3 THEORY AND APPLIED METHODS

Since the proposed study is based on both the experimental measurements and the numerical calculations the wide range of available methods are utilized. Measurements of velocity fields are carried out by laser Doppler anemometry (LDA) described in subsection 3.1. Dynamical behavior of the flow is extracted using the fast Fourier transformation (FFT) of measured signal from both the static pressure signal and LDA velocity signal. For the numerical calculations the approach employing the Reynolds averaged Navier-Stokes equations (RANS) together with the specified turbulence model and non-commercial software OpenFOAM are used, see sections 3.2 and 11 . The proper orthogonal decomposition (POD) is applied as the post-processing method for description of the spatio-temporal behavior of the flow, see section 3.3. Finally the energetic assessment of the swirling flows is evaluated using several integral characteristics, see section 3.4.

3.1 LASER DOPPLER ANEMOMETRY (LDA)

The Laser Doppler Anemometer, or LDA, is a widely accepted tool for fluid dynamic investigations in gases and liquids and has been used as such for more than three decades. It is a well-established technique that gives information about flow velocity.

Its non-intrusive principle and directional sensitivity make it very suitable for applications with reversing flow, chemically reacting or high-temperature media and rotating machinery, where physical sensors are difficult or impossible to use. It requires tracer particles in the flow [13]. The overall view of LDA measuring principle is presented in Figure 4

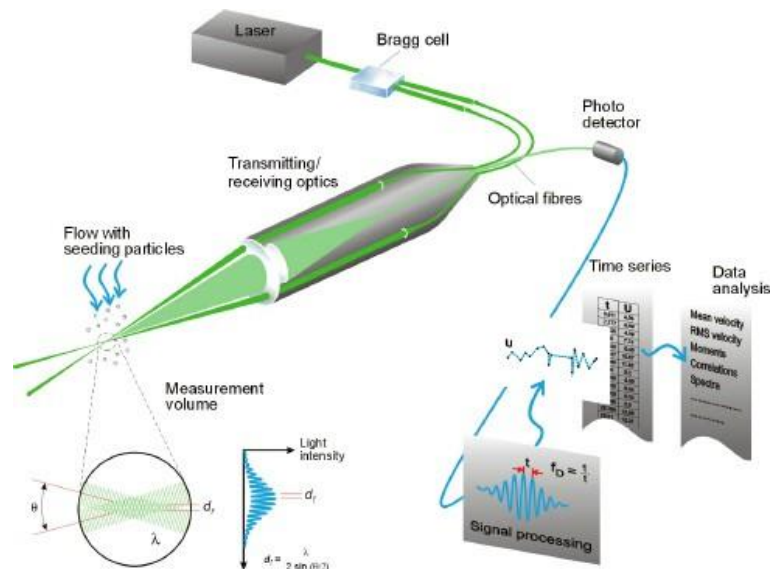


Figure 4 Graphically visualized principle of LDA [18]

3.1.1 Principle

Advanced systems may include traverse systems and angular encoders. A Bragg cell is often used as the beam splitter, see Figure 5. It is a glass crystal with a vibrating piezo crystal attached. The vibration generates acoustical waves acting like an optical grid.

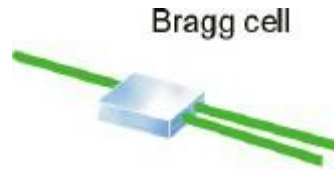


Figure 5 The Bragg cell used as a beam splitter [18]

The output of the Bragg cell is two beams of equal intensity with frequencies f_0 and f_{shift} . These are focused into optical fibers bringing them to a probe. In the probe, the parallel exit beams from the fibers are focused by a lens to intersect in the probe volume. The probe volume is typically a few millimeters long. The light intensity is modulated due to interference between the laser beams. This produces parallel planes of high light intensity, so called fringes. The fringe distance d_f is defined by the wavelength of the laser light and the angle between the beams:

$$d_f = \frac{\lambda}{2 \sin(\theta/2)} \quad (3.1)$$

Each particle passage scatters light proportional to the local light intensity.

Flow velocity information comes from light scattered by tiny "seeding" particles carried in the fluid as they move through the probe volume. The scattered light contains a Doppler shift, the Doppler frequency f_D , which is proportional to the velocity component perpendicular to the bisector of the two laser beams, which corresponds to the x axis shown in the probe volume.

The scattered light is collected by a receiver lens and focused on a photo-detector. An interference filter mounted before the photo-detector passes only the required wavelength to the photo-detector. This removes noise from ambient light and from other wavelengths [13].

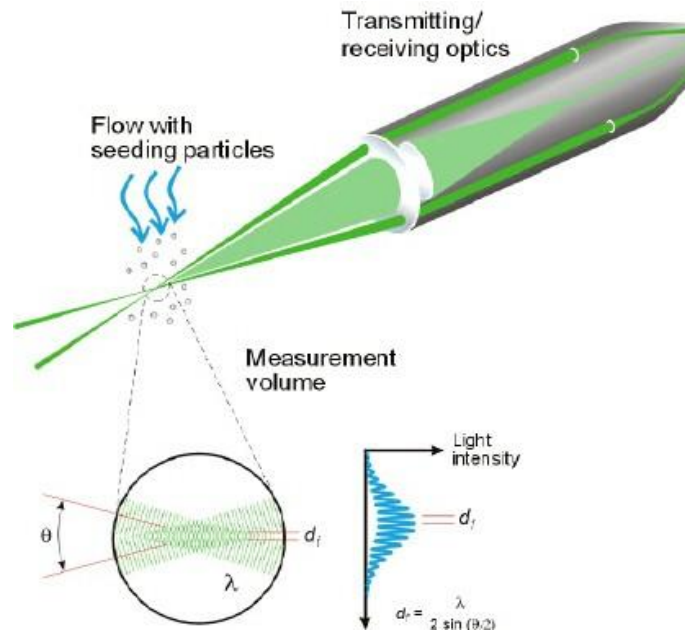


Figure 6 LDA probe volume [18]

The photo-detector converts the fluctuating light intensity to an electrical signal, the Doppler burst, which is sinusoidal with a Gaussian envelope due to the intensity profile of the laser beams. The Doppler bursts are filtered and amplified in the signal processor, which determines f_D for each particle, often by frequency analysis using the robust Fast Fourier Transform algorithm. The fringe spacing, d_f provides information about the distance travelled by the particle, see Figure 6. The Doppler frequency f_D provides information about the time:

$$t = 1/f_D \quad (3.2)$$

Since velocity equals distance divided by time, the expression for velocity thus becomes:

$$V = d_f \cdot f_D \quad (3.3)$$

3.1.2 Determination of the sign of the flow direction

The frequency shift obtained by the Bragg cell makes the fringe pattern move at a constant velocity. Particles which are not moving will generate a signal of the shift frequency f_{shift} . The velocities U_{pos} and U_{neg} will generate signal frequencies f_{pos} and f_{neg} , respectively. The frequency shift is drawn in Figure 7

LDA systems without frequency shift cannot distinguish between positive and negative flow direction or measure zero velocity [13].

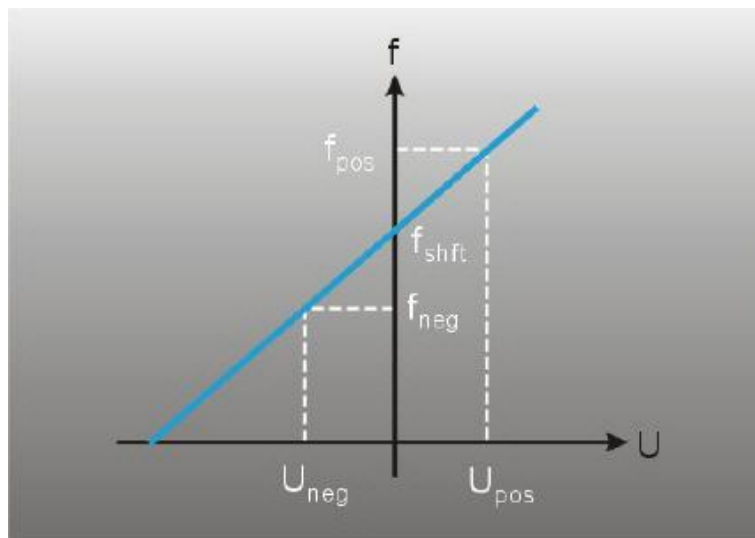


Figure 7 Doppler frequency to velocity transfer function for a frequency shifted LDA system [18]

3.1.3 Two- and three-component measurements

To measure two velocity components, two extra beams can be added to the optics in a plane perpendicular to the first beams, see Figure 8.

All three velocity components can be measured by two separate probes measuring two and one components, with all the beams intersecting in a common volume as shown below. Different wavelengths are used to separate the measured components. Three photo-detectors

with appropriate interference filters are used to detect scattered light of the three wavelengths [13].

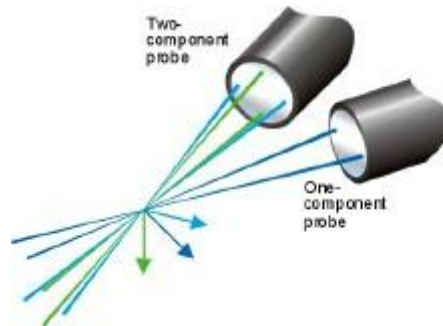


Figure 8 LDA optics for measuring three velocity components [18]

3.2 COMPUTATIONANAL FLUIDS DYNAMICS (CFD)

Nowadays the computational fluid dynamic and relevant commercial software codes are well known and widely used for broad range of fluid flows applications. In this thesis both the commercial CFD software ANSYS Fluent and open source CFD code OpenFOAM are used.

While the numerical simulation of “BUT” swirl generator is carried out using OpenFOAM in version 2.2.2 the ANSYS Fluent R14 was used for calculation of “UPT” swirl generator. For generation of computational grids of both “BUT” and “UPT” swirl generators the Gambit software was used.

Both calculations employ the Reynolds Average Navier-Stokes approach together with specified turbulence models. Two kinds of turbulence models are used. While for the calculation of “BUT” swirl generator using the OpenFOAM the realizable k-ε turbulence model is considered the calculation of “UPT” swirl generator is carried out with the Reynolds stress model (RSM) which is well implemented in ANSYS Fluent.

Detailed descriptions of numerical calculations are presented in section 11 for case of “BUT” swirl generator and in section 17.1 for case of “UPT” swirl generator.

3.2.1 Reynolds Averaged Navier-Stokes (RANS)

Solution of the RANS equations together with a specified turbulence model and wall function is typical engineering approach for the turbulent flow computations.

The unsteady Reynolds Averaged Navier-Stokes (URANS) equations for incompressible flow are written

$$\frac{\partial \bar{v}_i}{\partial t} + \frac{\partial \bar{v}_i}{\partial x_j} \bar{v}_j = -\frac{1}{\rho} \frac{\partial \bar{p}}{\partial x_i} + \frac{\partial}{\partial x_j} \left(\nu \frac{\partial \bar{v}_i}{\partial x_j} - \overline{v'_i v'_j} \right) + g_i \quad (3.4)$$

By averaging the new term representing the correlation between fluctuating velocities called Reynolds stress tensor appears.

$$\tau_{ij} = \rho \overline{v'_i v'_j} \quad (3.5)$$

The Reynolds stress tensor is generally unknown, makes the system of the equations unsolvable and must be modeled in order to eliminate number of unknowns in URANS equations.

TURBULENCE MODELLING

In order to model Reynolds stress tensor many different approaches were developed [19]. The two-equations models using Boussinesque assumption are the most common. The Boussinesque assumption relates the Reynolds stress tensor to the strain tensor and turbulent viscosity as

$$\overline{v'_i v'_j} = -2\nu_t \bar{S}_{ij} + \frac{2}{3} \delta_{ij} k \quad (3.6)$$

where $\bar{S}_{ij} = \frac{1}{2} \left(\frac{\partial \bar{v}_i}{\partial x_j} + \frac{\partial \bar{v}_j}{\partial x_i} \right)$ is rate-of-strain tensor and $k = \frac{1}{2} \overline{v'_i v'_i}$ is turbulent kinetic energy. The last term $\frac{2}{3} \delta_{ij} k$, so called turbulent pressure, is added to make equation valid when it is contracted. This is a drastic simplification, since it enforces turbulent isotropy, but the 6 unknown turbulent stress components are now replaced with only one new unknown, the turbulent viscosity ν_t . The most common two-equation models are as follows: $k - \epsilon$ [45] and its enhanced variants (RNG $k - \epsilon$, Realizable $k - \epsilon$), $k - \omega$ [110] and $k - \omega$ SST [51]. Nevertheless more complex models abandoning the isotropic eddy-viscosity hypothesis also exist. The Reynolds stress model (RSM) closes the RANS and URANS equations respectively by solving transport equations for the component of Reynolds stress tensor, together with an equation for the dissipation rate. This means that five respectively seven additional transport equations are required for 2D respectively 3D flow. The sufficient ability of RSM model to predict main flow features of high swirling flow is presented in [32].

In RANS respectively URANS calculations the turbulence model has been found to be of high importance for an accurate prediction of complex swirling flows where the vortex structure dominates [23], [79]. Ruprecht et al. [87] have shown the large influence of used turbulence model, to perform proper simulation of the vortex rope in an elbow draft tube. By comparison of computed and measured pressure pulsations was concluded, that the vortex rope is strongly damped by any of the turbulence models.

3.3 PROPER ORTHOGONAL DECOMPOSITION (POD)

Proper orthogonal decomposition (POD) was introduced into the field of fluid mechanics by Lumley [47], [6] as a technique which enables to bridge time and frequency domains and obtains spatio-temporal information about the flow in form of spatio-temporal eigenfunctions. Comprehensive theoretical description of POD, including classical approach and its properties, can be found in [30]. POD provides a basis for the modal decomposition of a set of functions and most efficient way of capturing the dominant components, i.e. coherent structures. The POD can be used to analyze experimental as well as numerical data being applied to scalar or vectorial functions. The scalar function $p(\mathbf{x}, t_k)$, e.g. pressure field, is considered in the following theoretical explanation. For instance, a set of data $p(\mathbf{x}, t_k)$ as a

function of physical space \mathbf{x} and discrete time t_k , can be expressed using POD as a set of orthogonal spatial basis functions $\phi_i^k(\mathbf{x})$ (i.e. spatial modes), and temporal functions $a_k(t_k)$ (i.e. temporal modes), respectively. Where $i = 1, 2, \dots, N$, N is the number of grid points and $k = 1, 2, \dots, M$, M is the number of snapshots. Accordingly, the approximation of the data set onto the first k snapshots can be written in terms of the spatial and temporal functions as follows

$$\hat{p}_i(\mathbf{x}, t_k) = \sum_{k=1}^K a_k(t_k) \phi_i^k(\mathbf{x}) \quad (3.7)$$

where $K < M$ and approximation onto the first K functions has the largest mean square projection [29].

In method of snapshots suggested by Sirovich [89], the general $N \times N$ eigenvalue problem is reduced to $M \times M$ eigenvalue problem. Especially, this solution brings a substantial reduction of computational effort if the number of grid points N significantly exceeds number of data set snapshots. The numerical simulation is an appropriate example to use the snapshot method. The inner product between every pair of the pressure fields, i.e. snapshots, is the temporal correlation matrix $\mathbf{C}(t'_k, t_k)$ used as the kernel and defined in the discrete form by eq. (3.8):

$$\mathbf{C}(t'_k, t_k) = M^{-1} \mathbf{P}'(\mathbf{x}, t_k) \mathbf{P}(\mathbf{x}, t_k) \quad (3.8)$$

The $\mathbf{P}(\mathbf{x}, t_k)$ is the data matrix where the columns are snapshots $p(\mathbf{x}, t_k)$.

$$\mathbf{P}(\mathbf{x}, t_k) = \begin{bmatrix} p_{x_1, y_1, z_1, t_1} & \cdots & p_{x_1, y_1, z_1, t_M} \\ \vdots & \ddots & \vdots \\ p_{x_N, y_N, z_N, t_1} & \cdots & p_{x_N, y_N, z_N, t_M} \end{bmatrix} \quad (3.9)$$

Solving the eigenvalue problem of form

$$\mathbf{C}\mathbf{A} = \lambda\mathbf{A} \quad (3.10)$$

we obtain the matrix of eigenvectors \mathbf{A} where \mathbf{a}_k is the k -th column and corresponding eigenvalues λ_k . Because the \mathbf{C} is the temporal correlation matrix the resulting eigenvectors are directly temporal modes. The correlation matrix \mathbf{C} is symmetric and positive definite. Thus the eigenvalues are real and define the contribution of the coherent structure into complex flow [48]. Correspondingly, the eigenvalue magnitude of one single mode represents an amount of this contribution from the total sum $\sum_{i=1}^N p(\mathbf{x}, t_k) p(\mathbf{x}, t_k)$ [29]. In order to deal only with the most dominant modes the temporal modes are sorted according to the eigenvalue magnitude. Then the spatial shape $\phi_i^k(\mathbf{x})$ of the most dominant modes is calculated based on the orthogonal property

$$\phi_i^k(\mathbf{x}) = \sum_{k=1}^M p_i(\mathbf{x}, t_k) a_k(t_k) \quad (3.11)$$

where $a_k(t_k)$ is the k -th element of the k -th eigenvector of correlation matrix \mathbf{C} .

The backward reconstruction of instantaneous snapshot of pressure or velocity field retrospectively can be obtained based on the computed spatial and temporal POD modes using eq. (3.12):

$$\hat{p}_i(\mathbf{x}, t_k) = \lambda_0^{-1} M^{-1} a_0(t_k) \phi_i^0(\mathbf{x}) + \sum_{k=1}^K \lambda_k^{-1} M^{-1} a_k(t_k) \phi_i^k(\mathbf{x}) \quad (3.12)$$

where K is number of total spatio-temporal modes including the mode #0 associated with the mean flow (i.e. time averaged), M number of snapshots and λ corresponding eigenvalue. The full range of instantaneous pressure fields can be reconstructed using eq. (3.12) for time sequence t in which data samples for POD decompositions were collected.

Further utilization of POD with description of application to the swirling flows with the coherent vortex structure is presented in the second part of this thesis, see sections 15 and 17 .

3.4 ENERGETIC ASSESSMENT

The main purposes to use the draft tube for the reaction turbine are that the turbine can be placed above the level of the tail water without losses of available head and transformation of residual kinetic energy at the turbine outlet into the static pressure thereby increasing overall turbine efficiency. In order to assess energetic performance of the diffuser the hydraulic efficiency η , pressure recovery coefficient c_p and hydraulic loss coefficient ξ will be evaluated.

$$\eta = \frac{p_{s(2)} - p_{s(1)}}{p_{d(1)} - p_{d(2)}} \quad (3.13)$$

$$c_p = \frac{p_{s(2)} - p_{s(1)}}{\frac{1}{2} \rho \alpha_{(1)} \bar{v}_{(1)}^2} \quad (3.13)$$

$$\xi = \frac{2}{\bar{v}_{(2)}^2} \left[\left(\frac{\alpha_{(1)} \bar{v}_{(1)}^2 - \alpha_{(2)} \bar{v}_{(2)}^2}{2} \right) + \frac{p_{s(1)} - p_{s(2)}}{\rho} \right] \quad (3.15)$$

In above written equations the static pressure p_s , dynamic pressure p_d , mean velocity \bar{v} and kinetic energy correction factor α are found in relevant cross sections described by numbers in brackets, where 1 means upstream and 2 downstream position. The variation of these integral quantities from diffuser inlet to the diffuser outlet for various discharges and influence of spiral vortex structure will be discussed.

Using POD decomposition described in section 3.3 the complex flow will be decomposed and the most dominant modes responsible for the dynamic behaviour of the compact coherent structure will be identified. This is ensured by the fact that eigenvalue λ_k of single mode

represents its particular contribution Λ_k to the complex unsteady flow field, which is equal to the sum over all eigenvalues.

$$\Lambda_k = \frac{\lambda_k}{\sum_{i=1}^N \lambda_i} \quad (3.16)$$

Let's consider the unsteady static pressure field $p(\mathbf{x}, t)$ for example from CFD calculation. The ensemble of snapshots is made dimensionless with respect to the dynamic pressure at the inlet of the diffuser.

$$p^*(\mathbf{x}, t) = \frac{p(\mathbf{x}, t)}{1/2 \rho v_{ref}^2} \quad (3.17)$$

Where the reference velocity v_{ref} at the diffuser inlet is computed from discharge and by considering the inlet diameter d of diffuser as following:

$$v_{ref} = \frac{4Q}{\pi d^2} \quad (3.18)$$

Afterwards this allows clear comparison of energy contribution of modes when the discharge is changed. Finally the spatio-temporal modes are calculated, sorted by magnitude of relevant eigenvalues and marked by increasing numbers starting by one for the most energetic. The lower modes (according to assigned numbers) describe regular movement of coherent structure and higher modes are responsible for disintegration and dissipation of the vortex rope [83].

Consequently the spatio-temporal variation of modes, when the discharge increases/decreases, will be carried out and possible influence on changes in diffuser performance described by equations (3.13) – (3.15) will be discussed. Distinguishing of the different modes and their energetic contribution also forms important base for development of control mechanism of the unstable swirling flow. In other words it enables better understanding in changes of flow field, when the external forces or shape modifications are applied in order to suppress vortex rope formation and enhance diffuser performance. The influence of external force (axial water jet) to the decomposed flow fields is scope of second part of this thesis.

4 TEST CASES

The main part of present study is carried out for a test case of decelerated swirling flow in conical diffuser as a component of swirl generator apparatus included in a test rig situated in a hydraulic laboratory of V. Kaplan Department of Fluid Engineering. Additionally, due to collaborative reasons, the part of the study is concerned with a test case of swirl generator apparatus developed by research group at “Politehnica” University of Timisoara in Romania. Both above mentioned test cases are described in following subsections.

4.1 SWIRL GENERATOR APPARATUS DESIGNED AT BRNO UNIVERSITY OF TECHNOLOGY (“BUT”)

The swirl generator apparatus consists of two main parts, the swirl generator itself and the conical diffuser. The swirl generator was designed so that it converts fully axial flow into flow with significant tangential component. Ten stationary blades are situated on the inner spike which acts as a hub. The trailing edge deflection from axial direction is 30 degrees at spike side and linearly changes to 50 degrees towards outer wall. The blade length is 40 mm and blade thickness is 1 mm. The leading edge is rounded and trailing edge has sharp end. The blade geometry shown in Figure 9 was created in BladeGen software and then exported in *.igs format to the meshing software.

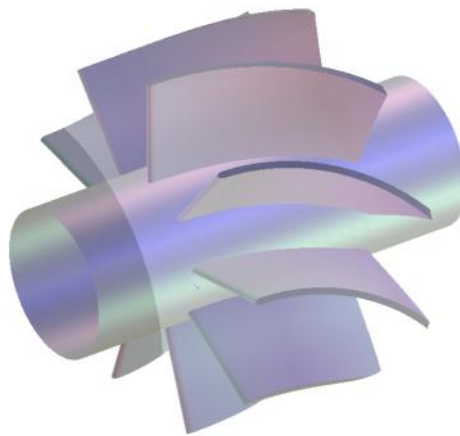


Figure 9 Resulting blades shape constructed in BladeGen software

The conical diffuser is connected downstream of the swirl generator. The inlet to the diffuser cone is 115 mm behind the blade trailing edge. Two diffusers were prepared for the experimental investigation. The transparent diffuser made from the plexiglas with five holes for the pressure sensors alongside of the cone was used for LDA measurements and visual observation of the cavitating vortex. The second diffuser includes totally 20 holes for the pressure sensors and is used for the measurements of pressure pulsations. The longitudinal cross-section through the swirl generator apparatus is shown in Figure 10 while the main dimensions are presented in Figure 11.

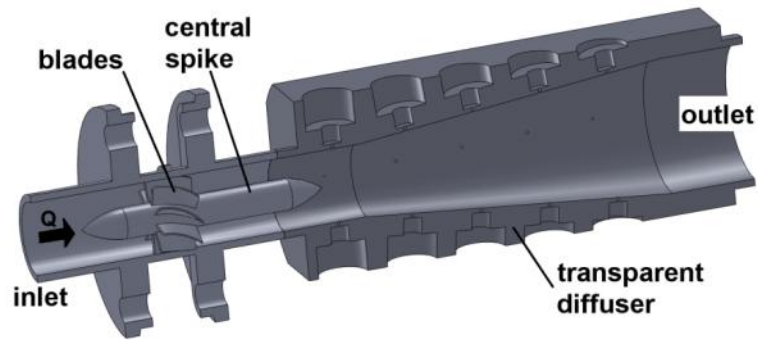


Figure 10 Scheme of swirl generator apparatus

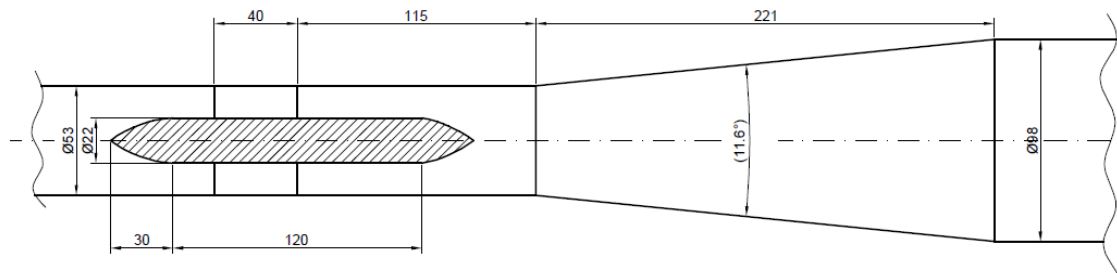


Figure 11 Dimensions of the swirl generator apparatus

4.2 SWIRL GENERATOR APPARATUS DESIGNED AT “POLITEHNICA” UNIVERSITY OF TIMISOARA (“UPT”)

This swirl generator apparatus has been developed at “Politehnica” University of Timisoara (UPT) as a simplified device for experimental investigation of decelerated swirling flow with self-induced instability (e.g. precessing helical vortex). The swirl generator apparatus is installed in the test rig with a closed loop hydraulic circuit described in [8]. The swirl generator provides at cone inlet a flow similar to the one encountered in the draft tube of Francis turbine operated at partial discharge, e.g. at 70% of the best efficiency point [98]. The swirl apparatus test section is shown in Figure 12 with position of pressure transducers marked as MG0 – MG3. Detailed information about design and manufacturing of the swirl generator can be found in [101], [9]. The axial water injection through the turbine hub into the draft tube cone was introduced by Susan-Resiga et al. [102] as an active control technique for vortex rope mitigation in hydraulic turbines. This technique is well integrated in swirl generator apparatus for experimental investigation on simplified test case. The water can be supplied in three different ways. Firstly, the water jet is supplied from the tank using an auxiliary energy source. Secondly, the water is collected from the discharge cone outlet supplying the jet without any additional energy source, which is so called flow-feedback method (FFM) introduced by Resiga et al. [99] and tested by Tanasa et al. [104]. Thirdly, a combination of first two methods introducing the flow feedback method with additional energy (FFM+) was experimentally investigated by Tanasa et al. [105]. Extensive experimental investigations performed with axial water injection method showed that the wall pressure fluctuations are successfully mitigated when the jet reaches 12% of the main flow discharge. Nevertheless the 12% jet discharge bypassing the turbine runner would be too large, since it is associated with the volumetric loss which cannot be transformed to the power

generation. Therefore, about 10% of the jet discharge is supplied by the plain flow feedback, and only 2% boost is insured by additional energy source using FFM+. The previous numerical results [53] proved very good ability of this technique to mitigate the vortex rope and its associated pressure pulsations.

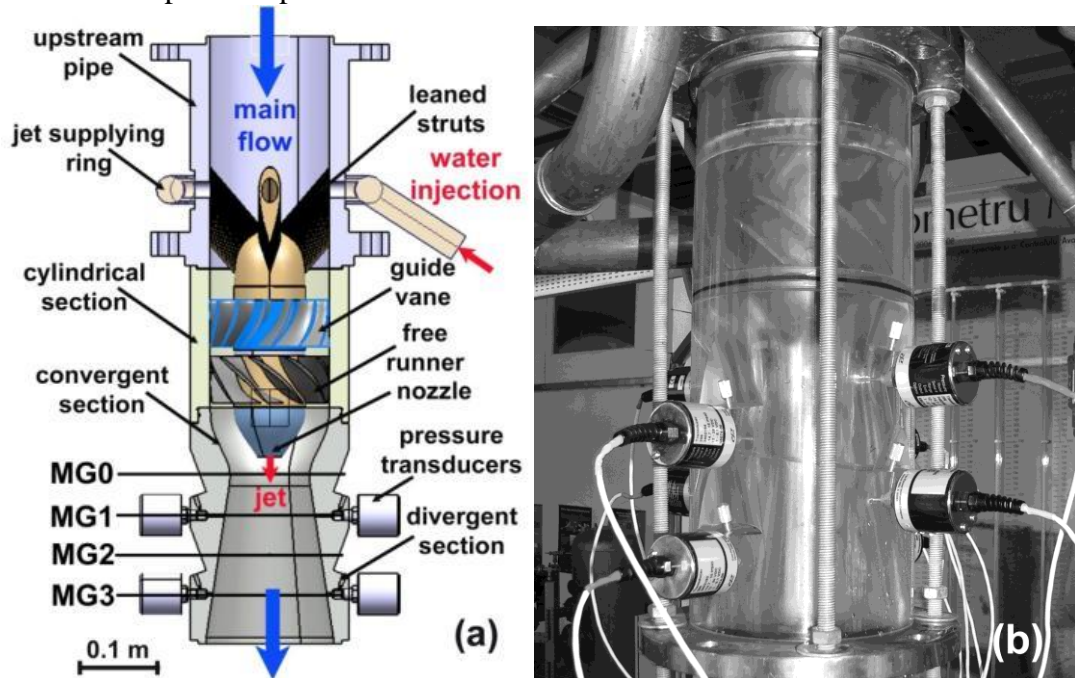
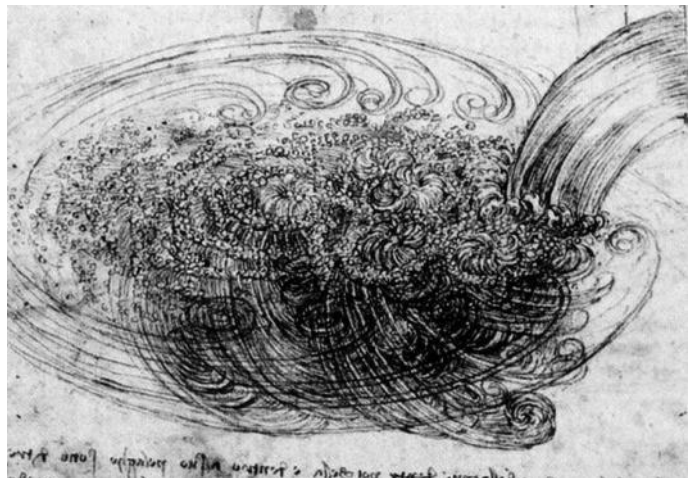


Figure 12 Swirl generator apparatus installed on the experimental test rig: a cross section (a) and a general view (b)

The decelerated swirling flow with the vortex rope in this particular geometry is defined as a test case problem, because the geometry and the experimental data are available [72]. Several groups have already validated their numerical results against experimental data in order to assess the accuracy of the computer codes [5], [53], [67], [72], [90]. However, a deep analysis of the flow dynamics using an appropriate tool like POD is believed to bring a new perspective. As a result, this investigation paves the way towards practical applications in real hydraulic turbines.

PART I - INVESTIGATION OF SWIRLING FLOW GENERATED BY THE “BUT” SWIRL GENERATOR



“Observe the motion of the surface of the water, which resembles that of hair, which has two motions, of which one is caused by the weight of the hair, the other by the direction of the curls; thus the water has eddying motions, one part of which is due to principal current, the other to the random and reverse motion.”

Leonardo da Vinci (April 15, 1452 – May 2, 1519)

5 EXPERIMENTAL MEASUREMENTS

The experimental measurements were performed in the laboratory of Viktor Kaplan Department of Fluid Engineering. The existing circuit of the gravity driven flow with the constant head was equipped with the section including the swirl generator apparatus. The main geometrical features of test rig and location of the swirl generator apparatus are shown in the scheme, see Figure 13.

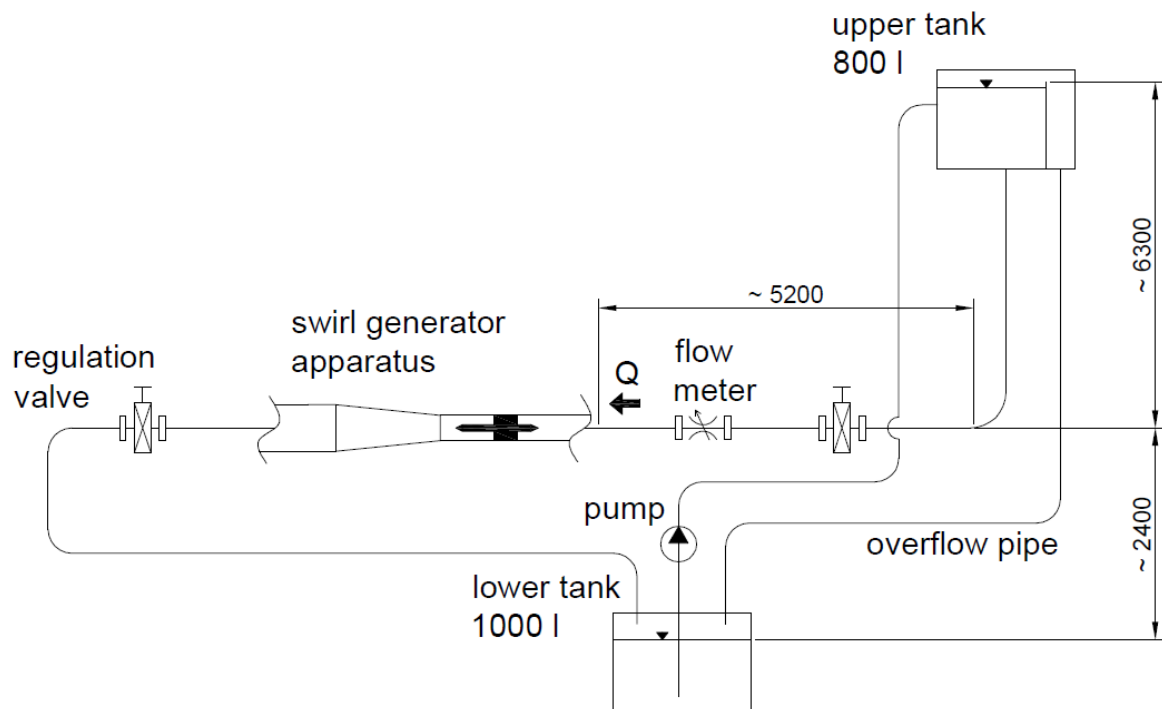


Figure 13 Scheme of the experimental test rig with the swirl generator apparatus

The test rig consists of lower and upper tanks, the centrifugal pump supplying the water from the lower to the upper tank, the pipeline system, flow meter, thermo meter and control valve. The upper tank is equipped by the overflow (ensuring the constant head) where the excess water flows through the overflow pipe back to the lower tank.

The three main measurements were performed:

- The LDA measurement of axial and tangential velocities in the conical diffuser
- The image recording of the cavitating vortex structure using the high speed camera
- The complex measurements of the pressure pulsations in the diffuser

Each of measurement is comprehensively analyzed in the following sections. The additional post processing methods applied to the measured data are presented in the corresponding subsections.

5.1 MEASURING EQUIPMENTS AND UNCERTAINTIES

In this subsection the measuring equipments used to obtain experimental data of “BUT” swirl generator are described together with the uncertainties of particular measuring apparatus.

The experimental test rig was equipped with the magnetic-inductive flow meter ELA MQI 99 with accuracy 0.5% from the measured value. The temperature was measured using thermometer LA340 with accuracy 0.5%. The actual net head can be evaluated from the pressure sensor p_0 situated in front of the swirl generator, see Figure 23. As can be seen the static pressure respectively the net head vary with the actual flow rate. Therefore inaccuracy in the net head determination is related to the inaccuracy of mean static pressure measurements in p_0 sensor location.

In case of LDA measurements the DANTEC laser and optic apparatus together with software environment was used. The uncertainties are presented as the variation of Random Mean Square Velocity (u_{RMS}) for each measured point in a form of error bars. See the section 12.2 where the measured velocity profiles are compared with the numerically computed ones.

For the unsteady pressure measurements the BD piezoelectric sensors were used with accuracy 0.25% to full scale output (according to standard IEC 60770). The measuring ranges of particular pressure sensor are presented in section 7 dealing with the pressure measurements.

5.1.1 Measuring uncertainties

In measurements two main kinds of uncertainties are considered. While the uncertainties of type A yields statistics processing of data, the uncertainties of type B include everything which does not relate with the statistics. It means mainly the uncertainty of measuring equipment (directly measured quantity), from which the non-direct measured quantities are further evaluated.

In following the uncertainties of type B are evaluated for the pressure and flow rate measurements. For the pressure the uncertainty of type B is calculated considering only the influence of the sensor accuracy. The uncertainties of the signal converter and the sensor calibration are neglected due to one order higher accuracy. The uncertainty of type B for the pressure measurements are then calculated using equation:

$$U_{B,p} = A \cdot R \quad (5.1)$$

where A is the pressure sensor accuracy and R is the pressure sensor range. As was mentioned above the pressure sensors used for the experimental measurements have accuracy $A = 0.0025$ with used ranges $R = 1.6, 2.5$ and 4 bars.

Table 1 Uncertainties of pressure sensors

Sensor range (bars)	Uncertainty of type B (bars)
1.6	0.004
2.5	0.00625
4	0.01

The uncertainties of type B for measurements of the flow rate are calculated from the flow meter accuracy and actual measured flow rate.

$$U_{B,Q} = A \cdot Q \quad (5.2)$$

The accuracy of flow meter used for the experimental measurements is $A = 0.005$. This leads to uncertainties presented in Table 2 for several flow rates.

Table 2 Uncertainties of flow rate measurements

Flow rate Q (l/s)	Uncertainty of type B (l/s)
5	0.025
7	0.035
9	0.045
11	0.055
13	0.065

6 VELOCITY MEASUREMENTS IN THE CONICAL DIFFUSER

The LDA (Laser Doppler Anemometry) measurements were performed in three cross-sections through the diffuser cone for the flow rates ensuring non-cavitation regimes. The overall view of experimental measurements is shown in Figure 14.



Figure 14 Overall view of LDA measurements

The axial and tangential velocities were measured simultaneously starting 2 mm from the diffuser cone wall and going perpendicularly to the diffuser axis with the 2 mm step for the axial velocity. The measuring step for tangential velocity is different due to curvature of the diffuser cone causing different refraction of the laser beams for each new probe location. The laser probe size is approximately 2 mm long and 0.75 mm wide. In case of measurements of two velocity components (axial and tangential) the argon-ion laser producing two most powerful colors from the light spectra (blue and green) is used. The laser beams are separated through the optical passage with color filters and divided into four (two for axial and two for tangential velocity) laser beams, see Figure 15.

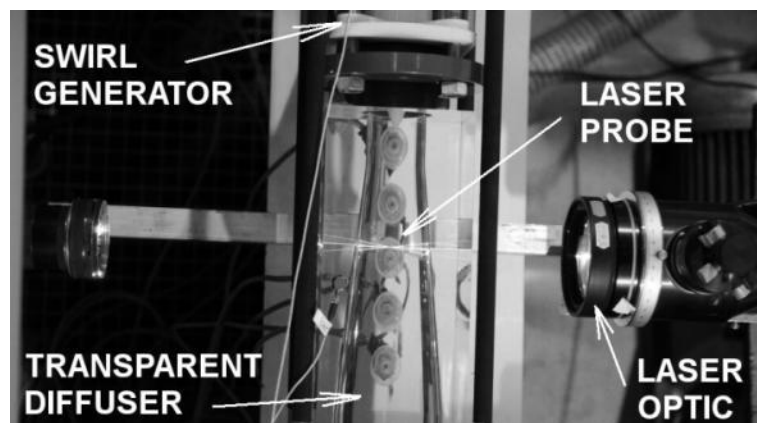


Figure 15 Detailed view of LDA measurements

The velocity measurements were carried out in three locations S1 = 23 mm, S2 = 50 mm and S3 = 75 mm from the beginning of the diffuser cone, see Figure 16. The diameters of measured cross-sections are presented in Table 3. The measured flow rates are $Q = 5, 7, 8$ and 11.5 l/s. Note that velocities for flow rate $Q = 11.5$ l/s were measured only in S2 and S3 cross-sections.

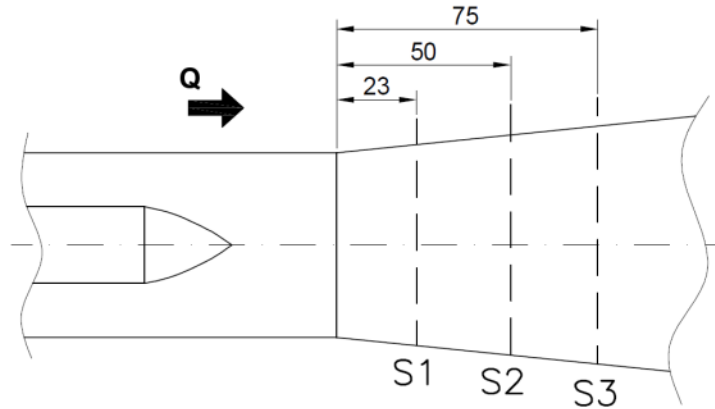


Figure 16 Locations of LDA measurements

Table 3 Diemeteres of measured cross-sections

Cross – section	Diameter (m)
S1	57.7
S2	63.2
S3	68.3

In Figure 17 the measured axial and tangential velocity profiles in all three investigated cross-sections S1, S2 and S3 are plotted for measured flow rates. One can see that magnitude of axial and tangential velocities is almost unchanged in central region when the flow rate increases. The main flow is realized close to the diffuser wall. This is typical for flows where the spiral vortex structure is developed. It is also clear that due to effect of the diffuser flow the pressure increases and thus the axial velocity decreases. This can be seen when the velocity profiles of corresponding flow rate are compared through different cross-sections.

The tangential velocity profile of flow rate $Q = 11.5$ l/s in the last investigated cross-section S3 = 75 mm is with very low magnitude compared to one in S2 cross-section. This can be caused due to decaying process of the vortex structure.

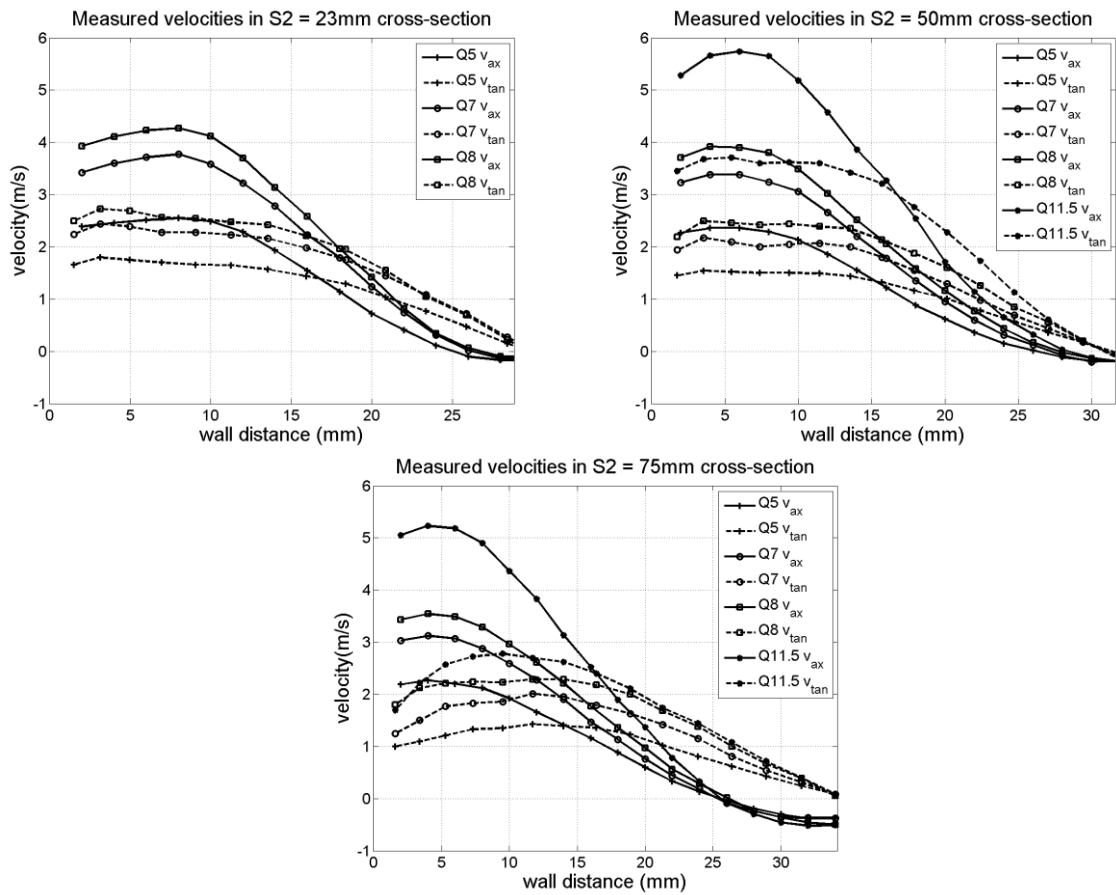


Figure 17 Overview of measured velocity profiles (axial and tangential) in all three cross-sections S1, S2 and S3

From the measured profiles the mean velocity was computed using numerical trapezoid integration. The resulting values are plotted in Figure 18 and Figure 19 for each measured cross-section.

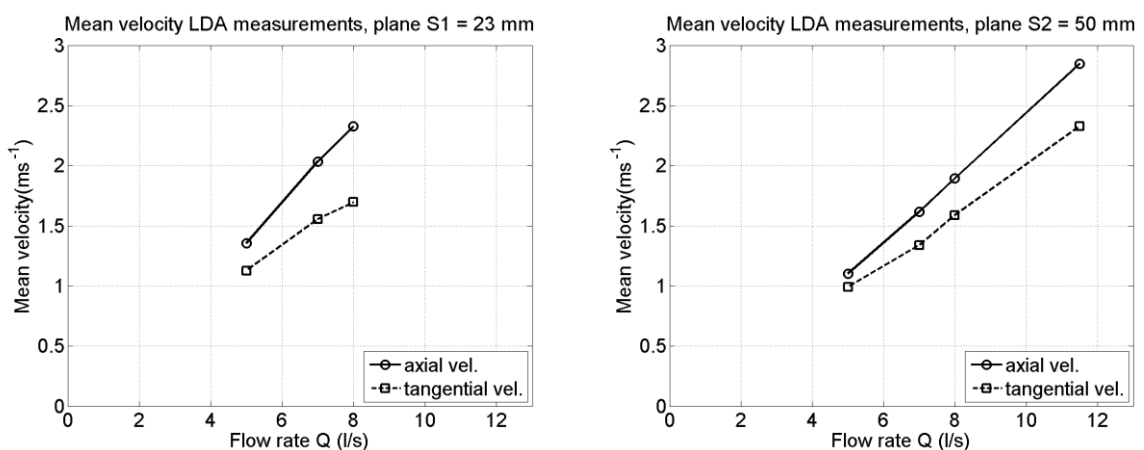


Figure 18 Mean velocity integrated from the velocity profiles (axial and tangential) in cross-sections S1 and S2

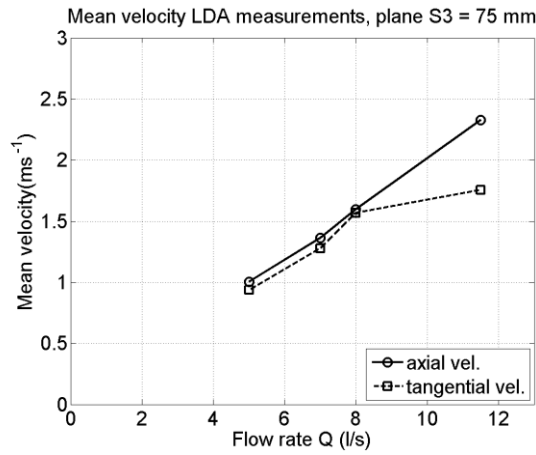


Figure 19 Mean velocity integrated from the velocity profiles (axial and tangential) in cross-sections S3

6.1 VELOCITY UNSTEADINESS

In order to assess unsteadiness in the velocity fields obtained by the LDA measurements it is necessary to make interpolation of the velocity signals which are recorded with the unequal time period. This is caused due to nature of the LDA mechanism where the information is obtained only if the particle in the water passes the laser probe.

The linear interpolation is executed using the script written in MATLAB[®], and then the power spectra are computed for particular measured points. Nonetheless for more accuracy result the advanced statistical methods should be applied [33], [61]. The frequencies of velocity fields averaged alongside measured line are plotted for all three measured cross-sections in Figure 20. One can see that averaged frequency of unsteady velocity field decreases downstream of the diffuser. The identical behavior is observed for pressure measurements and proves significant link between velocity and pressure field.

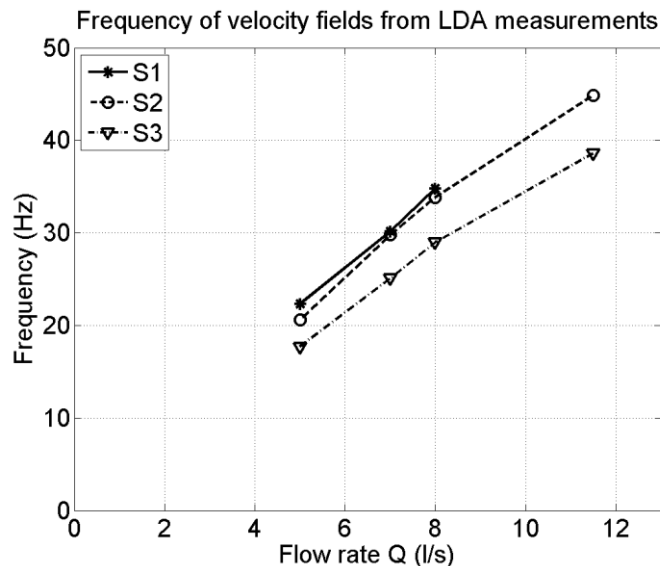


Figure 20 Dominant (rotational) frequency extracted from unsteadiness of velocity measurements

7 UNSTEADY PRESSURE PULSATIONS

The unsteady pressure pulsations are measured in seven locations $p_0 - p_6$. The first pressure sensor p_0 is situated in front of the swirl generator apparatus in distance of 591 mm from the cone inlet, the five pressure sensors are situated in the conical diffuser (sensor p_1 is situated in front of the cone and $p_2 - p_5$ are situated in the cone) and p_6 is placed downstream in the outlet of the diffuser in the distance of 291 mm downstream of cone inlet. The overall view of sensors locations can be seen in Figure 21.

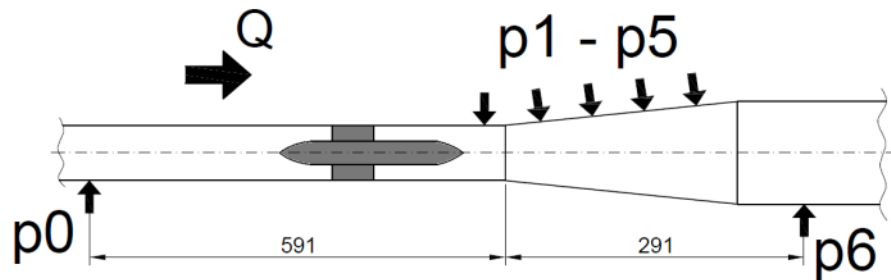


Figure 21 Sensors locations p_0 and p_6 situated in front of swirl generator and at the outlet of the diffuser

The cone inlet has diameter $D = 0.0536\text{m}$, sensor p_1 is located 20 mm in front of the cone inlet while the sensors p_2 is 33.6 mm, p_3 is 83 mm, p_4 is 132.6 mm and p_5 is 182mm downstream of cone inlet. In order to carry out measurement of static pressure correctly the sensor holes are drilled perpendicularly to the inner wall and respect the cone angle. The detailed layout of the sensor locations is in Figure 22 while the dimensionless sensor locations L/D according to cone inlet are presented in Table 4.

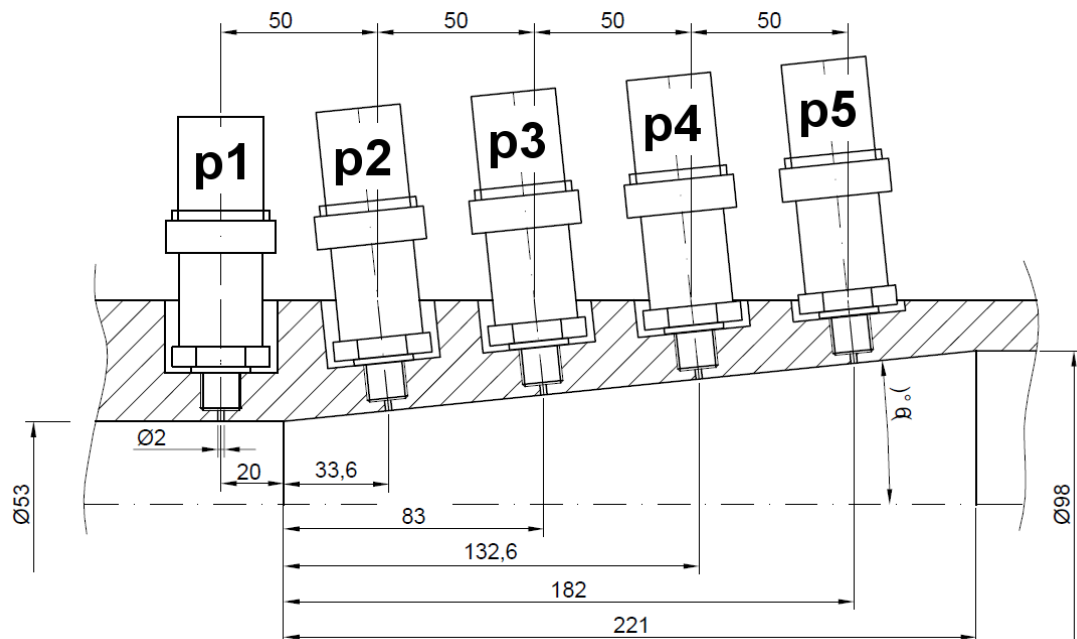


Figure 22 Detailed view to the sensors locations $p_1 - p_5$ in the diffuser

The measuring ranges of particular pressure sensors are presented in Table 4 for sensors p0 – p6. The information regarding to additional sensors are presented in relevant subsections.

Table 4 Measuring ranges of pressure sensors p0 – p6 and locations

Sensor no.	Measuring range (bars)	Location L/D (1)
p0	4	-11.026
p1	1.6	-0.3731
p2	2.5	0.6269
p3	1.6	1.5485
p4	2.5	2.4720
p5	1.6	3.3955
p6	4	5.4291

7.1 MEAN STATIC PRESSURE

First the averaged static pressure is evaluated. The measurements were carried out for flow rates up to 13 l/s with 0.5 l/s step. The evolutions of the mean static pressure for the particular pressure sensors are presented in Figure 23. It is clear that with increasing flow rate we can observe quadratically decreasing value of mean pressure in all sensors locations.

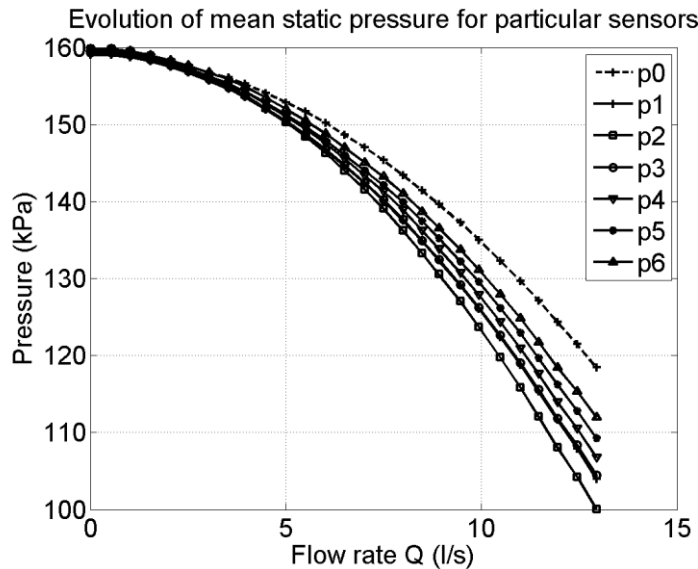


Figure 23 Evolution of the static pressure for full range of measured flow rates

One can see that with increasing flow rate the pressure difference increases between pressure sensor p0 (located in front of swirl generator) and p1 (located in front of conical section of the diffuser). This pressure difference, plotted in Figure 24 (left), is caused by the hydraulic losses within the swirl generator. Due to diffuser effect the pressure increase is expected alongside the diffuser cone. This effect is presented as the difference between pressure sensors p6 and p1, see Figure 24 (right).

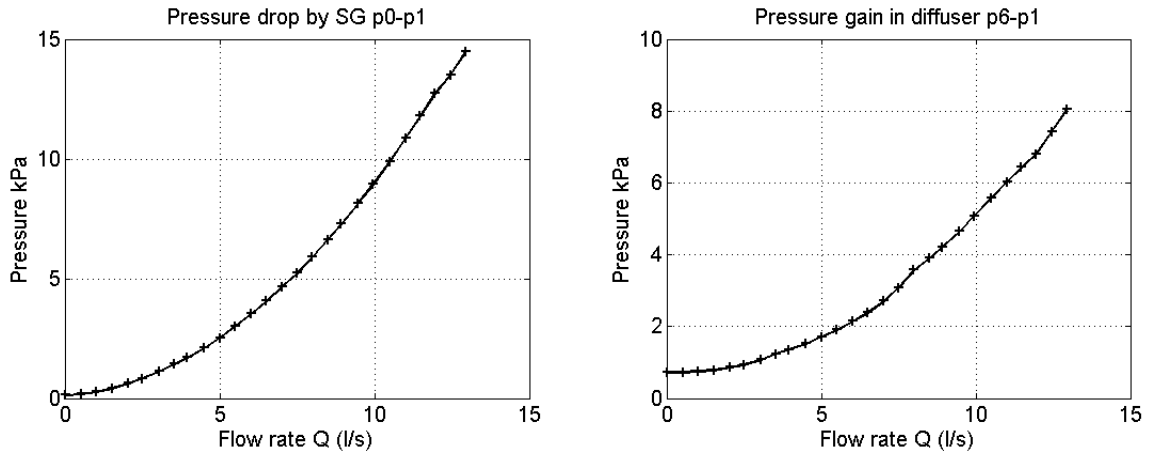


Figure 24 Evolution of pressure drop between p0 and p1 sensors (left) and evolution of the pressure gain (pressure recovery) in diffuser (right) for full range of measured flow rates

In order to compute diffuser performance the pressure recovery c_p is computed according to

$$c_p = \frac{p_{s(i)} - p_{s(1)}}{\frac{1}{2} \rho \bar{v}_1^2} \quad (7.1)$$

The $p_{s(i)}$ is pressure in the i -th location, $p_{s(1)}$ is pressure in the first location and \bar{v}_1 is mean velocity in the first location. Resulting pressure recovery factor is plotted for several of investigated flow rates in Figure 25. The steep drop in pressure recovery in the second sensor location for flow rates $Q > 5$ l/s is caused by the well developed cavitating vortex structure which is most pronounced in this part of the diffuser.

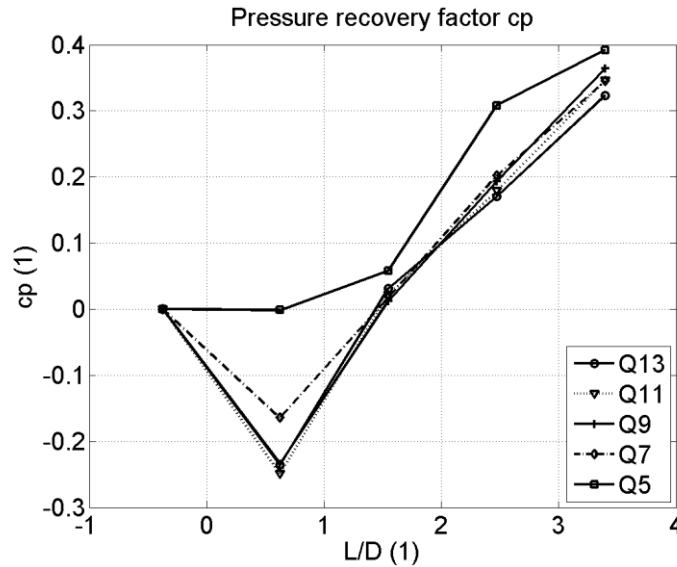


Figure 25 Pressure recovery factor for flow rates $Q = 13, 11, 9, 7$ and 5 l/s

In order to compare flow conditions during the measurements of pressure pulsations in non-transparent diffuser with the flow conditions during the experiments when the cavitating vortex structure was recorded by the high speed camera the Thoma cavitation number σ is evaluated and compared for the both measurements in Figure 26.

$$\sigma = \frac{p_0 - p_v}{\frac{1}{2}\rho\bar{v}_0^2} \quad (7.2)$$

The p_0 and \bar{v}_0 are mean pressure and mean velocity in front of the swirl generator apparatus (sensor p0), ρ is the water density and p_v is the pressure of saturated vapor in water for measured temperature. One can see that both curves are very close to each other, especially for the higher flow rates $Q > 10$ l/s when the cavitating vortex structure is well developed. Therefore we can consider the cavitating vortex structure identical for both of measurements - pressure measurements with non-transparent diffuser and recording of cavitating vortex structure by the high speed camera (see the section 9).

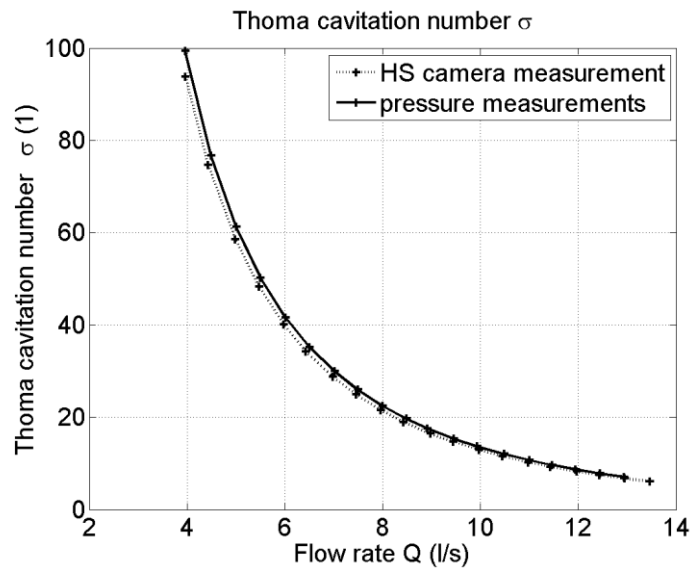


Figure 26 Comparison of Thoma cavitation number of HS camera measurements (transparent diffuser) and pressure measurements (non-transparent diffuser)

7.2 UNSTEADY PRESSURE PULSATIONS

The pressure measurements were performed using non-transparent diffuser with five cross-sections where the pressure sensors can be mounted. Each cross-section includes totally four holes for pressure sensors (each with 90° shift in the circumferential direction). This leads up to 20 holes. Due to limited number of available pressure sensors in our laboratory it was not possible to equip all available holes. Therefore several measurements were performed separately.

Firstly the second and the third cross-sections were equipped with the pressure sensors together with one full row (see Figure 27), secondly the pressure sensors from the second and the third cross-sections were moved to the fourth and fifth cross-sections (see Figure 28).

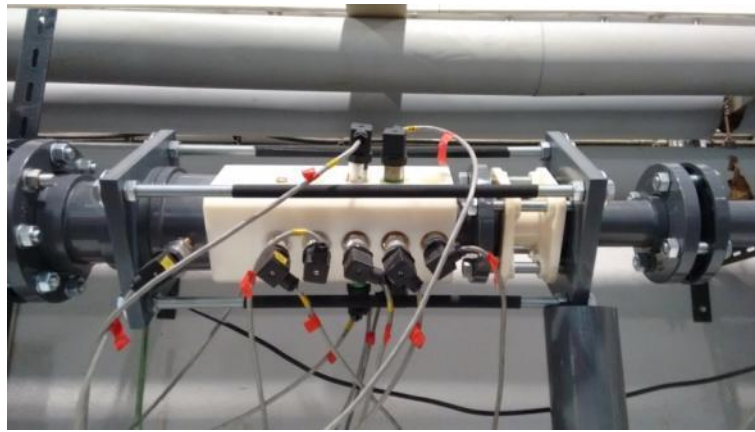


Figure 27 Pressure measurements with fully equipped second and third cross-sections

These two measurements were done for full range of flow rates (0 – 13 l/s) and were used to verify which cross-sections are still sufficient for evaluation of asynchronous pressure pulsations. Due to the vortex decay downstream of the diffuser the assumption is that the pressure amplitudes in the last two cross-sections will be very weak to determine the dominant vortex frequency in the power spectra. The first cross-section was not tested because it was found from previous measurements (LDA and high-speed camera recording) with the transparent diffuser using one sensors row, that the pulsations in the first and the second cross-sections are strong enough.



Figure 28 Pressure measurements with fully equipped fourth and fifth cross-sections

The present results showed that in the fifth cross-section the vortex structure is already too weak that it is not possible to find dominant amplitude of asynchronous frequency corresponding to the vortex rotation. The measurements were performed also to test possible differences in the power spectra of two different sensor pairs. In each cross-section two sensors pairs exists. It was found that except negligible discrepancy in amplitudes the frequency values fit very well comparing two sensors of single sensor pair. Nevertheless in order to evaluate asynchronous pulsations in all cross-sections for identical flow rate all five cross-sections are equipped by two oppositely oriented pressure sensors at the same time.

For this measurement the pressure sensors ($p1^*$ - $p5^*$) were included creating oppositely oriented row (180° shifted in circumferential direction, see Figure 29). This enables to separate pulsations propagated either in longitudinal or in transverse direction in all five cross-sections for identical flow rate.

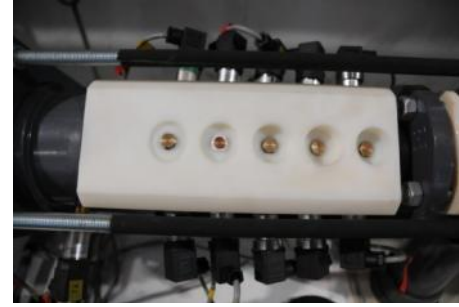
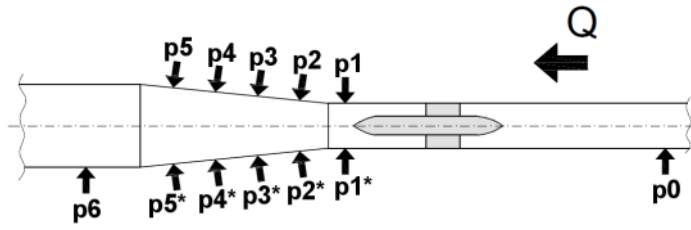


Figure 29 Measurements with fully equipped pressure sensors in two oppositely oriented rows.

The measuring ranges of oppositely oriented sensors (indexed by *) are presented in Table 5.

Table 5 Measuring ranges of pressure sensors p1a – p5a

Sensor no.	Measuring range (bars)
p1*	1.6
p2*	2.5
p3*	1.6
p4*	2.5
p5*	1.6

7.3 DISTINGUISHING BETWEEN SYNCHRONOUS AND ASYNCHRONOUS PRESSURE PULSATIONS ARISING FROM THE SPIRAL VORTEX DYNAMIC

In case of hydraulic machines the movement of corkscrew vortex in the draft tube produces synchronous and asynchronous pulsations. This distinction was introduced by Nishi et al. [57] who devised an analytical method how to separate these components. While the synchronous component has equal phase and amplitude through the whole water conduit, the asynchronous component is a pressure pattern rotating about circumference of the draft tube, i.e. pressure signals in oppositely oriented pressure sensors with inverse phase [22].

The measured pressure signal is decomposed into the synchronous (longitudinal) pulsations

$$p_{synch} = \frac{p_i + p_i^*}{2} \quad (7.3)$$

and to the asynchronous (transverse) pulsations

$$p_{asynch} = \frac{p_i - p_i^*}{2} \quad (7.4)$$

where index number $i = 1 - 5$ refers sensors order in the flow direction. In Table 6 the pressure sensor pairs creating particular cross-sections s1 – s5 are summarized.

Table 6 Sensor pairs locations

Sensor pairs	Location L/D (1)
s1 - p1/p1*	-0.3731
s2 - p2/p2*	0.6269
s3 - p3/p3*	1.5485
s4 - p4/p4*	2.4720
s5 - p5/p5*	3.3955

7.3.1 Asynchronous pressure pulsations

The asynchronous pressure pulsations are realized in a transverse direction. The amplitude-frequency spectra of pressure records were performed for all five cross-sections. While for the cross-sections s1, s2, s3 and s4 the frequencies of asynchronous pulsations are well recognized by the dominant amplitude for the fifth cross-section the amplitudes are too low to determine dominant frequency. Therefore in Figure 30 the asynchronous pressure pulsations are presented only for the first four cross-sections.

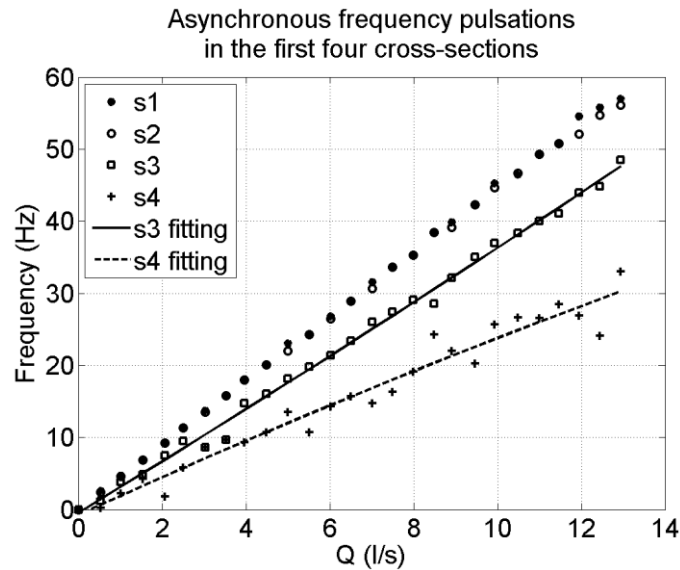


Figure 30 Relation of the vortex rotating frequency (asynchronous pressure pulsations) in the first four cross-sections (s1, s2, s3 and s4) to flow rate

In Figure 31 the amplitudes of asynchronous pressure pulsations are plotted for chosen flow rates $Q = 5, 7, 9, 11$ and 13 l/s. One can see that the largest amplitudes for entire range of flow rates are found for the second cross-section – location of the first pressure sensor in the diffuser cone.

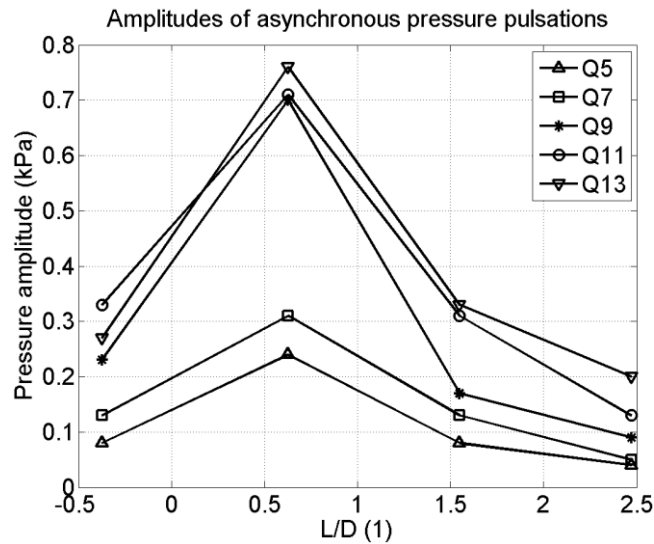


Figure 31 Amplitudes of asynchronous pressure pulsations

The evolution of amplitude magnitudes of asynchronous pressure pulsations in second cross-section against flow rate is plotted in Figure 32 for flow rates between $Q = 2$ and 13 l/s. It is noticeable that until flow rate 8.5 l/s the increase in amplitude magnitudes is nearly linear. On the other hand for higher flow rates the amplitude magnitude evolution oscillates increasingly. At higher flow rates $Q > 7$ l/s the cavitating vortex appears. The strength of cavitating core increases with increasing flow rate. In cavitating flows the density stratification is an additional production term in transport equation of vorticity (so called baroclinic vorticity production) [81], see eq. (7.5).

$$\frac{1}{\rho^2} \text{grad}\rho \times \text{grad}p \quad (7.5)$$

Therefore onset of the cavitating vortex core brings the additional source of energy dissipation. The vortex core became more complex with higher dynamics resulting in the more broad frequency spectra with lower amplitude at higher flow rates.

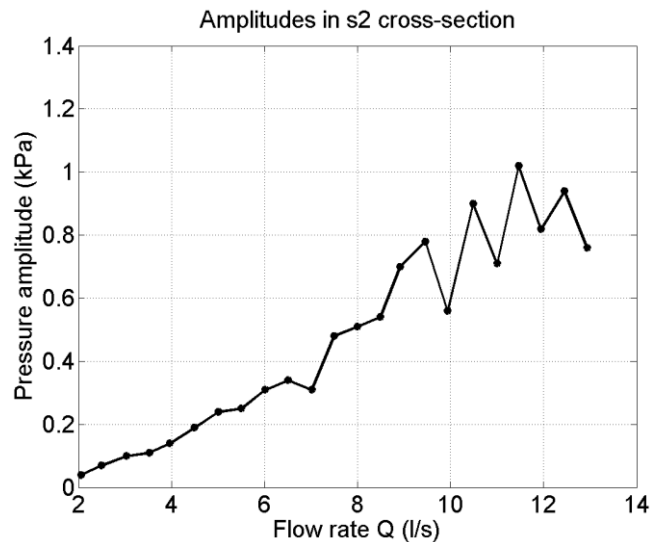


Figure 32 Amplitude magnitudes of asynchronous pressure pulsations in s2 cross-section

7.3.2 Synchronous pressure pulsations

The synchronous pressure pulsations are realized in a longitudinal direction. Therefore the assumption is that the frequencies should remain unchanged through the investigated cross-sections for particular flow rates. The results of synchronous pressure pulsations in the first three cross-sections are presented in Figure 33. One can see that this assumption is proved with slight discrepancies due to the complicated vortex behavior. It has to be mentioned that for flow rates lower than $Q < 4$ l/s it was already not possible to clearly distinguish exact frequency value, thus the results are presented only for higher flow rates.

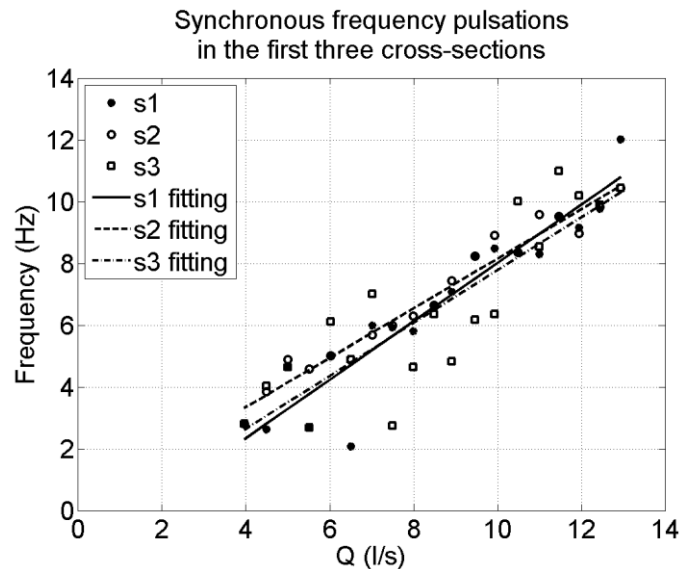


Figure 33 Synchronous pressure pulsations in the first three cross-sections (s1, s2 and s3) vs. flow rate

Interesting finding is that the strongest synchronous pressure pulsations (highest amplitudes) were found in the second cross-section (the first one in the cone part). On the other hand in the fourth and the fifth cross-section the power spectra were so noisy and amplitudes of these pulsations so low that it was not possible to find exact values. This is the reason why results in these cross-sections are not presented.

From visual observations it was found that the spiral vortex generated by the “BUT” swirl generator behaves unstably in time. The spiral form develops and decays periodically generating strong synchronous pressure pulsations. The main longitudinal instability of the vortex structure is realized within the first three cross-sections where the amplitudes are significant. The unstable time evolution of the vortex structure will be further discussed in section 9 where the time evolution of the vortex shape is presented from the image ensemble recorded using high speed camera and in section 12.1.3 where the vortex shape evolution is presented in a form of static pressure iso-contour. Moreover agreement with numerical simulation will prove that the spiral vortex decay is not consequence of any other source as a natural frequency of experimental test rig.

8 COMPARISON OF PRESSURE AND VELOCITY FIELDS DYNAMIC

The pressure and velocity fields are linked together through the Navier-Stokes equation. Therefore every unsteadiness in the velocity field must be observed in the pressure field and vice versa. In this section the dominant frequencies extracted from the signal of LDA measurements are correlated with the ones obtained from the unsteady pressure measurements. The frequencies of velocity fluctuations are calculated as the average value of dominant frequencies obtained from the amplitude-frequency spectra of all measured points through the corresponding cross-section S1, S2 and S3. In Figure 34 the location of LDA measuring cross-sections (S1, S2 and S3) are shown together with adjacent locations of pressure sensor holes.

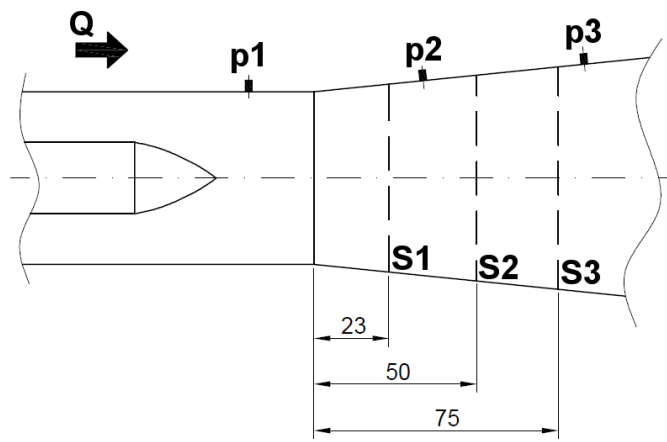


Figure 34 Location of LDA measuring cross-sections vs. locations of pressure sensors

One can see that pressure signal from sensor p2 can be correlated with the either LDA cross-section S1 or S2 and pressure signal from sensor p3 can be correlated with the LDA cross-section S3.

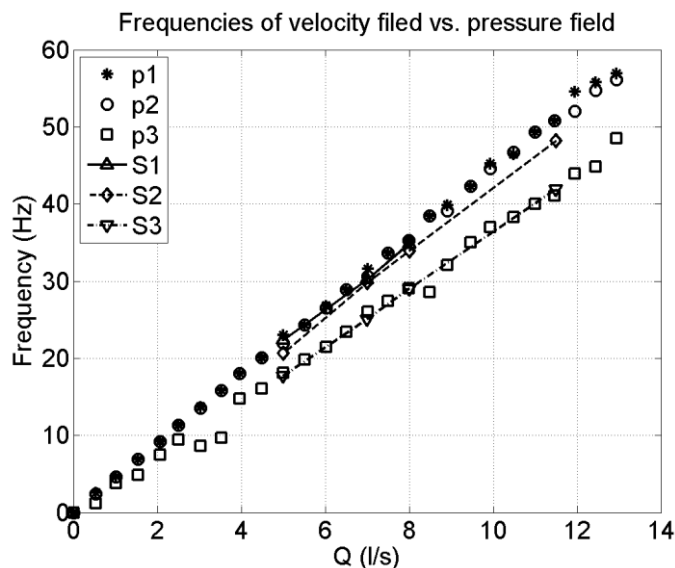


Figure 35 Frequencies of velocity field fluctuations correlated with the frequencies of pressure pulsations

From the Figure 35 it is clear that the magnitude of dominant (asynchronous) frequency extracted from pressure signal well corresponds with the one extracted from the LDA measurements. Moreover the decrease in the frequency magnitude downstream of the diffuser well corresponds, see e.g. frequencies of p3 sensor pressure signal versus the LDA in S3 cross-section.

9 HIGH SPEED CAMERA RECORDING OF THE CAVITATING VORTEX

When the static pressure in the vortex core drops below the value of saturated vapor pressure the cavitation appears. Due to the light reflection the vortex core is well visible. In this case the cavitating vortex occurs at flow rates higher than $Q = 7$ l/s. In order to experimentally investigate the behavior of the cavitating vortex structure the ensembles of the instantaneous images were recorded using the high speed camera *Baumer HX Series*, see Figure 36.

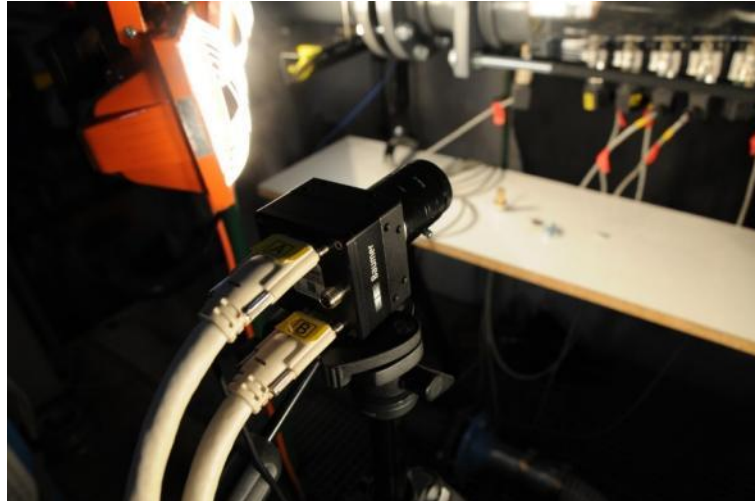


Figure 36 The Baumer HX Series high speed camera

The measurements were performed for flow rates $Q = 7 - 13.5$ l/s with the step of 0.5 l/s. Each image ensemble consists of 10 000 instantaneous snapshots of the cavitating vortex. The resolution of the recorded pictures is 1024 x 544 pixels. The sampling frequency was chosen $f = 619$ Hz in order to get sufficient light for this resolution and aperture ratio. Then the resulting time spanned by the image ensemble is approximately 16 sec. The scene was additionally illuminated by two halogen lamps in order to provide sufficient light for the high speed camera. The overall view of the recording scene is presented in Figure 37.

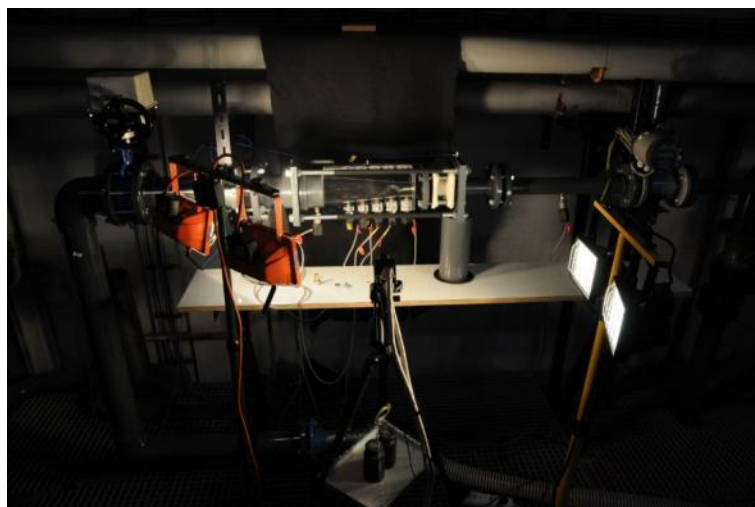


Figure 37 Overall view of recording scene

The swirl generator apparatus was equipped with five pressure transducers mounted at the bottom of the transparent diffuser, see Figure 38. Additionally one pressure sensor was located upstream of the swirl generator blade section and one pressure sensor was situated downstream of the transparent diffuser (see the sensor arrangement in Figure 21). Hence the visual observation of the cavitating vortex can be further correlated with the pressure conditions in the test rig. This enables to calculate the Thoma cavitation number and performs the FFT analysis for the particular pressure record.

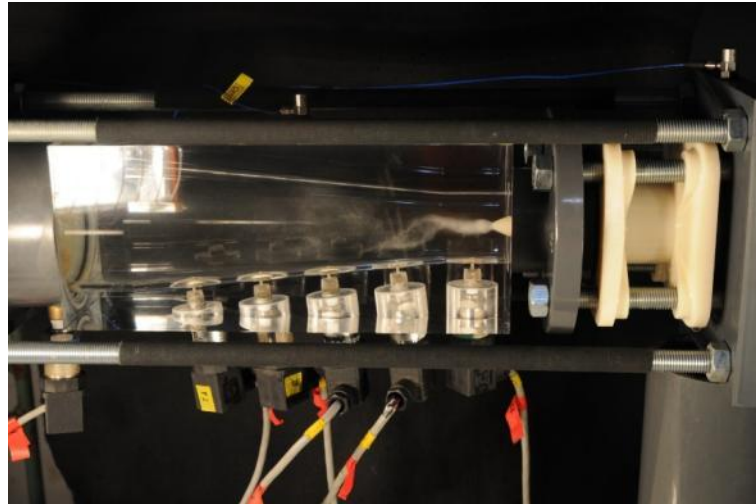


Figure 38 Closer look on the photographed area (picture from DLSR camera)

The Figure 39 shows the instantaneous snapshot produced by the high speed camera. One can see the cavitating vortex at flow rate $Q = 13.5$ l/s and its development downstream of the diffuser.

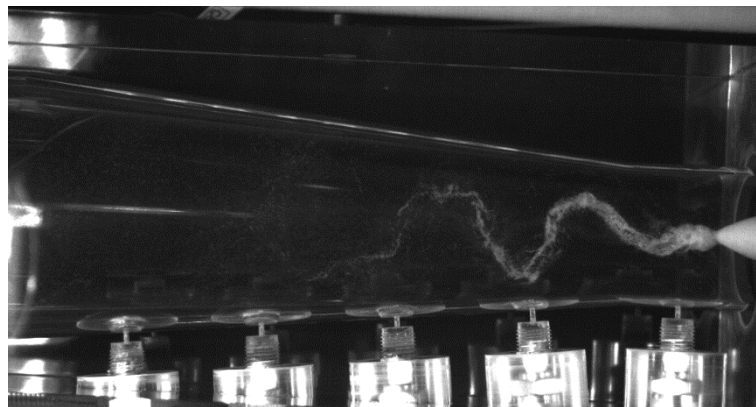


Figure 39 Instantaneous snapshot of the cavitating vortex structure at flow rate $Q = 13.5$ l/s (picture from high speed camera)

9.1 TIME EVOLUTION OF THE SPIRAL VORTEX

The spiral vortex generated by the “BUT” swirl generator behaves unstably in time. The spiral rolls up and decays periodically generating the synchronous pressure pulsations propagated upstream, see section 7.3.2. The unstable movement can be seen in Figure 40 where the time evolution of cavitating vortex at flow rate $Q = 13.5$ l/s is shown in selected time periods. At time $t = 0$ sec the fully developed spiral vortex is observed. The rotating

spiral vortex disintegrates ($t = 0.013 - 0.021$ sec) leading to the short straight vortex ($t = 0.034$ sec). Due to swirling flow instability the straight vortex later breaks up into spiral shape again ($t = 0.058 - 0.108$ sec).

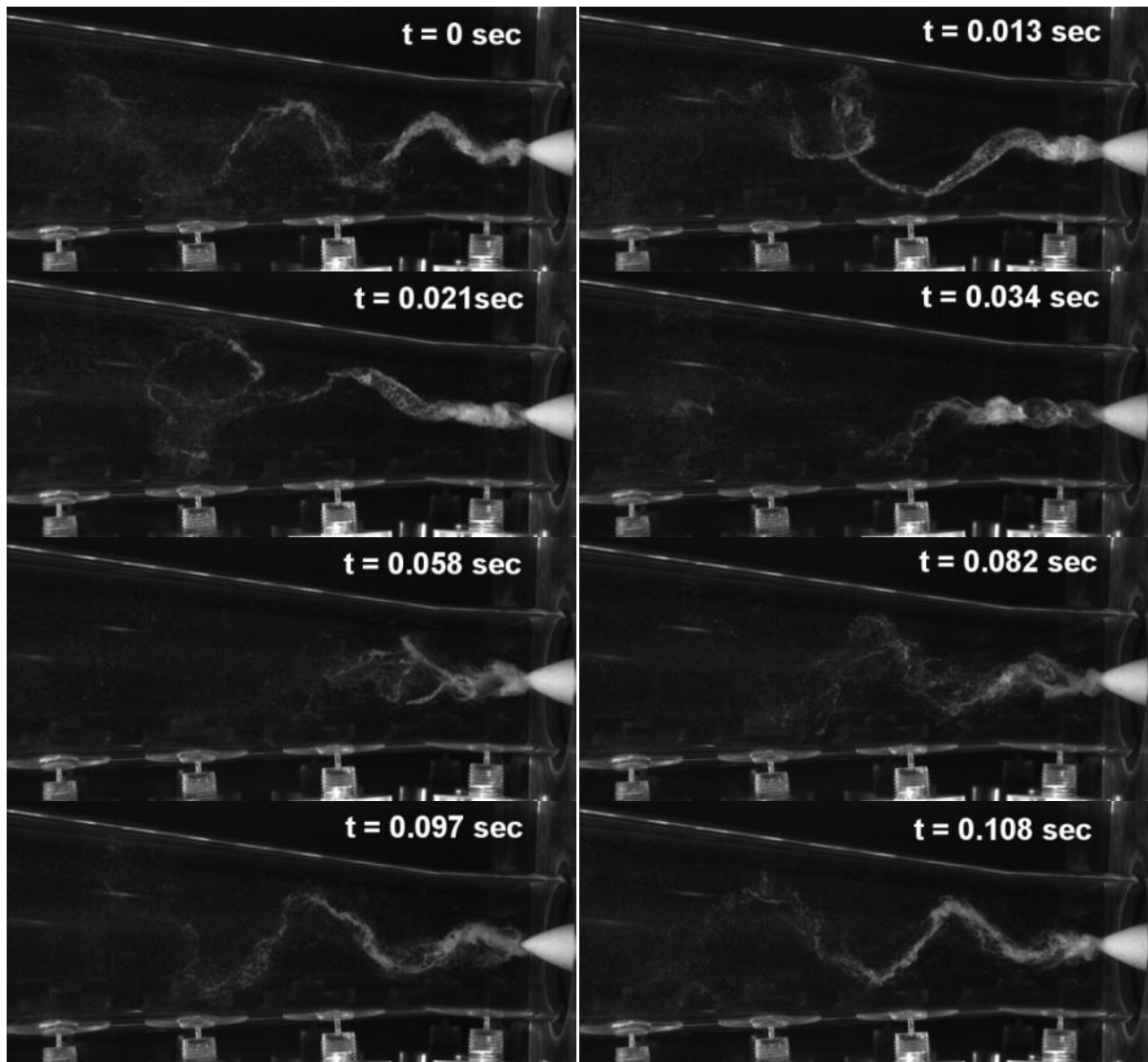


Figure 40 Time evolution of the vortex structure at flow rate $Q = 13.5$ l/s

9.2 ESTIMATION OF THE CAVITATION VAPOR FRACTION

In this section the idea to estimate dependence of the vapor fraction of cavitation when the flow rate increase is described. The series of snapshots from the high speed camera is used to make a post-processing. The grayscale images are imported to the MATLAB[®] using “imread” function returning 24-bit color data where the sample size for each color component is 8bits. In case of grayscale the value between 0 (for black) and 255 (for white) is assigned to each pixel. The size of recorded images is 1024 x 544 pixels. In order to decrease amount of the post-processed data, the images were reduced to the small constrained domain, see the bounded area in Figure 41. The constrained domain is chosen to cover the main region where the vortex core is developed just at the end of the spike with dimension of 381 x 141 pixels. From the known diffuser dimensions the image pixels are converted to the millimeters. Then

the domain dimensions are 102.9 x 43 mm. Note that the orientation of post-processed images is inverted in the stream direction compared to the images from the high speed camera and real test-rig proportions. Thus the flow direction in following figures is from left to right.

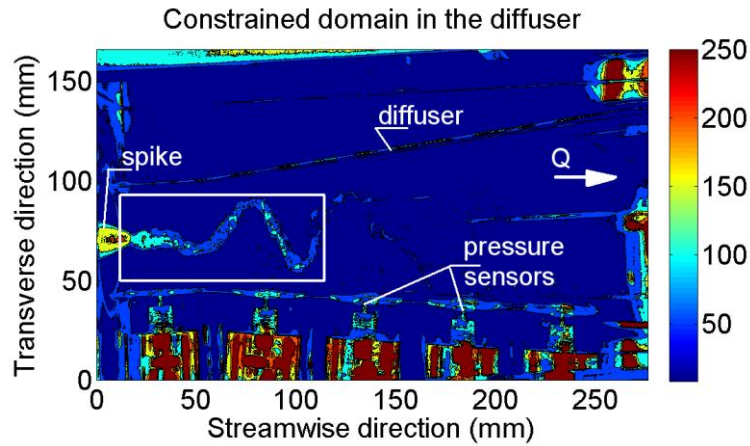


Figure 41 Situation of investigated area in the diffuser

For the particular flow rate the series of snapshots are averaged in time t and space x . The averaging is based on $M = 10000$ snapshots. Considering that the scene illumination and the camera position stay unchanged the average amount of the vapor fraction \bar{w} is computed using numerical integration

$$\bar{w} = \frac{\sum_{n=1}^N \sum_{m=1}^M w_{mn}}{N \cdot M} \quad (9.1)$$

where M is total number of snapshots and N is total number of image pixels.. The resulting number denotes the relative amount of the vapor contained in the flow bounded by the constrained domain. The relation of average vapor fraction \bar{w} to the flow rate is presented in Figure 42. One can see that approximately up to the flow rate $Q = 10$ l/s the average vapor fraction \bar{w} remains almost constant while for the higher flow rates increases quadratically.

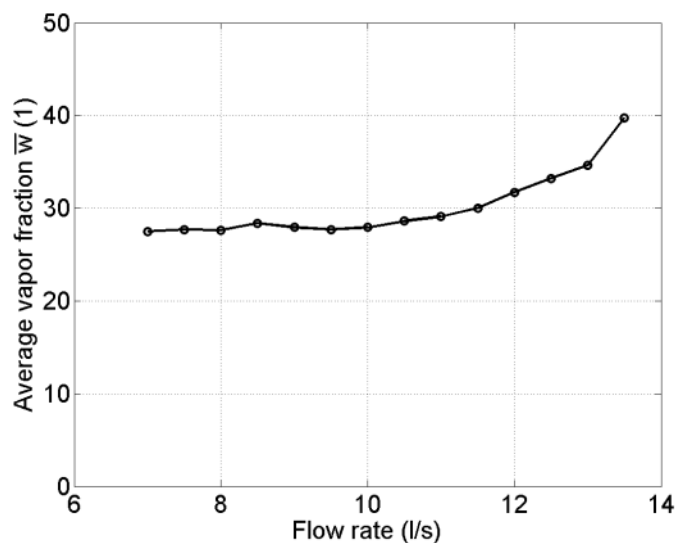


Figure 42 Dependency of average vapor fraction \bar{w} to the flow rate

9.3 SPATIAL REPRESENTATION OF THE TIME-AVERAGED CAVITATING VORTEX

The time-averaged spatial representation of the cavitating vortex structure can be created using the ensemble of the instantaneous snapshots from the high speed camera. The time-averaging process showed that the credible results of spatial representation can be carried out starting at flow rate $Q = 11$ l/s. At lower flow rates $Q < 11$ l/s the cavitating vortex structure is too weak for the averaging process.

The resulting time-averaged spatial representations of cavitation vortex are plotted in Figure 43 as the contours of grayscale for flow rates $Q = 11.5, 12.5$ and 13.5 l/s. One can see large increase of the clearly bounded contours while the flow rate increases.

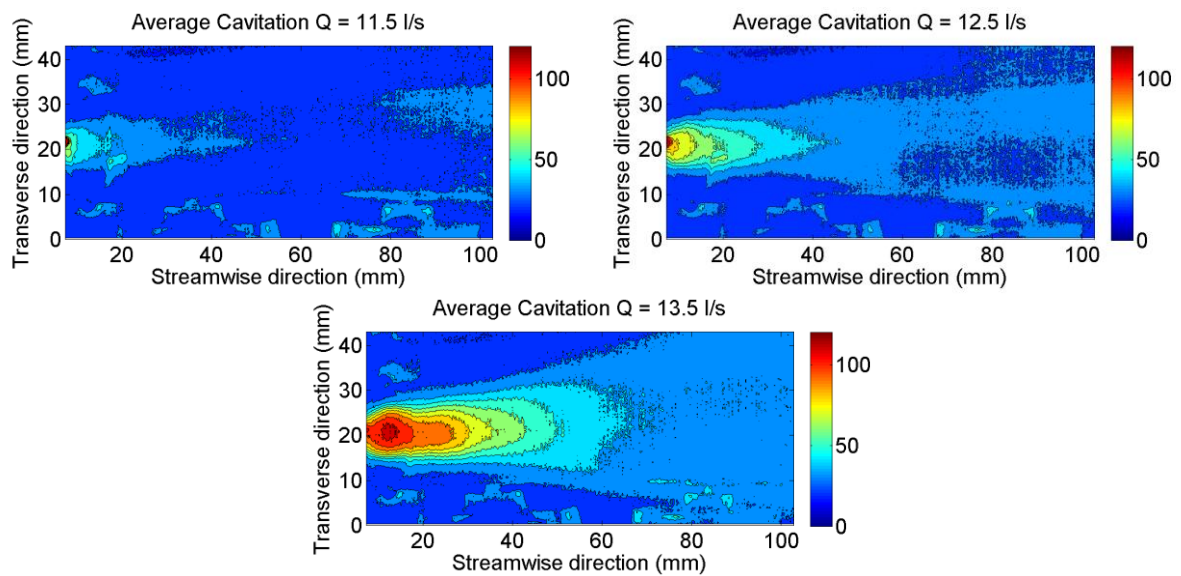


Figure 43 Spatial representations of the time-averaged cavitation vortex, $Q = 11.5, 12.5$ and 13.5 l/s

In order to assess decaying process of the cavitating vortex downstream of the diffuser, the profiles of time-averaged cavitation are extracted in the six cross-sections S1 – S6, see the Figure 44.

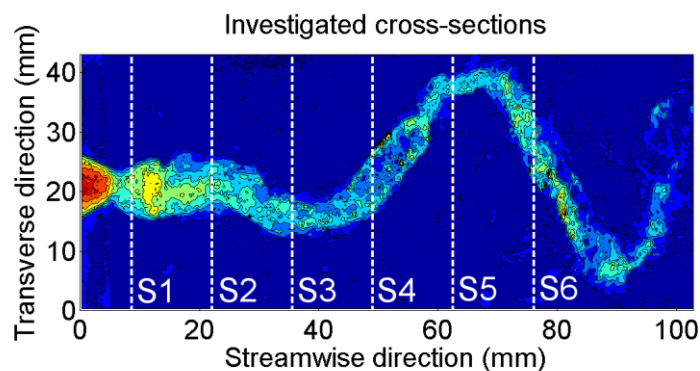


Figure 44 Locations of investigated cross-sections

In Figure 45 the time-averaged cavitation profiles are plotted in six locations S1 – S6 for range of flow rates $Q > 11$ l/s.

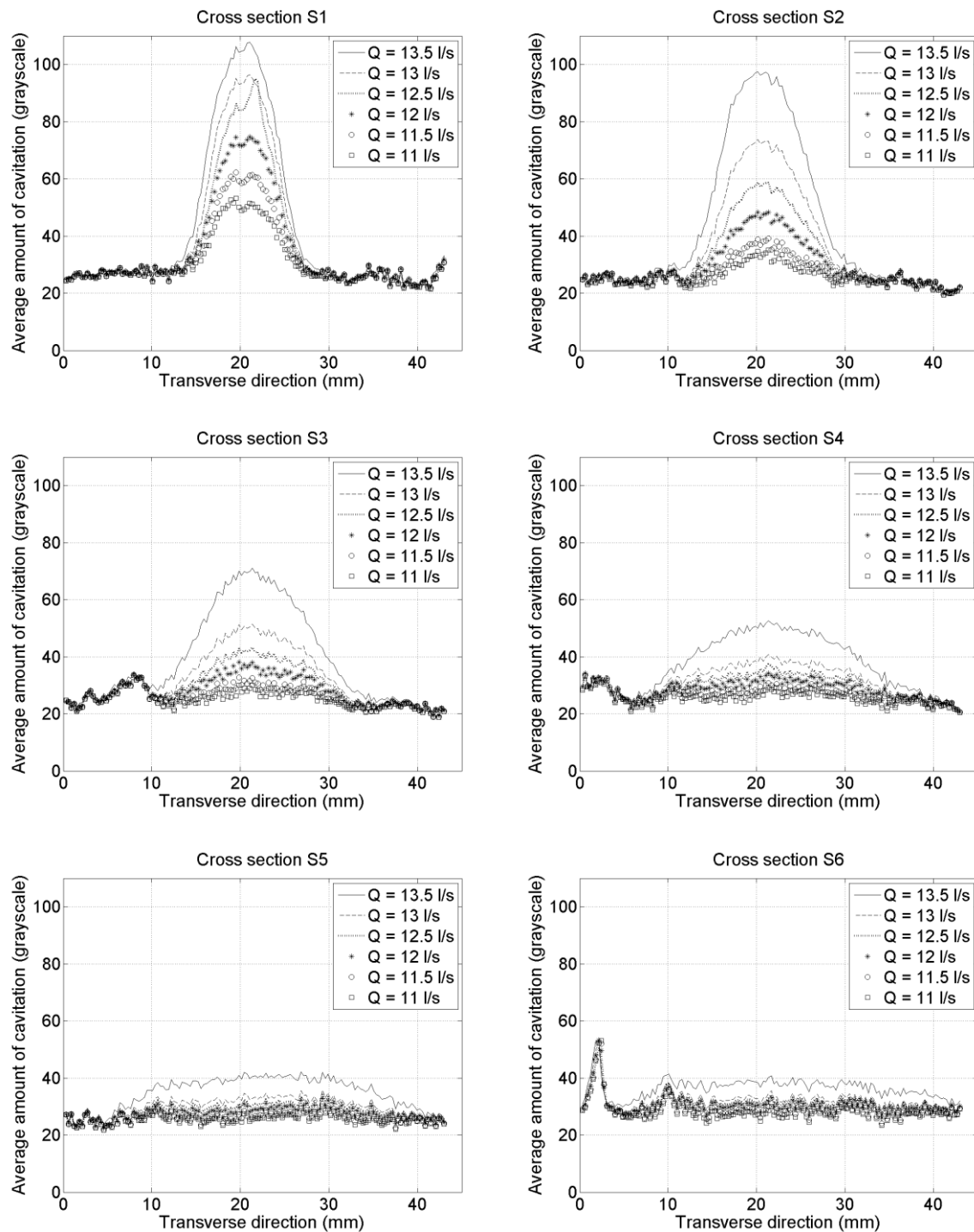


Figure 45 Time-averaged cavitation profiles in cross-sections S1 – S6

One can see how the region influenced by the cavitation develops downstream of the diffuser. While at flow rate $Q = 11$ l/s the peak in time-averaged cavitation profile is hardly visible in the second cross-section at flow rate $Q = 13.5$ l/s the time-averaged cavitation profile is well developed even in the sixth cross-section. The peak close to the diffuser wall in S6 cross-section is consequence of light reflection from rounded diffuser wall.

In Figure 46 the profiles of time averaged cavitation in particular cross-sections are presented for flow rate $Q = 13.5$ l/s as the grayscale magnitude. The red line in figures represents average value corresponding to the cross-sections at the end (102.9 mm in

streamwise direction) of investigated domain, see Figure 44. In order to estimate relative amount of the water vapor \bar{w} in each of cross-section, the region of time-averaged cavitation profile above the red line was integrated. This was done for all cross-sections of entire range of investigated flow rates.

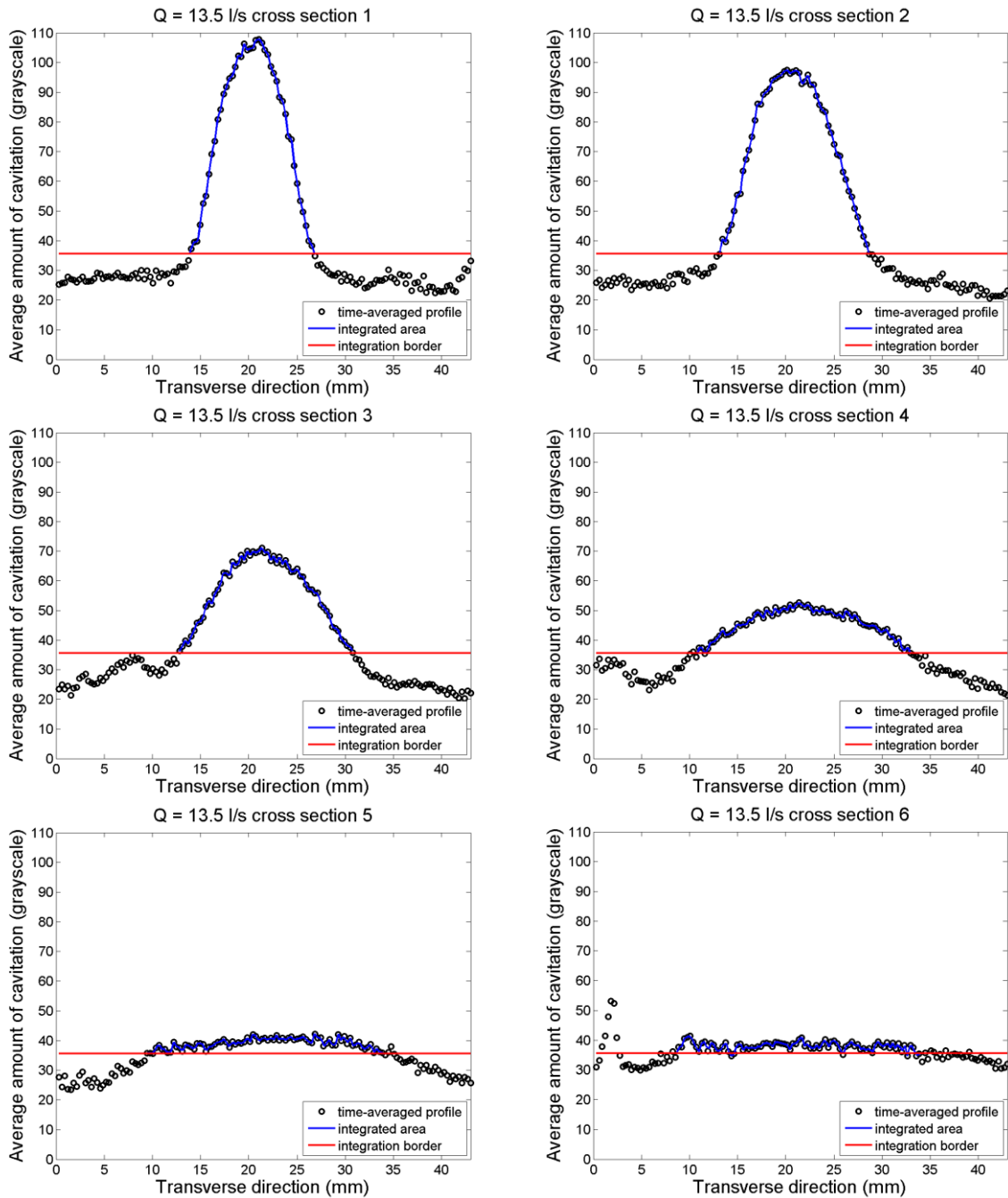


Figure 46 Average amount of cavitation in particular cross-section at flow rate $Q = 13.5$ l/s

The evolution of relative amount of the water vapor \bar{w} in particular cross-sections when the flow rate increase is plotted in Figure 48. On the other hand evolution of relative amount of the water vapor \bar{w} downstream of the diffuser is plotted in Figure 48 for investigated flow rates.

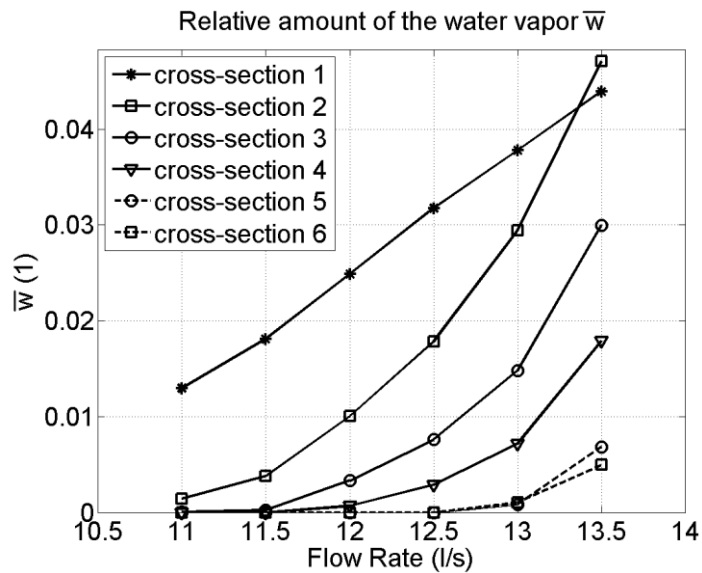


Figure 47 Relative amount of the water vapor in particular cross-sections against flow rate

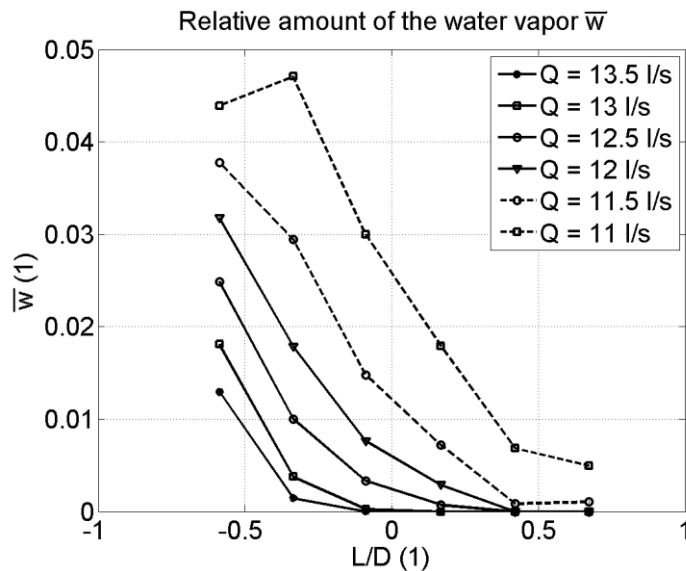


Figure 48 Evolution of relative amount of the water vapor downstream of the diffuser for particular flow rates

Beside the relative amount of the water vapor in particular cross-sections the width of area influenced by the cavitation can be estimated. For this purpose the width of integrated area bounded by the red line is used as can be seen in Figure 46. In the Figure 49 is plotted relative width of the region influenced by the cavitation as the ratio d/D (where d is the width of this region and $D = 53.6$ mm is the inlet diameter of the diffuser) against L/D (where L is the distance from the diffuser inlet). One can see that the width of this region increases in the downstream part of the diffuser and depends to the flow rate.

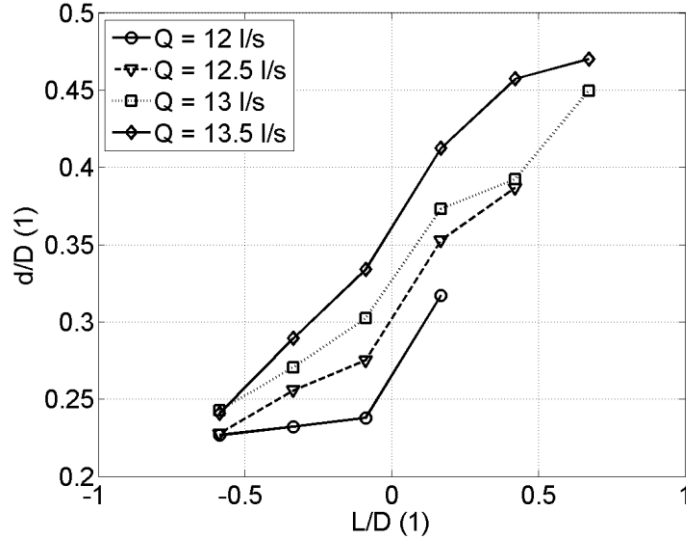


Figure 49 Width of the area influenced by the cavitation

One of the main triggers causing the spiral vortex breakdown is the diffuser type of flow. Therefore it is clear that the increase in the width of the area influenced by the cavitating vortex should be in relation with the diffuser opening angle α . The ratio of increase in the width of area influenced by the cavitating vortex is defined as

$$tg\beta = \frac{d_{i+1} - d_i}{L_{i+1} - L_i} \quad (9.2)$$

where the d_i is width of the area influenced by the cavitating vortex in the i -th cross-section and L_i is location of i -th cross-section, see schema in Figure 50 where area influenced by cavitation is bordered by dashed lines.

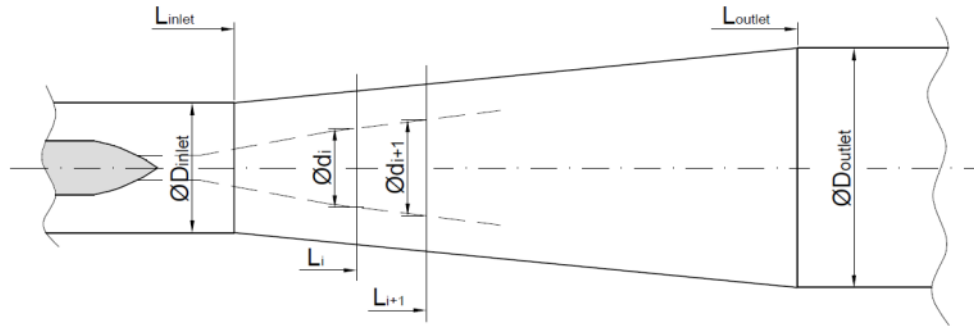


Figure 50 Geometry of area influenced by cavitation

In Figure 51 evolution of $tg\beta$ in particular cross-sections is plotted for different flow rates. The red line indicates the diffuser opening ratio $tg\alpha$ defined as following:

$$tg\alpha = \frac{D_{outlet} - D_{inlet}}{L_{outlet} - L_{inlet}} \quad (9.3)$$

One can see that for all investigated flow rates the value of $tg\beta$ is under the value of $tg\alpha$ in region in front of diffuser entrance $L/D < 0$. On the other hand for $L/D = 0.1683$ the value

of $tg\beta$ is much higher than $tg\alpha$. This indicates large influence of the diffuser opening to the vortex unsteadiness caused by the abrupt geometrical change. Further downstream the value of $tg\beta$ decreases again under the value of $tg\alpha$. In the last cross-section $L/D = 0.672$ the results can be influenced by the incorrectly estimated width of the region influenced by the cavitation.

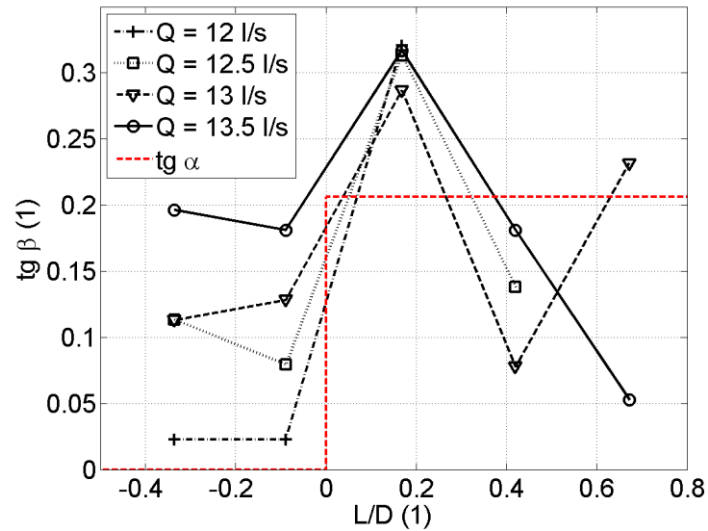


Figure 51 Increase in the width of area influenced by the cavitating vortex in particular cross-sections correlated with the diffuser opening

10 INVESTIGATION OF FREQUENCY DECREASE OF ASYNCHRONOUS PRESSURE PULSATIONS ALONG THE DIFFUSER CONE

In section 9.1 it is shown that the spiral vortex decays and rolls up periodically. From closer visual observation of image ensemble (see Figure 40) it was found that the upstream part of the vortex rotates faster than the downstream part. Consequently the vortex spiral turns into the loop and collapses upstream in form of straight short vortex (see $t = 0.013 - 0.034$ sec in Fig.5.). While the frequency magnitudes of asynchronous pulsations are equal in the first and second cross-sections, the frequency magnitudes decrease in the third and fourth cross-section. Two reasons of asynchronous frequency decrease downstream of the diffuser are assumed 1.) diameter differences respectively differences in the circumference of particular investigated cross-sections (see Figure 52) and 2.) vortex collapse upstream of the diffuser.

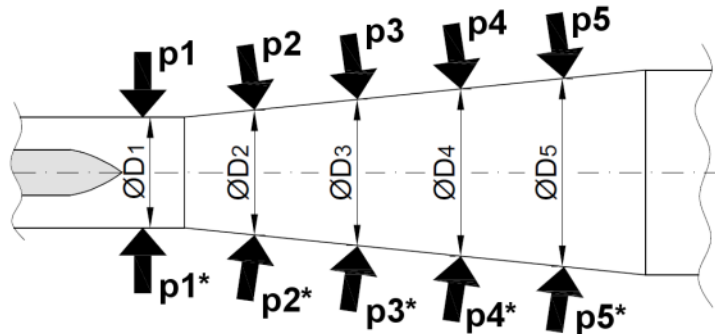


Figure 52 Diameters of pressure sensors cross-sections

According to the first assumption the frequencies in the third and fourth cross-sections are treated from the increasing diameter ratio of the diffuser opening. Considering the diameter of the second cross-section $D_2 = 0.05973$ as an initial one and diameter D_k related to the k -th cross-section the ratio of the diameter growth defined as D_k/D_2 can be computed, see Table 7.

Table 7 Diameter grow ratios in corresponding cross-sections.

Cross – section	Diameter (m)	D_k/D_2 (1)
no. 2	0.05973	1
no. 3	0.07	1.17194
no. 4	0.08	1.33936

This ratio is then used to increase (i.e. “correct”) frequency magnitudes in the third and fourth cross-sections, thus the new value of frequency in the third cross-section is defined as:

$$f_3^* = f_3 \cdot D_3/D_2 \quad (10.1)$$

The evolution of these treated frequencies against the flow rate is plotted in Figure 53. One can see that while for the third cross-section the agreement with upstream cross-sections s1 and s2 is achieved, for the fourth cross-section the values of frequencies are still lower.

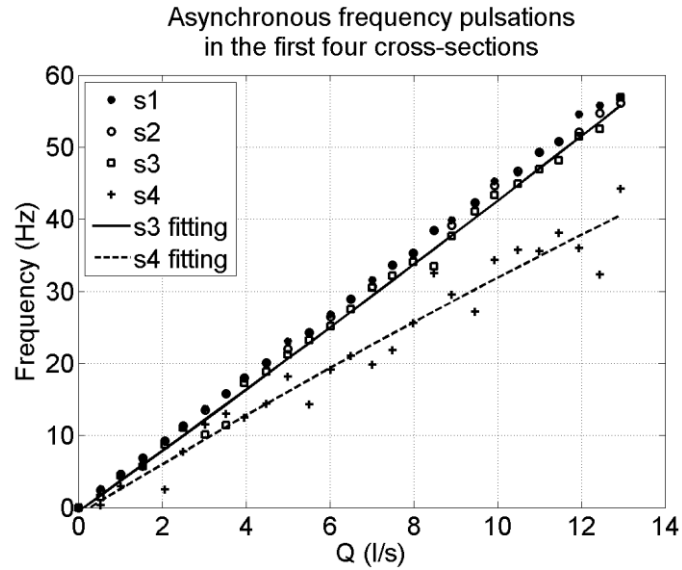


Figure 53 Frequency values of asynchronous pressure pulsations in the third and the fourth cross-sections treated by diameter growth ratio

The collapsing spiral form of the vortex is consequence of significant synchronous pulsations. As was shown in section 7.3.2 the synchronous pressure pulsations are realized mainly in the first three cross-sections. Consequently the synchronous frequency portion is added to the fourth cross-sections deprived from the vortex rotation when the spiral vortex collapses upstream. One can see in Figure 54 that the frequencies for full range of flow rates in the fourth cross-section now fits very well with ones in the upstream cross-sections.

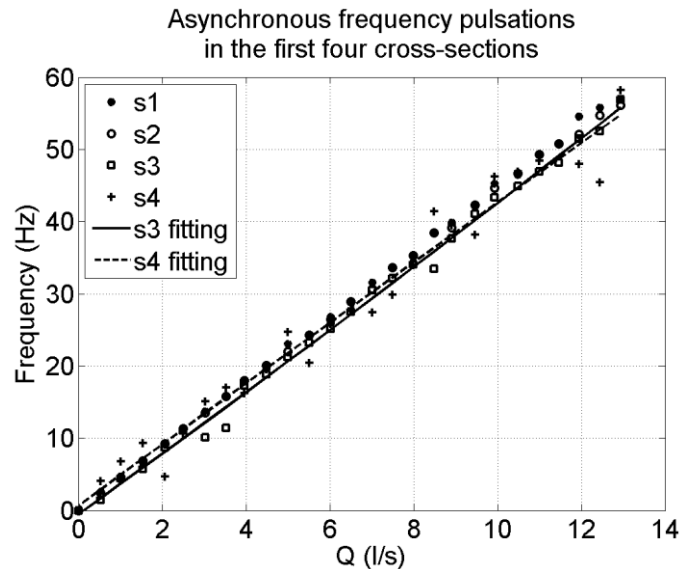


Figure 54 Frequency values of asynchronous pressure pulsations in the fourth cross-sections treated by influence of synchronous pulsations

In some previous studies of the draft tube surge [25], [58] was concluded that the synchronous part of pressure pulsations are related to the interaction of the vortex rope with the elbow of bended draft tube and cannot be found in the straight draft tubes. Nonetheless as

11 CFD CALCULATION USING OPEN-SOURCE SOFTWARE OpenFOAM [68]

The OpenFOAM can be used as a standard simulation package, but it offers much more because it is open source and it is designed to be flexible, programmable environment for simulation by having top-level code that is direct representation of the equations being solved, e.g.:

$$\frac{\partial \rho \mathbf{U}}{\partial t} + \nabla \cdot \rho \mathbf{U} \mathbf{U} - \nabla \cdot \mu \nabla \mathbf{U} = -\nabla p \quad (11.1)$$

is represented by the code:

```
solve
(
    fvm::ddt(rho, U)
    + fvm::div(phi, U)
    - fvm::laplacian(mu, U)
    ==
    - fvc::grad(p)
);
```

This makes OpenFOAM an excellent choice for customisation, compared to closed source (“black box”) software [68].

11.1 SOLVER THEORY

In the following sub-sections the basics of CFD solver using OpenFOAM packages is described. For the deeper understanding reader is referred to relevant literature.

11.1.1 Numerical schemes

The choice of discretisation schemes is selected by the user through the `fvSchemes` file of the case being simulated. OpenFOAM has a comprehensive range of discretisation schemes, allowing full control over accuracy, boundedness and conservation. The schemes are generally limited to the second-order to enable reliable simulation on real engineering geometries with cells of arbitrary shape. The `fvSchemes` file also contains controls for the coupling algorithms to provide complete control to optimize simulations.

Comprehensive description of all available numerical schemes prescribed in `fvSchemes` dictionary can be found in OpenFOAM documentation [68]. In following subsections only the brief overview about schemes used in this case are summarized for both `simpleFoam` and `pimpleFoam` solvers [68].

11.1.2 Time schemes

The first derivative terms $\frac{\partial}{\partial t}$ are specified in the `ddtSchemes` sub-dictionary. The `steadyState` entry is prescribed for steady solution using `simpleFoam` and `Euler` (first

order, bounded, implicit) later changed to backward (second order, implicit) is used for unsteady solution within `pimpleFoam`.

11.1.3 Gradient schemes

For standard finite volume discretisation the Gaussian integration is used which requires the interpolation of values from cell centers. Therefore, the `Gauss` entry must be followed by the choice of interpolation scheme. In most cases the linear scheme is an effective choice. Therefore in the `gradSchemes` sub-dictionary there is for both `grad(p)` and `grad(U)` the `Gauss linear` entry.

11.1.4 Divergence schemes

The `divSchemes` sub-dictionary contains divergence terms. For a typical convection term found in fluid dynamics $\nabla \cdot (\rho \mathbf{U}\mathbf{U})$, is in OpenFOAM applications given the identifier `div(phi,U)`, where `phi` refers to the flux $\phi = \rho \mathbf{U}$. The `Gauss` scheme is the only choice of discretisation and requires a selection of the interpolation scheme for the dependent field, i.e. `U`. Summary of used schemes for both steady and unsteady solution is presented in Table 8.

Table 8 Used divergence schemes

	simpleFoam	pimpleFoam
<code>div(phi,U)</code>	<code>bounded Gauss linearUpwindV grad(U)</code>	<code>Gauss limitedLinearV 1</code>
<code>div(phi,k)</code>	<code>bounded Gauss upwind</code>	<code>Gauss limitedLinear 1</code>
<code>div(phi,epsilon)</code>	<code>bounded Gauss upwind</code>	<code>Gauss limitedLinear 1</code>
<code>div(phi,omega)</code>	<code>bounded Gauss upwind</code>	<code>Gauss limitedLinear 1</code>
<code>div(phi,nuTilda)</code>	<code>bounded Gauss upwind</code>	<code>Gauss limitedLinear 1</code>
<code>div((nuEff*dev(T(grad(U)))))</code>	<code>Gauss linear</code>	<code>Gauss linear</code>

After obtaining periodic state of solution the pressure probes and cutting planes were prescribed in `controlDict` for sampling of pressure record in points corresponding with positions of pressure transducers in experimental facility. The values of pressure in cutting planes were later used for POD analysis, see section 16.2.

11.1.5 Laplacian schemes

The typical Laplacian term found in the fluid dynamics $\nabla \cdot (\nu \nabla \mathbf{U})$ is given the word identifier `laplacian(nu,U)`. The `Gauss` scheme is the only choice of discretisation and requires a selection of surface normal gradient scheme, i.e. $\nabla \mathbf{U}$. Therefore the forms of required entries are:

```
Gauss <interpolationScheme> <snGradScheme>
```

In this case the `Gauss linear corrected` entry is chose for all Laplacian terms.

11.1.6 Interpolation schemes

The `interpolationSchemes` sub-dictionary contains terms that are interpolations of values typically from cell centers to face centers. In this case the linear interpolation scheme was set as `default` for all terms requiring interpolation.

11.1.7 Surface normal gradient schemes

A surface normal gradient is evaluated at a cell face; it is the component, normal to the face, of the gradient of values at the centres of the 2 cells that the face connects. In this case default entry `corrected` was applied for all terms require surface normal gradients.

11.1.8 Flux calculation

The `fluxRequired` sub-dictionary lists the fields for which the flux is generated in the application. For example, in many fluid dynamics applications the flux is generated after solving a pressure equation, in which case the `fluxRequired` sub-dictionary would simply be entered as follows, `p` being the word identifier for pressure:

```
fluxRequired
{
    p;
}
```

The overall views of the `fvSolution` dictionary used for all calculations are presented in appendix 1 (for `simpleFoam`) and appendix 2 (for `pimpleFoam`).

11.1.9 Solution and algorithm control

The equation solvers, tolerances and algorithms are controlled from the `fvSolution` dictionary in the `system` directory. The `fvSolution` contains a set of sub-dictionaries that are specific to the solver being run. These sub-dictionaries include `solvers`, `relaxationFactors`, `PISO` and `SIMPLE`.

The first sub-dictionary in our example, and one that appears in all solver applications, is `solvers`. It specifies each linear-solver that is used for each discretised equation. The syntax for each entry within `solvers` uses a keyword that is the word relating to the variable being solved in the particular equation, e.g. `U` and `p` entries for velocity and pressure respectively. The keyword is followed by a dictionary containing the type of solver and the parameters that the solver uses. The preconditioned (bi-)conjugate gradient solver is used for all variables. While the `PCG` is for the symmetric matrices the `PBiCG` is for asymmetric ones. In Table 9 is presented overview of used solvers together with solution tolerances and preconditioners used for preconditioning of matrices in the conjugate gradient solvers. The solution tolerances and preconditioning are described in following subsections.

Table 9 Solvers set-up used in the calculation

	p	pFinal	U k epsilon	UFinal k epsilon (Final)
solver	PCG	PCG	PBiCG	PBiCG
preconditioner	DIC	DIC	DILU	DILU
tolerance	1e-6	1e-7	1e-5	1e-6
relTol	0.1	0	0.1	0

The iterative solution is based on reducing the equation residuals. The residual is ostensibly a measure of the error in the solution so that the smaller it is, the more accurate the solution. More precisely, the residual is evaluated by substituting the current solution into the equation and taking the magnitude of the difference between the left and right hand sides; it is also normalized to make it independent of the scale of the problem being analyzed. Before solving an equation for a particular field, the initial residual is evaluated based on the current values of the field. After each solver's iteration the residual is re-evaluated. The solver stops if either of the following condition is reached:

- the residual falls below the solver tolerance (`tolerance`)
- the ratio of current to initial residuals falls below the solver relative tolerance (`relTol`)
- the number of iterations exceed a maximum number of iterations (`maxIter`)

The solver tolerance should represent the level at which the residual is small enough that the solution can be deemed sufficiently accurate. The solver relative tolerance limits the relative improvement from initial to final solution. In transient simulations, it is usual to set the solver relative tolerance to 0 to force the solution to converge to the solver tolerance in each time step. The `maxIter` input is optional.

There are a range of options for preconditioning of matrices in the conjugate gradient solvers, represented by the `preconditioner` keyword in the `solver` dictionary. Regarding to Table 9 the diagonal incomplete-Cholesky (symmetric) preconditioner (`DIC`) is used for pressure and diagonal incomplete-LU (asymetric) preconditioner (`DILU`) is used for velocity and turbulence variables k and ϵ .

11.1.10 PISO and SIMPLE algorithm

Most fluid dynamics solver applications in OpenFOAM use the pressure-implicit split-operator (PISO) or semi-implicit method for pressure-linked equations (SIMPLE) algorithms. These algorithms are iterative procedures for solving equations for velocity and pressure, PISO being used for transient problems and SIMPLE for steady-state. Both algorithms are based on evaluating some initial solutions and then correcting them. SIMPLE only makes 1 correction whereas PISO requires more than 1, but typically not more than 4. The user must therefore specify the number of correctors in the `PISO` dictionary by the `nCorrectors` keyword.

An additional correction to account for mesh non-orthogonality is available in both SIMPLE and PISO. A mesh is orthogonal if, for each face within it, the face normal is parallel to the vector between the centers of the cells that the face connects, e.g. a mesh of hexahedral cells whose faces are aligned with a Cartesian coordinate system. The number of non-orthogonal correctors is specified by the `nNonOrthogonalCorrectors` keyword. The number of non-orthogonal correctors should correspond to the mesh for the case being solved, i.e. 0 for an orthogonal mesh and increasing with the degree of non-orthogonality up to 20 for the most non-orthogonal meshes.

While for the pressure one inner correction (`nCorrectors`) was prescribed two outer corrections (`nOuterCorrections`) were prescribed for pressure and velocity, see Table 10.

Table 10 Correctors used in calculations

Number of corrections	
<code>nOuterCorrectors</code>	2
<code>nCorrectors</code>	1
<code>nNonOrthogonalCorrectors</code>	1

11.1.11 Solution under-relaxation

The `relaxationFactors` sub-dictionary controls under-relaxation in order to improve stability of computation, particularly in solving steady-state problems. Under-relaxation works by limiting the amount which a variable changes from the one iteration to the next, either by modifying the solution matrix and source prior to solving for a field or by modifying the field directly. An under-relaxation factor α ($0 < \alpha \leq 1$) specifies the amount of under-relaxation.

- α is not specified: no under-relaxation.
- $\alpha = 1$: guaranteed matrix diagonal equality/dominance.
- α decreases, under-relaxation increases
- $\alpha = 0$: solution does not change with successive iterations.

An optimum choice if α is small enough to ensure stable computation but large enough to move the iterative process forward quickly. The under relaxation factors used in present calculation are shown in Table 11.

Table 11 Used under-relaxation factors

Variable	α
p	0.3
<code>U k epsilon</code>	0.7

11.2 COMPUTATIONAL DOMAIN

The computational mesh of swirl generator was built in the software Gambit and then converted into OpenFOAM format using `fluent3DMeshToFoam` utility. The overall view of domain dimensions is presented in Figure 55. Two kinds of elements are used. While the major part of the domain contains hexahedral elements the tetrahedral elements had to be used in order to treat regions of sharp spikes, see Figure 56 and Figure 57. Whole mesh consists of 3 967 877 elements.

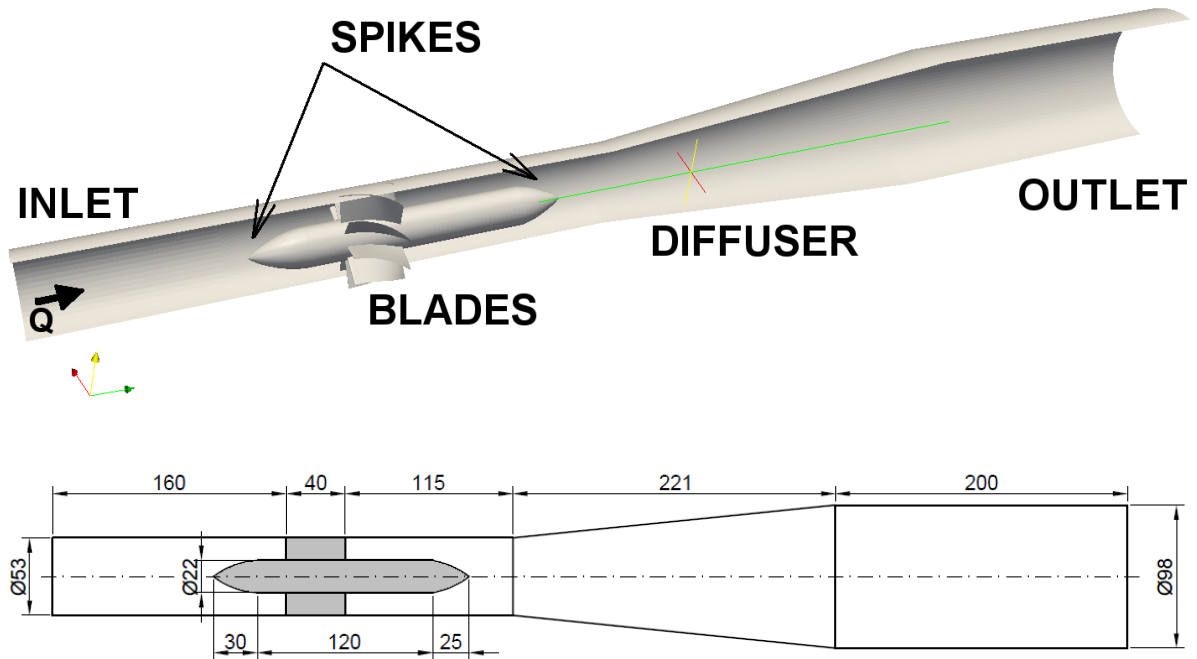


Figure 55 Overall view on computational domain (top) and its dimensions (bottom)

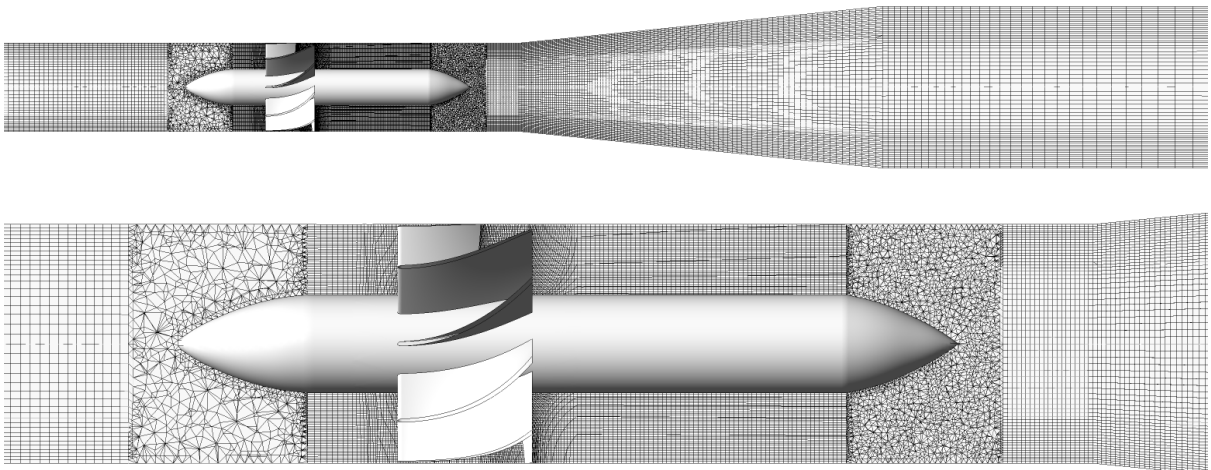


Figure 56 Detailed views on the computational grid

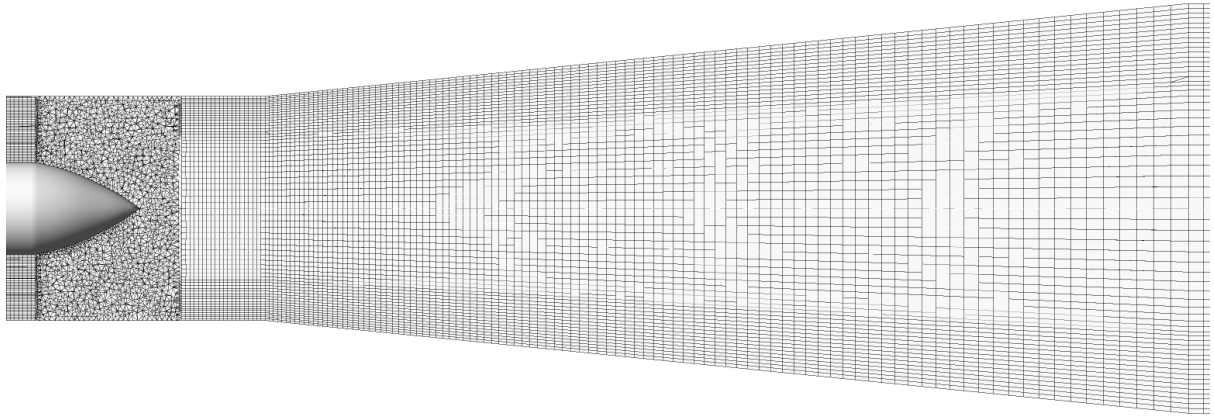


Figure 57 Detailed views on the computational grid - diffuser

11.3 NUMERICAL SOLUTION OF “BUT” SWIRL GENERATOR

The numerical simulation of “BUT” swirl generator is carried out using OpenFOAM in version 2.2.2. The main aim is to exempt from the expensive commercial licences inhibiting advantages of massive parallel computations. The faculty cluster named Thor including totally 35 nodes, each composed of 32 processors cores was available for the numerical calculations.

For each calculation the case was decomposed into 32 processors directories in order to run solution under the particular cluster’s node. The `foamJob` parallel procedure was used which enables to run calculation remotely.

The solution was first pre-computed as a steady state one using the `simpleFoam` solver (for the steady state incompressible turbulent flow) in order to obtain realistic steady or quasi-steady velocity field from the initially prescribed boundary conditions of constant velocity at the inlet patch and constant pressure at the outlet patch. The realizable $k-\varepsilon$ turbulence model (`realizableKE`) is used, according the previous author’s experience with this turbulence model in other CFD software and according to the initial testing of several turbulence models (Standard $k-\varepsilon$, Realizable $k-\varepsilon$, $k-\omega$) in OF where the Realizable $k-\varepsilon$ turbulence model shows the most complex spatial shape of the vortex structure [93]. The values of turbulent quantities - turbulent kinetic energy k and turbulent dissipation rate ε were computed considering 5% of turbulent intensity at the inlet boundary. The walls were treated by the `kqRWallFunction` for turbulent kinetic energy, `epsilonWallFunction` for turbulent dissipation rate and `nutkWallFunction` for turbulent viscosity. The list of boundary conditions used in presented calculations is summarized in Table 12.

Table 12 Boundary conditions

	inlet	outlet	wall
U	<code>fixedValue</code>	<code>zeroGradient</code>	<code>fixedValue</code>
p	<code>zeroGradient</code>	<code>fixedValue</code>	<code>zeroGradient</code>
k	<code>fixedValue</code>	<code>zeroGradient</code>	<code>kqRWallFunction</code>
epsilon	<code>fixedValue</code>	<code>zeroGradient</code>	<code>epsilonWallFunction</code>
nut	<code>calculated</code>	<code>calculated</code>	<code>nutkWallFunction</code>

At the inlet boundary the fixed value of velocity according to the flow rate and at the outlet boundary the fixed value of pressure $p = 0$ Pa are prescribed. Note that some OpenFOAM solvers (e.g. `simpleFoam` and `pimpleFoam`) use the specific pressure energy (defined as $p' = p/\rho$) instead of pressure. The steady state calculation was finished after 500 iterations which were enough to obtain convergent solution for the further unsteady computations.

For unsteady state of calculation the `pimpleFoam` solver was used which is large time-step transient solver for incompressible flow using the PIMPLE (merged PISO and SIMPLE) algorithm. The PIMPLE algorithm enables to prescribe number of inner (for pressure) and outer (for velocity and pressure) corrector loops. In this case the two outer and two inner corrections were utilised, see Table 10.

The numerical stability of solution was controlled using adjustable time-step size ensuring the maximal value of Courant number (Co) which can be user-defined in `controlDict` dictionary. For stable calculations the maximal value of Courant number should be $Co < 1$ but depending on the complexity of the calculated flow and used numerical schemes it can be larger. The Courant number is then defined

$$Co = \frac{\delta t |\mathbf{U}|}{\delta x} \quad (11.2)$$

where δt is time step, $|\mathbf{U}|$ is the magnitude of velocity through that cell and δx is the cell size in the direction of the velocity. Therefore the δt is chosen based on the worst case: the maximum Co corresponding to the combined effect of large flow velocity and small cell size.

In order to compare numerical simulations with experimental measurements several flow rates are chosen in order to cover full range of flow rates. It was found that unsteady solution using `pimpleFoam` solver runs stable on the presented computational domain of the swirl generator with the Courant number up to $Co = 3$. Therefore at the beginning of unsteady simulation the `adjustableTimeStep` was prescribed which enables to solver change the time-step size such that the maximal user-defined Courant number is not exceeded. After the periodic solution is obtained the fixed time-step size is defined according to the time-step size which corresponds to $Co = 3$. The fixed time-step size is necessary for the data sampling (probes signal for FFT, field slices for POD). The value of computed flow rates and corresponding time-step sizes are summarized in Table 13.

Table 13 Computed flow rates and solution time-steps

Flow rate Q (l/s)	Time-step (s)	
5	2.17e-5	4.87e-4
7	1.5e-5	4.80e-4
9	1.1e-5	4.61e-4
11	5.5e-6	3.22e-4
13	4.55e-6	2.7

It is necessary to verify if the time-step size is sufficiently small in order to capture main unsteadiness arising from the vortex structure behavior. For that reason the time-step period of numerical calculation is recommended at least one hundred times smaller (preferably even smaller in order to capture also higher frequencies related to the complex turbulences) than the characteristic time period of the phenomenon which is numerically investigated. In case of spiral vortex the characteristic time period can be linked to the time period of the spiral vortex dominant motion, i.e. rotation. From the initial numerical calculation considering the highest investigated flow rate the rotational (dominant) frequency of the vortex structure is around 57 Hz. According the previous, the time-step period of numerical calculation should be $T \leq 1/(57 * 100) = 1.75e^{-4}s$. According Table 13 one can see that for flow rate $Q = 13$ l/s the time-step size corresponding to the $Co = 3$ is almost forty times smaller than the recommended value. In the same way the time-step sizes for lower computed flow rates were verified.

The kinematic viscosity ν used in `transportProperties` subdirectory was chosen to be equal $\nu = 1e^{-6}m^2s^{-1}$ what corresponds to the water kinematic viscosity at temperature approximately equal to 20°C.

11.4 RESULTS OF NUMERICAL SIMULATIONS

Both the steady and unsteady static pressure and velocity fields are closely examined in order to study the spiral vortex structure while the flow rate increases. The steady pressure and velocity fields are obtained from the unsteady-calculation using `fieldAverage` utility included in the `controlDict` dictionary. Then the profiles of axial and tangential velocity for comparison with LDA measurements can be extracted using `sampleDict` dictionary included in the system directory. There the starting and ending points of line, sampling field, number of points and interpolation scheme are specified. The sampling utility can be executed for user defined time directory where the time-averaged fields are saved and results are then written in form of column data into `sets` directory situated in the `postProcessing` directory.

According to experimental measurements the probe locations for sampling of static pressure signal are included into `controlDict` dictionary through the `probes` sampling utility. The coordinates of point location, field which is sampled (e.g. pressure) and number of time-steps in which the sampling is executed are user defined. Appropriate sampling period is determined from the main rotational frequency of the vortex structure together with known time-step period of calculation in order to have sufficient number of samples for FFT analysis.

For post processing of the flow visualization the ParaView software is used by executing the `paraFoam` command in a case directory. The instantaneous velocity (Figure 58) and pressure (Figure 59) fields for flow rate $Q = 7$ l/s are presented together with spatial shape of the vortex structure visualized by the low-static pressure iso-contour (Figure 60). It has to be noted that here (it is nature of some OpenFOAM solvers, e.g. `simpleFoam` and `pimpleFoam`) the pressure field is plotted for values of specific pressure energy p' where the pressure p is divided by the fluid density ρ . Consequently in Figure 59 the contours of specific pressure energy $p' = p/\rho$ (m^2s^{-2}).

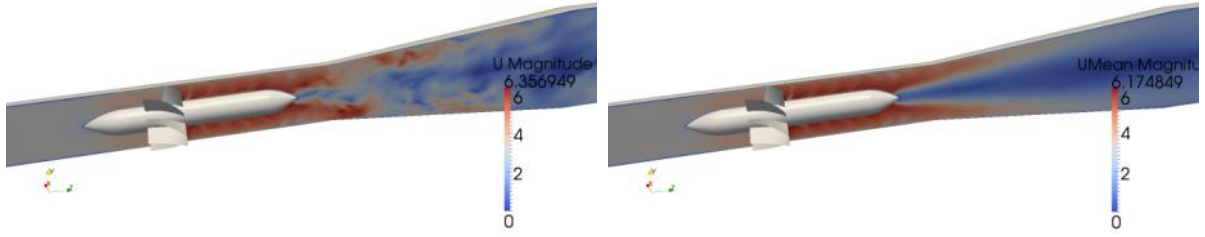


Figure 58 Instantaneous (left) and time-averaged velocity magnitude fields at flow rate $Q = 7$ l/s

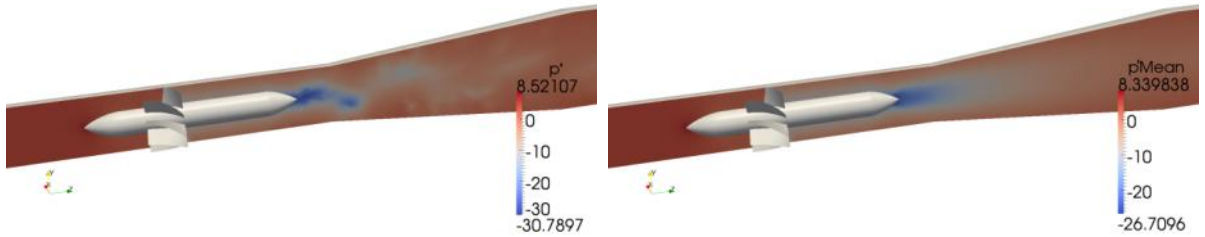


Figure 59 Instantaneous (left) and time-averaged specific pressure energy fields at flow rate $Q = 7$ l/s

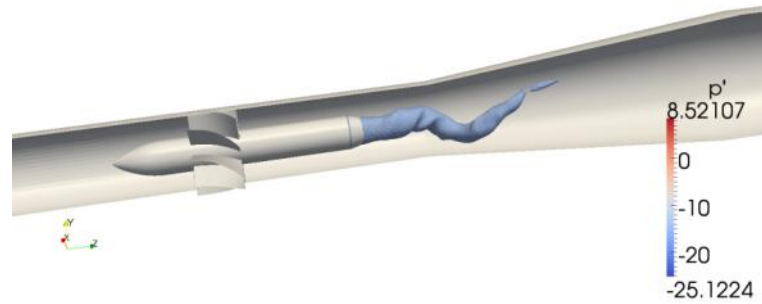


Figure 60 Instantaneous snapshots of the vortex core at flow rate $Q = 7$ l/s (iso-contour of low specific pressure energy)

In case of RANS calculations the correctly evaluated hydraulic losses strongly depend on the near wall modeling. In this case the high Re wall functions are used see boundary conditions for the walls in Table 12. Consequently the dimensionless wall distance y^+ was computed for wall regions of central spike, generator blades and outer walls according to equation (10.3)

$$y^+ = \frac{yu_\tau}{\nu} \quad (11.3)$$

where y is the perpendicular distance from the wall, the ν is kinematic viscosity and u_τ the friction velocity calculated from wall shear stress and fluid density according to equation (10.4)

$$u_\tau = \sqrt{\frac{\tau_w}{\rho}} \quad (11.4)$$

The resulting values of minimal, average and maximal values of y^+ for particular wall region are summarized in Table 14.

Table 14 Average values of y^+

Wall region	Min y^+	Average y^+	Max y^+
spike	6.9	33.1	96
blades	2.95	10.2	29.4
outer walls	7.2	40.3	149.4

Using the realizable $k-\epsilon$ turbulence model with the wall functions the y^+ is recommended to be in interval 30 – 120 in order to fit the log-wall region. One can see that for blades region average y^+ is lower, nevertheless other two regions fulfil this recommendation.

11.4.1 Computed pressure fields

The time-averaged value of specific pressure energy $p' = p/\rho$ calculated from the unsteady signal in monitoring points is plotted in Figure 61 (left). Using the pressure conditions (corresponding with computational domain outlet) and water density ρ from the experimental measurements, the calculated specific pressure energy p' can be converted to the mean static pressure p (see Figure 61 (right)). It is necessary for further comparison of numerically computed pressure fields with the experimental results.

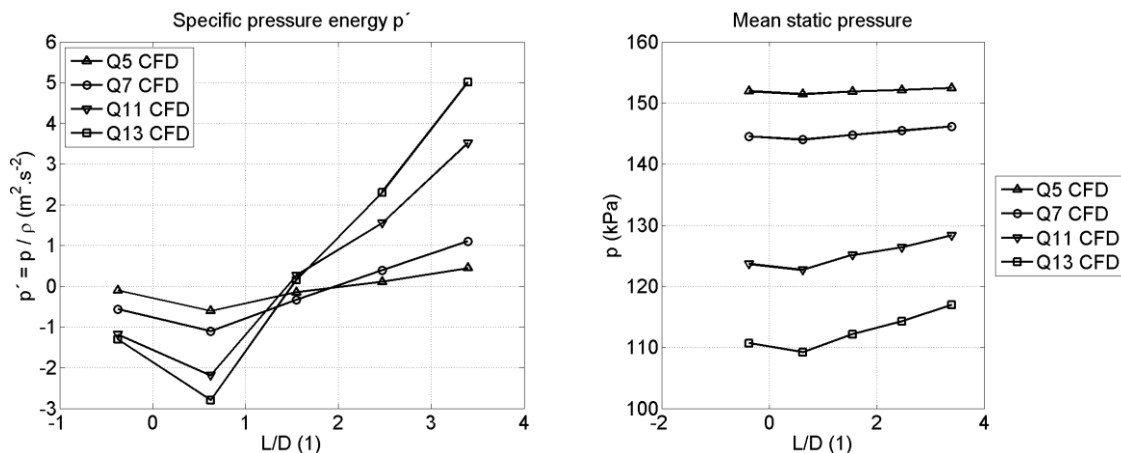


Figure 61 Mean specific pressure energy from CFD calculation (left) and its conversion to the mean static pressure (right)

The numerical pressure recovery is calculated and plotted in Figure 62. While for flow rates $Q = 7, 11$ and 13 l/s the values of pressure recovery are almost similar alongside the diffuser the pressure recovery at flow rate $Q = 5$ l/s is much lower. One of the reasons is that the partial separations from diffuser wall occur for flow rate $Q = 5$ l/s, thus the diffuser kind of flow (increasing pressure in streamwise direction) is not sufficient enough compared to higher flow rates.

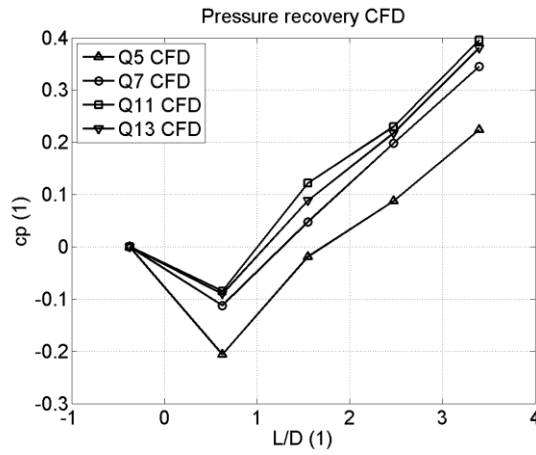


Figure 62 Pressure recovery of numerically computed flow rates

The computed unsteady static pressure signal is used for the power spectra analysis. Totally 10 sampling probes situated in the diffuser section are defined corresponding to the experimental set-up (see Figure 29). The first five probes correspond to the single row of pressure transducers and the others five probes form oppositely oriented pairs. Two oppositely oriented rows are used in order to distinguish between longitudinal and transverse pressure pulsations (i.e. synchronous and asynchronous), which are further compared with experimentally measured ones in section 12.1.2.

The evolution of frequency and amplitude magnitudes of numerically computed asynchronous pressure pulsations is plotted in Figure 63.

In agreement with the experimental measurements the largest amplitudes are found in sensor location s2 ($L/D = 0.627$) for entire range of flow rates except the $Q = 11$ l/s where the largest magnitude is in s3 cross-section. Similarly to experimental results the asynchronous frequencies decrease downstream of diffuser.

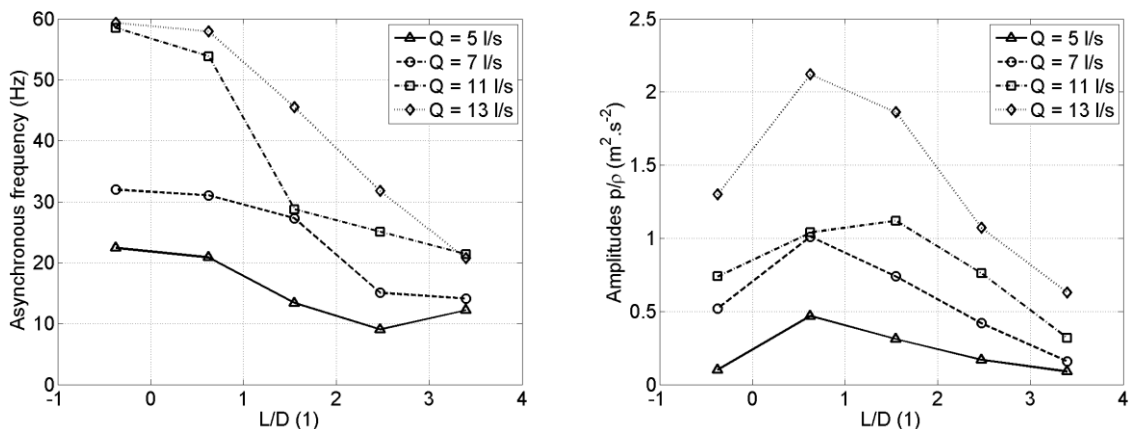


Figure 63 Frequency (left) and amplitudes (right) of numerically computed asynchronous pressure pulsations

11.4.2 Computed velocity fields

The computed mean velocities are obtained using the surface integral over the particular cross-section in ParaView post-processing interface. In the Figure 64 the mean time-averaged velocities are plotted against L/D ratio for computed flow rates $Q = 5, 7, 11.5$ and 13 l/s.

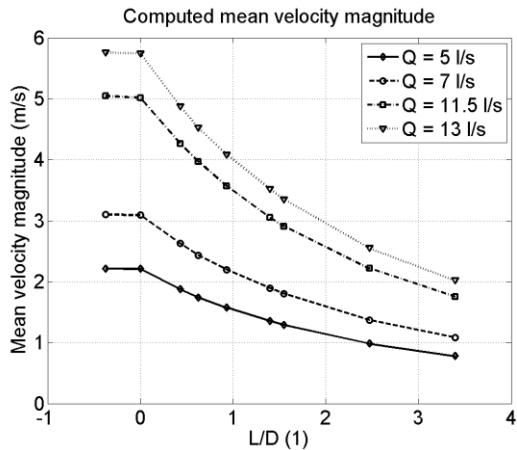


Figure 64 Computed mean velocity magnitude

In Figure 66 the evolution of mean time-averaged velocity is plotted in cross-section s1 – s5 located according to Figure 65. While the cross-section s1 is located 20 mm in front of the diffuser inlet, the cross sections s2 – s5 are situated within of the diffuser.

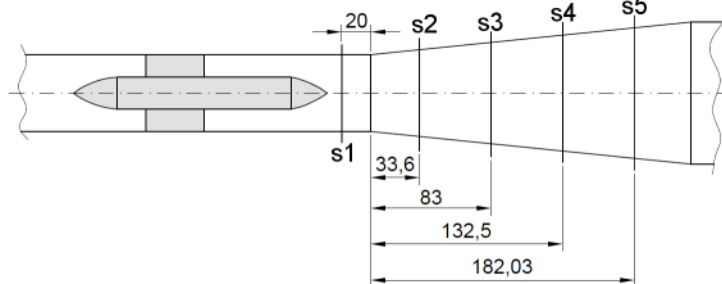


Figure 65 Location of cross-sectional planes

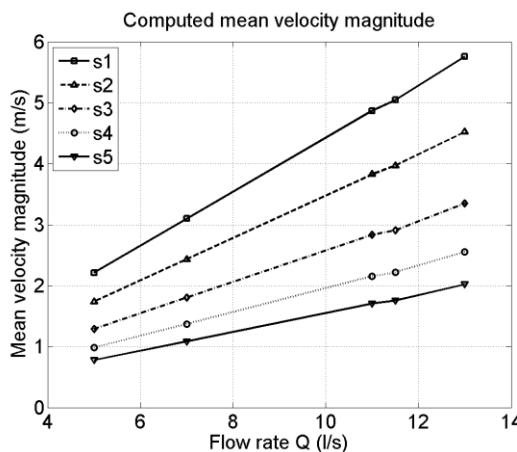


Figure 66 Computed mean velocity magnitude plotted against flow rate

One can see that while for particular flow rate the mean time-averaged velocity decrease parabolically downstream of the diffuser, for the particular cross-section the velocity increase linearly with increasing flow rate.

In order to compare computed and measured velocity fields the computed velocity profiles are extracted in locations S1, S2 and S3 corresponding to the ones where the LDA measurements were realized, see Figure 67.

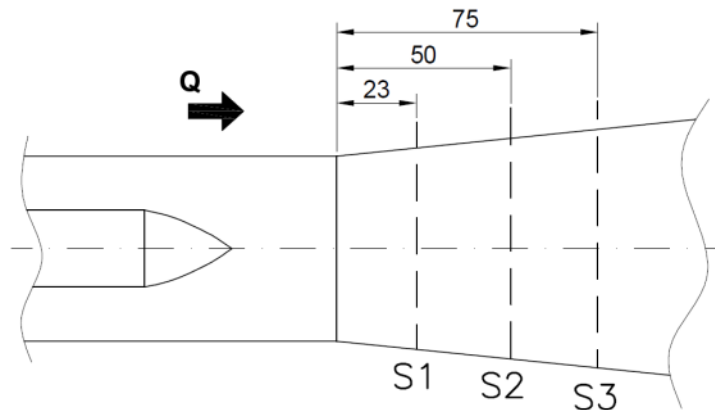


Figure 67 Locations of LDA measurements

Both axial and tangential velocity profiles are plotted in Figure 68 and Figure 69 against the wall distance for computed flow rates $Q = 5, 7, 11$ and 13 l/s. One can see that maximum value of axial velocity for all three investigated cross-sections is between 5 and 10 mm from the diffuser wall. In the diffuser centre the back-flow region occurs with the maximum negative value of velocity increasing with the flow rate. The tangential velocity profiles are nearly flat in the main flow region and almost linearly decrease towards diffuser axis. Interesting finding is that the width of the back-flow region in particular cross-section remains almost unchanged with increase of flow rate.

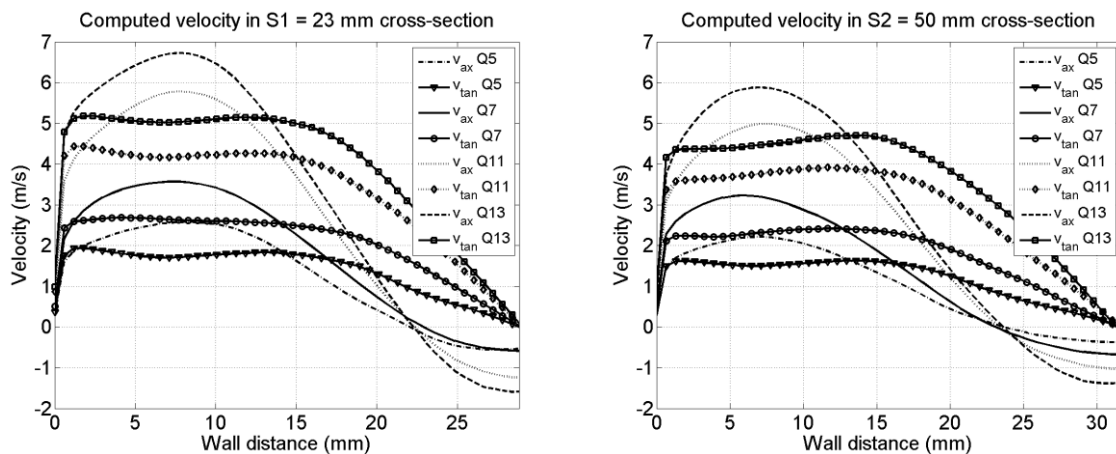


Figure 68 Comparison of computed velocity profiles for different flow rates $Q = 5, 7$ and 13 l/s in S1 and S2 cross-section

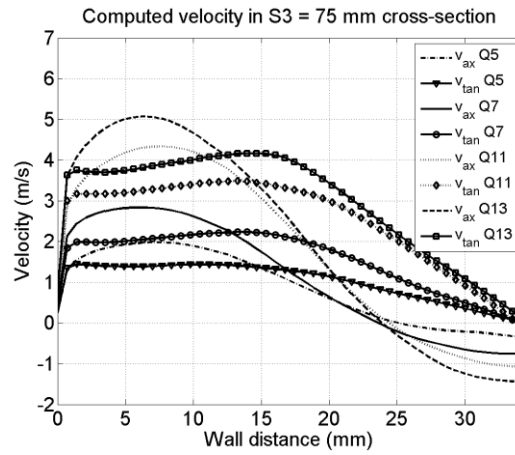


Figure 69 Comparison of computed velocity profiles for different flow rates $Q = 5, 7$ and 13 l/s in S3 cross-section

11.4.3 Estimation of the swirl number S_r along the diffuser length

As was mentioned in section 1.1 and according to [100] the vortex breakdown in the conical diffusers is a mechanism for limiting increase in the swirl number S_r . The swirl number defined as

$$S_r = \frac{\int v_{ax} v_{tan} r dS}{R \int v_{ax}^2 dS} \quad (11.5)$$

is calculated in several cross-sections downstream of the conical diffuser see Figure 70.

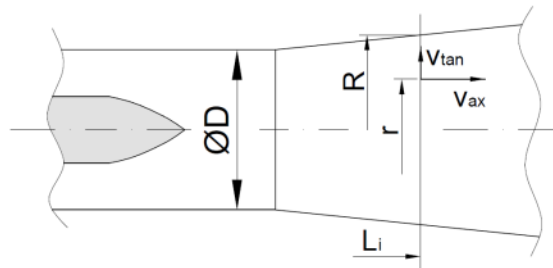


Figure 70 Velocities influencing swirl number S_r

The evolution of S_r against L/D for three calculated flow rates $Q = 5, 7$ and 13 l/s is plotted in Figure 71. One can see that for all three flow rates the back-flow region (approximately bounded between $L/D = 0.5$ and $L/D = 2$) appears. On the other hand in downstream part of diffuser $L/D > 2$ the swirl number increases quadratically.

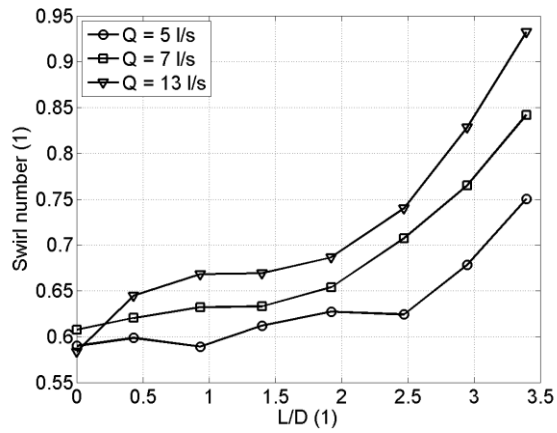


Figure 71 Comparison of computed swirl number for three different flow rates

It was shown in section 7.3.1 that asynchronous pressure pulsations generated by the unsteady vortex dynamics have significant amplitudes up to sensor p4 located in station $L/D = 2.472$. If we look at Figure 71 it is clear that abrupt increase in the swirl number is related with the decay of the vortex structure. In other words it proves above mentioned statement that the spiral form of vortex breakdown limits increase of swirl number.

12 COMPARISON OF EXPERIMENTAL MEASUREMENTS AND NUMERICAL RESULTS

In this section the experimentally obtained data are correlated with the numerical results including pressure and velocity fields.

12.1 COMPARISON OF PRESSURE RESULTS

Since the CFD calculations are available for several chosen flow rates the comparison with the pressure measurements can be done. Both the mean static pressure field (in form of mean pressure and pressure recovery factor c_p) and unsteady pressure pulsations (in form of amplitude-frequency spectra) are compared.

12.1.1 Mean static pressure field

In Figure 72 the comparison of mean static pressure for particular sensor locations is plotted. The CFD calculations are carried out using single phase flow. From experimental measurement it is known that cavitation in the vortex core begins to appear for flow rates $Q > 7$ l/s and relevant pressure conditions at the diffuser outlet. One can see that the large discrepancy in values of mean static pressure for higher flow rates is noticeable. The experimental values of static pressure underestimate numerical ones. This is probably due to cavitating vortex core which leads to lower value of static pressure. The location of pressure sensors are listed in dimensionless form of ratio L/D , where the L is length of diffuser measured from the entrance and $D = 0.0536$ m is the diffuser inlet diameter. The sensors locations are summarized in Table 15.

Table 15 Sensor locations

sensor number	L/D
1	-0.3731
2	0.6269
3	1.5485
4	2.4720
5	3.3955

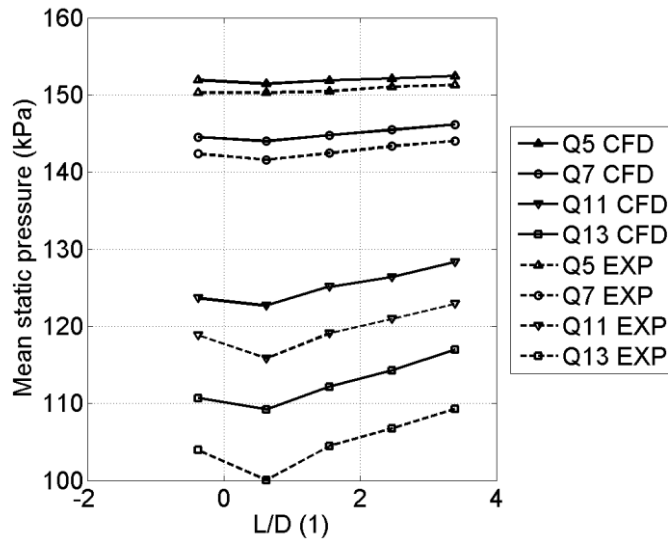


Figure 72 Mean static pressure EXP vs CFD

The comparison of pressure recovery factor is carried out for particular computed flow rates in Figure 73 and Figure 74. The best agreement between computed and experimentally measured pressure recovery c_p is obtained for flow rate $Q = 7$ l/s. On the other hand largest discrepancy is for the flow rate $Q = 5$ l/s where the computed pressure recovery underestimate experimental values in all sensor locations. For both higher computed flow rates $Q = 11$ and 13 l/s the numerical pressure recovery overestimates numerical one especially in the second sensor location situated $L/D = 0.6269$. It is location at the beginning of conical section where the vortex structure causes the largest amplitudes of pressure pulsations. Therefore the single phase computation is considered as the main source of result disagreement for higher flow rates.

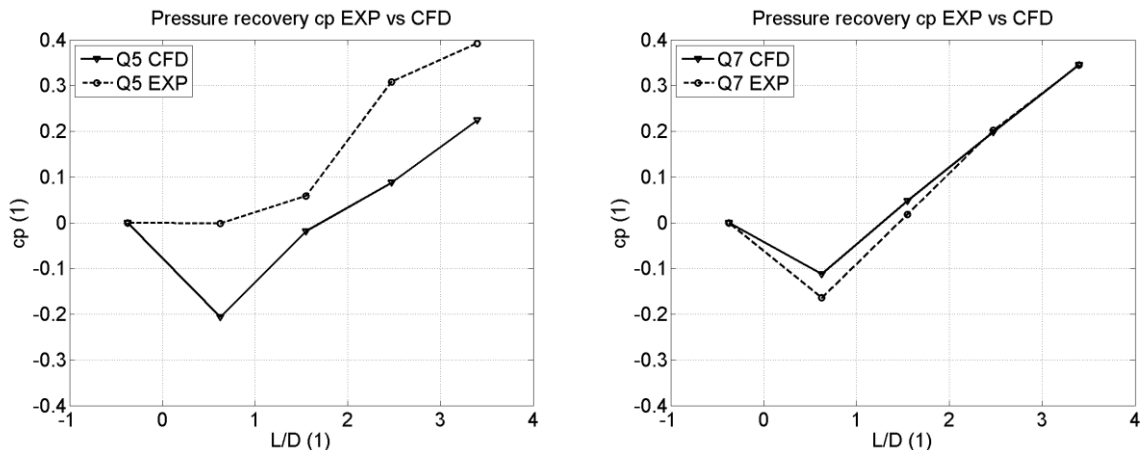


Figure 73 Pressure recovery factor EXP vs. CFD for flow rates $Q = 5$ and 7 l/s

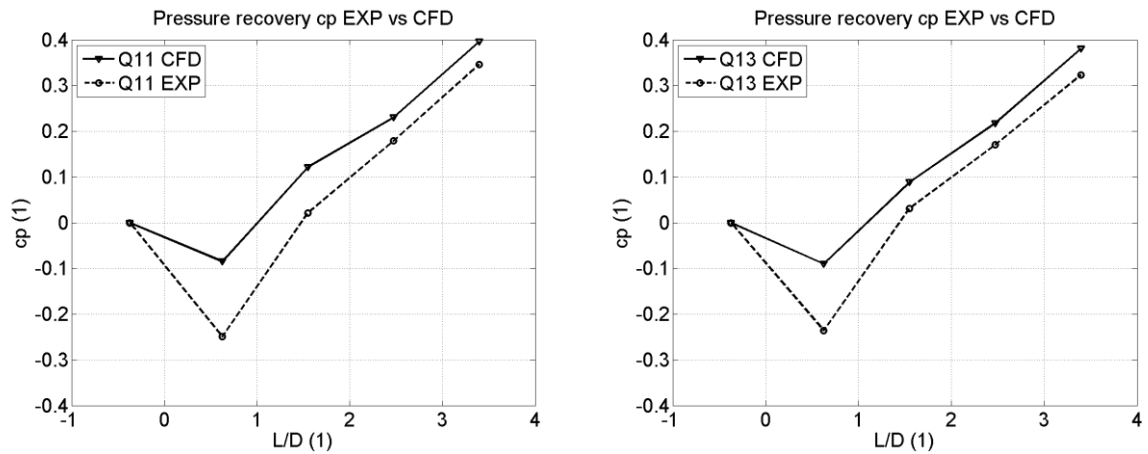


Figure 74 Pressure recovery factor EXP vs. CFD for flow rates $Q = 11$ and 13 l/s

12.1.2 Unsteady pressure pulsations

The numerically computed frequencies of the vortex rotation are compared with ones extracted from the experimentally measured pressure signal. The decomposition to the synchronous and asynchronous pressure pulsations (according to section 7.3) is done for both experimental and numerical data. Totally four computed flow rates $Q = 5, 7, 11$ and 13 l/s are considered for comparison. The results are presented only for asynchronous component because the estimation of synchronous component of numerically computed pressure suffers from inadequate length of processed signal. Due to short numerical signal (approximately 1 sec of flow time) the amplitudes of synchronous component with low frequency (2 – 12 Hz estimated from experimental results) are less significant.

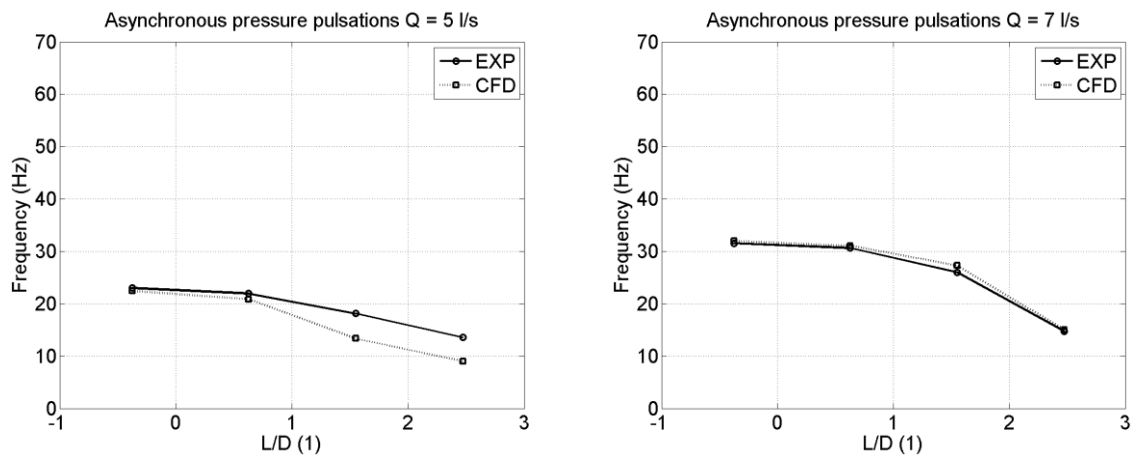


Figure 75 Asynchronous pressure pulsations at flow rate $Q = 5$ l/s (left) and 7 l/s (right)

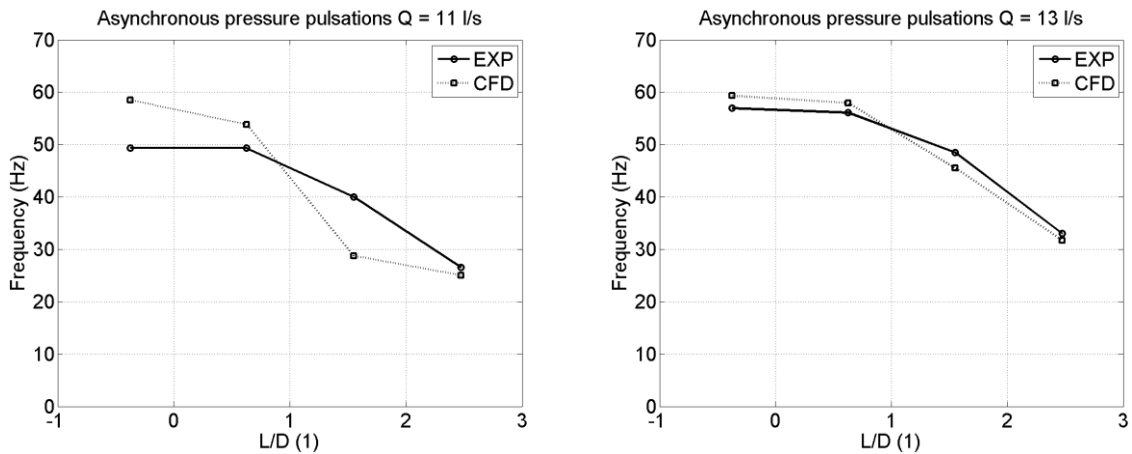


Figure 76 Asynchronous pressure pulsations at flow rate $Q = 11$ l/s (left) and 13 l/s (right)

The best agreement between numerical and experimental results is obtained for flow rate $Q = 7$ l/s, see figure Figure 75 (right). Both the magnitude of asynchronous pressure pulsations and decreasing along the diffuser is well predicted. On the other hand the largest discrepancy can be found at flow rate $Q = 11$ l/s, see Figure 76 (left). While the frequency magnitudes are overestimated for first two locations of pressure sensors the large underestimation is obtained for the third sensor location. Adequate results are also for flow rates $Q = 13$ l/s, see Figure 76 (right). Nevertheless underestimation of experimentally obtained asynchronous frequency can be found for the third and fourth sensor location at flow rate $Q = 5$ l/s, see Figure 75 (left).

12.1.3 Time evolution of numerically computed spiral vortex

According to visual observations of cavitating vortex (see section 9.1) the time-evolution of numerically computed vortex structure (represented as the iso-contour of low static pressure) is carried out in Figure 77. It has to be noted that while the experimental observation is presented for flow rate $Q = 13.5$ l/s (due to the strongest cavitation well visualizing the vortex core) the numerical results presented below are for flow rate $Q = 7$ l/s. Nevertheless comparing the time evolution of computed vortex structure in Figure 77 with the experimental observation of cavitating vortex (see Figure 40) one can see that the collapse of spiral vortex is well predicted in numerical simulation as well. Agreement between numerical computation (where the potential influence of experimental test rig is eliminated) and experimental observation proves that this vortex behavior is related to the self-excited instability (producing the synchronous pressure pulsations discussed in section 7.3.2) and is not consequence of any other source as for example natural frequency of experimental test rig.

In some previous studies of the draft tube surge [25], [58] was concluded that the synchronous part of pressure pulsations are related to the interaction of the vortex rope with the elbow of bended draft tube and cannot be found in the straight draft tubes. Nonetheless as was presented here the synchronous pulsations can arise also from the vortex instability in the straight diffuser. This is recently well demonstrated in [94]. Although it has to be noted, that this instability (periodically decaying and forming spiral vortex) is strongly depending to the angle of diffuser opening. From numerical analysis (not presented here) was found, that for larger angles (15° and 18°) of diffuser opening the spiral vortex become stable without significant periodic decay.

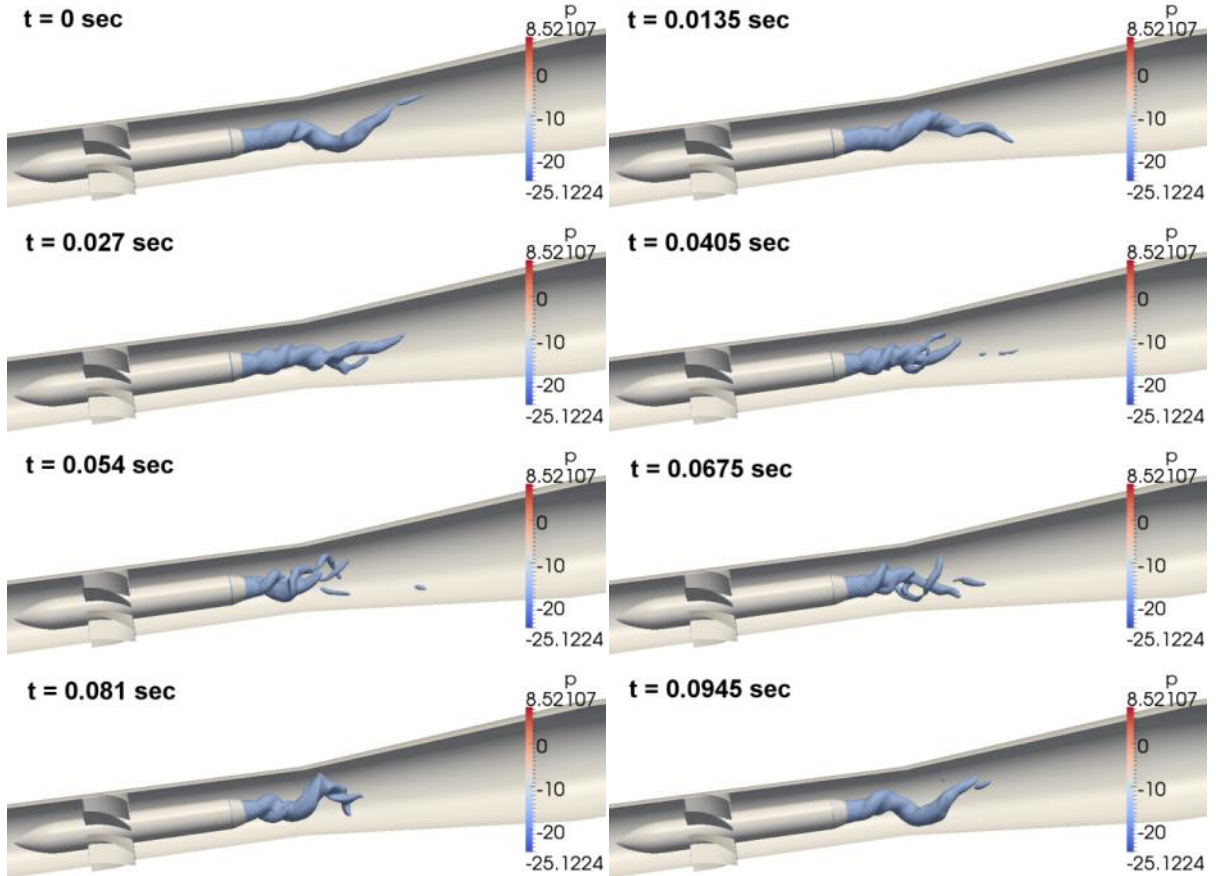


Figure 77 Time evolution of numerically computed vortex structure at flow rate $Q = 7 \text{ l/s}$ (iso-contour of static pressure)

12.2 COMPARISON OF VELOCITY RESULTS

The mean (time-averaged) velocity magnitude V_{CFD} of numerically computed velocity fields is calculated as follows

$$V_{CFD} = \sqrt{V_{ax_CFD}^2 + V_{tan_CFD}^2} \quad (12.1)$$

where particular components (V_{ax_CFD} and V_{tan_CFD}) of velocity magnitudes are extracted using surface integral over cross-sectional plane in corresponding location. The velocity magnitude of experimentally measured velocity fields (using LDA) is calculated assuming axial and tangential components (the radial component was not measured) according following equation

$$V_{EXP} = \sqrt{V_{ax_EXP}^2 + V_{tan_EXP}^2} \quad (12.2)$$

where the magnitude of axial and tangential components is estimated using trapezoid integration of measured velocity profiles. The comparison of both numerically computed and experimentally measured velocity magnitudes is presented in Figure 78 for three measured flow rates $Q = 5, 7$ and 11.5 l/s.

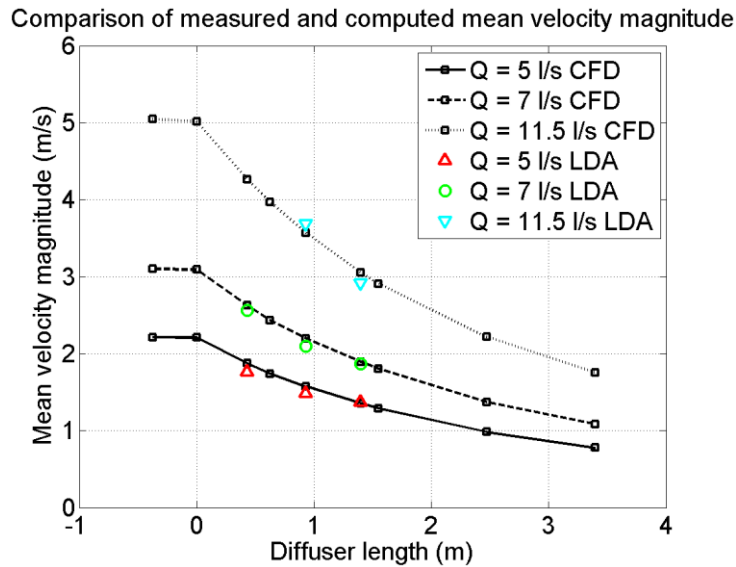


Figure 78 Comparison of computed and measured mean velocity magnitude

One can see that computed velocity magnitudes are in very good agreement with the measured ones. At flow rates $Q = 5$ and 7 l/s slight overestimation of numerical results can be found for the first two measured locations situated 0.023 and 0.05 m downstream of diffuser inlet. On the other hand in the third location (0.075 m downstream of the diffuser inlet) the excellent agreement is achieved. For the higher investigated flow rate $Q = 11.5$ l/s the comparison is done only for the second and the third measured locations.

The comparisons of computed and measured axial and tangential velocity profiles in corresponding cross-sections are plotted in Figure 79 for $Q = 5$ l/s, in Figure 80 for $Q = 7$ l/s and in Figure 81 for $Q = 11.5$ l/s. Note that for $Q = 11.5$ l/s measurements are carried out only in the second and the third cross-sections. The variation of Random Mean Square Velocity (u_{RMS}) for each measured point is presented in a form of error bars. u_{RMS} was calculated using following equation:

$$u_{RMS} = \sqrt{\sum_{i=0}^{N-1} \frac{1}{N} (u_i - \bar{u})^2} \quad (12.3)$$

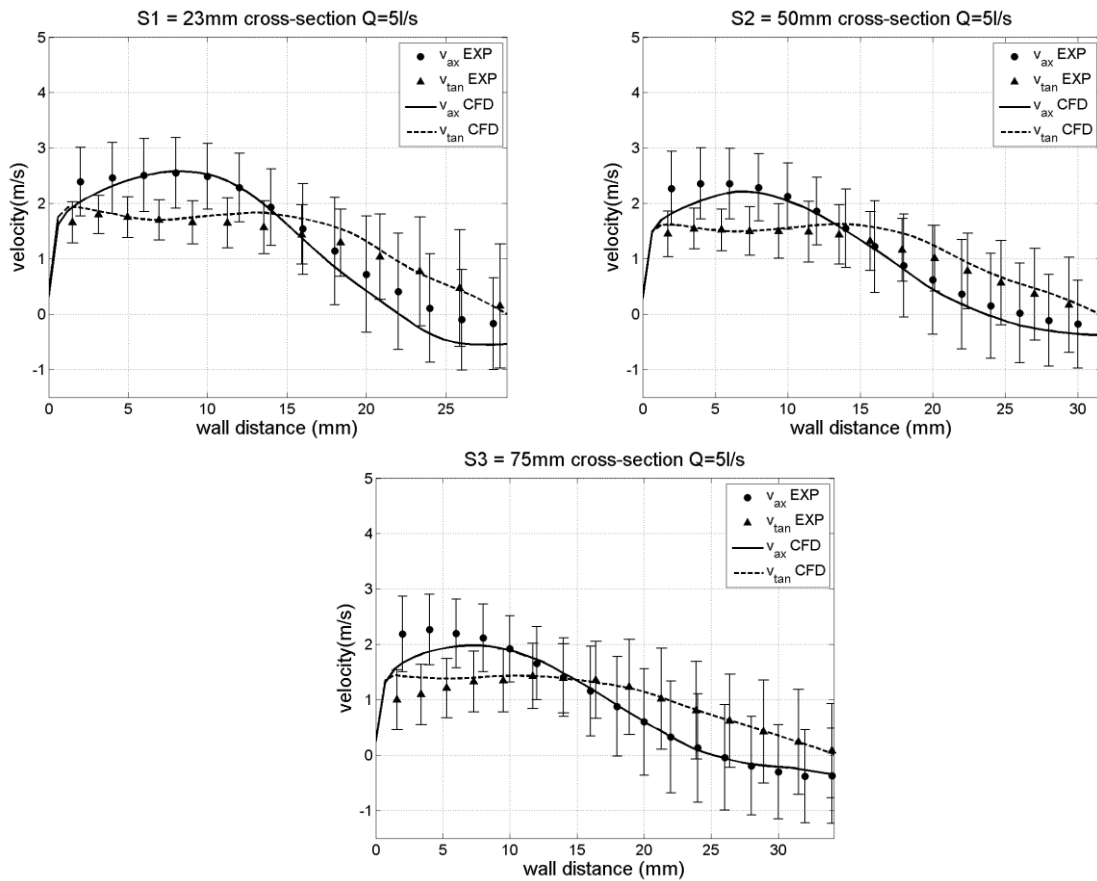


Figure 79 Comparison of measured and computed velocity profiles for flow rate $Q = 5 \text{ l/s}$

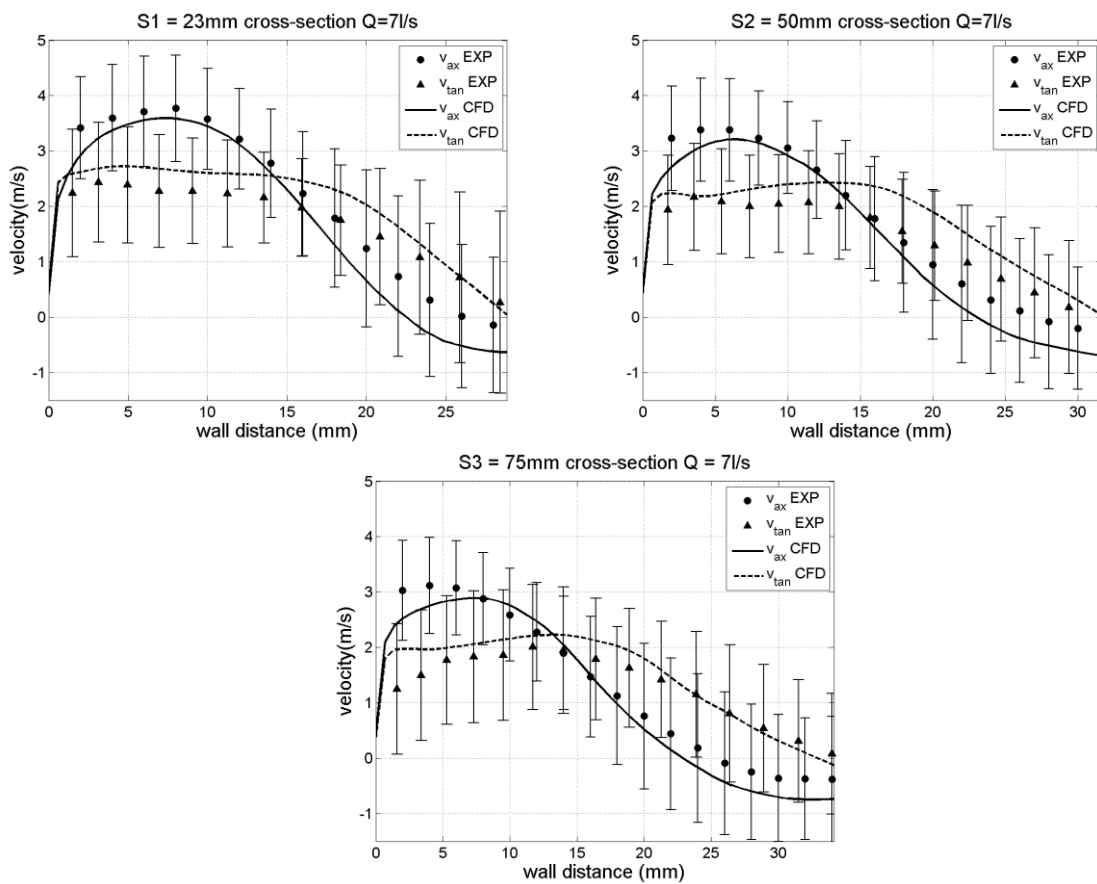


Figure 80 Comparison of measured and computed velocity profiles for flow rate $Q = 7 \text{ l/s}$

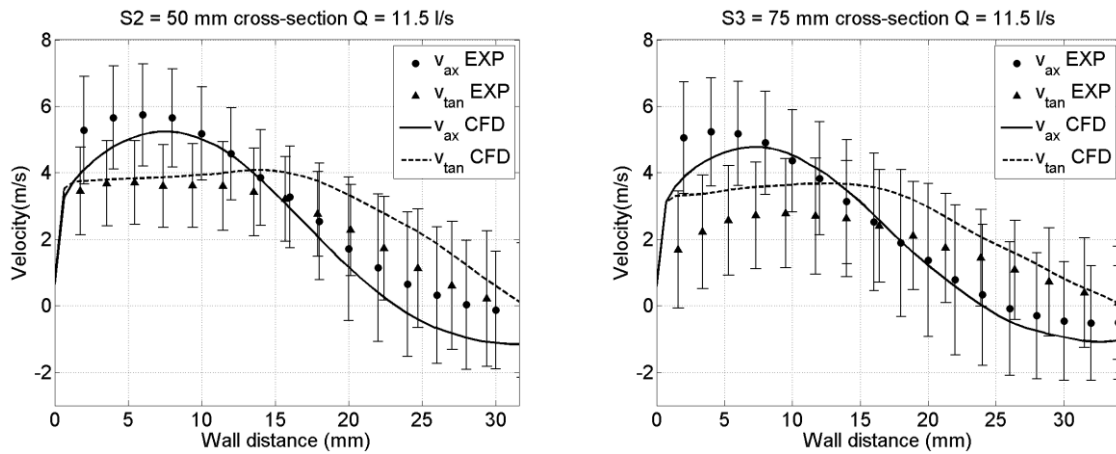


Figure 81 Comparison of measured and computed velocity profiles for flow rate $Q = 11.5$ l/s

It is clear that computed velocity profiles fit sufficiently with the measured ones for all three investigated flow rates. The largest discrepancies occur in the near wall region and close to the diffuser axis. While in the near wall region the numerical results are influenced by the RANS based calculation (suffering from the boundary layer modeling using the wall function) the result disagreement in the diffuser central region is caused by the large fluctuating part of the velocity magnitude which is close to zero value [114]. Another possible source of disagreement in the near wall region can arise from the large pressure gradient (resulting from the diffuser kind of flow) which causes the flow separation from the diffuser walls. Another source of disagreement in the near wall region can be related to the used turbulence model which does not affect strong turbulence anisotropy. Thus the utilization of higher order turbulence model (e.g. Reynolds stress turbulence model RSM [32]) or two-equation models with quadratic or cubic strain-stresses relationship can be recommended [4], [111].

13 ENERGY DISSIPATION IN THE DOWNSTREAM PART OF THE DIFFUSER

In this section the deeper assessment of energy dissipation related to the flow with the spiral vortex generated by “BUT” swirl generator is carried out. While in the first subsection the unsteady character of the static, dynamic and total pressure is examined resulting in the time evolution of power dissipated between upstream (s1) and downstream (s4) cross-sections, in the second subsection the time-averaged evolution of the static, dynamic and total pressures are assumed in order to calculate pressure recovery factor c_p , loss coefficient ξ and diffuser efficiency η for several computed flow rates. Moreover the time-averaged dissipation function arising from the irreversible part of the stress tensor in Navier-Stokes equation is examined for entire range of computed flow rates.

13.1 UNSTEADY EVOLUTION OF ENERGY DISSIPATION

Unsteady evolution of static, dynamic and total pressure is plotted in four cross-sections (see Figure 82) for two computed flow rates $Q = 5$ and 11 l/s.

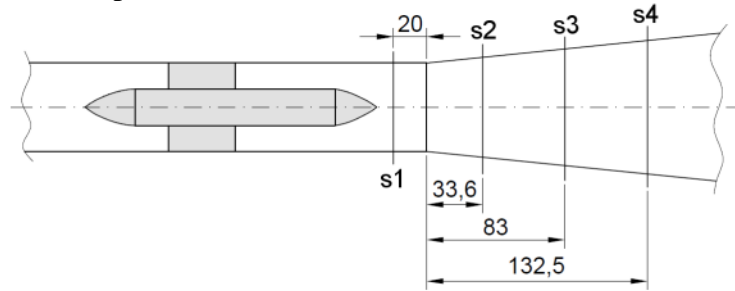


Figure 82 Locations of cross-sectional planes.

The numerical data of specific pressure energy $p' = p/\rho$ and velocity components are sampled in time then the average values over cross-sectional surfaces are computed. For better interpretation the specific pressure energy p' is later transformed to the pressure by multiplying it with density. Due to the highly uneven velocity profiles in the particular cross-sections the kinetic energy correction factor α is considered for calculation of dynamic pressure $p_{dyn} = \frac{1}{2}\rho\alpha v^2$. The kinetic energy correction factor is defined as follows

$$\alpha = \frac{\int v^2 \cdot v_n dS}{\bar{v}^3 \cdot S} \quad (13.1)$$

where v is velocity magnitude, v_n is velocity component normal to the cross-section (in this case axial velocity) and \bar{v} is bulk velocity. The kinetic energy correction factor is evaluated for each instantaneous velocity field and its time evolution is plotted in Figure 83. One can see very highly unsteady character of the velocity field which increases in the downstream part of the diffuser and as a consequence of unstable behavior of the vortex structure in time (see section 12.1.3).

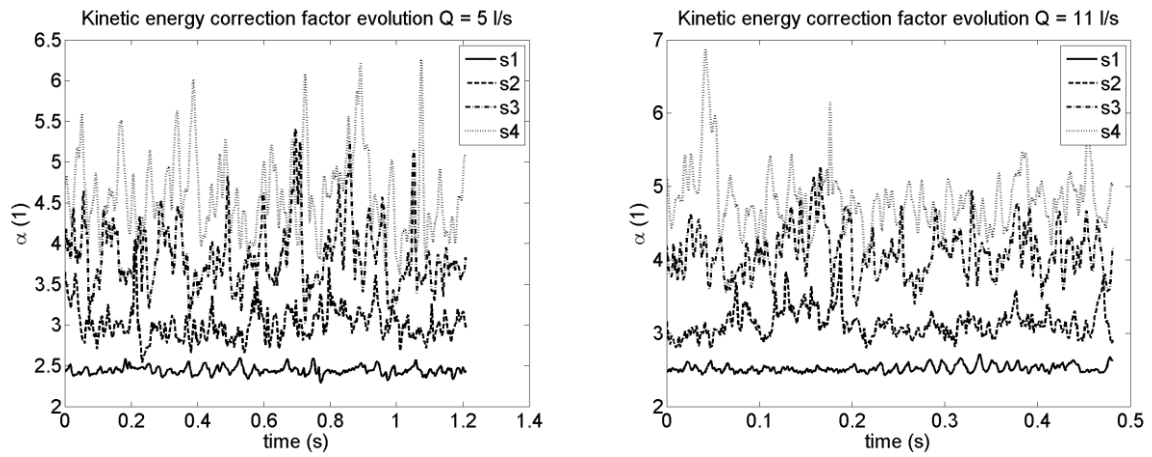


Figure 83 Time evolution of kinetic energy correction factor for $Q = 5$ l/s (left) and $Q = 11$ l/s (right)

The time-averaged values of kinetic energy correction factor, static, dynamic and total pressure for both flow rates are summarized in Table 16 ($Q = 5$ l/s) and Table 17 ($Q = 11$ l/s). One can see that the dynamic pressure decreases, static pressure increases and total pressure related to the energy dissipation decreases downstream of the diffuser.

Table 16 Time-averaged values $Q = 5$ l/s

Cross section	Kinetic energy correction factor α (1)	Static pressure (Pa)	Dynamic pressure (Pa)	Total pressure (Pa)
s1	2.44	-2495.5	6138.93	3643.43
s2	3.01	-1856.65	4871.216	3004.582
s3	3.84	-1068.07	3363.934	2295.86
s4	4.58	-489.118	2405.662	1916.544

Table 17 Time-averaged values $Q = 11$ l/s

Cross section	Kinetic energy correction factor α (1)	Static pressure (Pa)	Dynamic pressure (Pa)	Total pressure (Pa)
s1	2.5183	-12607.8	31024.75	18416.99
s2	3.1253	-9241.73	24685.99	15444.35
s3	4.0873	-5425.32	17522.7	12097.39
s4	4.8080	-1981.53	12358.71	10377.29

The time evolutions of static and dynamic pressure are plotted in Figure 84 and Figure 85 respectively.

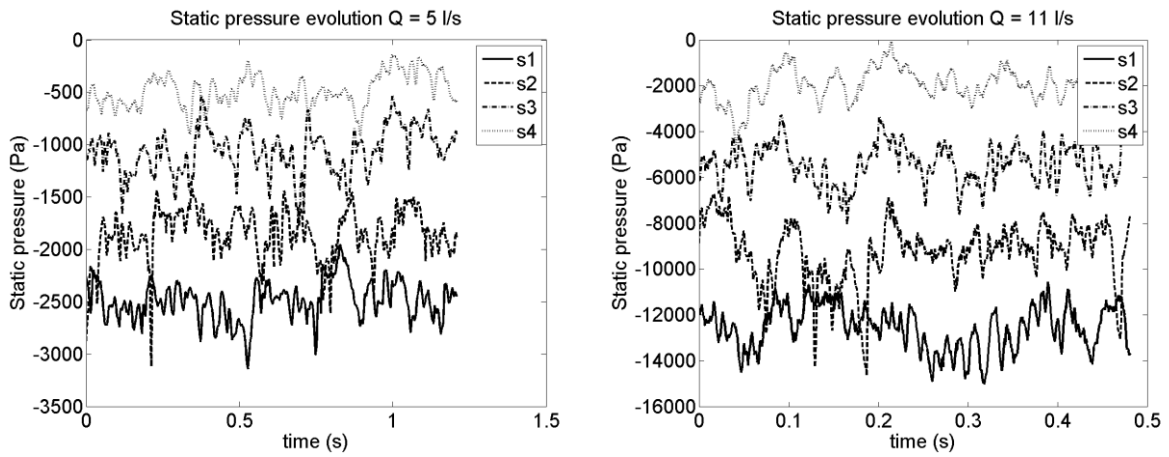


Figure 84 Time evolution of static part of specific pressure energy for $Q = 5$ l/s (left) and $Q = 11$ l/s (right)

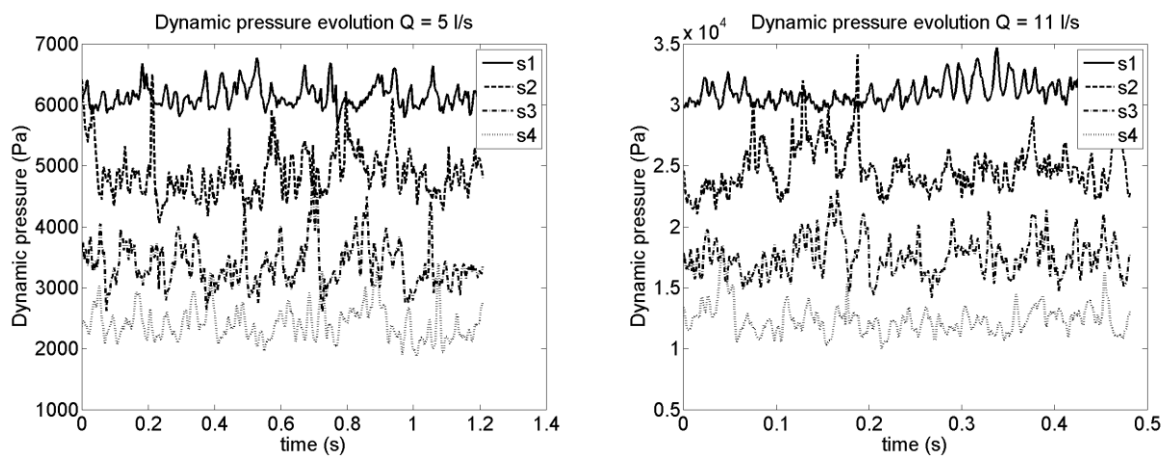


Figure 85 Time evolution of dynamic part of specific pressure energy for $Q = 5$ l/s (left) and $Q = 11$ l/s (right)

The total pressure is calculated considering the sum of static and dynamic pressure. The resulting time evolutions of total pressure are plotted in Figure 86.

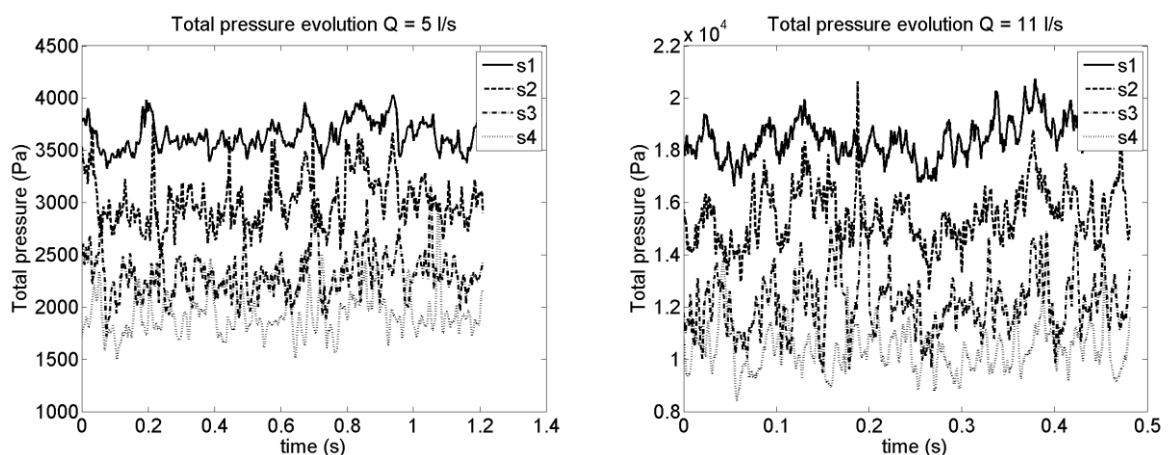


Figure 86 Time evolution of total specific pressure energy for $Q = 5$ l/s (left) and $Q = 11$ l/s (right)

From the evaluation of static pressure the amplitude-frequency spectra are calculated for each cross-section. Frequencies of pulsations are summarized in Table 18. It is clear that these

frequencies are related to the synchronous pressure pulsations. Therefore later in the section 16.2.2 the static pressure modes related to the synchronous pulsations can be easily identified.

Table 18 Frequency of the static pressure pulsations (Hz)

Cross section	Q = 5 l/s	Q = 11 l/s
s1	4.96	4.47
s2	4.96	2.23
s3	1.65	6.70
s4	1.65	8.94

Moreover agreement in the frequency magnitude of synchronous static pressure pulsations compared to the frequency of synchronous static pressure modes is discussed later in conclusion of POD analysis, see section 16.3.

In Figure 87 the fluctuating parts of static, dynamic and total pressure records are plotted in second cross-section s2 for both computed flow rates Q = 5 and 11 l/s. One can see that peaks of static pressure are in reverse phase to the peaks of dynamic pressure, which is justified by the basic equations of the fluid flow

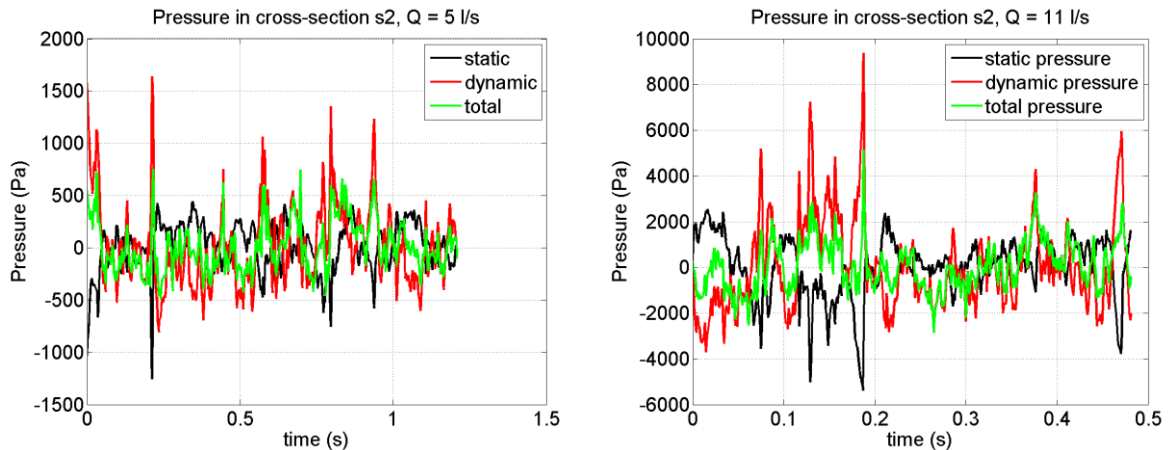


Figure 87 Fluctuating part of static, dynamic and total pressures at flow rates Q = 5 and 11 l/s

The time evolution of the power loss ΔP is calculated from the specific energy difference ΔY between s1 and s4 cross-sections according the following equation:

$$\Delta P = \rho \cdot Q \cdot \Delta Y = \rho \cdot Q \left(\frac{p_{s1} - p_{s4}}{\rho} + \frac{\alpha_{s1} \cdot v_{s1}^2 - \alpha_{s4} \cdot v_{s4}^2}{2} \right) \quad (13.2)$$

In Figure 88 there are plotted both unsteady (black) and averaged (red) values of power dissipated at flow rates Q = 5 and 11 l/s. One can see that strong unsteady character of the flow (periodically collapsing spiral vortex described in section 12.1.3) is reflected in the unsteady power dissipation. The power dissipation increases when the flow rate increases

from $Q = 5$ l/s to 11 l/s. Nevertheless the amplitudes of fluctuating part seem to be of similar magnitude for both flow rates. It shows that the main feature of spiral vortex decay is independent on the flow rate. While the largest dissipated power corresponds with the well developed spiral vortex the lowest value is achieved when the spiral vortex collapse upstream.

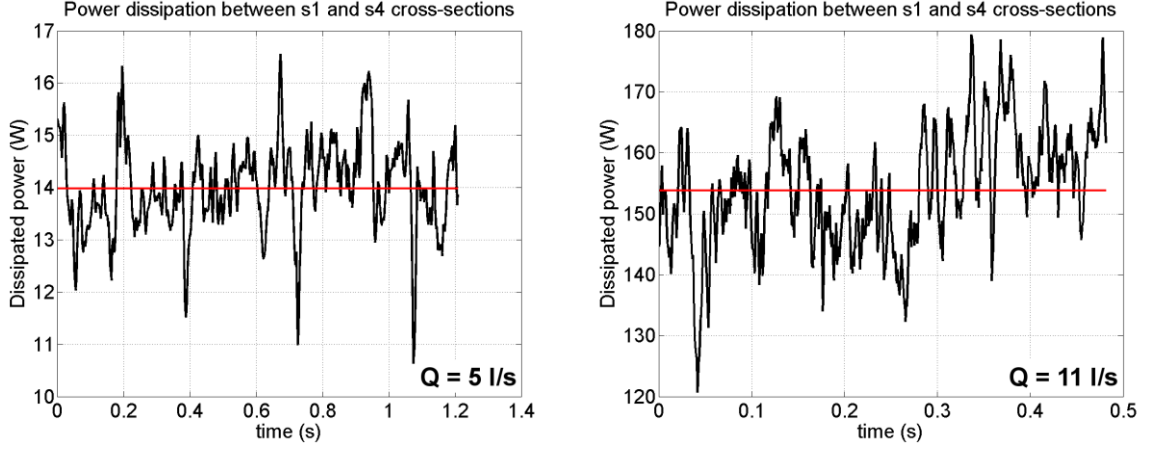


Figure 88 Unsteady power dissipation between s1 and s2 cross-sections.

13.2 STEADY EVOLUTION OF ENERGY DISSIPATION

For the steady evolution of energy dissipation the three integral characteristics are evaluated – pressure recovery factor c_p , loss coefficient ξ and diffuser efficiency η . The pressure recovery c_p is evaluated according to equation (7.1) with consideration of kinetic energy correction factor α

$$c_p = \frac{p_{s(i)} - p_{s(1)}}{\frac{1}{2}\rho\alpha_1\bar{v}_1^2} \quad (13.3)$$

the diffuser loss coefficient is computed from

$$\xi = \frac{2}{\alpha_{(i)}\bar{v}_{(i)}^2} \left(\frac{\alpha_{(1)}\bar{v}_{(1)}^2 - \alpha_{(i)}\bar{v}_{(i)}^2}{2} + \frac{p_{s(1)} - p_{s(i)}}{\rho} \right) \quad (13.4)$$

and the diffuser efficiency from

$$\eta = \frac{p_{s(i)} - p_{s(1)}}{p_{a(1)} - p_{a(i)}} \quad (13.5)$$

where (1) is the first cross-section (the diffuser entrance in case of diffuser efficiency η) and (i) is the i-th cross-section downstream of the diffuser. Totally 6 cross-sections are considered five of them corresponding with locations of pressure transducers and one as the diffuser entrance, see Figure 89. Integral characteristics are plotted against L/D distance from the diffuser entrance where the $D = 0.0536$ m is the inlet diameter.

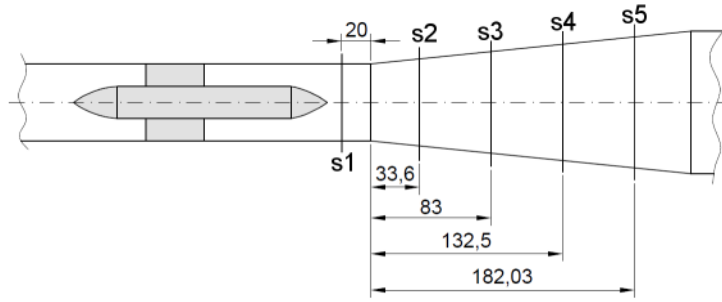


Figure 89 Location of cross-sectional planes

The integral characteristics of the loss coefficient and pressure recovery from the time-averaged computed flow fields are plotted in Figure 90.

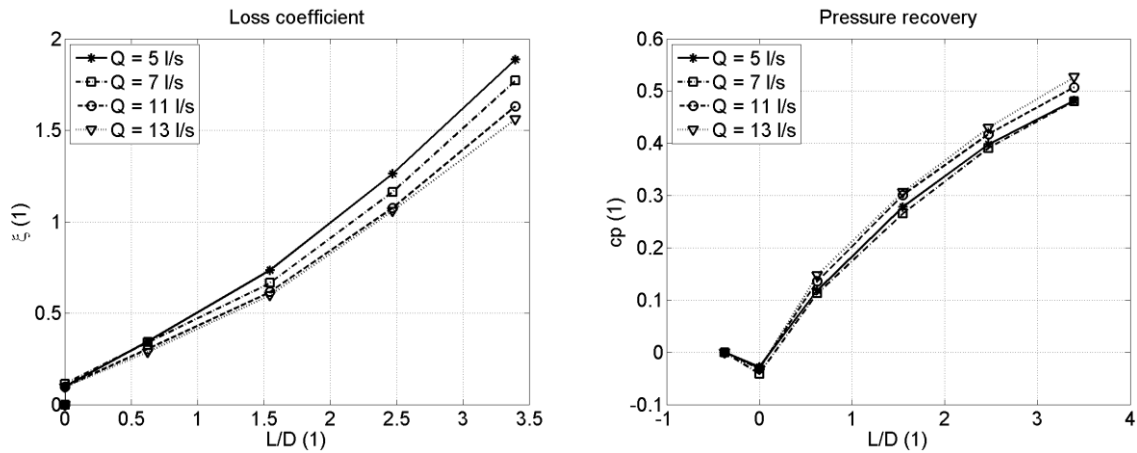


Figure 90 Loss coefficient (left) and pressure recovery (right)

One can see that for flow rates $Q = 5$ and 7 l/s the diffuser loss coefficient ξ in the downstream part of the diffuser is larger compared to other two presented flow rates $Q = 11$ and 13 l/s. The diffuser loss coefficient represents the ratio of pressure loss related to the dynamic pressure. Despite the lowest value of ξ for flow rate $Q = 13$ l/s, it does not mean that the overall pressure losses are the smallest for this flow rate. The pressure losses dependent to both the diffuser loss coefficient and the inlet velocity are calculated as follows:

$$\Delta p = \xi \cdot \rho \frac{v_{inlet}^2}{2} \quad (13.6)$$

The decreasing diffuser loss coefficient with increasing flow rate is reflected in the evolution of pressure recovery where at flow rate $Q = 13$ l/s the transformation of the dynamic pressure to the static pressure is the largest.

Diffuser efficiency describing how the dynamic pressure is transformed to the static pressure alongside of the diffuser is plotted in the Figure 91. The lowest loss coefficient and largest pressure recovery factor at flow rate $Q = 13$ l/s is reflected in the best diffuser efficiency compared to other flow rates. While at flow rate $Q = 5$ l/s the largest gradient of efficiency curve is at the beginning of the diffuser between $L/D = 0.5$ and 1.5 at flow rate $Q = 13$ l/s the largest gradient of efficiency curve is downstream between $L/D = 2.5$ and 3.5 .

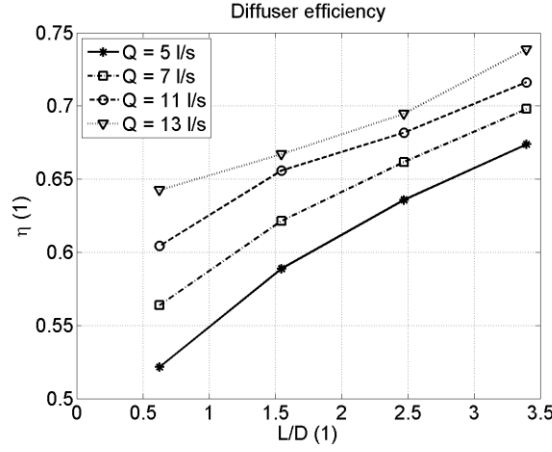


Figure 91 Diffuser efficiency

13.2.1 Dissipation function

On the base of irreversible part of stress tensor $\Pi_{ij} = 2\mu v_{ij} + b\delta_{ij}v_{kk}$ arising from the Navier-Stokes equation the dissipation function \mathcal{D} , which represents power dissipated in the volume of fluid is calculated using equation

$$\mathcal{D} = \iiint_V \Pi_{ij} \frac{\partial v_i}{\partial x_j} dV \quad (13.7)$$

Assuming the incompressible fluid the irreversible part of stress tensor is reduced to $\Pi_{ij} = 2\mu v_{ij}$ and equation (13.7) can be then expressed to form

$$\mathcal{D} = 2\mu \iiint_V v_{ij} v_{ij} dV \quad (13.8)$$

Considering the RANS equation using Boussinesq hypothesis the dissipation function yields following form including the eddy viscosity μ_t

$$\mathcal{D} = 2 \iiint_V [(\mu + \mu_t) \cdot \bar{v}_{ij} \cdot \bar{v}_{ij}] dV \quad (13.9)$$

Using the tensor operations the equation (13.8) can be further expressed into final form of dissipation function \mathcal{D}

$$\mathcal{D} = 2 \iiint_V \left\{ (\mu + \mu_t) \left[\left(\frac{\partial v_x}{\partial x} \right)^2 + \frac{1}{2} \left(\frac{\partial v_x}{\partial y} + \frac{\partial v_y}{\partial x} \right)^2 + \frac{1}{2} \left(\frac{\partial v_x}{\partial z} + \frac{\partial v_z}{\partial x} \right)^2 + \left(\frac{\partial v_y}{\partial y} \right)^2 + \frac{1}{2} \left(\frac{\partial v_y}{\partial z} + \frac{\partial v_z}{\partial y} \right)^2 + \left(\frac{\partial v_z}{\partial z} \right)^2 \right] \right\} dV \quad (13.10)$$

Calculating velocity derivatives the dissipation function can be represented as the scalar field resulting from the numerical calculations. In OpenFOAM the kinematic turbulent viscosity ν_t

(nut) appears. Therefore the water density corresponding to the molecular kinematic viscosity ν (nu) defined in the `transportProperties` is used to calculate dynamic turbulent viscosity μ_t . In Figure 92 the contours of instantaneous and time-averaged dissipation function \mathcal{D} are presented for flow rate $Q = 11$ l/s. It is clear that with increasing flow rate the energy dissipation increases. The dissipation is the largest in the regions with the largest velocity gradients. Generally the largest dissipation occurs in the boundary layer where the velocity gradients are highest due to no slip boundary conditions. Therefore the upper contour value is reduced in order to represent the dissipation caused by the spiral vortex as well.

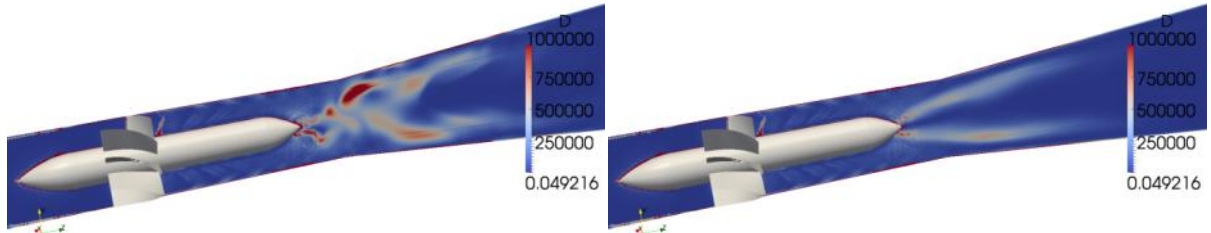


Figure 92 Instantaneous (left) and time-averaged (right) contours of dissipation function \mathcal{D} in the longitudinal slice for flow rate $Q = 11$ l/s

One can see that large dissipation appears for both the boundary layer of wetted walls (inner walls of pipes and diffuser together with spike and swirl generator blades) and the shear layer between vortex core and the main stream (vortex shedding behind generator blades and the spiral vortex in the diffuser). Dissipation caused by the spiral vortex is represented in Figure 93 where the instantaneous snapshot of dissipation function in the longitudinal plane is shown together with the core of spiral vortex. It is obvious that the large dissipation appears in the intersection between vortex core and the main flow.

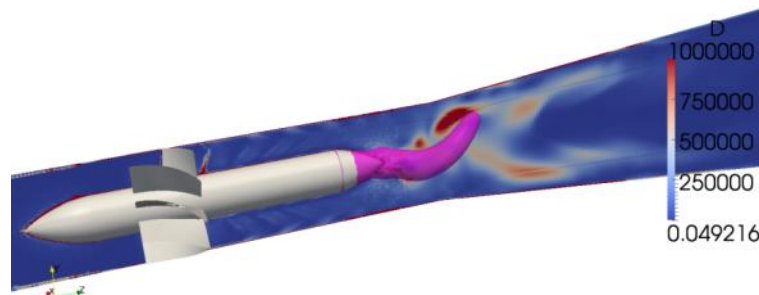


Figure 93 Vortex core (iso-contour of low static pressure) with the slice of instantaneous snapshot of dissipation function

The dissipation calculated in a form of dissipation function (13.10) should be in agreement with the power loss ΔP between domain inlet and outlet calculated from the specific energy difference ΔY .

$$\Delta P = \rho \cdot Q \cdot \Delta Y = \rho \cdot Q \left(\frac{p_{inlet} - p_{outlet}}{\rho} + \frac{\alpha_{inlet} \cdot v_{inlet}^2 - \alpha_{outlet} \cdot v_{outlet}^2}{2} \right) \quad (13.11)$$

Comparison of resulting dissipation function \mathcal{D} with power loss ΔP is plotted in Figure 94.

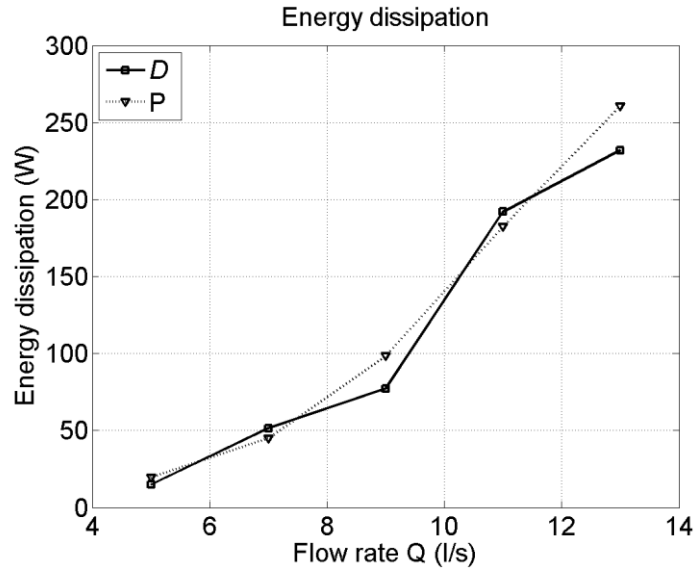


Figure 94 Power dissipated in the volume of fluid

One can see that power dissipation quadratically grows with increasing flow rate. The particular discrepancies can be found arising from the proper computation of turbulent kinetic energy and turbulent dissipation rate further used for evaluation of turbulent viscosity defined in case of realizable $k-\varepsilon$ turbulence model as follows [88]:

$$\mu_t = \rho C_\mu \frac{k^2}{\varepsilon} \quad (13.12)$$

14 CONCLUSIONS OF PART I

In this section the overall conclusions regarding to Part I (including sections 5 - 13) of this thesis are presented. The comprehensive study of swirling flow with the spiral vortex structure was carried out. Both the pressure and velocity fields were investigated using experimental measurements and numerical calculations. Besides this the advantage of visual observations of cavitating vortex leads to the application of the high speed camera used for study of time evolution of the vortex structure shape. It was found that the spiral vortex generated by the “BUT” swirl generator is strongly unstable in time. The spiral decays and rolls up periodically producing the strong longitudinal pressure pulsations propagated upstream. Both pressure and velocity fields are influenced by this vortex features. Consequently the pressure and velocity pulsations are decomposed into synchronous (longitudinal) and asynchronous (transverse) pulsations.

The asynchronous pressure pulsations decrease along the diffuser. From the analysis presented in section 10 it was shown that the main reason of asynchronous pressure pulsations decrease is the diffuser opening together with the temporal instability of the spiral vortex. The spiral vortex collapse causes the strong synchronous pressure pulsations propagated upstream. Consequently when the spiral vortex collapses the vortex dynamics is diminished in downstream part of the cone. Moreover it was shown that the synchronous part of pressure pulsations is not related only to the elbow draft tube surge but it can be also found in the straight diffusers.

From the experimentally measured axial and tangential profiles the mean time-averaged velocity components were computed for each of measured cross-sections. The decrease in both axial and tangential velocity magnitudes in the downstream part of the diffuser was observed. Moreover the unsteadiness in the measured velocity field is in good agreement with the one extracted from the pressure fields. In section 8 it was shown that the magnitude of asynchronous pulsations and its frequency decrease downstream of the diffuser well correspond for both the static pressure and velocity fields. It proves the significant link between pressure and velocity field through the Navier-Stokes equation.

In the experimental measurements the cavitating vortex core appears for flow rates higher than $Q = 7$ l/s. With increasing flow rate the cavitation increases and vortex core becomes more visible. Nevertheless in section 9.3 it was documented that for flow rates higher than $Q = 11$ l/s the cavitating vortex is sufficiently strong to perform the image processing analysis using picture ensemble from the high speed camera.

From the pressure measurements it was found that the largest amplitudes and lower values of the mean static pressure are obtained for the pressure sensor p2 situated at the beginning of the cone. In this section the vortex core is the most significant which is also reflected in the steep drop of pressure recovery for higher flow rates. For the higher flow rates when the cavitation occurs the pressure drop is much more highlighted.

It was found that cavitation increases significantly when the flow rate increase. Moreover the influence of the diffuser kind of flow (as a consequence of the vortex instability) was shown in section 9.2 where the width of region (at the beginning of the cone) influenced by the cavitating vortex core is much wider than the diffuser opening.

The numerical calculations were carried out using OpenFOAM package in version 2.2.2. The RANS calculation employing realizable $k-\epsilon$ turbulence model was used to simulate several flow rates $Q = 5, 7, 9, 11$ and 13 l/s in order to compare resulting flow fields with the experimental measurements. The detailed overview of calculation set-up is presented in section 11.3.

Very good agreement was obtained for instability of the spiral vortex. From computed pressure field was shown that the periodically decaying character of the vortex is well captured by the numerical calculation therefore it is not consequence of any other source as a natural frequency of experimental test rig.

The swirl number was evaluated for three numerically computed flow rates $Q = 5, 7$ and 13 l/s. It was found that so called quasi-stagnant region (where the increase in the swirl number is limited) appears between $L/D = 0.5$ and $L/D = 2$. This region is well correlated with the area where the largest asynchronous pulsations are produced by the spiral vortex. Therefore the limitation in the swirl number increase proved to be good measure of the vortex instability.

The comparison of numerically computed and experimentally measured pressure fields was carried out in the form of mean static pressure, pressure recovery and asynchronous pressure pulsations. It was found that the largest discrepancies of mean static pressure are obtained for the higher flow rates $Q > 7$ l/s where the cavitating vortex appears. This can be limitation of single phase calculation used in present analysis. Obviously the cavitating vortex causes the larger decrease in the mean static pressure. The best agreement in pressure recovery was obtained for flow rate $Q = 7$ l/s. The main disagreement in pressure recovery was found for second sensor location where for higher flow rates (including $Q = 7$ l/s) the experimental pressure recovery underestimates the computed one. This is probably also consequence of single phase simulation causing the insufficient static pressure drop at the beginning of conical section where the vortex structure has largest amplitudes.

The comparison of static pressure field unsteadiness is presented in form of frequency of asynchronous pressure pulsations. In agreement with experimental measurements the largest amplitudes of asynchronous pressure pulsations were found in the second sensor location. Both the frequency magnitude and the frequency decrease in the downstream part of the diffuser are well predicted by the numerical simulations for entire computed range of flow rates except $Q = 11$ l/s. It was found that the correct estimation of frequency magnitude of numerically computed asynchronous pulsations in the third sensor location is very sensitive to the length of pressure signal record. For this sensor location the large underestimations almost to the value corresponding with the frequency magnitude in the fourth pressure sensor were observed, e.g. comparison for flow rate $Q = 11$ l/s in Figure 76. This can be caused by complexity of decaying character of the vortex which is difficult to simulate by two equation $k-\epsilon$ turbulence model, which does not affect strong turbulence anisotropy. Thus the utilization of higher turbulence model (e.g. Reynolds stress turbulence model RSM) or two-equation models with quadratic or cubic strain-stresses relationship can be recommended.

The numerically computed velocity fields were compared with the LDA measurements. The time-averaged velocity magnitudes are compared using numerical integration of measured axial and tangential velocity profiles with the surface integration of numerically

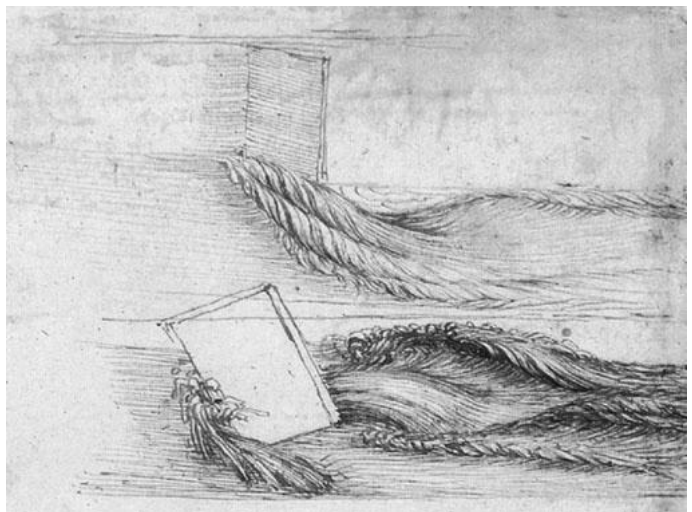
computed flow field. The numerical results are in very good agreement with the experimental ones. The particular disagreement can arise from trapezoidal integration of LDA velocity profiles. Consequently the numerically computed axial and tangential velocity profiles were compared. The largest discrepancy was found in the wall regions where the numerically computed velocity profiles suffer from the near wall modeling of RANS calculations using the wall functions.

The energy dissipation aspect of the flow with the spiral vortex was investigated for both time-averaged and instantaneous flow fields. The pressure recovery, diffuser loss coefficient, diffuser efficiency and dissipated power were calculated. The strong unsteady character of the flow downstream of the diffuser is reflected in the time-evolution of kinetic energy correction factor. The fluctuations in kinetic energy correction factor magnitude increase ten times downstream of the diffuser.

At flow rate $Q = 13$ l/s the lowest diffuser loss coefficient, highest pressure recovery and highest diffuser efficiency is achieved in the conical section compared to other numerically investigated flow rates. Nevertheless overall energy dissipation quadratically increases with increasing flow rate. The dissipation in a form of dissipation function calculated over entire volume of computational domain is compared with the dissipation calculated from the power loss between domain inlet and outlet. The evolution of dissipation function is in good agreement with curve of power dissipated between domain inlet and outlet.

The comprehensive analysis of flow generated by the “BUT” swirl generator continues in the second part of this thesis where the spatio-temporal decomposition of both experimentally recorded images of cavitating vortex and numerically computed pressure fields is carried out using POD technique.

PART II POD ANALYSIS



“So moving water strives to maintain the course pursuant to the power which occasions it and, if it finds an obstacle in its path, completes the span of the course it has commenced by a circular and revolving movement.”

Leonardo da Vinci (April 15, 1452 – May 2, 1519)

15 APPLICATION OF POD TO THE SWIRLING FLOW WITH THE SPIRAL VORTEX STRUCTURE

According to section 3.3 presenting overall view of POD technique this section describes further details of POD application to the swirling flows where the spiral vortex appears. Presented theory comes out from the previous POD utilization to the full range of applications and resulting experiences. For example POD was previously used for the numerical investigation of swirling flow in the draft tube cone of the Francis turbine operated at part load [83], [84]. Application of POD to the investigation of Francis turbine model operated at part load, BEP and full load can be found in [91]. Besides this the POD was applied to the initial design of “BUT” swirl generator for both experimental (PIV) [86] and numerical data [92].

The base for POD technique is an ensemble of data covering unstable character of the flow. Both numerical (e.g. pressure or velocity field) and experimental (PIV velocity field or images of cavitating flow) data can be used. Nevertheless several aspects have to be considered in order to carry out POD correctly.

First, the sampling frequency of snapshots collection has to be constant and defined so that all significant modes are correctly captured while only the necessary amount of snapshots is used. This will ensure reduction of computational effort of POD decomposition and data storage requirement. Second, the Nyquist–Shannon sampling theorem must be fulfilled [34] in order to prevent results from aliasing and loss of the data information. The ratio between the sampling frequency f_s and the maximum frequency f_{max} of the discrete function is defined by eq. (15.1):

$$f_s \geq 2f_{max} \quad (15.1)$$

Traditionally, the precession frequency f_V of the spiral vortex structure is obtained applying the FFT on the unsteady pressure signal. Nevertheless, the frequency of temporal modes is a-priori unknown to the POD decomposition. However, the temporal frequencies of the most dominant modes #1 and #2 are very close to the precession frequency of the vortex [78], [83], [84], [91]. In order to capture also modes with higher frequencies it is assumed that the maximal frequency f_{max} is four times the frequency of temporal modes #1 or #2. Consequently, the snapshots sampling frequency should be at least four times higher than the precession frequency of the vortex structure

$$f_s \geq 4f_V. \quad (15.2)$$

In following sections POD will be applied to different data obtained from both numerical simulations and experimental measurements. Therefore each section includes further explanation of data post-processing necessary for correct application of POD.

15.1 ASSIGNING OF MODES TO THE MODE PAIR

In case where some homogeneous and periodic directions (e.g. azimuthal direction in case of diffuser flow) exist and flow is statistically stationary in time the POD modes in these

directions are coincident with Fourier modes [108], [17]. In case that POD is applied on axisymmetric domain, then some modes appear in phase shifted couples (mode pairs) [64], [83], [86], [91], [92]. The phase shift can be extracted from time evolution of corresponding temporal modes a_k . Consequently the phase portrait can be plotted considering two temporal modes creating one mode pair. An example of phase portrait of two modes $\pi/2$ phase shifted in azimuthal direction is presented in Figure 95a. While the uniform circles refer to $\pi/2$ phase shift the $\pi/4$ phase shift leads to the phase portrait with one loop as can be seen in Figure 95b [63].

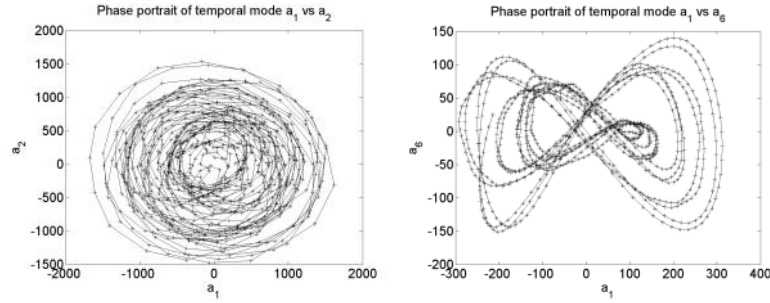


Figure 95 Phase portrait of the 90deg (left) and 45deg (right) phase shifted modes

It was pointed by Oberleithner et al. [64] that the mode pairs create a complex Fourier mode:

$$\widehat{\phi}_1 = \phi_1 + i\phi_2 \quad (15.3)$$

This approach is easier in terms of computational and post processing effort, but assigning of the Fourier mode number to the mode pairs is a bit tricky, not straightforward, especially for higher modes. Moreover, not all modes appear in mode pairs therefore this aspect will be further discussed.

The same behavior come out from the spatial representations, where the modes creating one complex mode pair have same spatial shape phase shifted in azimuthal direction. See an example of two static pressure modes creating single mode pair in Figure 96.

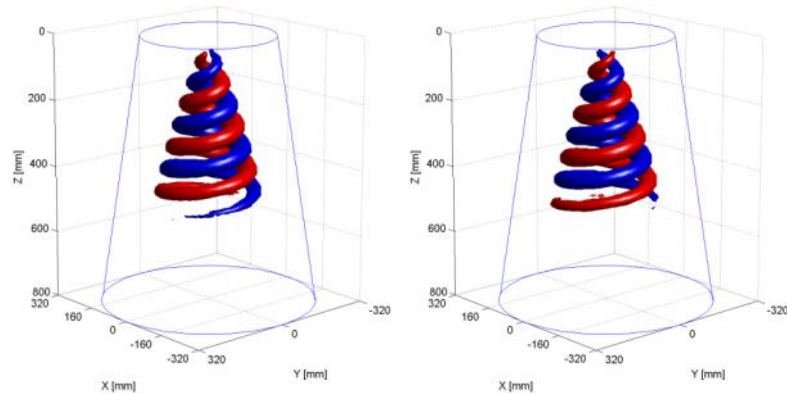


Figure 96 Static pressure modes #1 and #2 at 90% BEP of FLINDT [83]

In case of swirling flow where the spiral vortex appears both synchronous and asynchronous pulsations arise [23], [8], [58], [59]. According to frequencies of temporal modes the distinguishing between modes related to either synchronous or asynchronous

pulsations can be carried out. Generally beside the temporal features the modes related to the synchronous pulsations have different spatial shape compared to ones related to the asynchronous pulsations.

16 POD ANALYSIS OF “BUT” SWIRL GENERATOR

In this section the POD is applied to experimental and numerical data related to the flow generated by “BUT” swirl generator analyzed in the first part of this thesis. The experimental data includes image ensembles of cavitating vortex structure recorded by the high speed camera (HSC) for different flow rates. Due to the single phase character of numerical simulations the vapor fraction is not available for exact comparison with the experimental data. Therefore the static pressure field (which is most related to the cavitation) is chosen for the POD analysis of the numerical data.

16.1 POD OF CAVITATING VORTEX STRUCTURE

The POD of cavitating vortex structure is carried out using the image ensembles recorded by the high speed camera. The grayscale images are post-processed in MATLAB[®] identically following section 9.2. In this case the cavitation (respectively the concentration of the vapor) is represented by the number (representing color scale) in interval from 0 (water) to 255 (vapor).

According to section 9.2 and Figure 42, where is shown relation of vapor fraction \bar{w} to the flow rate, the significant increase of the cavitation starts at flow rate $Q = 10$ l/s. It was shown that relevant results are obtained for flow rates $Q > 11$ l/s. Thus the qualitative results of POD analysis are documented also for flow rates higher than 11 l/s.

The POD analysis is carried out in constrained domain situated downstream of the diffuser. The domain highlighted in Figure 97 is situated approximately 78 mm downstream of the trailing edge of the swirl generator blades. The image ensembles include 10000 snapshots for each flow rate and sampling frequency is 619Hz which leads to the $t = 16.2$ sec of sampled time interval. It has to be noted that this procedure is not exactly correct because the 2D flow field representation is assumed from the pictures capturing fully 3D flow field. The 2D flow field should be properly obtained for example using the laser sheet through the investigated domain, as in the case of PIV measurements.

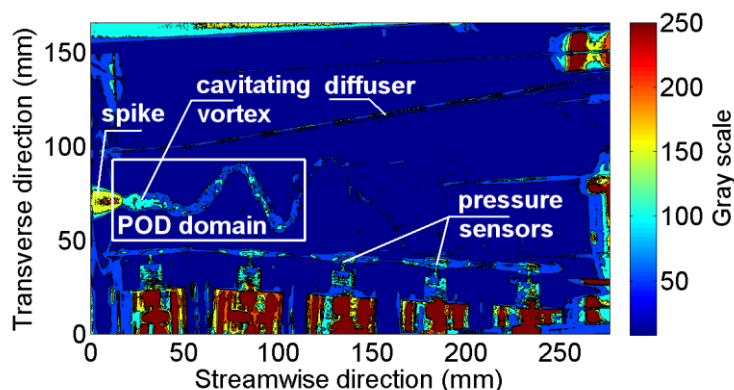


Figure 97 Constrained domain used for the POD analysis

In Figure 98 and Figure 99 the spatial shapes of cavitation modes are presented for flow rates $Q = 11.5$ l/s (left column) and flow rate $Q = 13.5$ l/s (right column) including the mode #0 representing the time-averaged cavitation field.

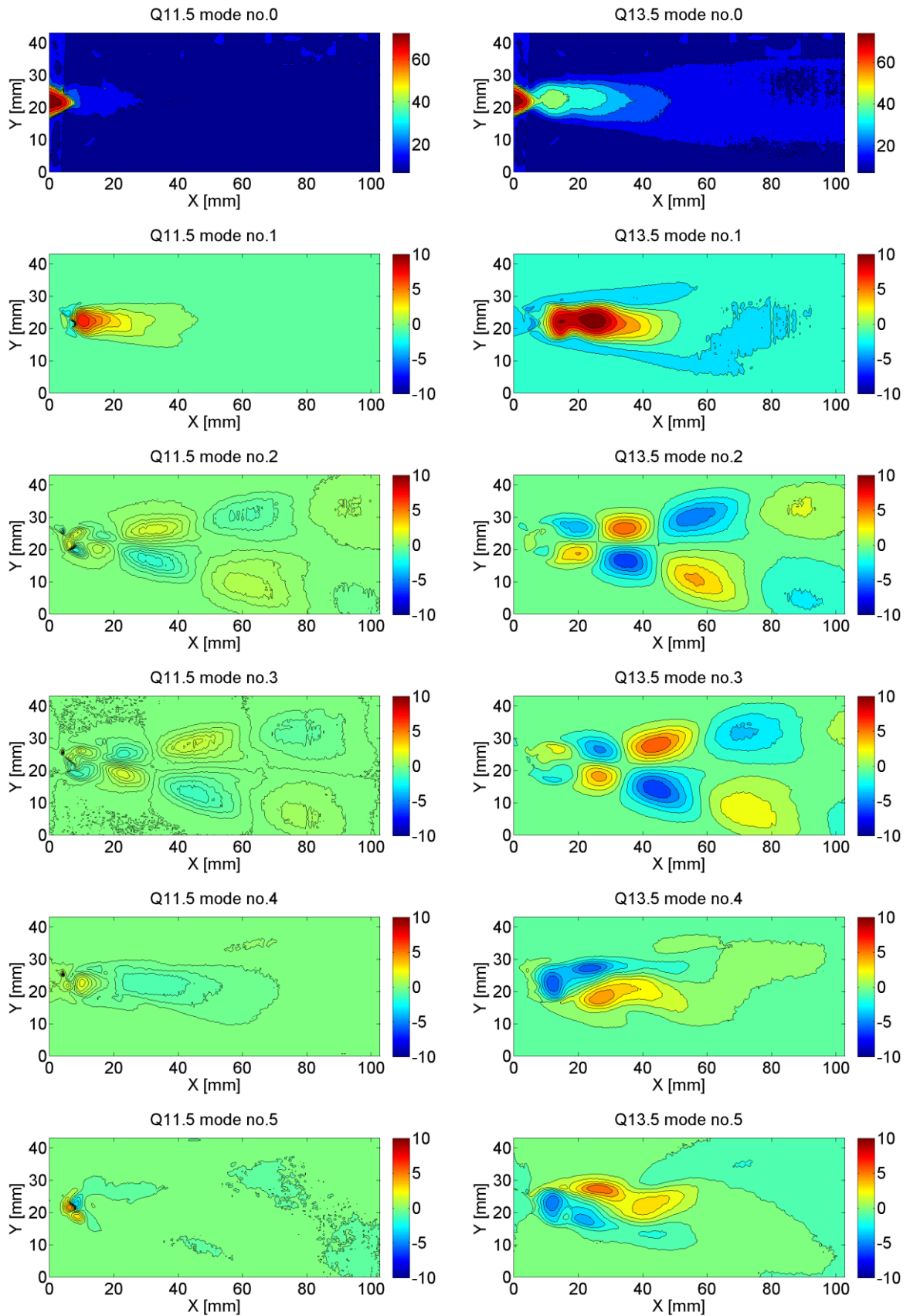


Figure 98 Cavitation modes (#0 - #5) for flow rate $Q = 11$ (left) and 13.5 l/s (right)

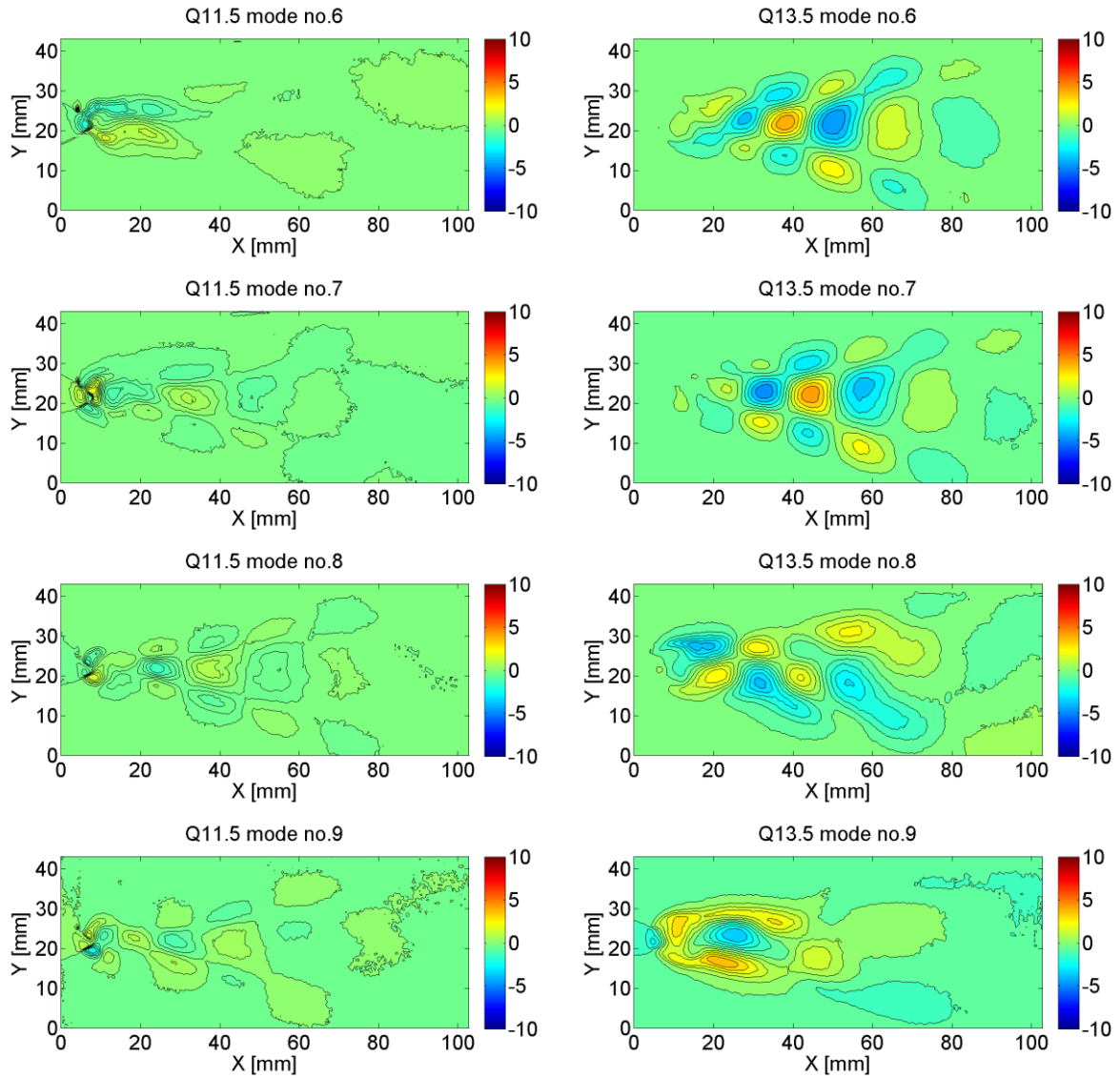


Figure 99 Cavitation modes (#6 - #9) for flow rate $Q = 11$ (left) and 13.5 l/s (right)

From figures presented above one can see that the spatial representation of the cavitation modes differs between flow rate $Q = 11.5$ and $Q = 13.5$ l/s. Increase of the flow rate brings both redistribution of the spatial shapes and increase of $\phi_i^k(\mathbf{x})$ magnitude. The main spatial shape of the first three modes stays unchanged while the flow rate increases. On the other hand spatial shape of higher modes is different for example modes #7 and #8 in case of $Q = 11.5$ l/s correspond to the modes #6 and #7 at flow rate $Q = 13.5$ l/s. In other words these modes became more dominant when the flow rate increased. It is necessary to mention that the mode number (respectively mode significance) is determined from the magnitude of the eigenvalue. Thus the mode with identical spatial shape might have different mode number comparing two different flow rates. For example spatial shapes of modes #7, #8 and #9 at flow rate $Q = 11.5$ l/s are comparable with modes #6, #7 and #8 at flow rate $Q = 13.5$ l/s.

The modes redistribution with change in flow rate can be seen also from the amplitude-frequency spectra of the temporal modes. In the Figure 100 the change in the frequency of particular mode number is plotted against flow rate. One can see that the frequencies of modes #1, #2 (respectively #3) and #7 show quasilinear dependency on the flow rate, while

the frequency of other modes vary between different frequency levels. For example mode # 6 has similar frequencies as the mode #7 for flow rates higher than $Q > 12$ l/s while for flow rates $Q = 11$ and 11.5 l/s the frequency of mode #6 is approximately 40 Hz.

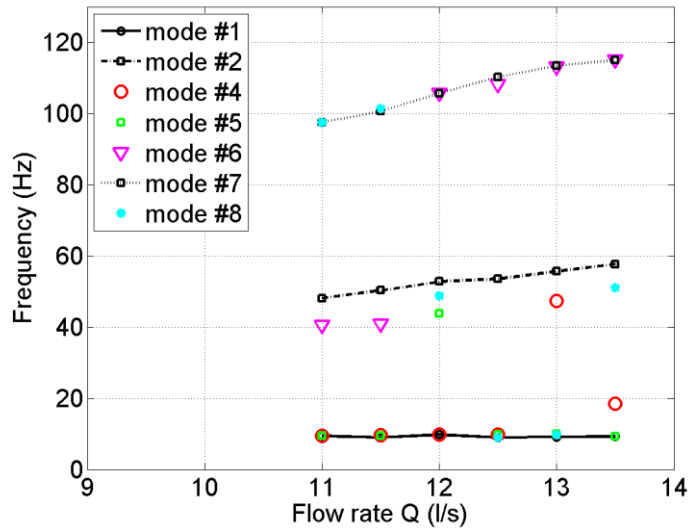


Figure 100 Frequency of the particular modes against flow rate

The strength of the spatial modes is represented in magnitudes of corresponding colorbars. Nonetheless the better measure of the modal intensity represents the eigenvalue magnitude. In Figure 101 the eigenvalue magnitude of mode #0 (mean time-averaged field) is plotted for flow rates $Q > 9$ l/s. The eigenvalue magnitude is plotted in percentage amount related to the whole modal range at particular flow rate. One can see the steep decrease in eigenvalue magnitude beginning at flow rate $Q = 11$ l/s. This is reflected by the abrupt increase of eigenvalue magnitudes of modes #1 - #10 plotted in Figure 102. Decrease in eigenvalue magnitude of mode # 0 together with increase of modes #1 - #10 show how the cavitation in the vortex core becomes stronger.

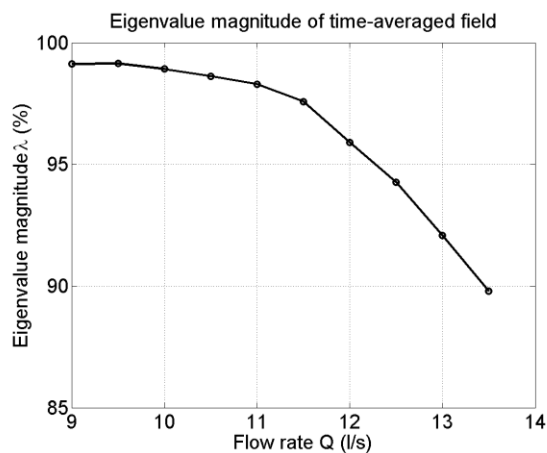


Figure 101 Eigenvalue magnitudes of mode #0 (mean field)

One can see that while the frequency of modes #4 and #5 vary for different flow rates (see Figure 100) the eigenvalue magnitude of both modes stays almost equal (see Figure 102 left).

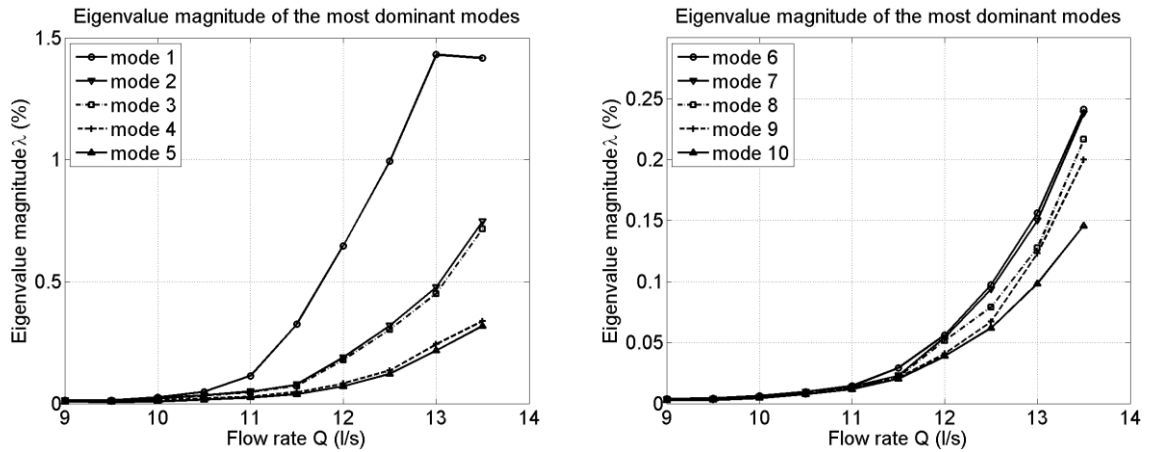


Figure 102 Eigenvalue magnitude of mode #1 - #5 (left) and #6 - #10 (right)

From the computed modes the backward reconstruction of instantaneous snapshot can be composed assuming the time averaged field (mode #0) and the most dominant modes (mode #1, #2, #3...). The quality of reconstruction depends on both the number of summed modes and significance of these modes to the complex flow field. The eigenvalue magnitude is the best measure of the significance of particular modes. For example for flow rate $Q = 13$ l/s the mode #0 represents 89.8% of original flow field and together with modes #1 - #5 it is over 93%. Assuming mode #0 together with the first 10 modes over 94% of original flow field should be reconstructed. In the Figure 103 the original snapshot of cavitation field (grayscale converted to the color scale) obtained by the high speed camera is plotted.

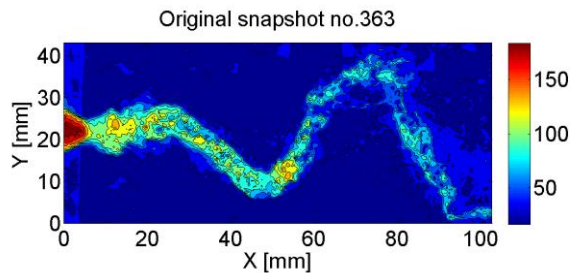


Figure 103 Original snap shot of spiral vortex

In the Figure 105 the reconstruction of the original snapshot is presented summing the most significant modes (mode #1 - #10) continuously to the time averaged field (mode #0) plotted in Figure 104.

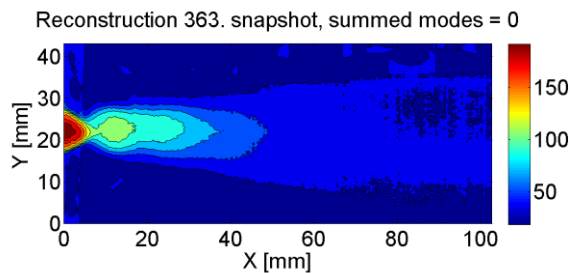


Figure 104 Reconstructed time-averaged field from the mode #0

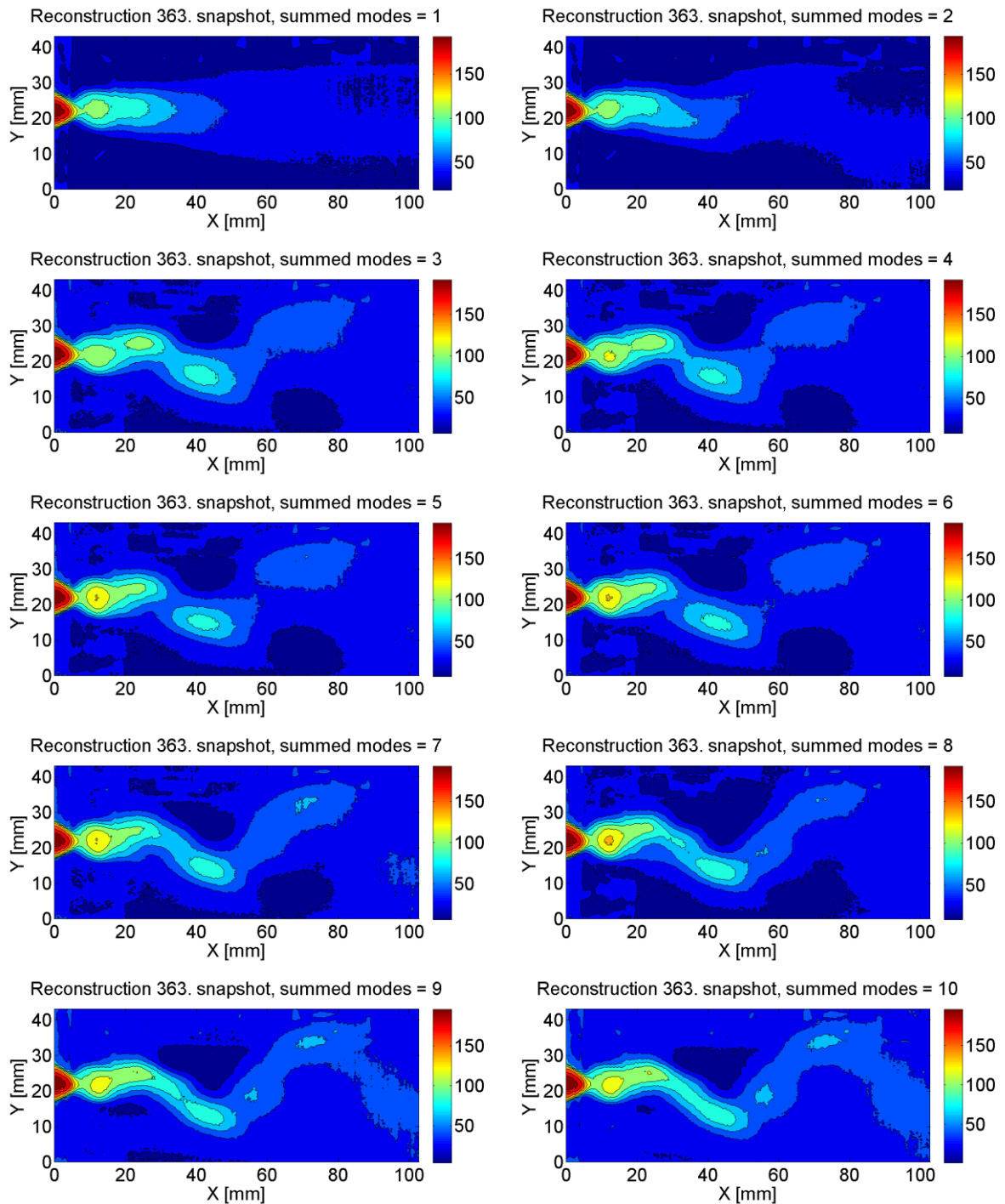


Figure 105 Reconstruction using the first ten most significant modes

One can see that the reconstructed snapshot using the first ten modes (94% of original field) approximate the original one with sufficient result in the spatial shape. It is clear that the shape of spiral vortex in reconstructed snapshot is smoothed compared to the original one. This is reason of neglecting of other modes related to the higher dynamics which bring further of complexity in the spatial shape.

16.2 POD OF NUMERICALLY COMPUTED PRESSURE FIELDS

In order to qualitatively compare dynamic behavior of the vortex structure, POD decomposition is carried out using the static pressure fields from CFD calculations. The node values in longitudinal slice through computational domain are stored in prescribed time steps.

The domain for POD is constrained similarly as in case of POD from HSC images ensemble. The position of constrained domain in the overall computational model can be seen in **Figure 106**.

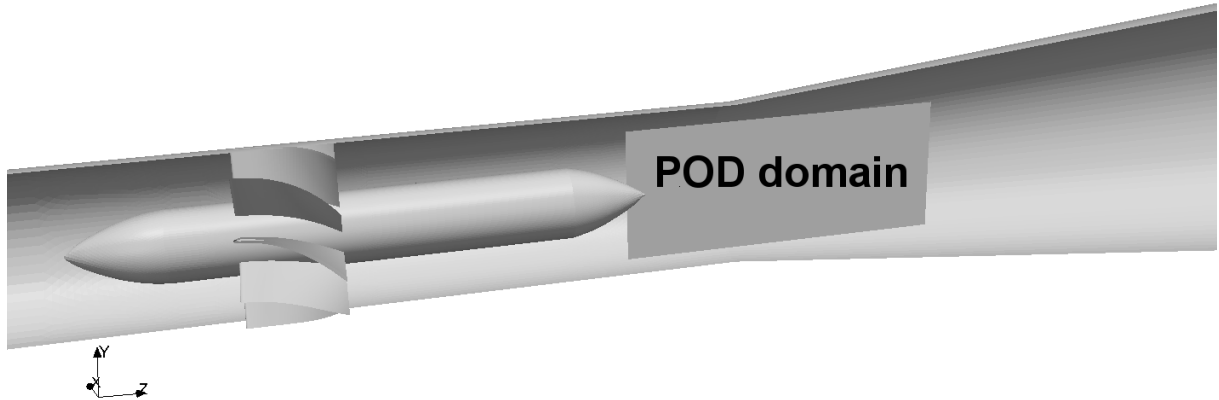


Figure 106 Constrained domain for POD of computed static pressure fields visualized in three-dimensional computational domain

The dimensions of POD domain shown in **Figure 107** are determined so that they correspond with the dimensions of constrained POD domain used in evaluation of cavitation modes (see section 16.1)

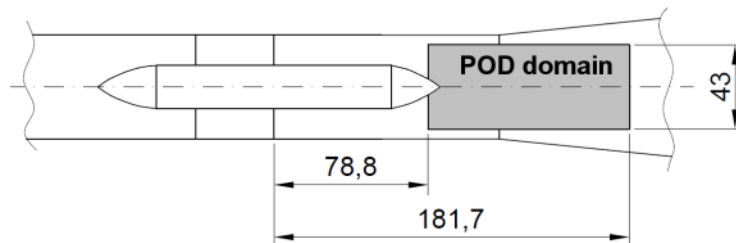


Figure 107 Dimension and location of POD longitudinal domain

The data sampling were executed through the OpenFOAM utility `cuttingPlane` which is prescribed in the `controlDict` where the plane orientation, sampled fields (i.e. U or p), interpolation scheme and sampling period are defined. Considering the main rotational frequency of the vortex structure the sampling period was chosen (according to section 15) keeping both reasonable data amount and as much as possible dynamic information, see Table 19.

Table 19 Sampling periods, number of snapshots and resulting sampled time for POD.

Flow rate Q (l/s)	Sampling period (s)	Number of snapshots	Sampled time (s)
5	2.17e-3	542	1.1761
7	1.5e-3	605	0.9075
9	1.1e-3	500	0.55
11	1.1e-3	456	0.5016
13	9.1e-4	796	0.7244

The sampled fields are stored in the `postProcessing` directory as the field data written in the user defined sample format. The `raw` format was used which store data file in the columns and can be read by mostly software. For the interpolation the `cellPointFace` scheme was used. The ensemble of the data files is then imported into MATLAB[®] software keeping the dimension coordinates in one matrix and pressure data in another one. The pressure matrix is therefore rectangular with dimension *number of domain values x number of sampled time snapshots*.

For the reason that the `cuttingPlane` utility creates slice through the whole computational domain the sampled fields were reduced in order to cover only the constrained POD domain presented in Figure 107.

In order to compare results associated to the different flow rates the static pressure data $p(\mathbf{x}; t)$ are made dimensionless according to

$$p(\mathbf{x}; t) \equiv \frac{p(\mathbf{x}, t)}{\frac{1}{2}\rho v_{ref}^2} \quad (16.1)$$

where $p(\mathbf{x}, t)$ is the static pressure field obtained in numerical simulation at each time step t and v_{ref} corresponds to the bulk velocity at the inlet to the diffuser. After that the POD analysis is executed and the first ten spatio-temporal modes are computed.

In Figure 108 and Figure 109 the POD modes are presented for the lowest and highest computed flow rates ($Q = 5$ and 13 l/s) in order to present the spatio-temporal changes of the vortex structure when the flow rate increases. Besides the spatial shapes represented as the contour of $\phi_i^k(\mathbf{x})$ the value of corresponding temporal mode frequency is added to the right corner.

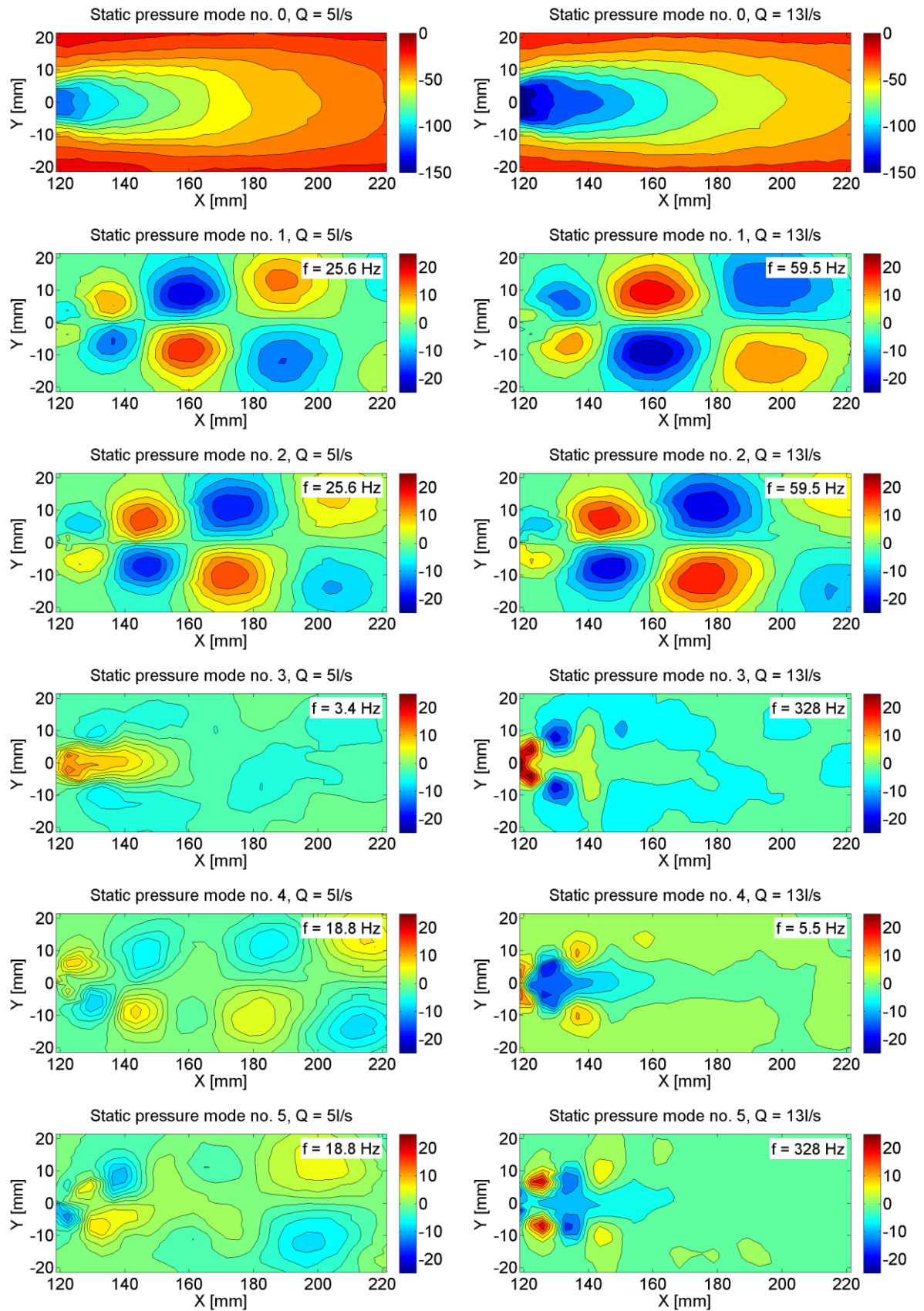


Figure 108 The spatial modes (#0 - #5) of static pressure, flow rate $Q = 5\text{ l/s}$ (left) and $Q = 13\text{ l/s}$ (right)

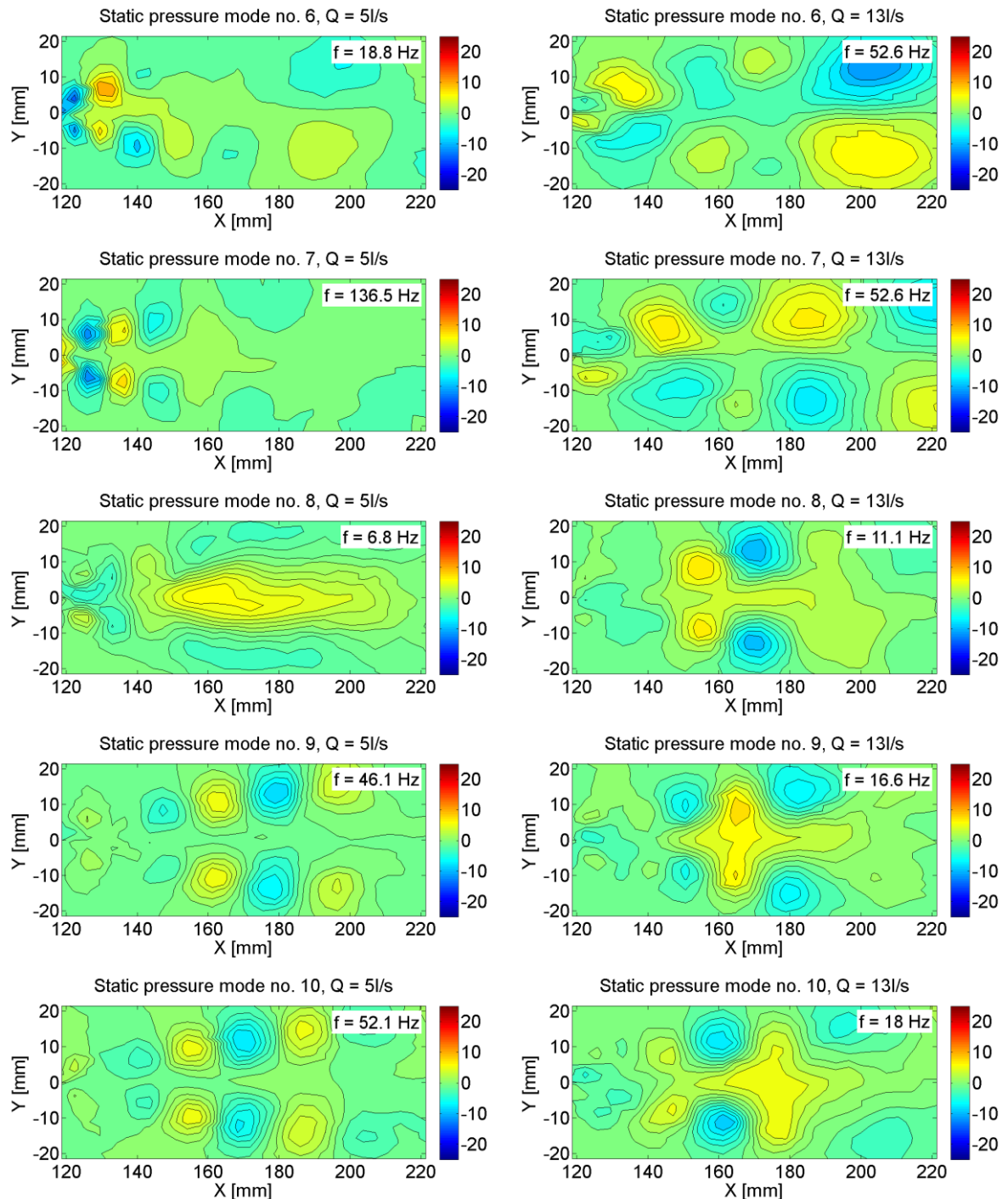


Figure 109 The spatial modes (#6 - #10) of static pressure, flow rate $Q = 5$ l/s (left) and $Q = 13$ l/s (right)

One can see that the spatio-temporal representation of modes vary when the flow rate increases from $Q = 5$ to 13 l/s. Nonetheless the spatial shape of the first two modes #1 and #2 remains unchanged for entire range of computed flow rates. In Figure 110 (left) the increasing temporal frequency of static pressure mode #1 is plotted. The phase portrait between mode #1 and #2 can be seen in Figure 110 (right) which shows that these two modes create one complex mode pair).

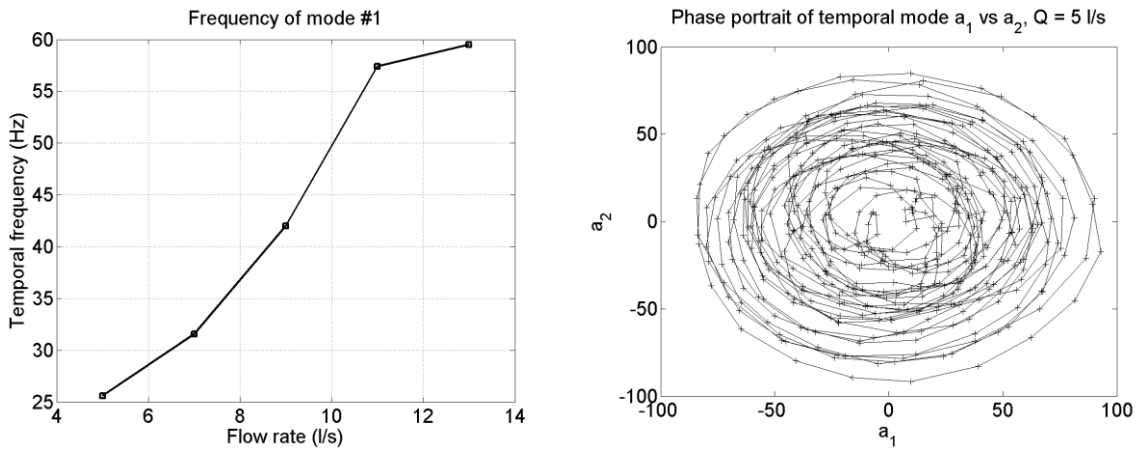


Figure 110 Temporal frequency of static pressure mode #1 (left) and phase portrait of mode #1 and #2 at flow rate $Q = 5$ l/s (right)

On the other hand higher modes (#3, #4, etc.) have either different spatial shape or different modal frequency in order to decide if there is another regular mode pair between the first ten modes.

In Figure 111 (left) the eigenvalue magnitude of static pressure mode #0 is plotted for entire range of computed flow rates. One can see that percentage magnitude changes with deviation less than 1 %. It means that the time-averaged static pressure field is almost unaffected by increasing flow rate at the expense of dynamic modes. Nevertheless it is clear that for flow rate $Q = 7$ l/s the lowest eigenvalue magnitude of mode #0 refers that this flow rate contains most of the flow dynamics compared to the other investigated flow rates. The eigenvalue magnitude of modes #1 - #6 is plotted in Figure 111 (right). The largest eigenvalue of the main unstable mode pair (mode #1 and #2) is at flow rate $Q = 7$ l/s. It has to be mentioned that this results are in good agreement with spatial shape of the spiral vortex which seems to be unchanged with increasing flow rate, thus decreasing pressure in the vortex core.

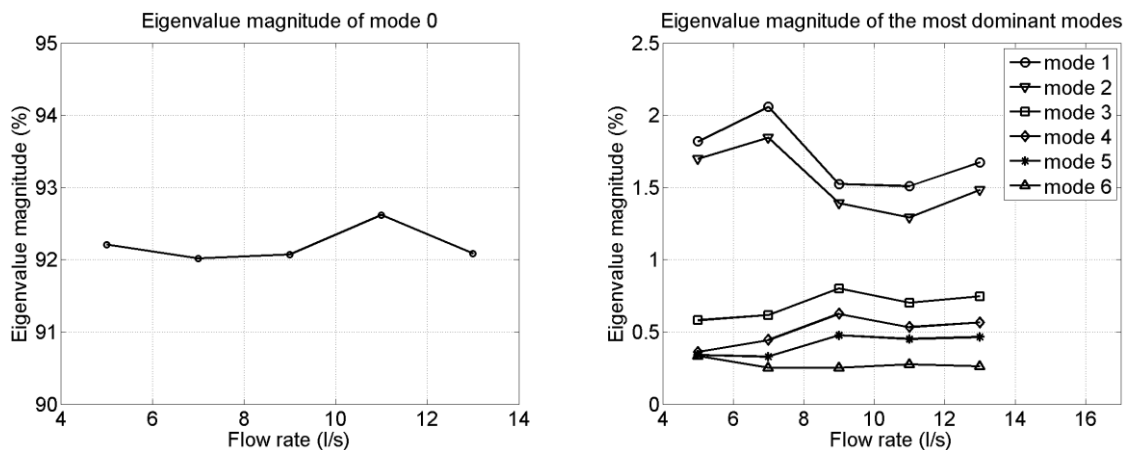


Figure 111 Eigenvalue magnitudes of static pressure mode #0 (left) and modes #1 - #6 (right)

Summing the first ten modes #1 - #10 (dynamic modes) is plotted in Figure 112 (left). This sum is largest at flow rate $Q = 7$ l/s and together with the lowest eigenvalue magnitude of mode #0 it proves that the vortex structure at this flow rate is the strongest. Analogous the first ten modes are added to the time-averaged field (mode #0) in Figure 112 (right). One can

see that at flow rate $Q = 7$ l/s this sum includes approximately 98.3% of whole decomposed field.

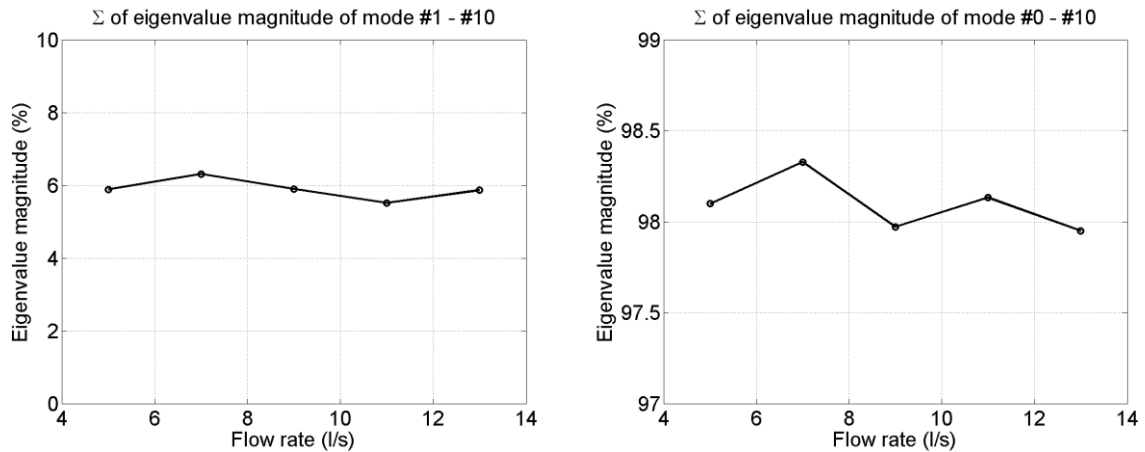


Figure 112 Sum of modes #1 - #10 (left) and mode #0 with modes #1 - #10 (right)

Regarding to section 3.3 where the theory of POD reconstruction is presented, the first ten modes are used for the reconstruction of the instantaneous pressure field. The spatial shape of original pressure field is compared with the reconstructed one in Figure 113 for flow rate $Q = 5$ l/s and in Figure 114 for flow rate $Q = 13$ l/s. The contours represent specific pressure energy $p' = p/\rho$.

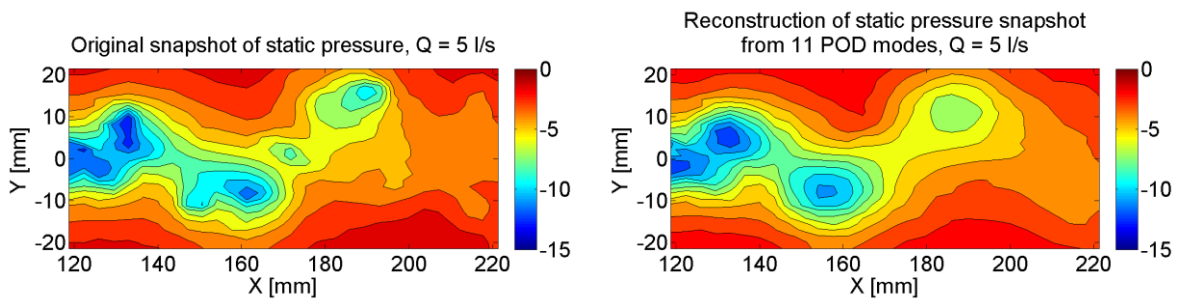


Figure 113 Original instantaneous static pressure field (left) and reconstructed field (right), flow rate $Q = 5$ l/s

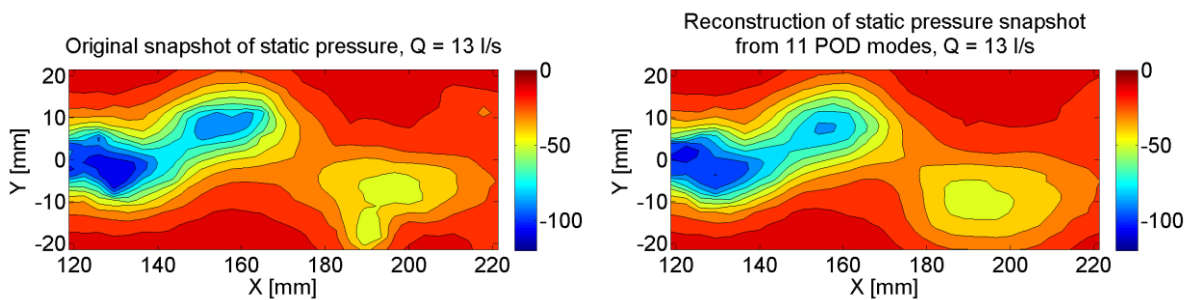


Figure 114 Original instantaneous static pressure field (left) and reconstructed field (right), flow rate $Q = 13$ l/s

One can see that the reconstruction suffers mainly from the neglecting of the higher modes which are related to the incoherent turbulences with the high frequency. This leads to the less complex shape of the vortex structure which is represented by the very low contour of specific pressure energy p' .

16.2.1 Comparison of numerically and experimentally decomposed flow fields

In this subsection the comparison of numerically computed static pressure field decomposition with the experimentally recorded image ensemble decomposition of cavitating vortex is presented. It is clear that decomposition of two different flow fields will show particular differences. Nonetheless at least some of the spatio-temporal features should correspond to both flow fields. First in Figure 115 the spatial shape of the main unstable modes (related to the strong asynchronous pressure pulsations) are compared for both decomposed fields.

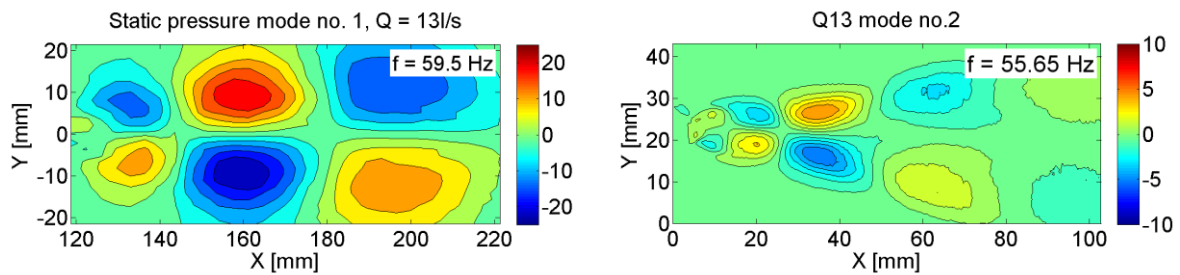


Figure 115 Spatial shape of the main asynchronous mode of numerically computed static pressure (left) and experimentally recorded cavitating vortex (right) field

One can see that for both flow fields the spatial shape of dominant unstable mode is very similar. The main differences arise from the nature of both decomposed fields when the numerically computed static pressure field versus image of cavitating vortex (in a form of color scale represented by numbers in interval 0 - 255) is compared. While in case of CFD information is available for each cell of computational domain in case of images of cavitating vortex the information is only in regions where some fraction of water vapor appears.

Consequently the evolution of temporal frequencies of these dominant asynchronous modes is compared against flow rate in Figure 116. One can see that only at flow rate $Q = 11 \text{ l/s}$ the numerically assessed frequency largely overestimates the experimental one. On the other hand the best agreement is obtained at flow rate $Q = 7 \text{ l/s}$.

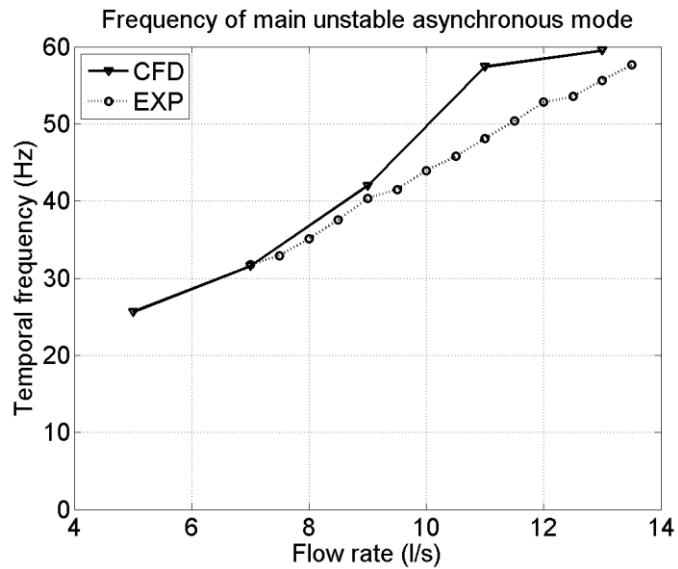


Figure 116 Comparison of the main unstable mode temporal frequencies

Differences at higher flow rates $Q > 10$ l/s can be caused by the single-phase flow calculation where the source of vorticity emerging from the transport equation is not solved. The vorticity arising from the interface of cavitating core with the main stream (so called baroclinic torque term) is additional source of hydraulic losses. The asynchronous frequency decrease (related to the movement of cavitating vortex rope in the draft tube of hydraulic turbine) with decreasing Thoma cavitating number while turbine operating point remains unchanged was documented in [14].

16.2.2 POD of numerically computed field in the cross-sectional planes

In order to study development of the vortex structure downstream of the diffuser the POD is carried out also in the several cross-sectional planes (s1, s2, s3 and s4) corresponding with the locations of pressure sensors see Figure 117. Two flow rates are investigated $Q = 5$ l/s and 11 l/s.

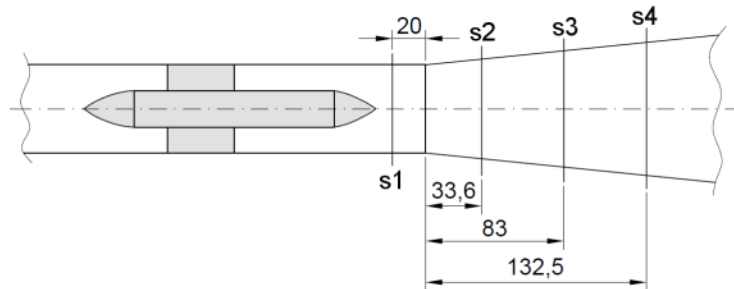


Figure 117 Location of cross-sectional planes for POD

The static pressure modes #1 - #5 are plotted in Figure 118 – Figure 122 for flow rate $Q = 5$ l/s and in Figure 123 – Figure 127 for flow rate $Q = 11$ l/s. Note that magnitude of ϕ_k contours is changing for particular cross-sections. Decrease in the contours level of ϕ_k in particular cross-sections refers to weakening dynamic behavior of the vortex structure in the downstream part of the diffuser.

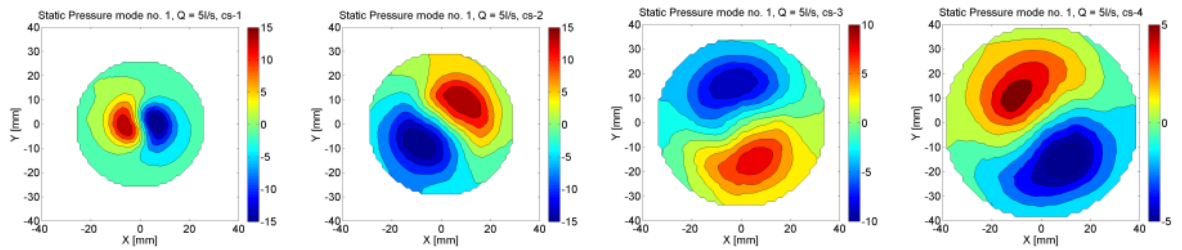


Figure 118 Static pressure mode #1 in cross-sectional planes s1, s2, s3 and s4, flow rate $Q = 5$ l/s.

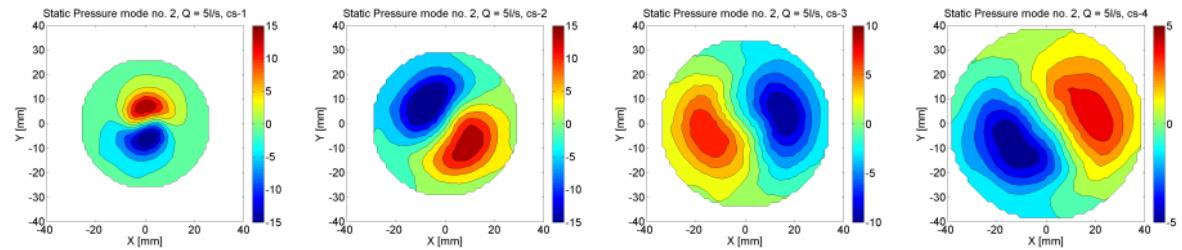


Figure 119 Static pressure mode #2 in cross-sectional planes s1, s2, s3 and s4, flow rate $Q = 5$ l/s.

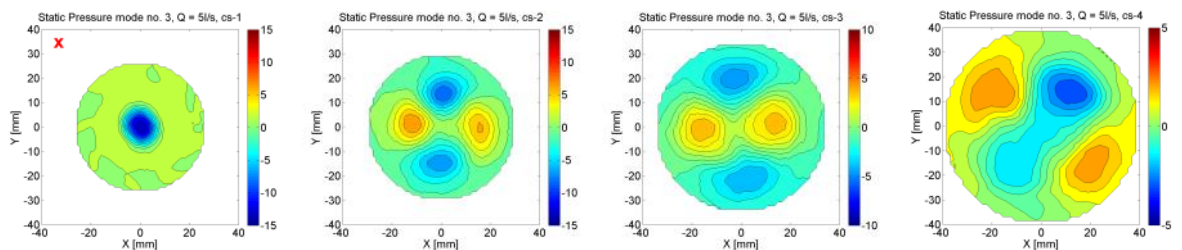


Figure 120 Static pressure mode #3 in cross-sectional planes s1, s2, s3 and s4, flow rate $Q = 5$ l/s.

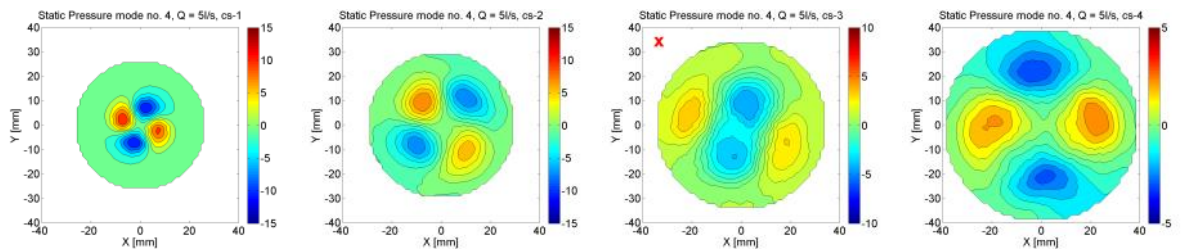


Figure 121 Static pressure mode #4 in cross-sectional planes s1, s2, s3 and s4, flow rate $Q = 5$ l/s.

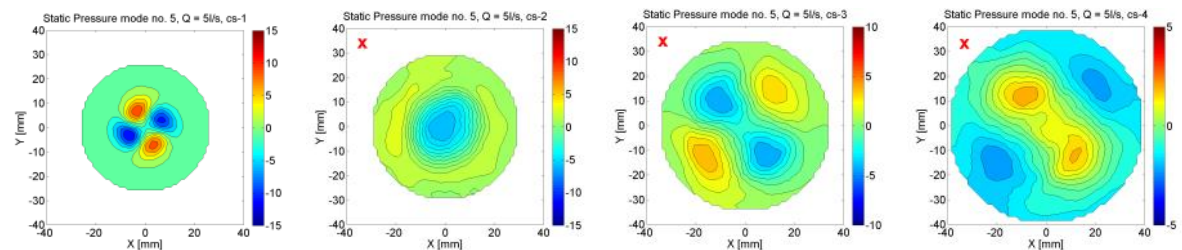


Figure 122 Static pressure mode #5 in cross-sectional planes s1, s2, s3 and s4, flow rate $Q = 5$ l/s.

For each cross-section the frequency of the temporal modes are extracted and summarized in Table 20. In comparison with the asynchronous pulsations the synchronous pulsations are characterized by the low frequency magnitude, thus the temporal frequency of synchronous

kind of modes should be same or very similar magnitude. In Table 20 the low frequencies identifying the synchronous modes are highlighted by red numbers.

Table 20 Frequency (Hz) of temporal modes, $Q = 5$ l/s

mode #	s1	s2	s3	s4
1	23.21	23.21	11.6	11.6
2	23.21	23.21	11.6	11.6
3	4.97	38.13	25.69	20.72
4	104.4	62.16	1.66	20.72
5	104.4	2.49	1.66	1.66

If we look at the spatial shape of the modes in particular cross-sections it is clear that mode #1 (respectively mode #2) have specific spatial shape which would be created by the quasi-spirals in full 3D domain. These modes are consequence of asynchronous pressure pulsations. On the other hand the modes related to the synchronous pressure pulsations (marked with red cross in the top-left corner) have generally different shape (i.e. very low or very high contour in the middle of investigated domain), e.g. mode #3 in the first cross-section and mode #5 in the second cross-section. Nonetheless it can be observed that some of the modes identified (according to low temporal frequency) have spatial shape something between asynchronous and synchronous ones, e.g. mode #5 in the third and fourth cross-section.

In Table 21 the synchronous frequencies of static pressure field (extracted in section 13.1) are compared with the frequencies of synchronous modes (noted as POD) for particular cross-sections. Despite disagreement in frequency magnitude in the second cross-section it is noticeable that the above identified synchronous modes are truly consequence of synchronous pressure pulsations.

Table 21 Synchronous static pressure pulsations (pressure field vs. POD) at flow rate $Q = 5$ l/s

$Q = 5$ l/s	Pressure field (Hz)	POD (Hz)
s1	4.96	4.97
s2	4.96	2.49
s3	1.65	1.66
s4	1.65	1.66

Similarly as for flow rate $Q = 5$ l/s the first five modes in particular cross-sections are plotted in following figures for flow rate $Q = 11$ l/s.

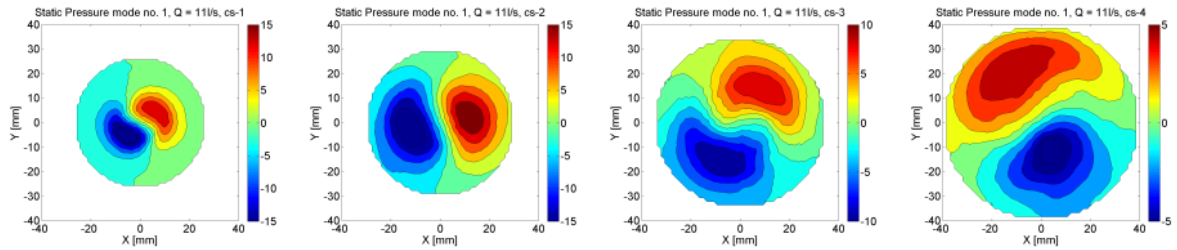


Figure 123 Static pressure mode #1 in cross-sectional planes s1, s2, s3 and s4, flow rate $Q = 11 \text{ l/s}$

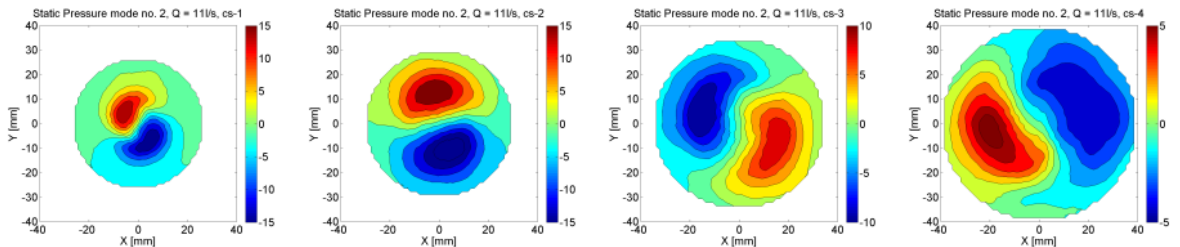


Figure 124 Static pressure mode #2 in cross-sectional planes s1, s2, s3 and s4, flow rate $Q = 11 \text{ l/s}$

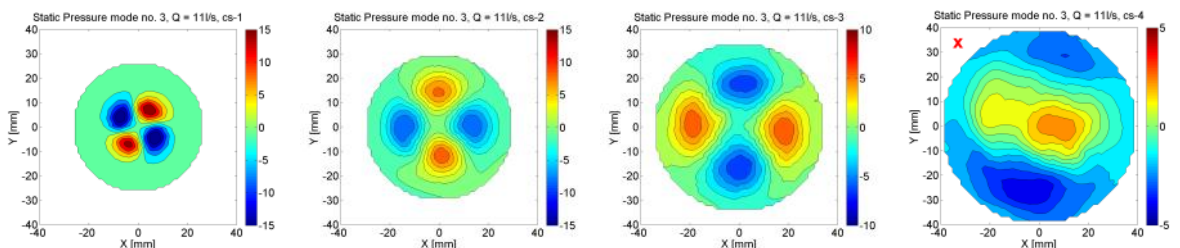


Figure 125 Static pressure mode #3 in cross-sectional planes s1, s2, s3 and s4, flow rate $Q = 11 \text{ l/s}$

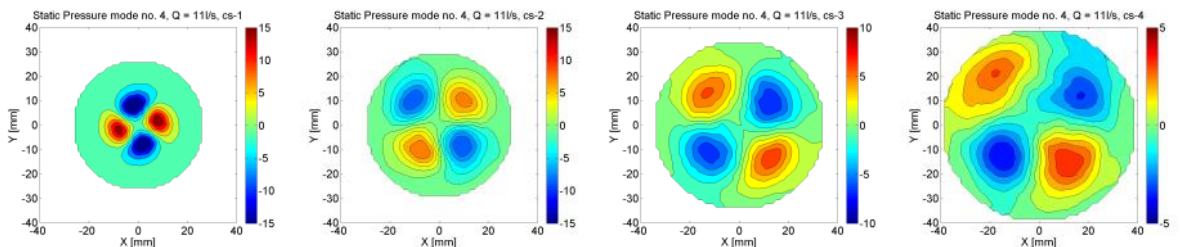


Figure 126 Static pressure mode #4 in cross-sectional planes s1, s2, s3 and s4, flow rate $Q = 11 \text{ l/s}$

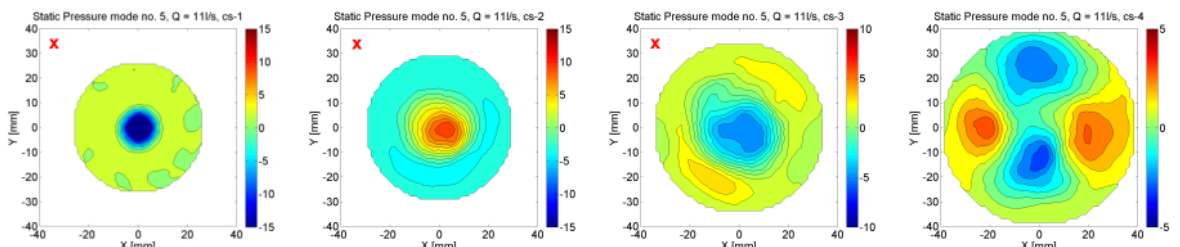


Figure 127 Static pressure mode #5 in cross-sectional planes s1, s2, s3 and s4, flow rate $Q = 11 \text{ l/s}$

The temporal frequencies of modes #1 - #5 can be found in Table 22 for all four cross sections s1 – s4. Consequently the modes related to the synchronous pulsations are identified

according to low frequency magnitude (highlighted by red numbers in Table 22) and specific spatial shape (red cross in the top-left corner in figures above)

Table 22 Frequency (Hz) of temporal modes, $Q = 11$ l/s

mode #	s1	s2	s3	s4
1	58.07	58.07	24.57	24.57
2	58.07	58.07	24.57	24.57
3	230.1	160.8	87.11	8.935
4	230.1	160.8	87.11	67.01
5	2.234	4.467	4.467	67.01

The frequencies of synchronous pressure pulsations of both the static pressure signal from discrete monitoring points and synchronous pressure modes are compared in Table 23.

One can see that compared to flow rate $Q = 5$ the larger disagreement in frequencies of synchronous frequencies of static pressure field and POD modes can be found. The discrepancy in frequency magnitude probably arises from the insufficient (very short) signal length used for FFT.

Table 23 Synchronous static pressure pulsations (pressure field vs. POD) at flow rate $Q = 11$ l/s

$Q = 11$ l/s	Pressure field (Hz)	POD (Hz)
s1	4.47	2.234
s2	2.23	4.467
s3	6.70	4.467
s4	8.94	8.935

Comparing the first five modes of two different flow rates $Q = 5$ and 11 l/s one can see that both, the spatial and temporal features vary when the flow rate increases. With increasing flow rate the modal frequency increases for both synchronous and asynchronous modes. Beside this, the synchronous kinds of modes are redistributed. For example, while for $Q = 5$ l/s the mode #3 is related to synchronous pressure pulsations in the first cross-section, at flow rate $Q = 11$ l/s it is in the fourth cross-section. Moreover the spatial shape of asynchronous kind of modes became more developed in the third and fourth cross-sections. This can be observed for flow rate $Q = 5$ l/s where in the third cross-section all modes look like the asynchronous ones, but dominant frequency of modes #4 and #5 is very low indicating synchronous character of pulsations. On the other hand for flow rate $Q = 11$ l/s recognition of asynchronous modes from their spatial shape is much more straightforward.

Comparison of frequency decrease of temporal mode #1 and frequency decrease of asynchronous pressure pulsations (numerically computed and experimentally measured) downstream of the diffuser is presented in Figure 128 for both investigated flow rates. At flow rate $Q = 5$ l/s the values of temporal frequency (POD) overestimate both the frequency

extracted from the numerical pressure signal (CFD) and the frequency extracted from the experimentally measured pressure signal (EXP) in the second sensor location. For the third sensor location the POD frequency underestimates experimental one while its magnitude is close to the numerical frequency. On the other hand for the fourth sensor the POD frequency overestimates numerical one and underestimates the experimental one. The best agreement is obtained for the location corresponding to the first pressure sensor which is situated 20 mm in front of the diffuser entrance.

At flow rate $Q = 11$ l/s both numerically computed (CFD) and modal (POD) frequencies overestimate the experimental ones (EXP) in the first two sensor locations and underestimate in the last two sensor locations. Contrary to flow rate $Q = 5$ l/s the best agreement in frequency magnitudes at flow rate $Q = 11$ l/s is obtained in the fourth sensor location.

The main disagreements can arise from the post-processing background where the data sampling period for POD is much higher ($2.17e-3$ sec) than in case of pressure probe sampling period ($4.88e-4$ sec) from CFD calculation. On the other hand this result shows that the modes #1 with #2 create the mode pair which is the main source of asynchronous pressure pulsations.

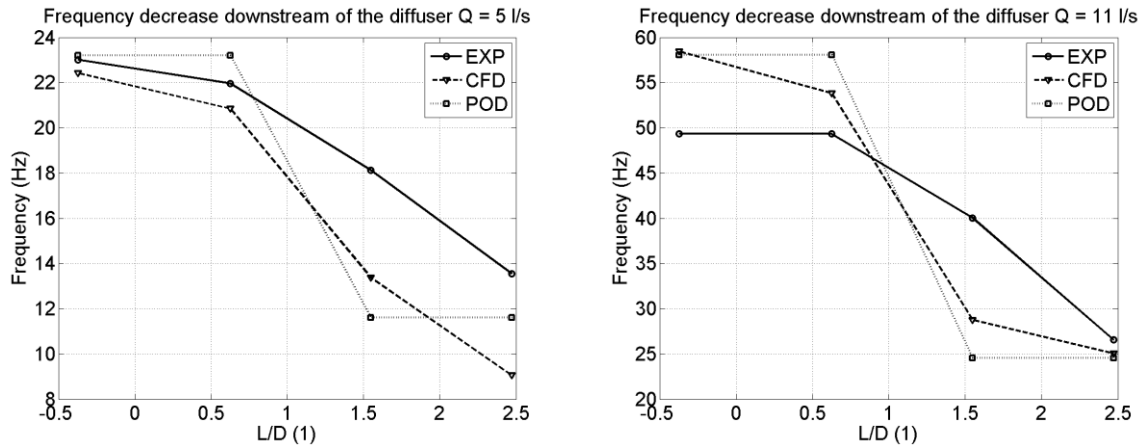


Figure 128 Comparison of frequency decrease (POD, CFD, and EXP) downstream of the diffuser for flow rate $Q = 5$ l/s (left) and $Q = 11$ l/s (right)

16.3 CONCLUSION OF POD ANALYSIS OF “BUT” SWIRL GENERATOR

In this section the POD was applied to both the experimental (image ensemble of cavitating vortex) and numerical (computed static pressure fields) data related to the flow generated by the “BUT” swirl generator. It is clear that resulting spatio-temporal modes are different due to different nature of flow fields POD was applied to. While the first field is related to the amount of cavitation (represented as the color scale magnitude) the second one represents numerically computed static pressure. In the first case the amount of cavitation increases with the flow rate. On the other hand the static pressure decreases when the flow rate increases. In case of POD applied to the cavitating vortex structure the information are available only when some vapor fraction exists in the flow field. This is limitation factor causing that with increasing flow rate the vortex structure became more visible in the

downstream part of the diffuser (where for flow rates with low cavitation the spiral vortex is not visible enough even it is certainly presented). This is probably also reason why in this case the main unstable mode is the synchronous one. The cavitation is strongest if the pressure drop is sufficient enough. This valid best for region just behind the swirl generator spike where the synchronous pulsations are dominant (see section 7.3.2). On the other hand in case of POD applied to the numerically computed static pressure field the information are available in whole investigation domain. The relevant agreements are expected if the vapor fraction field from multiphase flow calculation would be assumed for POD analysis.

Despite above presented disagreements it was shown that at least the spatio-temporal features in a form of temporal frequency and spatial shape of the most dominant unstable mode (as a consequence of the strong asynchronous pressure pulsations) correspond very well for both flow fields.

In case of POD applied to the numerically computed static pressure fields in several 2D cross-sectional planes situated in downstream part of the diffuser the spatio-temporal results showed decaying process of the vortex structure and its relation to the decreasing asynchronous pressure pulsations. The modal frequencies of static pressure modes assumed to be consequence of synchronous pulsations are correlated with the frequencies of static pressure pulsations (synchronous) through the particular cross-sections. The resulting agreement verifies that the synchronous modes were determined correctly.

Considering only finite number of the most dominant modes the approximate interpolation of original flow fields is executed through the backward reconstruction. It was shown that only finite number of modes (in this case 10 modes) is sufficient, moreover in this case where the one dominant mode pair appears.

The main outcomes of presented POD analysis are following:

- It was shown that modes related to the synchronous or asynchronous pulsations in the flow field can be easily identified from the entire modal spectrum. This is very good aspect enabling to study changes in the dynamical properties of the flow.
- The spatio-temporal character of the most unstable modes is analogous independently on the field used for decomposition.
- Disintegrating process of the spiral vortex downstream of the diffuser (discussed in the first part of this thesis) is well correlated with decreasing dynamic of the main unstable mode pair related to the strong asynchronous pulsations, see Figure 128 at the end of section 16.2.2.

17 POD ANALYSIS OF “UPT” SWIRL GENERATOR WITH THE AXIAL WATER INJECTION

As was mentioned in section 2 on the base of author’s internship at Politehnica University of Timisoara in Romania the collaborative work arose employing the POD technique for numerical calculation of “UPT” swirl generator apparatus designed by our colleagues in Timisoara. This work presents utilization of POD in order to study influence of the axial water injection as a methodology used to suppress the spiral vortex dynamics.

This analysis is focused on the active control method proposed by Resiga et al. [96] employing the axial water jet injected along of the diffuser axis. In contrary with the [65] where the helical instability is suppressed by changes in the fluid density this approach is based on the change of the mean flow. Particularly, the axial water jet method is tested on a straight draft tube using a swirl generator apparatus instead of the turbine runner [8]. Numerical computations of the jet influence on decelerated swirling flow in the diffuser for several jet discharges performed by Muntean et al. [56] are carried out in order to compare numerical results with experimental ones [10]. The data sets of velocity and pressure fields are used for the POD analysis. The computed pressure and velocity fields are further decomposed to extract the main significant modes. Based on the assumptions presented in section 15.1 it is decided which modes correspond to the asynchronous or the synchronous pressure oscillations. As a result, the particular modes influenced by the axial water injection method are quantified using the POD technique. In case of experimental investigations the POD is usually applied to the 2D velocity field obtained from the PIV measurements and can be well correlated with the POD results from the CFD calculations. The main aim of this investigation is the application of POD to the three-dimensional pressure field. Contrary to the velocity measurements (PIV or LDA) the pressure is measured in discrete points which are usually far apart and situated on the domain boundary (e.g. pressure transducers). One of the previous applications of POD to the experimentally measured pressure field can be found in [7], where almost 500 pressure taps were used for the modal analysis of wind forces to the building roof. It is clear that analogous measurements of the pressure field in case of hydraulic engineering would be too demanding. On the other hand, the pressure field obtained from the CFD calculation enables to apply the POD in a similar way as in case of PIV measurements. The main advantage of POD technique applied to the full 3D pressure field with the respect to extensively used FFT technique (in a form of discrete monitoring points) is that POD can additionally provide spatial representation of the pressure modes besides only a temporal view obtained by FFT. Therefore, it helps to decide in which part of the domain and in which direction the mitigation effort should be focused. It was shown by Bosioc et al. [8] that the self-induced instability and its associated pressure fluctuations are successfully mitigated by injecting water jet along the axis. However, the jet discharge is too large to be supplied with the water bypassing the runner, since this discharge is associated with the volumetric loss. As a result, the most significant unstable modes associated with the vortex rope are indentified based on the methodology developed in this thesis. This methodology supports our effort to improve capability of this active control method towards practical applications in the real hydraulic turbines.

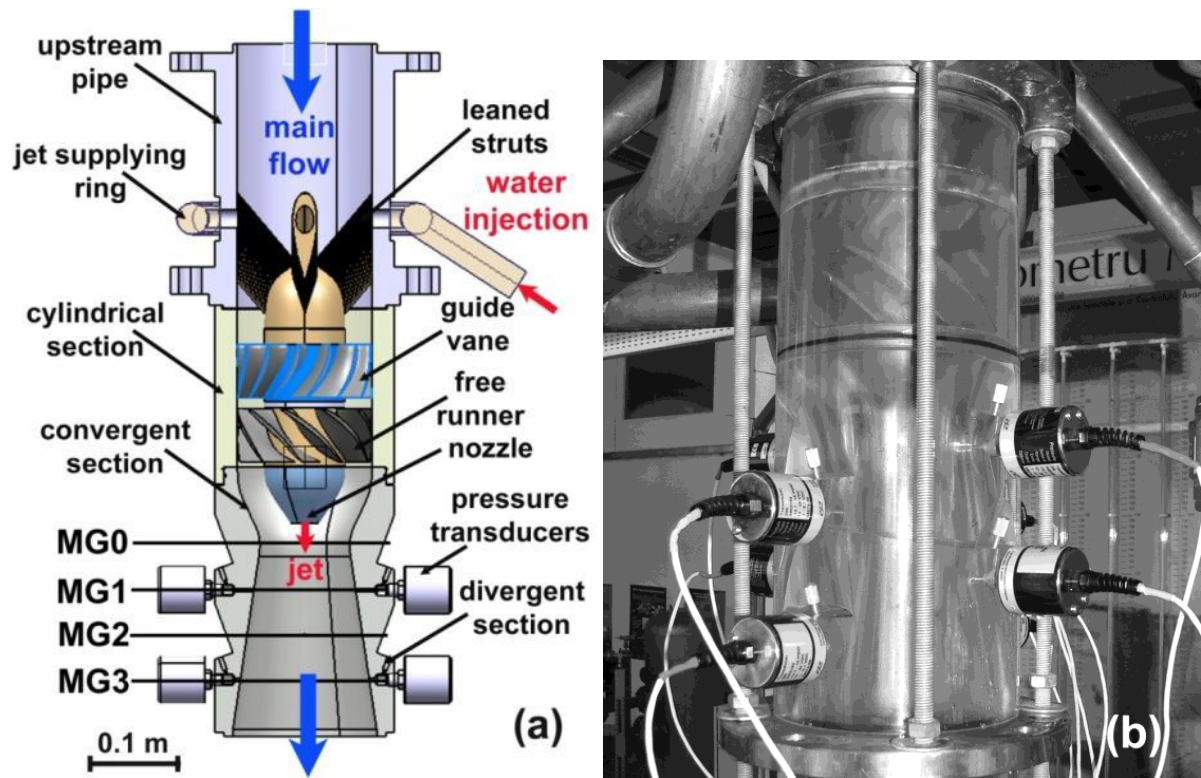


Figure 129 Experimental test section of the „UPT“ swirl generator

17.1 NUMERICAL SET-UP

The three-dimensional computational domain shown in Figure 130 corresponds to the convergent-divergent section of the experimental swirl generator apparatus described in Figure 129. The inlet boundary of the computational domain is the annular section located just downstream of the free runner while the outlet section belongs to a cylindrical extension of the divergent part. The turbulent velocity profiles used as the inflow condition in present numerical computation, together with the profiles of turbulent kinetic k energy and dissipation rate ε are results of previous numerical simulation [10]. The pressure outlet with the radial equilibrium condition, eq. (17.1), is prescribed on the outlet boundary located downstream of the conical section in the extended pipe, see Figure 130.

$$\frac{\partial p}{\partial r} = \rho \frac{v_{\theta}^2}{r} \quad (17.1)$$

The inflow boundary condition with normal velocity on the surface of the nozzle outlet (denoted “jet inlet” in Figure 130) is applied when the water jet is switched on.

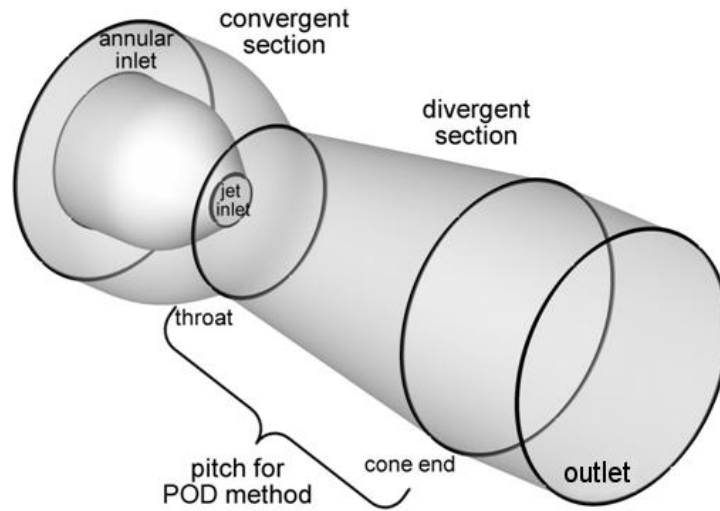


Figure 130 Three-dimensional computational domain of convergent-divergent section

A structured mesh with 267200 hexahedral finite volumes was generated using Gambit software. The three-dimensional domain selected for POD analysis is bounded by the nozzle inlet and the cone outlet containing 180000 volumes. This region was selected so that the whole vortex rope is captured inside. The detailed view of the mesh is shown in Figure 131.

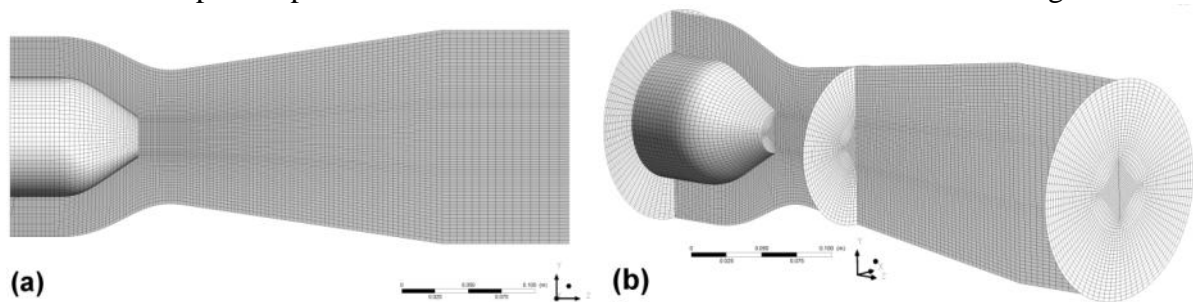


Figure 131 Computational mesh in detailed views, longitudinal (a) and transverse (b)

The three-dimensional turbulent unsteady computation with the time step of $\Delta t = 1.10^{-4}$ sec is carried out using the commercial software ANSYS Fluent R14 [2]. The Reynolds stress model (RSM) with second-moment closure was chosen in order to include the effect of strong turbulence anisotropy [2], [32], [79]. The Reynolds stress model involves calculation of the individual Reynolds stresses using differential transport equations. The individual Reynolds stresses are then used to obtain closure of the Reynolds-averaged momentum equation (RANS). The PISO algorithm for pressure-velocity coupling is selected based on our systematic investigation of the swirling flows [53], [54], [55]. For the spatial discretization of momentum and turbulence quantities (k , ϵ and Reynolds stresses) the 2nd order upwind scheme was selected, while the PRESTO! scheme was chosen for the pressure. The second order implicit scheme was chosen for transient formulation.

The mesh convergence was tested for coarser (approximately 200k elements) and finer mesh (approximately 350k elements) without significant difference in results. Thus the mesh density is considered to have minor influence on the presented results.

In our case, the computed precession frequency of the spiral vortex is $f_v = 13.26$ Hz. According to section 15 the minimum sampling frequency of data for POD is $f_s = 53.04$ Hz corresponding to the maximum sampling period $dt = 0.189$ sec.

The numerical results are validated against the experimental data then the decomposing POD technique is applied to the three-dimensional pressure and velocity fields. Approximately 1000 instantaneous snapshots were taken into account. Each data set contains values in 187960 mesh nodes. The POD decomposition provides spatial and temporal representations and backward reconstruction for each field and was carried out using our own implementation of POD procedure in MATLAB® [49].

The numerical results are compared with the experimental data performed by Bosioc et al. [8]. The influence of the axial water injection method on the diffuser efficiency is quantified by the pressure recovery factor c_p defined in eq. (17.2) as:

$$c_p = \frac{\bar{p} - \bar{p}_{ref}}{\frac{1}{2}\rho v_{ref}^2} \quad (17.2)$$

\bar{p}_{ref} is the mean static pressure in the reference section, \bar{p} the mean static pressure, ρ water density and v_{ref} the reference velocity defined by eq. (17.3)

$$v_{ref} = \frac{4(Q + Q_{jet})}{\pi D_{ref}^2} \quad (17.3)$$

where $Q = 30$ l/s is the swirl generator discharge, Q_{jet} (l/s) the jet discharge and $D_{ref} = 0.1$ m the reference section diameter.

Strouhal number is evaluated on entire range of investigated jet discharges in order to capture the behavior of coherent structure during the axial water injection.

$$St = \frac{f D_{ref}}{v_{ref}} \quad (17.4)$$

The values of Strouhal number are computed using both frequency of pressure signal from CFD computation and the frequency of pressure signal obtained from the backward POD reconstruction. The amplitudes of pressure signals from CFD computation and backward POD reconstruction are made dimensionless with respect to the dynamic pressure from the reference section. These numerical values are compared with the experimental ones for several particular jet discharges.

The dimensionless pressure amplitude will be defined [8]:

$$A = \frac{\sqrt{2}p_{rms}}{\frac{1}{2}\rho v_{ref}^2} \quad (17.5)$$

where pressure root mean square (rms) is defined according to the following equation:

$$p_{\text{rms}} = \sqrt{\frac{1}{2} \int_{t_0}^{t_0+T} [p(t) - \bar{p}]^2 dt} \quad (17.6)$$

17.2 POD OF PRESSURE AND VELOCITY FIELDS IN THE CONICAL DIFFUSER

As was mentioned above, POD is usually applied to the velocity field obtained from the PIV measurements or CFD calculations. Nevertheless later it will be shown that besides the velocity field the POD can be well applied to the static pressure field with analogous results. First, the POD of axial, tangential and radial velocity fields is carried out and compared with the POD of static pressure field for the case of decelerated swirling flow with the vortex rope. Second, the POD modes of the radial velocity field are chosen to presents changes in the modal decomposition when the axial water jet is applied. Third, the comprehensive POD analysis of the static pressure field is carried out for different jet discharges and compared with the modes of the radial velocity field.

Generally the vortex rope is visible when the pressure drops under the value of the saturated vapor. Then the vortex core is filled with the vapor and due to the light reflection the helical structure can be observed. This vortex structure is called the cavitating vortex rope. Using the single phase CFD simulation (as in our investigation) the vortex rope shape can be captured by the iso-surface of the low pressure. The shape of the vortex core created by the iso-surface of the low pressure is visually very similar to the shape of cavitating vortex core [35]. In order to show that only finite number of several static pressure modes is main source of the strong unsteady behavior, the backward reconstruction of the static pressure field is carried out. This includes the spatial shape of the reconstructed vortex core and comparison of the pressure recovery and pressure amplitudes from the reconstructed pressure fields with the results from the CFD and experimental measurements. This is one of the main reasons why the POD of the static pressure field was chosen in this investigation.

Throughout, the decomposed function $p(\mathbf{x}; t)$ is considered in dimensionless form in order to compare the values associated with the different investigated cases (e.g. increasing flow rate), the dimensionless form of the pressure field is defined as follows:

$$p(\mathbf{x}; t) \equiv \frac{\Delta p(\mathbf{x}, t)}{\frac{1}{2} \rho v_{ref}^2} \quad (17.7)$$

where $\Delta p(\mathbf{x}, t) = p(\mathbf{x}, t) - \overline{p_{ref}}$, $p(\mathbf{x}, t)$ is the static pressure field obtained in numerical simulation at each time step t , $\overline{p_{ref}}$ is value of mean static pressure on the outlet surface computed as a mass-weighted surface integral in form:

$$\overline{p_{ref}} = \frac{1}{Q_m} \int_0^{Q_m} p \, dQ_m \quad (17.8)$$

and v_{ref} corresponds to the bulk velocity in the reference section. Subtraction of $\overline{p_{ref}}$ is due to radial equilibrium pressure condition at the outlet boundary which applies specified gauge pressure only to the position of minimum radius at the boundary. The static pressure on the rest of zone is calculated from the assumption that the radial velocity is negligible, so that the pressure gradient is given by eq. 17.1. Similarly the velocity field, further decomposed into cylindrical velocity components – axial, tangential and radial, is made dimensionless by the bulk velocity v_{ref} in the reference section.

$$v(\mathbf{x}; t) \equiv \frac{\Delta v(\mathbf{x}, t)}{v_{ref}} \quad (17.9)$$

17.3 DECELERATED SWIRLING FLOW WITH THE VORTEX ROPE

In following subsection the POD is applied to the velocity field decomposed into cylindrical components (axial, tangential and radial) and to the static pressure field in case of swirling flow with the vortex rope. For each of the flow fields the first nine spatial modes are presented together with the power spectra of the temporal modes and corresponding dimensionless eigenvalue magnitudes λ_k .

Most of the authors [50], [1], [36], [63], [71] applied POD to the fluctuating part $\mathbf{v}'(x, t_k)$ of the complex velocity field $\mathbf{v}(x, t_k)$ subtracting the mean flow $\mathbf{V}(x)$.

$$\mathbf{v}'(x, t_k) = \mathbf{v}(x, t_k) - \mathbf{V}(x) \quad (17.10)$$

In these cases the eigenvalues λ_k represent twice the amount of the fluctuating kinetic energy contained in the particular POD mode. Then the total kinetic energy (TKE) is the sum of all eigenvalues and its amount contained in corresponding velocity mode is expressed in percent of this sum [64]. Nonetheless this approach does not provide any information about relative ratio of the kinetic energy within the modes to the kinetic energy of the mean flow. Therefore in our investigation we will use the complete instantaneous velocity field $\mathbf{v}(x, t_k)$. This enables also better comparison between individual velocity components (axial, tangential and radial). For all three investigated velocity fields the eigenvalues λ_k are presented in the dimensionless form.

Similarly as in the case of the velocity fields we will use the complete instantaneous static pressure field $\mathbf{p}(x, t_k)$.

$$\mathbf{p}(x, t_k) = \mathbf{P}(x) + \mathbf{p}'(x, t_k) \quad (17.11)$$

Then the eigenvalues λ_k directly correspond to the power of the square of function $\mathbf{p}(x, t_k)$ [7].

Graphically, both the velocity and the pressure spatial POD modes are plotted by iso-surface of the eigenfunction ϕ_k . Similarly as the eigenvalue magnitude λ_k the magnitude of the eigenfunction ϕ_k quantifies the contribution of the each particular mode to the flow field.

17.3.1 POD modes of axial velocity field

In Figure 132 the spatial modes #1 - #9 of the axial velocity field are presented. While the relevant eigenvalue magnitudes are plotted in Figure 133a, the power spectra of the first ten modes of the axial velocity field is shown in waterfall diagrams, Figure 133b. From the spatial shapes and modal frequencies it can be seen that modes #1 with #2, #4 with #5 and #6 with #7 create particular mode pairs. The mean (time-averaged) mode #0 contains 85.5% of the axial kinetic energy budget. Together with mode #1 (2.9%), mode #2 (2.8%) and mode #3 (2.2%) it is over 93%.

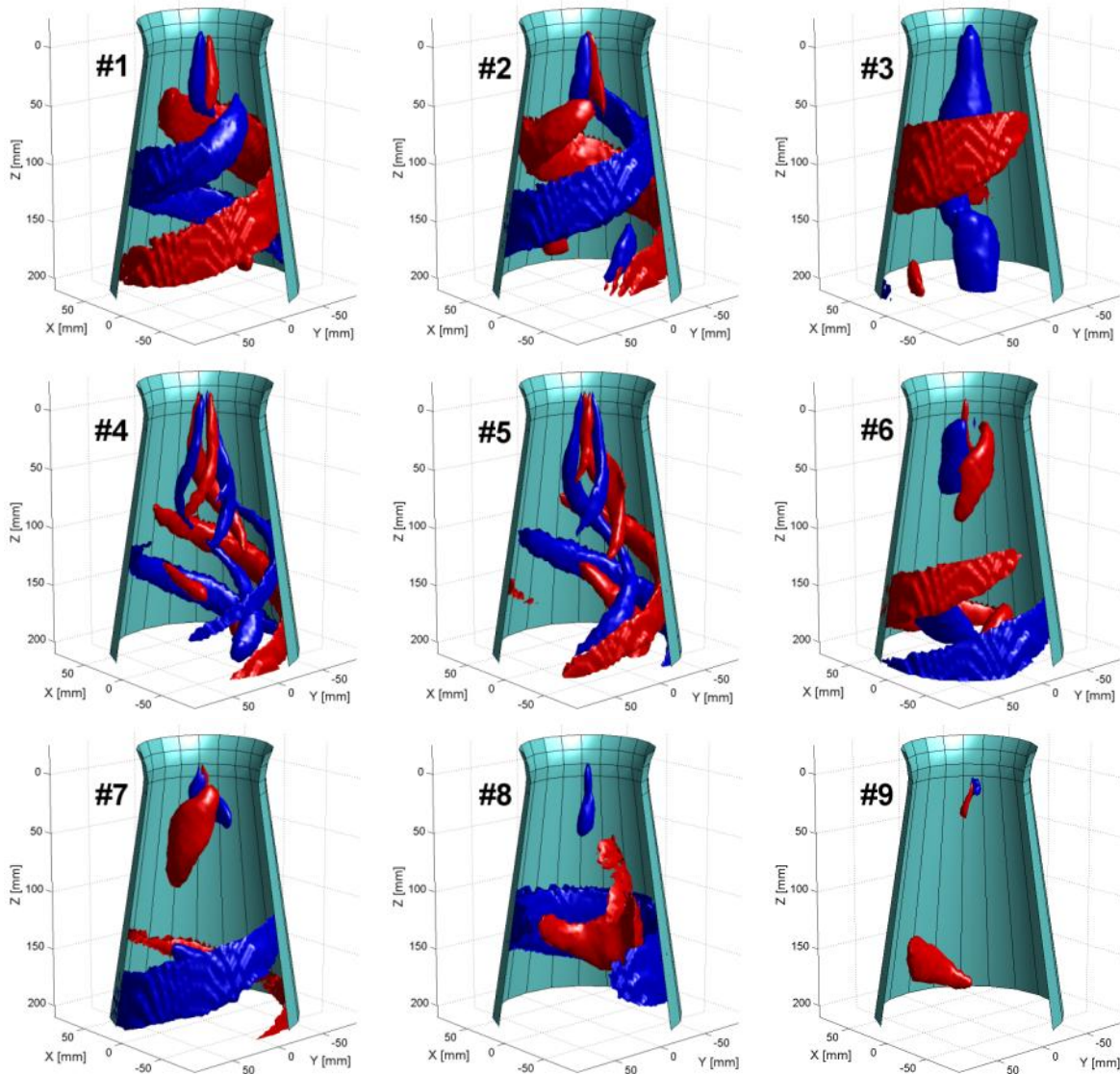


Figure 132 Spatial shape of the axial velocity modes #1 - #9 in case of decelerated swirling flow with the vortex rope

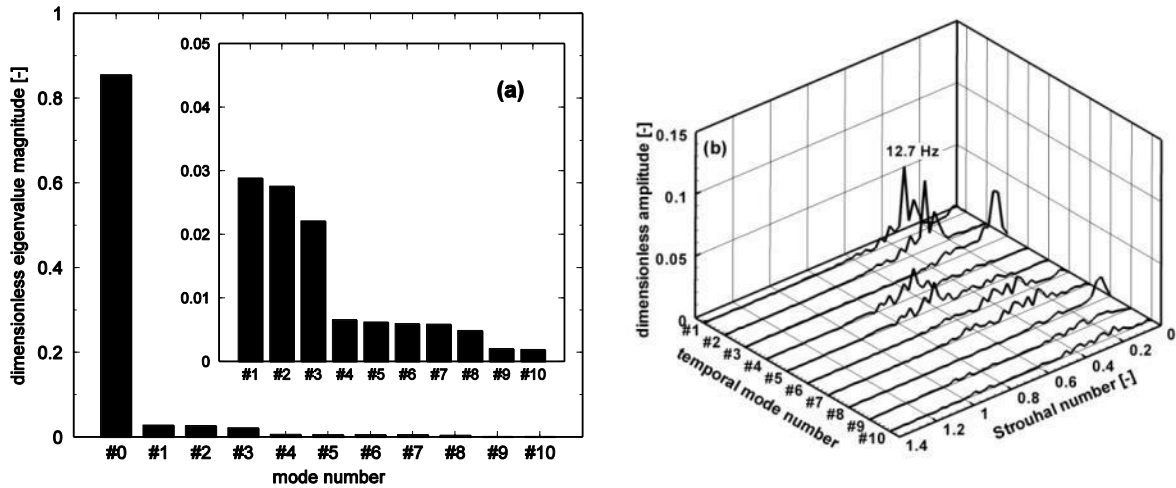


Figure 133 Eigenvalue magnitude of the axial velocity modes #0 - #9 (a) and power spectra of the temporal modes (b)

According to section 15.1 the above mentioned mode pairs are consequence of asynchronous pulsations in velocity field. On the other hand the synchronous pulsations are responsible for the modes #3 and #8 which are identified on the base of low frequency of temporal mode and specific spatial shape.

17.3.2 POD modes of tangential velocity field

The spatial shapes of tangential velocity modes #1 - #9 are presented in Figure 134 and Figure 135. The dimensionless eigenvalues magnitude of the tangential velocity modes are plotted in Figure 136a. The mean (time-averaged) mode #0 contains 84.2% of the energy budget. Together with mode #1 (4.3%), mode #2 (4.2%) and mode #3 (1%) it is almost 94%. One can see that in contrast with the axial velocity modes the tangential velocity modes #1 and #2 are stronger within tangential velocity field.

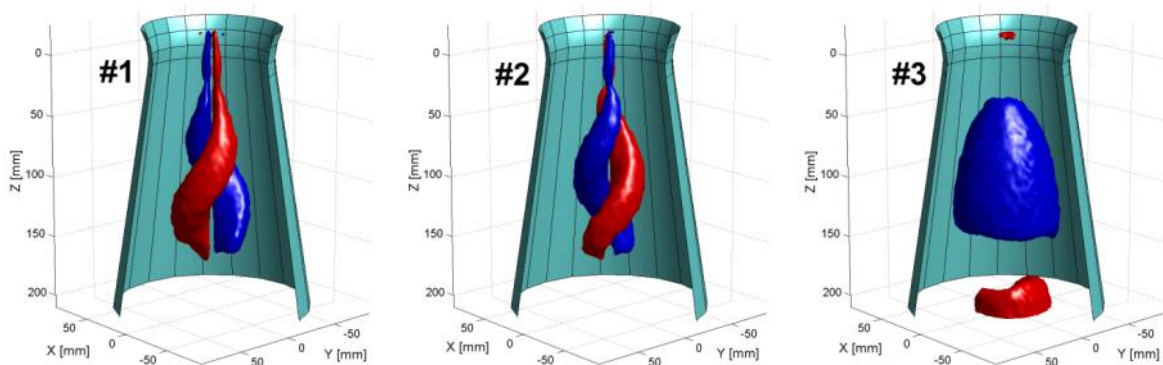


Figure 134 Spatial shape of the tangential velocity modes #1 - #3 in case of decelerated swirling flow with the vortex rope

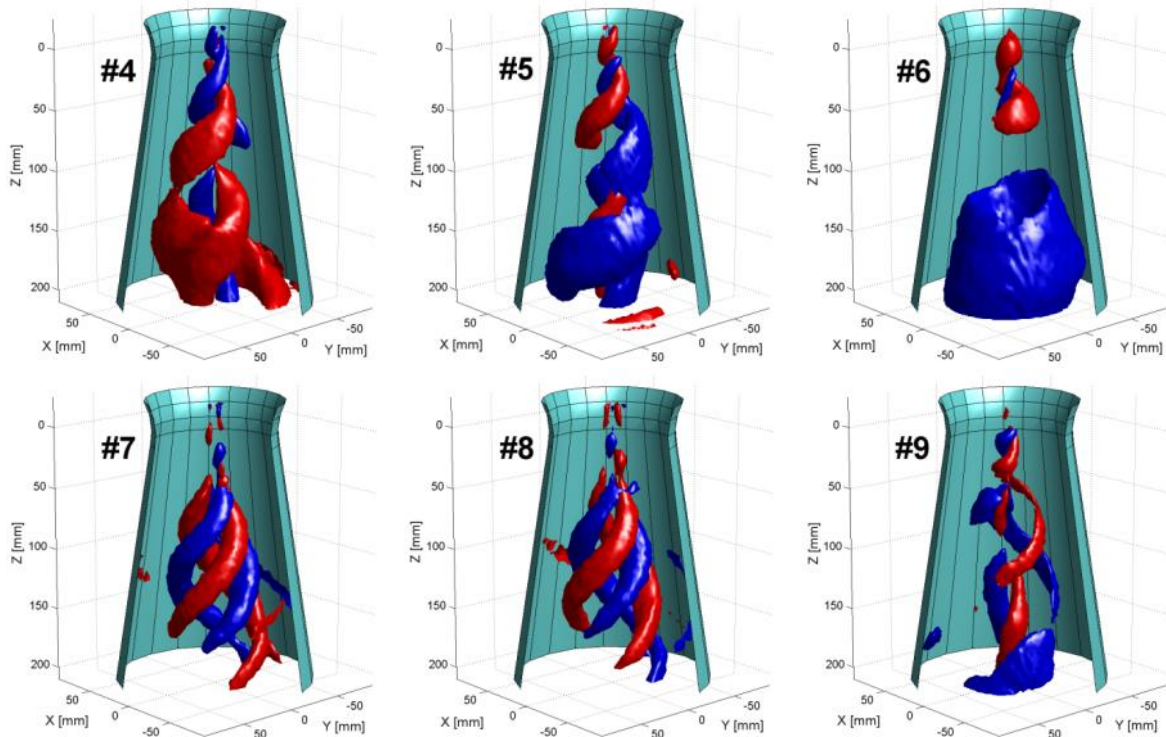


Figure 135 Spatial shape of the tangential velocity modes #4 - #9 in case of decelerated swirling flow with the vortex rope

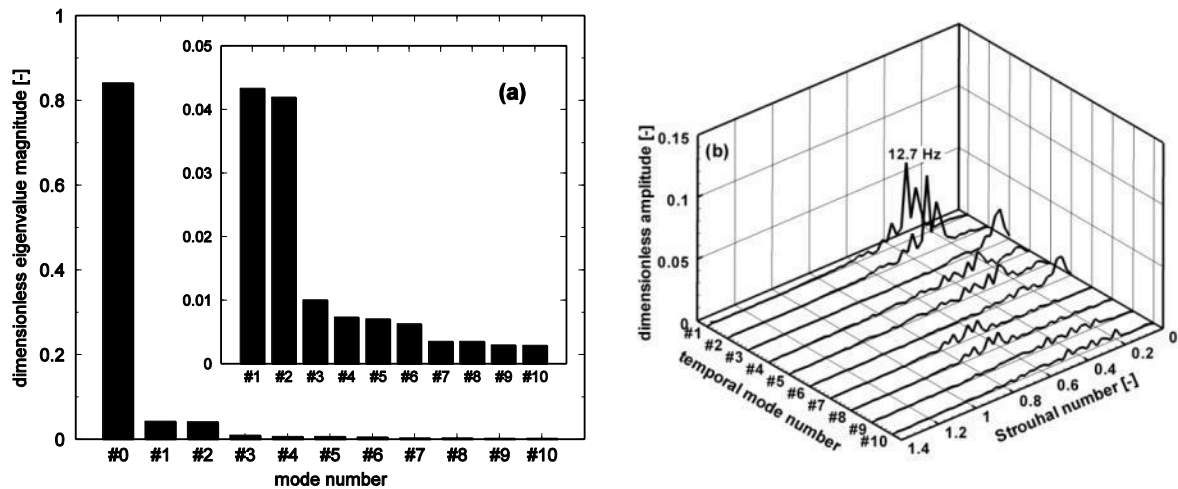


Figure 136 Eigenvalue magnitude of the tangential velocity modes #0 - #9 (a) and power spectra of the temporal modes (b)

Similarly as in previous, the modes of tangential velocity appearing in the mode pairs can be identified from the power spectra of the temporal modes (identical modal frequency, see Figure 136b) and from the spatial representations (same phase shifted spatial shape, see Figure 135). The mode pairs modes of tangential velocity as a consequence of asynchronous pulsations are modes #1 with #2, #4 with #5, #7 with #8 and #9 with #10. The synchronous pulsations in tangential velocity field are represented by modes #3 and #6. One can see that synchronous modes are much different from asynchronous ones (low temporal mode frequencies and specific spatial shape – which is not created by spirals as in case of asynchronous kind of modes but with structures similar to bubbles).

17.3.3 POD modes of radial velocity field

In Figure 137 the spatial modes #1 - #9 of the radial velocity field are presented. The relevant eigenvalue magnitudes are plotted in Figure 138a and power spectra of the temporal modes in Figure 138b.

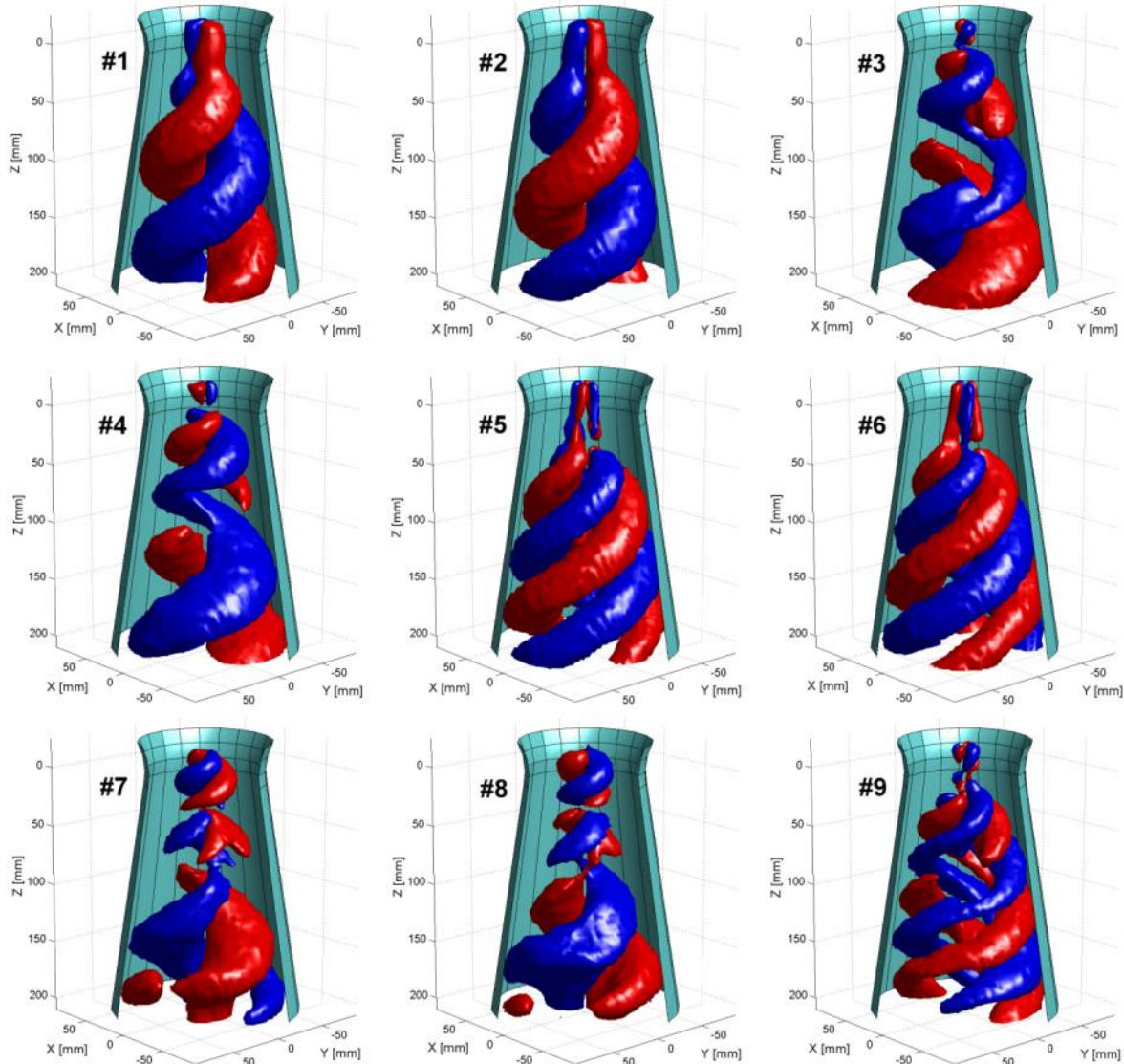


Figure 137 Spatial shape of the radial velocity modes #1 - #9 in case of decelerated swirling flow with the vortex rope

The mean (time-averaged) mode #0 contains only 11% of the energy budget. Together with mode #1 (26.9%), mode #2 (26.6%) it is around 65%. Apparently the eigenvalue magnitudes of mode pair #1 and #2 exceed the mean (time-averaged) mode #0. This means that from the energetic point of view the mean (time-averaged) radial velocity field is weaker than its dominant dynamic part represented by the modes #1 and #2. Generally the radial velocity is very sensitive measure of instability and vortex breakdown inception. This leads to consideration that the changes in the spatio-temporal behavior of the radial velocity modes can qualitatively show how the vortex structure is suppressed when the axial water jet is applied. Especially one interesting question arises. Will the weakening process of the modes

#1 and #2 under the mean (time-averaged) mode #0 linked to the suppression of the vortex rope?

Similarly to axial and tangential velocity fields the modes of radial velocity appear in the mode pairs. The mode pairs are continuously #1 with #2, #3 with #4, #5 with #6, #7 with #8 and #9 with #10. Important finding is that any mode related to synchronous pulsations is not identified from the first ten radial velocity modes.

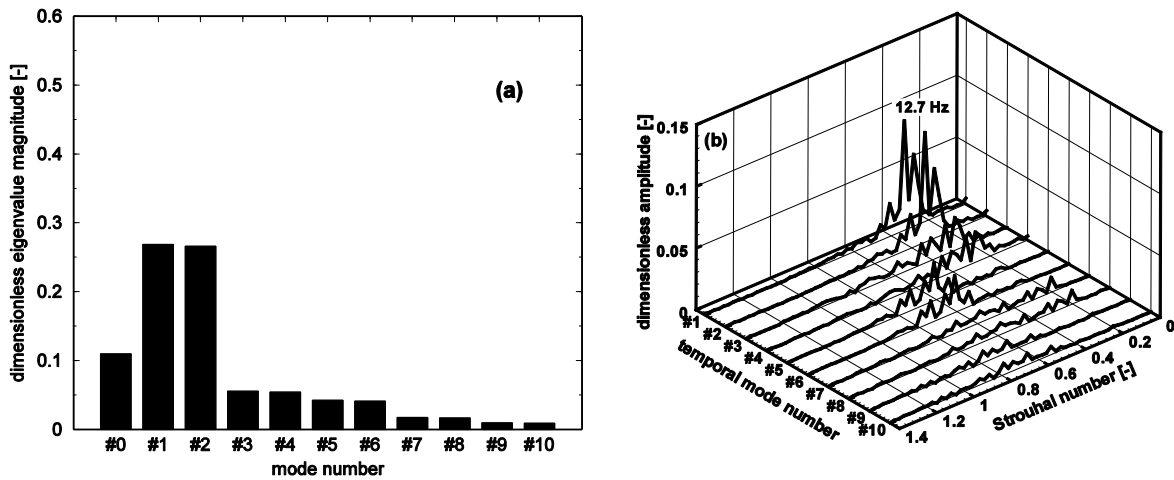


Figure 138 Eigenvalue magnitude of the radial velocity modes #0 - #9 (a) and power spectra of the temporal modes (b)

17.4 POD MODES OF STATIC PRESSURE FIELD

Analogous to the velocity field the static pressure field is decomposed. The spatial representations of the static pressure modes #1 - #9 are plotted in Figure 139 and Figure 140.

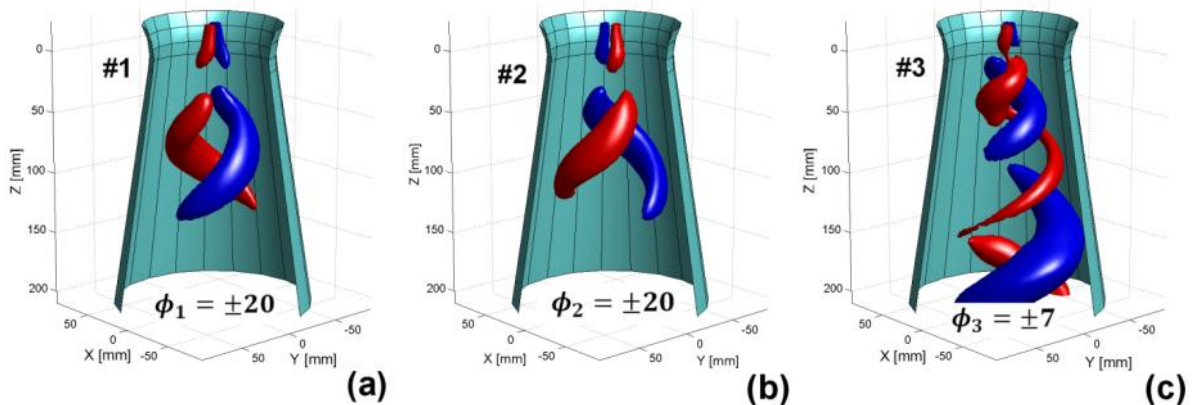


Figure 139 Spatial representation of the static pressure modes from #1 - #3

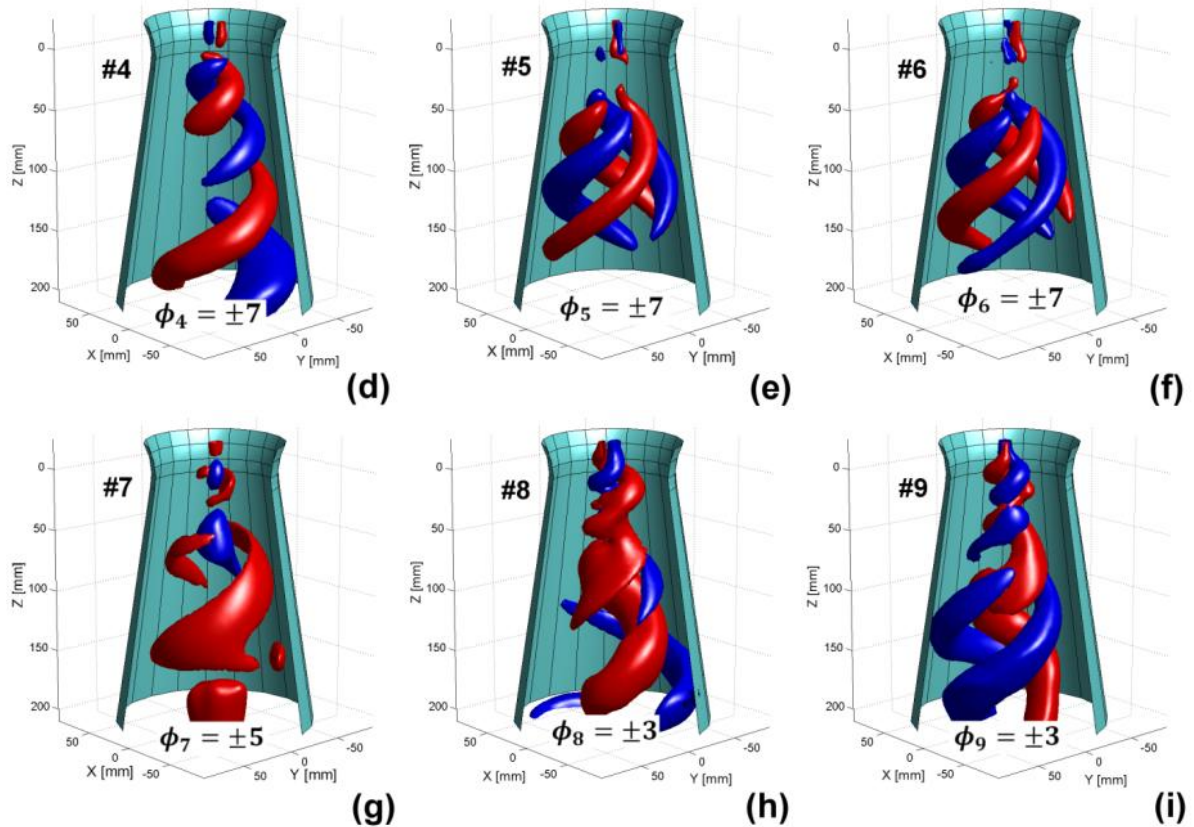


Figure 140 Spatial representation of the static pressure modes from #4 - #9

The resulting eigenvalue magnitudes (see Figure 141a) reveal that almost 74.5% from the budget corresponds to the mean flow (mode #0). The first ten modes of the static pressure include 21.4% and together with the mode #0 represent more than 95%. One can see that the eigenvalue magnitudes of the first two modes (#1 and #2) are significantly larger with respect to others. As a result, the first two modes are the most significant ones in case of static pressure field.

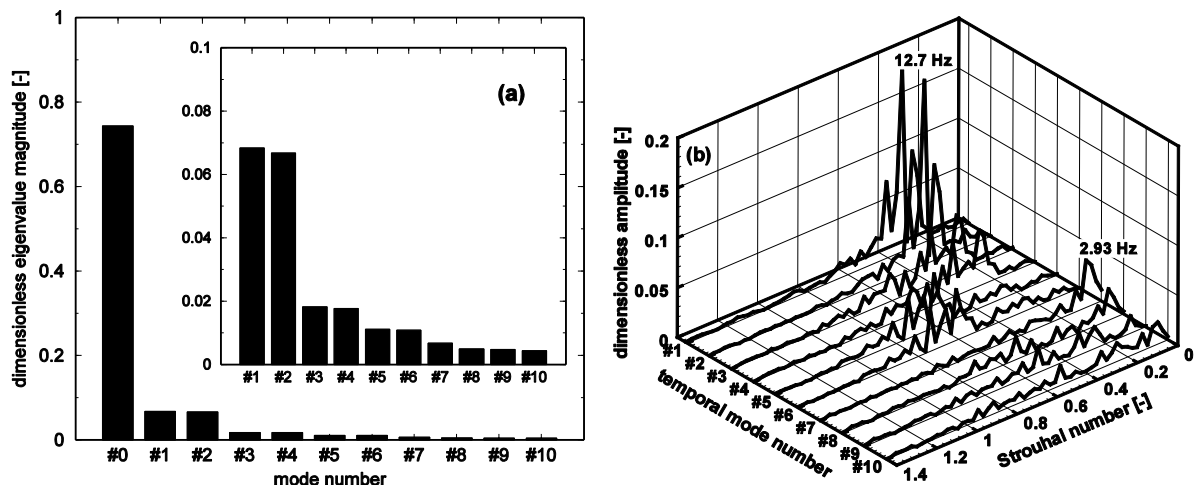


Figure 141 Dimensionless eigenvalue magnitude of the first ten static pressure modes (a) and the temporal power spectra (b) for decelerated swirling flow with vortex rope

It is observed that frequency of the first mode pair (modes #1 and #2) has one significant peak at 12.7 Hz close to the precession frequency of the vortex rope at 13.26 Hz extracted

from the pressure signal in monitoring point during CFD calculation. This is valid not only for the static pressure field but also for the velocity fields where the temporal frequency of the first mode pair is found to be 12.7 Hz. It shows that the first two modes (#1 and #2) act as the main unstable modes producing strong dynamic behavior associated with the precessing motion of the vortex rope. And also refer to the significant link between pressure and velocity field.

The frequency spectra of other two static pressure mode pairs (modes #3 with #4 and modes #5 with #6) contain more peaks in wider range of frequencies with much lower amplitudes. Those mode pairs are also related to the asynchronous pressure pulsations. On the other hand, the modes #7 and #8 have spectrum with one peak at low frequency of 2.93 Hz. These modes are related with the synchronous pulsation of the water column in the conical diffuser.

17.4.1 Backward reconstruction of static pressure field

The backward reconstruction of the static pressure field is performed based on the first ten modes including so-called mode #0 associated with the mean (time averaged) static pressure field. The dimensionless static pressure iso-surface of $(\Delta p_{stat}(\mathbf{x}, t) / \frac{1}{2} \rho v_{ref}^2) = -1.8$ representing original snapshot of the vortex rope shape is plotted in Figure 142b. Qualitatively, the original snapshot of vortex rope shape from Figure 142b recovers quite well the shape of the vortex rope visualized on the test rig by the gathered air in the vortex core, see Figure 142a. Also, this snapshot is compared with the reconstructed snapshots using four modes (see Figure 142c) and ten modes (see Figure 142d). The main discrepancy is caused by neglecting of higher modes related to the small scale turbulent eddies which are responsible for the vortex rope decay in the downstream part of the cone. Indeed, one can observe in Figure 142a that the vortex rope disintegrates in the downstream part of the cone. Therefore, the tail of the vortex rope is better captured if more than only ten modes are considered in the vortex rope reconstruction. Consequently, the higher modes play an important role in the downstream part of the cone. This observation is quantitatively supported by the Fourier spectra of the unsteady signals measured on the last two levels (MG2 and MG3, see locations of pressure transducers in Figure 129) located in the downstream part of the cone where the higher harmonics are more important [8]. Nevertheless, the main shape of the vortex rope is sufficiently captured. Visually, almost the same shape is obtained by summing approximately fifty modes (from totally 1000). An important note is that coarse spatial shape of the vortex rope is obtained already when only four modes are considered.

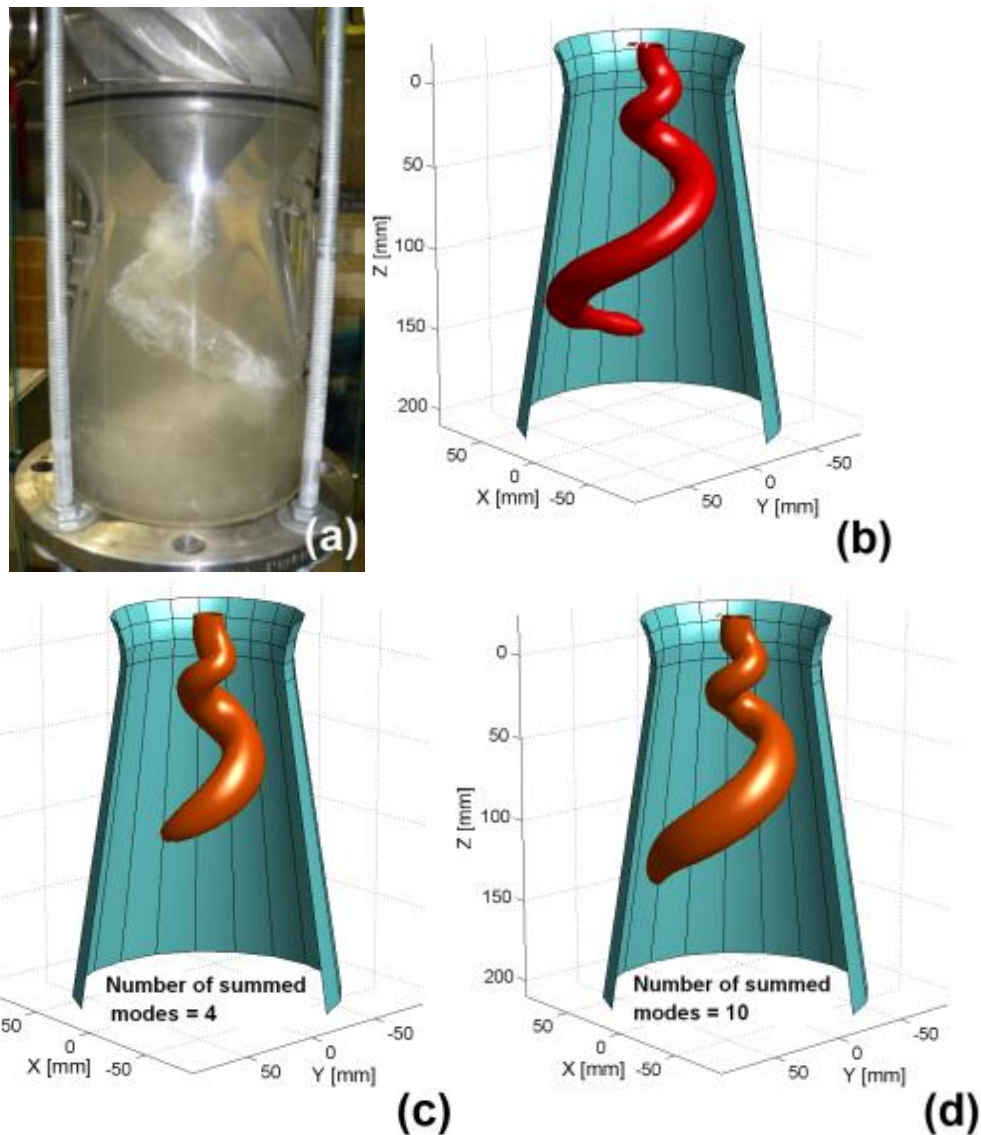


Figure 142 Vortex rope visualization on the test rig (a), the original snapshot from CFD computation (b), the reconstructed snapshots based on four modes (c) and ten modes (d)

17.5 DECELERATED SWIRLING FLOWS WITH THE AXIAL WATER INJECTION

In this section the influence of the axial water jet to the pressure and radial velocity fields is discussed. In experimental investigation [8] the critical threshold jet was identified at 11.5% of the overall swirl generator discharge. As a result, two domains are separated by the critical water injection threshold, the partial water injection below this critical value and the full water injection above it. Therefore, six jet discharges (2%, 5%, 8%, 11%, 12% and 14% of the overall swirl generator discharge) were selected for the numerical investigations for further correlation with experimental measurements. Two jet discharges belong to the full water injection region and five jet discharges including the regime without water injection are assigned to the partial water jet injection. The spatio-temporal behavior of the POD modes during the axial water injection is compared with the experimental data. Firstly, the evolution of Strouhal number during the axial water injection is plotted in Figure 143 against the

experimental data. The numerical results predict a monotone decrease of the Strouhal number over the region of partial water jet injection in a good agreement with the experimental ones. On the other hand, the Strouhal number evolution over the region of full water injection is captured incorrectly by the numerical results. This can be caused due to three reasons. First the simplification of numerical calculation where the blade parts (guide vanes and free runner) are not included, thus the influence of rotor-stator dynamics is eliminated. Second the influence of the test rig natural frequency can arise with the large jet discharge. Finally the relatively rough mesh was used in order to reduce number of cell values used for the POD execution. Therefore some of the flow field details could not be resolved sufficiently.

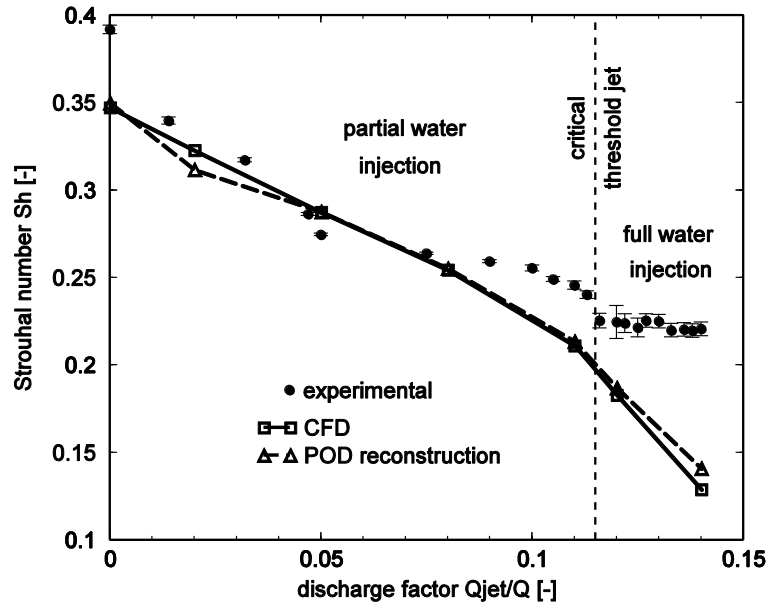


Figure 143 Strouhal number numerically computed for different values of the jet discharge against experimental data

The dimensionless amplitudes of pressure pulsations extracted from the numerical analysis for all four levels located in the cone diffuser (from MG0 to MG3) are plotted against measured ones in Figure 144. One can see that the computed amplitudes in the levels MG0 and MG1 are underestimated with respect to the experimental ones. The computed amplitude in the level MG3 is overestimated at 8% jet discharge and it is fully suppressed at 14% jet discharge. The comparison between the numerical and experimental amplitudes generated by the swirling flows with the vortex rope reveals the differences highlighted by other authors in [15]. Therefore, it is still an important challenge to accurately compute the pressure pulsation amplitudes.

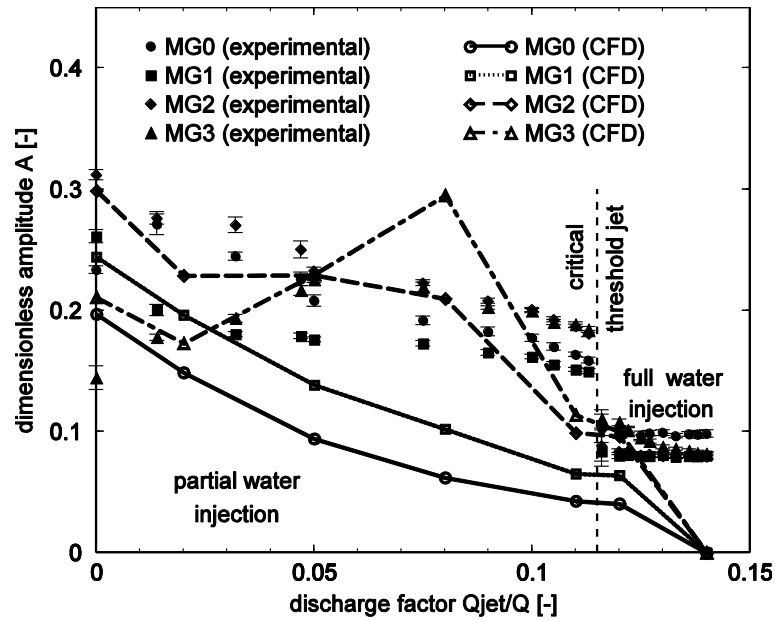


Figure 144 Dimensionless amplitudes numerically computed for different values of the jet discharge against experimental data

It was already revealed in the previous section that the first two modes #1 and #2 pose the most important contribution in flow field dynamic. Therefore, the evolutions of the eigenvalue magnitude of the static pressure and radial velocity modes #1 are plotted for different values of the jet discharges in Figure 145.

As was mentioned in section 17.3.3 it will be interesting to show the ratio between the radial velocity modes #1 (respectively #2) and time-averaged field represented by the mode #0. This can be seen from Figure 145 and Figure 147. One can see that dimensionless eigenvalue magnitude of radial velocity mode #1 increases until 8% jet discharge, then the abrupt drop follows for 11 and 12% jet discharges. It is important to say that between 8% and 11% jet discharges the mode #0 starts to exceed the modes #1 and #2. We suppose that these findings are related to the critical jet threshold which is approximately 11.5%. At the jet discharge 14% the radial velocity modes are totally neglected. This also shows that the radial velocity is very sensitive measure for the instability of the swirling flow. Decreasing frequency of radial velocity mode #1 can be seen in Figure 146 where the power spectra of temporal modes are plotted for entire range of jet discharges.

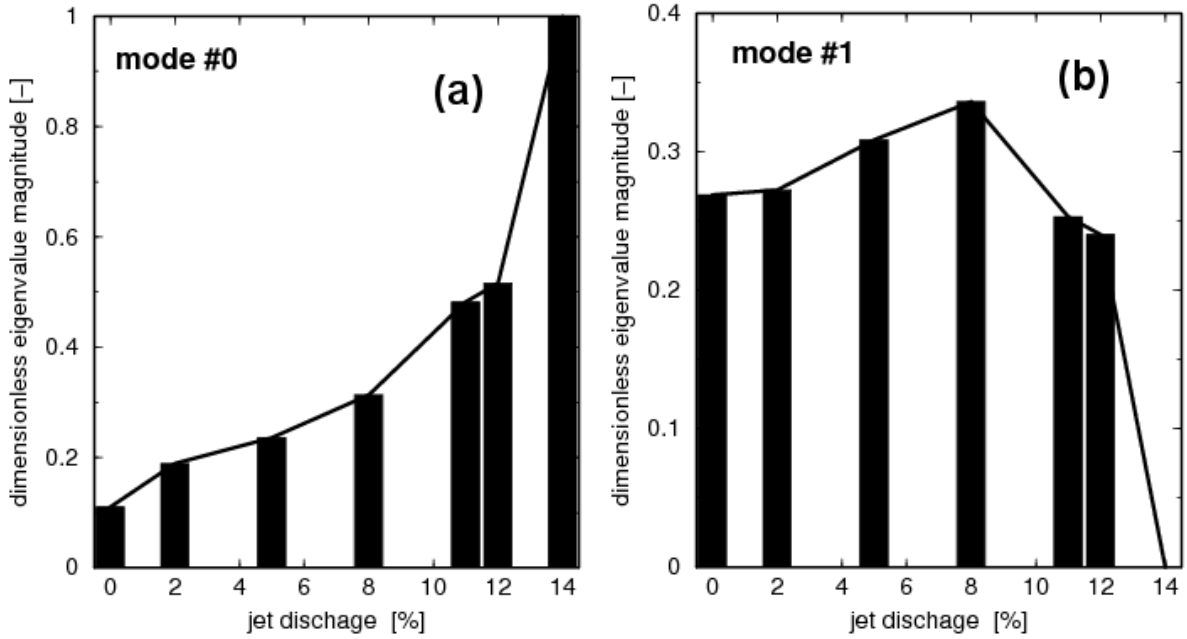


Figure 145 Dimensionless eigenvalue magnitude distribution of radial velocity mode #0 (a) and mode #1 (b) for entire jet discharges

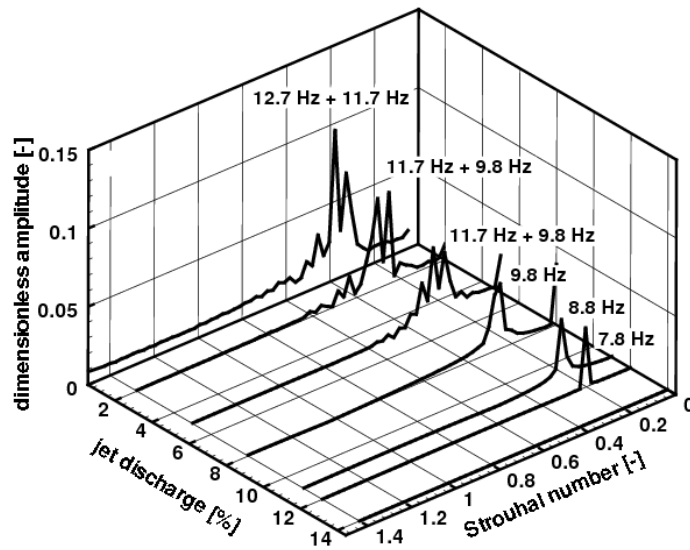


Figure 146 Power spectra of radial velocity mode #1 for entire jet discharges

The evolutions of eigenvalue magnitude of the static pressure mode #0 and #1 for different values of the jet discharge are plotted in Figure 147a and Figure 147b respectively. One can see that the eigenvalue magnitude of the static pressure mode #1 is diminished a quarter up to 5% jet discharge, one order of magnitude up to 8% jet discharge and at 14% jet discharge the eigenvalue magnitude is completely mitigated. The Consequently, an increased steadiness level of the flow can be observed in the eigenvalue magnitude of #0 mode corresponding to the time-averaged static pressure field.

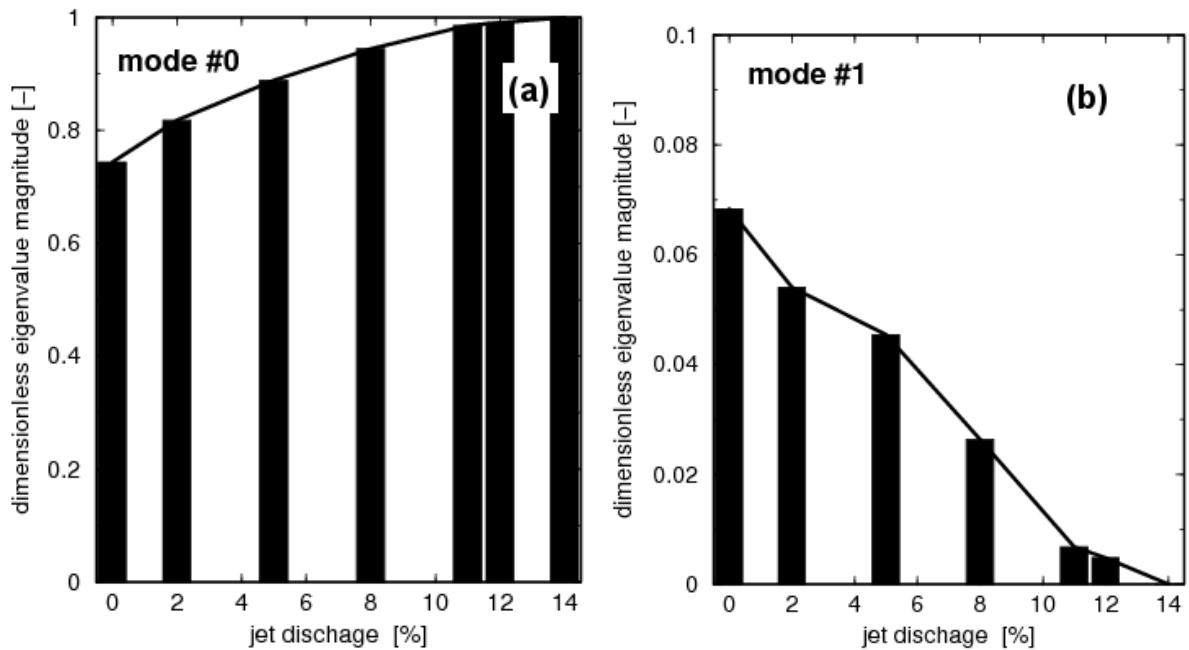


Figure 147 Dimensionless eigenvalue magnitude distribution of the static pressure mode #0 (a) and mode #1 (b) for entire jet discharges

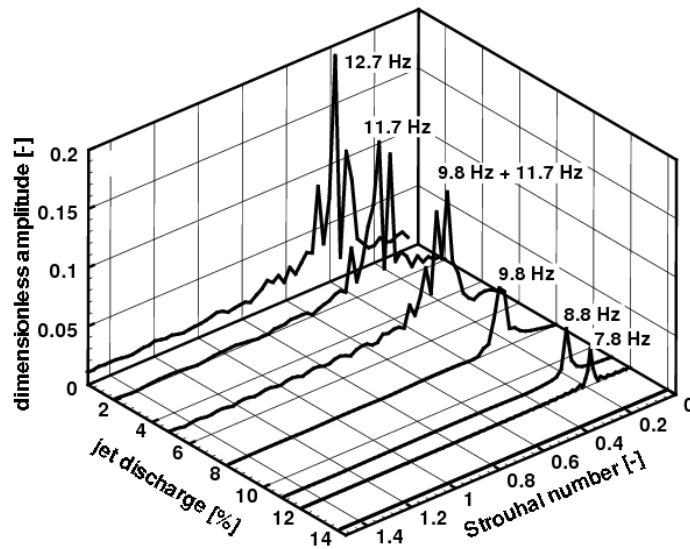


Figure 148 Power spectra of static pressure mode #1 for entire jet discharges

The evolution of temporal behavior quantified in the frequency spectra of the static pressure temporal mode #1 is shown for different values of the jet discharge in Figure 148. A monotonic decrease of the dimensionless amplitude and the dominant frequency is clearly distinguished once the jet discharge is increased. Moreover, the experimental investigations lead to a decay ratio of 0.65 being measured 14.9 Hz in the case with vortex rope and 9.7 Hz at 12% jet discharge [8]. It can be observed in the numerical analysis that the frequency evolves from 12.7 Hz in the case with the vortex rope to 7.8 Hz at 12% jet discharge yielding a decay ratio of 0.61 in excellent agreement with experimental value.

Further, a detailed analysis of the static pressure and radial velocity modes for the six values of jet discharges is performed taking into account the following aspects: (i) the modal strength (described by magnitude of eigenvalue λ_k or magnitude of ϕ_k); (ii) temporal behavior (described by frequency spectra of temporal modes a_k) and (iii) spatial behavior (described by iso-surface ϕ_k). The numerical results are compared with visualizations taken on the test rig.

17.5.1 2% jet discharge

The dimensionless eigenvalue magnitude of the static pressure and radial velocity modes for case of 2% jet discharge are plotted in Figure 149a and Figure 149b respectively.

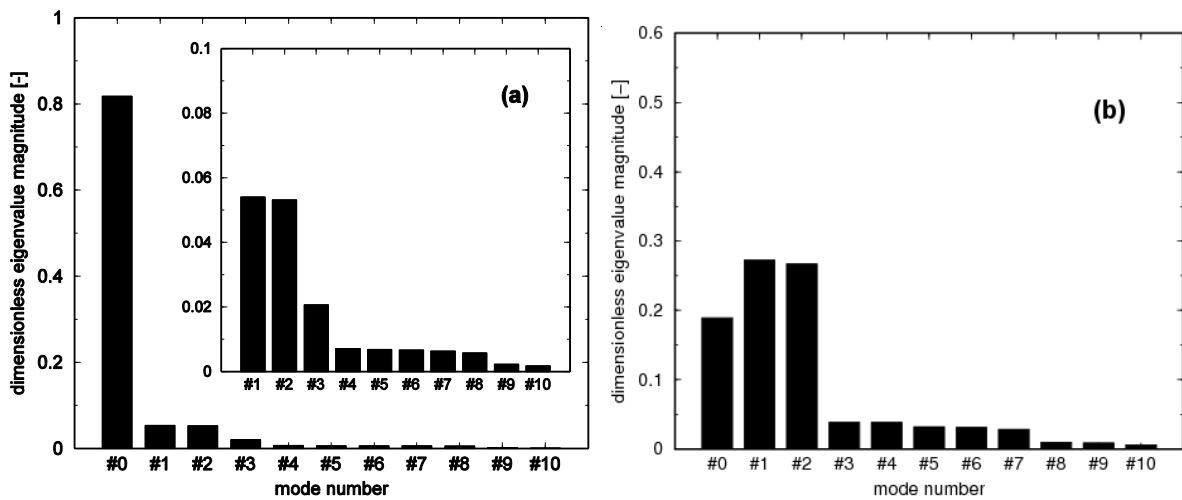


Figure 149 Dimensionless eigenvalue magnitude of the first ten static pressure modes (a) and radial velocity modes (b) at 2% jet discharge

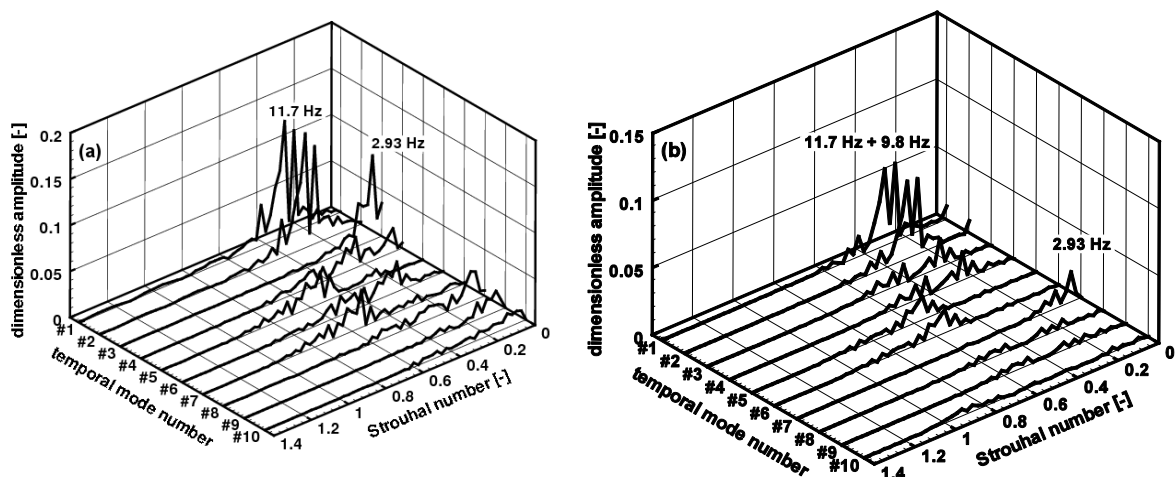


Figure 150 Power spectra of static pressure modes (a) and radial velocity modes (b) at 2% jet discharge

The power spectra of temporal modes are presented in Figure 150. According to Figure 145 and Figure 147 the eigenvalue magnitudes of pressure and radial velocity mode #0 increase. On the other hand, while the eigenvalue magnitude of static pressure modes #1 and

#2 decreases the eigenvalue magnitude of radial velocity modes #1 and #2 slightly increases. As a result, the first two modes remain the most significant although the strength of the modes is slightly reduced.

The spatial changes of both static pressure and radial velocity mode #1 are presented in Figure 151a and Figure 151b. Moreover, the static pressure mode related to the synchronous pressure pulsations (mode #3 with temporal frequency at 2.93 Hz) becomes much stronger which is represented by its relocation towards the higher eigenvalue magnitude just behind the modes #1 and #2. See the frequency spectra in Figure 150a and spatial shape of in Figure 152a.

Contrary to the case without axial water injection where the first nine radial velocity modes are related to the asynchronous pulsation, at 2% jet discharge the radial velocity mode #7 becomes the synchronous one. See its specific spatial shape in Figure 152b and low temporal frequency peak at 2.93 Hz in Figure 150b. Nevertheless one can deduce that the synchronous static pressure mode is much more dominant than the one decomposed from the radial velocity field. That is reasonable assuming that the jet is discharged in the axial direction, thus it influences mainly the axial velocity respectively the static pressure.

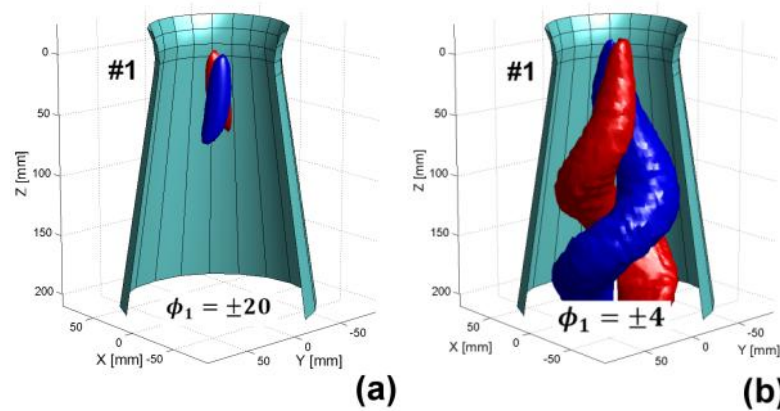


Figure 151 Spatial shape of static pressure (a) and radial velocity (b) mode #1 at 2% jet discharge

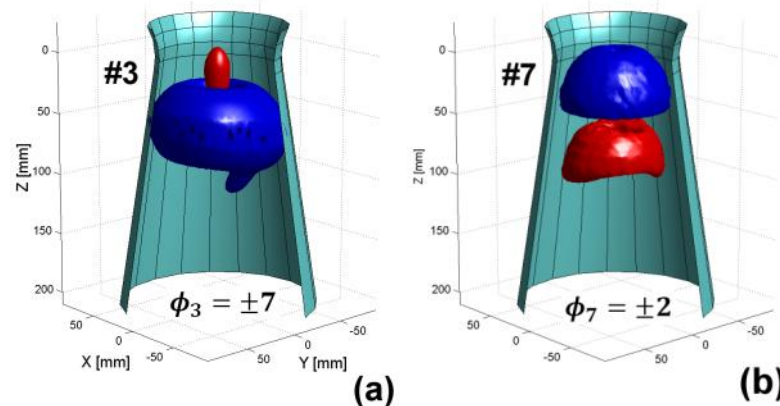


Figure 152 Spatial shape of static pressure mode #3 (a) and radial velocity mode #7 (b) at 2% jet discharge

The comparison of original snapshot (iso-surface of low static pressure) with the reconstructed ones is presented in Figure 153 for case of 5% jet discharge. Consequently the

reconstructed pressure field (using 4 and 10 modes) can be correlated with the visualization (Figure 153a) on the experimental test rig.

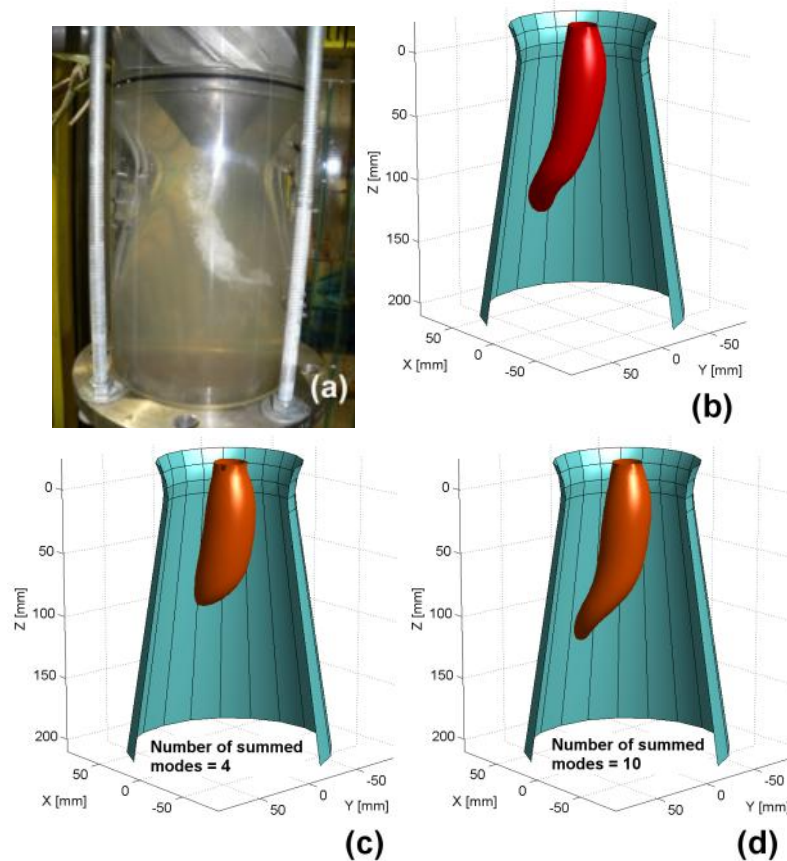


Figure 153 Vortex rope visualization on the test rig (a), the original snapshot from CFD computation (b), the reconstructed snapshots based on four modes (c) and ten modes (d), 2% jet discharge

17.5.2 5% jet discharge

At 5% jet discharge the continuous increase in eigenvalue magnitude of static pressure mode #0 and decrease in eigenvalue magnitude of modes #1 and #2 is observed, see Figure 154a. On the other hand, one can see much larger increase in eigenvalue magnitude of the radial velocity modes #1 and #2. Nevertheless the time-averaged radial velocity mode #0 increase as well. That means that the energy budget of radial velocity modes #1 and #2 increases at the expense of the rest modes which are strongly reduced, see Figure 154b. The relevant frequency spectra of both static pressure and radial velocity temporal modes are presented in Figure 155.

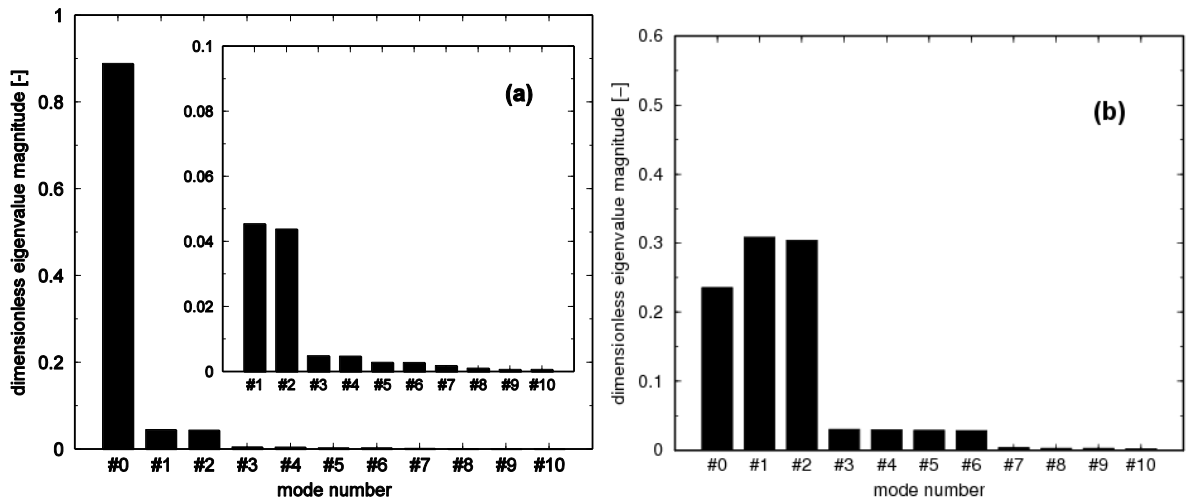


Figure 154 Dimensionless eigenvalue magnitude of the first ten static pressure modes (a) and radial velocity modes (b) at 5% jet discharge

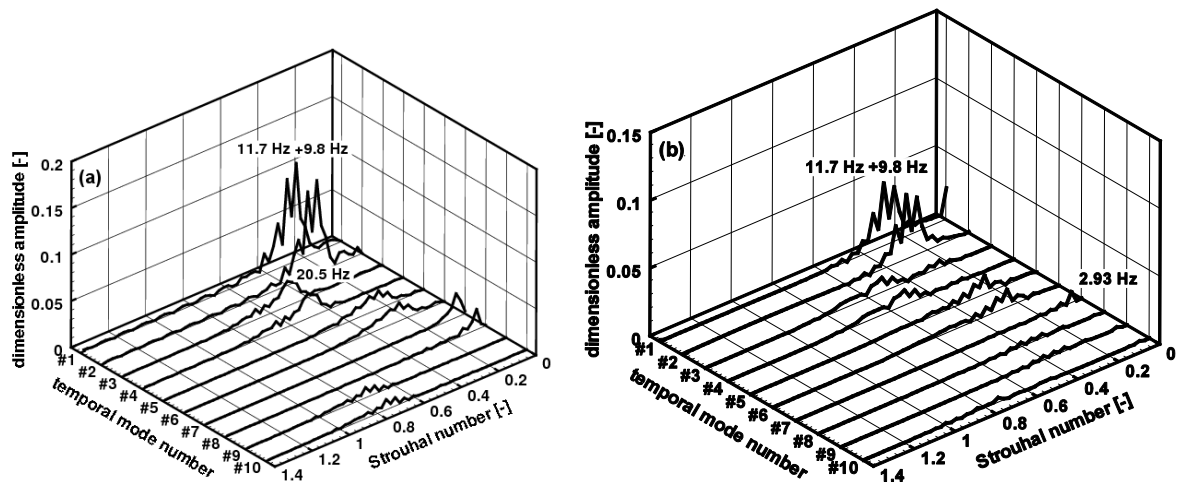


Figure 155 Power spectra of static pressure modes (a) and radial velocity modes (b) at 5% jet discharge

Positive influence of 5% jet to the flow dynamic suppression is clear from the spatial shapes of both static pressure and radial velocity mode #1. The modes are pushed further downstream to the diffuser, see Figure 156. This means that the jet discharge becomes strong enough to act on modes in the upstream part of the diffuser.

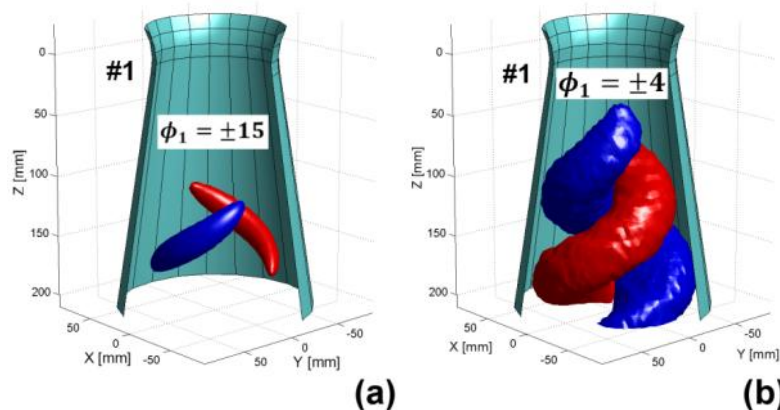


Figure 156 Spatial shape of static pressure (a) and radial velocity (b) mode #1 at 5% jet discharge

The comparison of original snapshot (iso-surface of low static pressure) with the reconstructed ones is presented in Figure 157 for case of 5% jet discharge. Consequently the reconstructed pressure fields (using 4 and 10 modes) can be correlated with the visualization (Figure 157a) on the experimental test rig. One can see that the vortex residue in the downstream part of the cone is sufficiently captured reconstructing the pressure field from 10 modes.

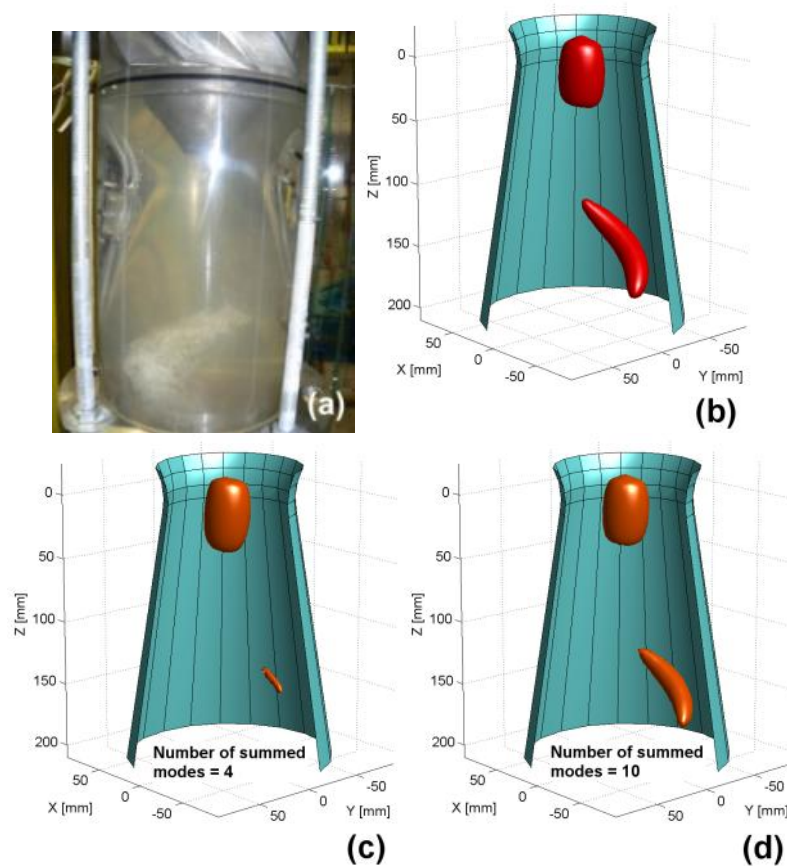


Figure 157 Vortex rope visualization on the test rig (a), the original snapshot from CFD computation (b), the reconstructed snapshots based on four modes (c) and ten modes (d), 5% jet discharge

17.5.3 8%, 11% and 14% jet discharges

A significant mitigation of the vortex dynamics is obtained at 8% jet discharge, see Figure 158. While only the modes #1 and #2 have noticeable frequency peaks (see Figure 159) and keeps position in downstream part of the diffuser (see Figure 160) the other higher modes are almost fully suppressed. In case of radial velocity field the mode #0 reached approximately the magnitude of modes #1 and #2, see Figure 158b. In the power spectra of temporal modes only these modes have significant amplitude peaks.

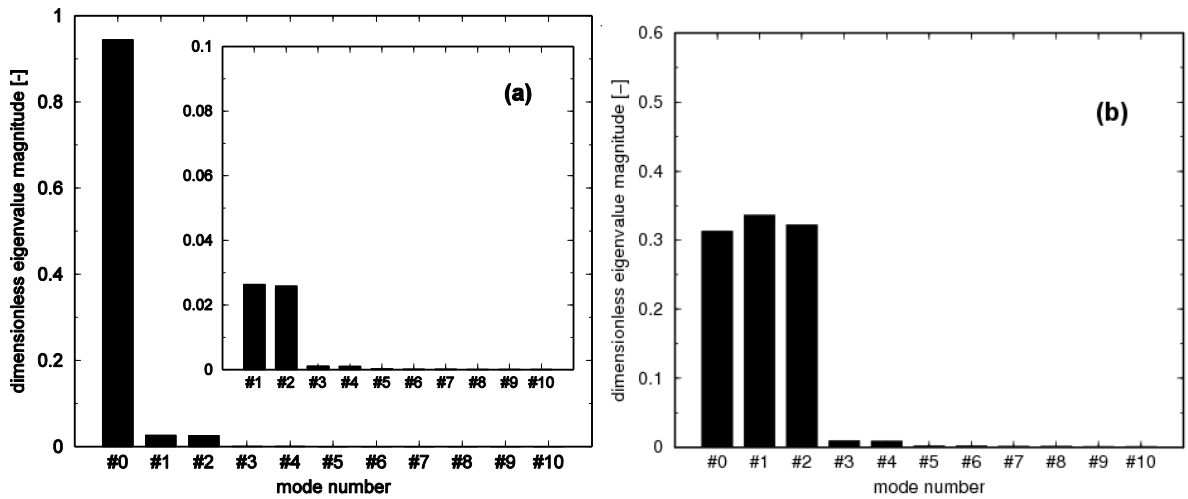


Figure 158 Dimensionless eigenvalue magnitude of the first ten static pressure modes (a) and radial velocity modes (b) at 8% jet discharge

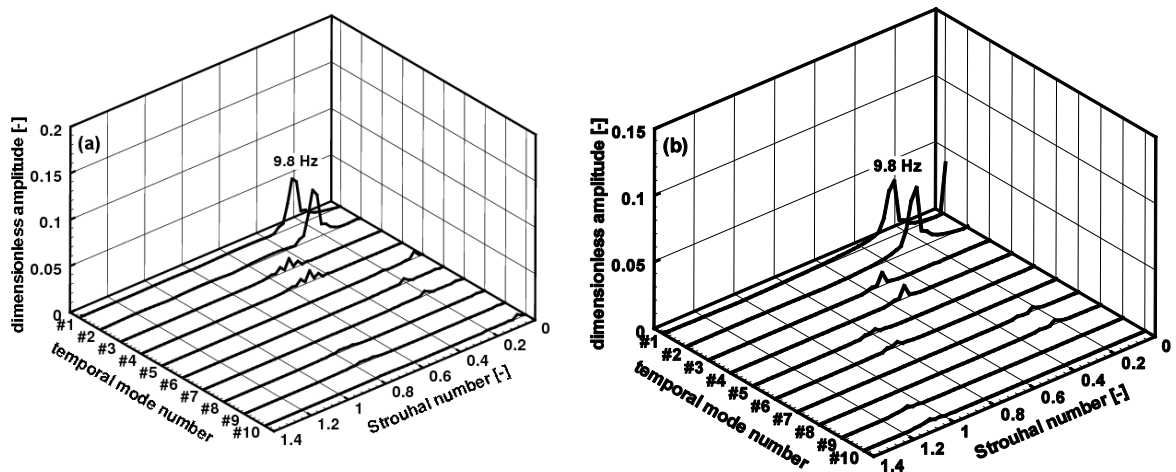


Figure 159 Power spectra of static pressure modes (a) and radial velocity modes (b) at 8% jet discharge

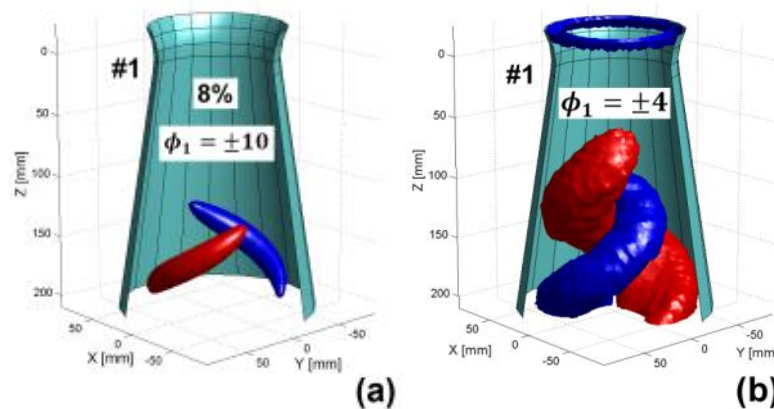


Figure 160 Spatial shape of static pressure (a) and radial velocity (b) mode #1 at 8% jet discharge

It is important to notice that after 8% jet discharge the eigenvalue magnitude of radial velocity modes #1 and #2 stop to increase and one can observe the abrupt drop at 11% jet

discharge, see Figure 145b. The spatial shapes stay very similar but the value of isosurface ϕ_k is very low. Further increasing of the jet discharge from 11% to 14% brings full suppression of the modes #1 and #2, see the spatial shapes and related value of ϕ_k in Figure 161.

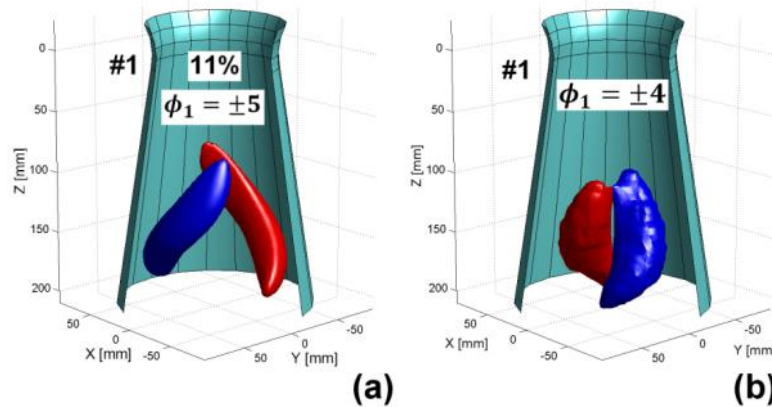


Figure 161 Spatial shape of static pressure (a) and radial velocity (b) mode #1 at 11% jet discharge

17.5.4 Backward reconstruction in cases of the axial water injection

The evolution of the pressure recovery factor c_p defined according to eq. (17.2) along the dimensionless cone length (L/R_{ref}) is plotted in Figure 162. The values obtained from the CFD computations (solid line) and backward reconstructions (dashed line) are compared against experimental data (dots) for two values of the jet discharge. The first value is associated to the case with the vortex rope without injection (labeled 0% jet) and the second value of 14% jet discharge corresponds to the maximum value of the axial jet investigated numerically. An acceptable agreement is obtained between numerical results and experimental data. Especially, the tendencies are well captured by numerical results. However, the numerically computed pressure recovery factor along to the entire cone length is overestimated up to 35% with respect to the experimental data at 14% jet discharge. This overestimation is caused due to results of numerical simulation, where the vortex disappeared for the full water injection. The reasons of discrepancy for highest jet discharges were discussed in section 17.5. Especially, the flow separation on the cone wall arising at full jet discharge in the downstream part of the cone is not captured in the numerical simulation.

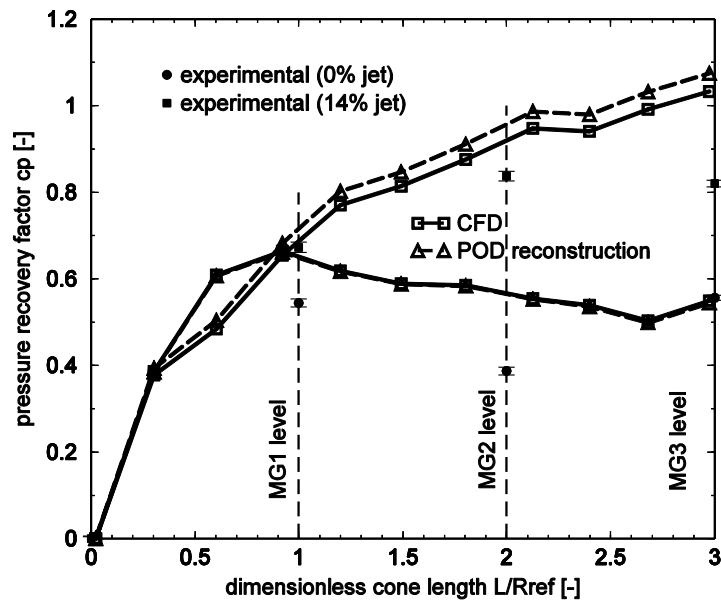


Figure 162 Computed and reconstructed pressure recovery factor against experimental data for the vortex rope case (0% jet) and full water injection (14% jet)

The evolutions of the computed and reconstructed pressure recovery factors in the sensor levels MG1, MG2 and MG3 are plotted in Figure 164 over full range of the investigated jet discharges. A good agreement between computed and reconstructed results against experimental data is obtained on the level MG1, Figure 163 (left). Also, an acceptable agreement between computed and reconstructed results against experimental data is observed on the levels MG2 (Figure 163 (right)) and MG3 (Figure 164) up to 8% jet discharge. Above the 8% jet discharge the experimental data are overestimated especially on the level MG3. As a result, the flow separation on the cone wall seems to be not captured by the numerical investigations at larger values of the jet discharge.

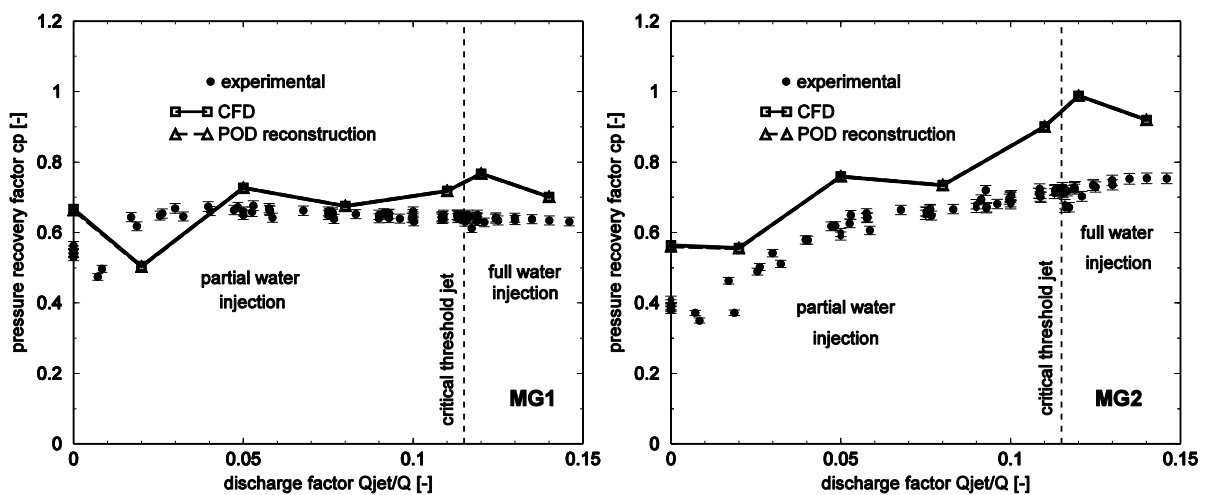


Figure 163 Distribution of computed and reconstructed pressure recovery factor in MG1 and MG2 positions during jet injection against experimental data

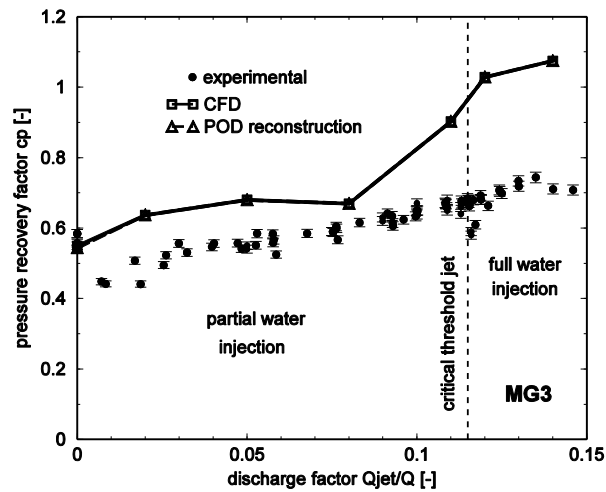


Figure 164 Distribution of computed and reconstructed pressure recovery factor in MG3 positions during jet injection against experimental data

The computed and reconstructed dimensionless amplitudes of the static pressure pulsations over full range of the jet discharges are compared against the experimental data in order to assess the ability of the backward reconstruction. The dimensionless amplitudes of the asynchronous and synchronous components of the pressure pulsations are evaluated for both experimental data [8] and numerical data (original and POD reconstruction). The synchronous and asynchronous components are achieved using equations presented in section 7.3. Expectedly, numerical results showed large discrepancy for synchronous type of oscillations. The synchronous oscillations became dominant at full water injection due to the interaction with the hydraulic circuit. This interaction cannot be captured by CFD simulations correctly if only the convergent-divergent part of the test section is taken into account. Therefore, only the results of synchronous components are presented.

The dimensionless amplitudes of the asynchronous component obtained from the backward reconstruction and CFD computation at all four levels (from MG0 to MG3) are plotted against experimental data in Figure 165. The results show that dimensionless amplitudes of asynchronous component obtained from the backward reconstruction fit very well with the dimensionless amplitudes from CFD computation. It means that synchronous component is negligible with respect to the asynchronous one. This result is also confirmed by the experimental data over partial water injection region where the asynchronous component is dominant.

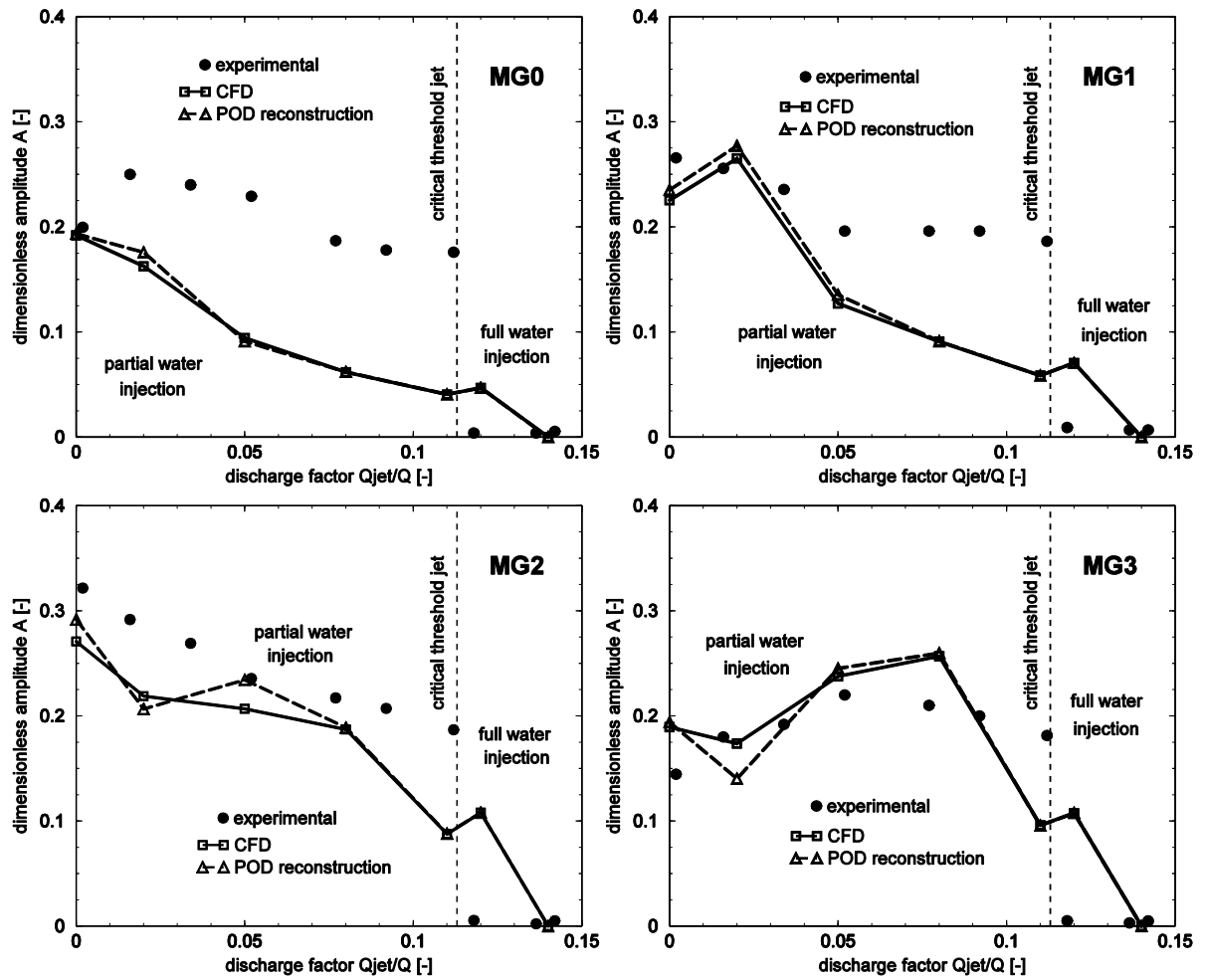


Figure 165 Comparison of dimensionless amplitudes computed in MG0, MG1, MG2 and MG3 positions against experimental data

17.5.5 Robustness of POD technique

The robustness of POD technique and its ability to capture all important features is verified for both different time spans and different snapshots sampling intervals. The results are presented for the static pressure field in case of decelerated swirling flow with the vortex rope. Different numbers of samples are taken from the initial data set including totally 920 samples with sampling period $dt = 0.001$ sec. Firstly, the sampling period is changed thus the data sets span same time of CFD computation (0.92 sec), but number of collected samples varies. The dimensionless eigenvalue magnitudes of the first ten modes of the static pressure field are plotted for different sampling periods dt in Figure 166a.

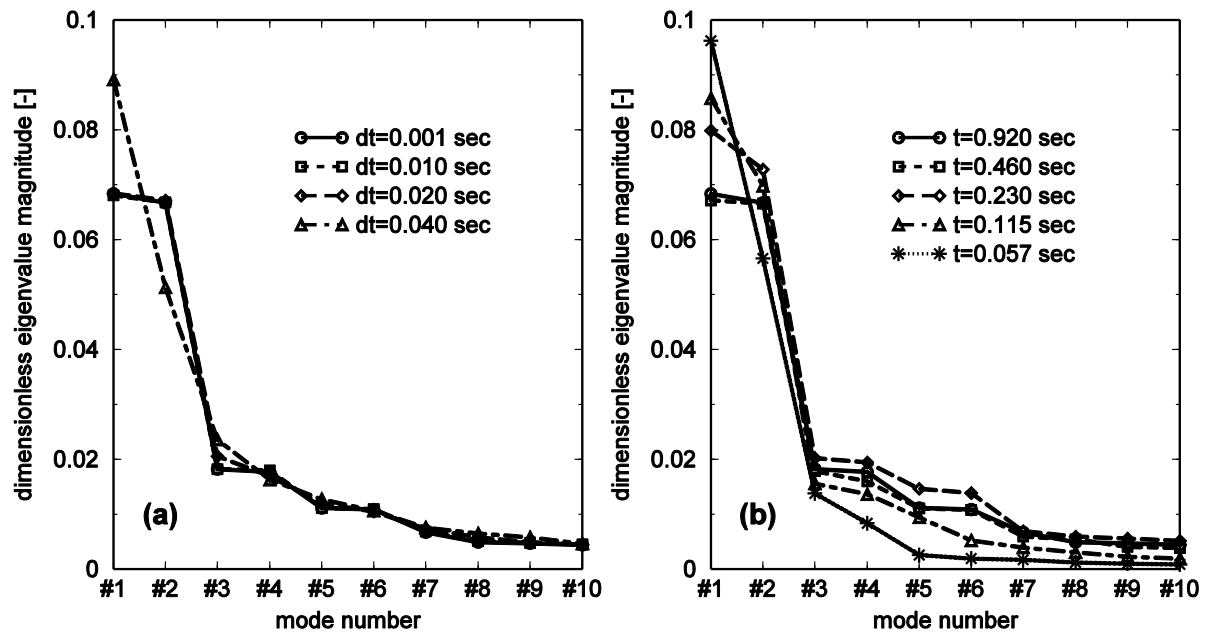


Figure 166 Dimensionless eigenvalue magnitude of the first ten static pressure modes for data sets with different sampling interval (a) and different length of time (b)

Secondly, the sampling period $dt = 0.001$ is unchanged and the length of data set is reduced (from 0.92 sec to 0.057 sec). Thus data sets are varying in number of samples and span different lengths of time. Results are plotted in Figure 166b. One can see that substantially better results are obtained for case with extended sampling period and same length of time than for case with unchanged sampling period and shorter length of time. Ensemble with sampling period $dt = 0.02$ sec containing 46 snapshots of instantaneous static pressure field shows only small discrepancy in spatial shape of mode (see Figure 167) compare to results obtained for the initial ensemble of 920 samples with the sampling period $dt = 0.001$ sec. Both ensembles span same length of time 0.92 sec thus covering approximately twelve periods of the vortex rope rotation. Consequently reduced ensemble of 46 snapshots has approximately 3.8 samples in one vortex rope rotation. One can see that the tested sampling period $dt = 0.02$ sec is very close to sampling period $dt = 0.0189$ sec defined by condition in eq. (15.2) which should be the longest possible to use.

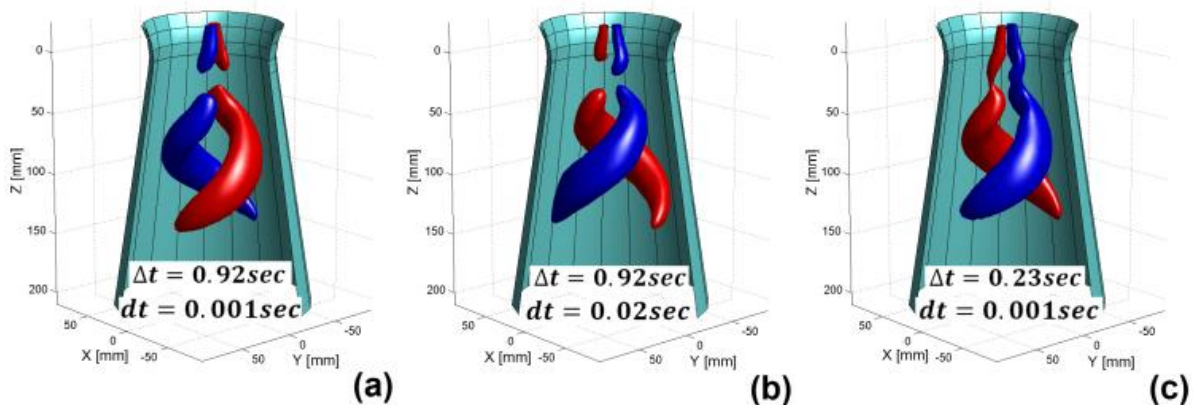


Figure 167 Mode #1 of the static pressure field: original data set $\Delta t = 0.92 \text{ sec}$, $dt = 0.001 \text{ sec}$ (a), the data set with longer sampling period $dt = 0.02 \text{ sec}$ (b) and data set with shorter length of time $\Delta t = 0.23 \text{ sec}$, $dt = 0.001 \text{ sec}$ (c)

17.6 CONCLUSIONS OF POD ANALYSIS OF “UPT” SWIRL GENERATOR

The POD analysis of “UPT” swirl generator was carried out in order to support investigation of decelerated swirling flow where the active control method (in the form of axial water jet) is applied to suppress unwanted flow features emerging from the spiral vortex formed downstream of the diffuser. The deeper understanding of changes in the flow fields when the axial jet is applied is necessary for further successful application of this method for the real hydraulic turbine. In real application the axial water jet would be supplied by the discharge bypassing the turbine runner. Nonetheless this leads to the volumetric losses which decrease overall turbine efficiency. Therefore qualitative assessment of this method must be known in order to balance advantages of steady flow conditions in the draft tube with decrease of turbine efficiency.

In presented analysis both velocity and pressure fields were decomposed in a form of spatio-temporal modes. Compare to other studies the compete (assuming both mean and fluctuating part) instantaneous velocity $v(\mathbf{x}, t_k)$ and static pressure fields $p(\mathbf{x}, t_k)$ were decomposed. This enabled both better comparison between particular flow fields (velocity and pressure) and quantitatively study the redistribution of energy between the time-averaged field (mode #0) and dynamic modes #1, #2, etc.

In case of swirling flow with the spiral vortex (without axial jet injection) the temporal frequency of the first mode pair (modes #1 and #2) is close to equal to the dominant one extracted from the numerically computed pressure signal in monitoring point during CFD calculation. This is valid for both the static pressure and velocity fields (axial, radial and tangential). Consequently this mode pair (modes #1 and #2) acts as the most unstable one and is responsible for the main vortex instability.

Decomposing both velocity (axial, tangential and radial) and static pressure fields in case of the spiral vortex shows differences in significance of particular modes. While for the axial and tangential velocity fields the sum of eigenvalue magnitude of time-averaged field (mode #0) together with the first three modes (mode #1, #2 and #3) is equal to 93% and 94 % respectively, in case of radial velocity and static pressure fields the eigenvalue magnitudes are much more redistributed to the higher modes. This shows that for POD study of spiral vortex dynamics the radial velocity or static pressure fields are more convenient (sensitive). Nonetheless this almost excludes usability of data from the experimental measurements, where the measuring of radial velocity or static pressure field is a bit of challenge. Nonetheless the radial velocity can be computed from the other measured velocity components using the continuity equation.

Applying the axial jet, the synchronous kind of modes became stronger (in the sense of eigenvalue magnitude) for both the radial velocity and the static pressure fields. While for the static pressure field the synchronous mode is shifted from mode #7 to the mode #3 when the 2% jet is applied, in the case of radial velocity field the synchronous mode (#7) arises in ten most dominant modes compared to case without water jet. While at 2% jet discharge the most dominant modes #1 and #2 stay close below the swirl generator hub, at 5% jet discharge the modes are pushed further downstream to the diffuser. This means that at 5% jet discharge the jet becomes strong enough to act on modes in the upstream part of the diffuser.

The frequency of the most dominant mode #1 (respectively #2) decreases continuously (from 2% to 14% jet discharge) with equal values for both static pressure and velocity fields, although the magnitudes of temporal modes are approximately twice higher in case of static pressure field.

The main conclusions arising from the present POD analysis are summarized below:

- The radial velocity field is very good measure of the flow instability. The eigenvalue magnitude (measure of the modal significance) of radial velocity modes #1 and #2 creating the most dominant mode pair exceeds the one of time-averaged field (represented by the mode #0) in cases when the spiral vortex dynamic is significant (large asynchronous pulsations, decrease in the pressure recovery). On the other hand the time-averaged radial velocity field (mode #0) is dominant when the spiral vortex is mitigated. It is believed that the transition of time-averaged radial velocity field (mode #0) to dominance over the modes #1 and #2 is in agreement with critical jet threshold which is approximately 11.5% of the jet discharge.
- The spatio-temporal behavior of the static pressure modes is in excellent agreement compared to one obtained from the velocity field.
- Moreover in order to compare the reconstructed flow field (assuming only several most dominant modes) with the experimental one, it is much more advantageous to consider the static pressure field for the POD execution. First the pressure measurements are much easier than the relatively difficult velocity measurements (LDA or PIV). Second the several commonly used quantities (pressure recovery, pressure amplitudes, frequency of synchronous and asynchronous pressure pulsations) can be correlated. Third the experimentally visualized vortex shape (e.g. by cavitation or air injection) can be compared with the reconstructed one. Moreover the modes related to synchronous pulsations can be separated from the modes related to the asynchronous pulsations and above mentioned comparisons can be carried out for the static pressure field reconstructed assuming only particular synchronous or asynchronous components. Therefore in some cases the POD of static pressure field can be preferable (in case of numerical data) compared to the POD of velocity field.
- The backward reconstruction of static pressure field executed using only the finite number of modes (consideration only 10 most significant modes) is able to approximate the original one with sufficient accuracy (spatial shape of spiral vortex, amplitudes and frequencies of asynchronous pulsations, pressure recovery). Consequently only a few modes are responsible for the main dynamic behavior of investigated flow fields.

- The main discrepancy in spiral vortex spatial shape is caused by neglecting of higher modes related to the small scale turbulent eddies which are responsible for the vortex rope decay in the downstream part of the cone.
- Testing the robustness of POD decomposition and backward reconstruction respectively, the results show that both length of sampled time and the sampling period of the data must be controlled. While the data sampling period yields the Nyquist–Shannon sampling theorem together with assumptions presented in section 15 the quality of POD results increase with the length of sampled time. Nevertheless the quantity of sampled data must stay in reasonable amount for suitable execution of POD (depending on the data storage capability and operating memory).

Suggestions arising from presented analysis towards the further investigation:

- One of the advantages is that POD analysis shows where the dominant mode pair (modes #1 and #2) appears. Therefore the modified shape of the jet – e.g. conically shaped jet respecting the widening of the diffuser can be tested in order to improve mitigation efficiency.
- Methodology how to act on the vortex in downstream part of the diffuser in order to enhance its mitigation
- Besides this, the different methods of jet supply can be tested – so called flow-feedback method (FFM) introduced by Resiga et al. [99] and tested by Tanasa et al. [104] or combination of first two methods introducing the flow feedback method with additional energy (FFM+) experimentally investigated by Tanasa et al. [105]. Those two enhancements decrease influence of energetic losses to the overall efficiency.

18 GLOBAL CONCLUSIONS

This thesis aims to contribute to the study of the vortex breakdown in the field of draft tube flow. The spiral form of vortex breakdown appears when the Francis turbine is operated for lower flow rates (part load) than the optimum one. Consequently the coherent structure of vortex rope appears below the turbine runner.

The behavior of corkscrew partial load vortex strongly depends on the flow rate. While for one flow rate it can be fairly robust flow pattern rotating very uniformly for another one the very unsteady corkscrew vortex rope with transition to different shapes occurs. Nonetheless the regular movement in upstream part of the draft tube is accompanied by the dissipating process in downstream part where this coherent structure decays. In order to mimic this flow phenomenon in the easiest way the swirl generator apparatus were designed to imitate flow similar to one in the draft tube of real hydraulic turbine. The detailed description of both swirl generators is presented in section 4 . Whole thesis is divided into two main parts:

The first part of the thesis is dedicated to comprehensive experimental and computational investigation of flow generated by the swirl generator designed at Viktor Kaplan Dept. of Fluid Engineering, Brno University Technology (“BUT” swirl generator). This simplified apparatus generates swirling flow which breaks down in the diffuser to the spiral vortex with cavitating core at higher flow rates. Unlike the hydraulic turbine where the flow passes through guide vanes and runner blades (thus the mismatch between swirl generated by the guide vanes and angular momentum extracted by the turbine runner is realized) here the changes in flow pattern and behavior are realized only by the increasing or decreasing flow rate. Nonetheless the main vortex features can be established – the instability trigger leading to the spiral form of vortex breakdown, the source of synchronous and asynchronous pressure pulsations, effect of cavitating vortex core, etc. The conclusions of this part can be found in section 14 .

The second part of thesis is dedicated to the POD application for study of spatio-temporal features of spiral vortex. The theory arising from our previous experiences to the full range of POD applications is presented at the beginning of section 15 . The subsections of second part are following:

- 1) The flow generated by the “BUT” swirl generator is analyzed using both experimentally and numerically obtained flow fields. These results are extension of investigation presented in the first part of thesis. The conclusions summarizing POD results and discussing connections to the general flow investigation (presented in the first part of thesis) can be found in section 16.3.
- 2) The POD is utilized in order to investigate spatio-temporal changes in the vortex dynamics when the active control (in a form of axial water jet) is applied. This study is realized on the base of collaboration using the swirl generator designed by the researchers from the Politehnica University of Timisoara in Romania (“UPT” swirl generator). The swirl generator consists of both guide vanes and free runner

and the design is so that the resulting flow is similar to one encountered in the draft tube of the Francis turbine (FLINDT project) operated at partial discharge, e.g. at 70% of the best efficiency point. Both the pressure and velocity fields are investigated. The conclusions summarizing these results are presented in section 17.6.

The results from well-conducted experimental measurements are usually considered as undoubtedly true (with respect to the measuring uncertainties). However, the strength of CFD is such that it provides full three-dimensional representation of the flow field. Moreover the numerically computed flow field can be expressed using various quantities (i.e. pressure, velocity components, vorticity, strain rate). It would be very difficult to record pressure in such many points in space or measure velocity vectors in such many planes to cover full three-dimensional representation of the flow experimentally. Therefore the CFD calculations, carefully verified by the experimental results, enable easy representation of this complex flow for further investigations. In this thesis the results of numerical simulations are compared with experimental ones for both swirl generator cases. Both the open-source and commercial CFD softwares were used. While the flow in “BUT” swirl generator is calculated using the OpenFOAM, the numerical data of “UPT” swirl generator are carried out in commercial ANSYS Fluent. Therefore one section (see section 11) of this thesis describes (in short) solver theory and post-processing methodology of numerical data for comparison with experimental measurements and for POD analysis.

The main thesis outcomes:

- Comprehensive study of spiral vortex dynamics and dissipation effects.

- In the first part analyzing flow generated by “BUT” swirl generator was shown that the magnitude of asynchronous pulsations and its frequency decrease downstream of the diffuser well correspond for both the static pressure and velocity fields. It proves the significant link between pressure and velocity field through the Navier-Stokes equation. From the pressure measurements it was observed that the largest amplitudes and lower values of the mean static pressure are obtained for the pressure sensor p2 situated at the beginning of the cone. In this location the vortex core is the most significant which is also reflected in the steep drop of pressure recovery for higher flow rates. Very good agreement was obtained for instability of the spiral vortex. From computed pressure field was shown that the periodically decaying character of the vortex is well captured by the numerical calculation therefore it is not consequence of any other source as a natural frequency of experimental test rig. It was shown that the synchronous part of pressure pulsations is not related only to the elbow draft tube surge but it can be also found in the straight diffusers. The complexity of decaying character of the vortex is difficult to simulate by two equation $k-\varepsilon$ turbulence model, which does not affect strong turbulence anisotropy. Moreover due to disagreement in results for higher flow rates the two phase numerical simulation can be recommended for the cases where the cavitating vortex core appears. At flow rate $Q = 13$ l/s the lowest diffuser loss

coefficient, highest pressure recovery and highest diffuser efficiency is achieved in the conical section compared to other numerically investigated flow rates. Nevertheless overall energy dissipation quadratically increases with increasing flow rate. Finally the vortex rotational frequency decrease along the diffuser axis was clarified considering two reasons – increase of diffuser diameter and collapsing spiral vortex.

- The main outcomes of POD decomposition are following: The radial velocity field is very good measure of the flow instability. The spatio-temporal behavior of the static pressure modes is in excellent agreement with the one obtained from the velocity field. In some cases the POD of static pressure field can be preferable (in case of numerical data) compared to the POD of velocity field. The backward reconstruction of static pressure field executed using only the finite number of modes (e.g. consideration of only 10 most significant modes) is able to approximate the original one with sufficient accuracy. The main discrepancy in spiral vortex spatial shape is caused by neglecting of higher modes related to the small scale turbulent eddies which are responsible for the vortex rope decay in the downstream part of the cone. The quality of POD results increases with the length of sampled time.
- Advantages of POD decomposition in study of active flow control for mitigation of vortex dynamics were presented.
- POD provides basis for further utilization of reduced order model (ROM), sometimes called low order dynamical model for the draft tube flow control. The ROM model is derived by projection of Navier-Stokes equation onto POD basis. One of the first applications of ROM can be found in [84] and [85].

LITERATURE

- [1] Andrienne, T., Razak, N. A., Dimitriadis, G. (2011). Flow Visualization and Proper Orthogonal Decomposition of Aeroelastic Phenomena, Wind Tunnels, Prof. Satoru Okamoto (Ed.), ISBN: 978-953-307-295-1, InTech, Available from: <http://www.intechopen.com/books/wind-tunnels/flow-visualization-andproper-orthogonal-decomposition-of-aeroelastic-phenomena>
- [2] Ansys Inc., 2011, ANSYS FLUENT 14.0 User's Guide, Canonsburg, Pennsylvania, USA.
- [3] Avellan, F.: Flow investigation in a Francis draft tube: the FLINDT project, in: *Proceedings of the 20th IAHR Symposium on Hydraulic Machinery and Systems, IAHR, Charlotte (NC), U.S.A., 2000. Paper DY-03.*
- [4] Azzi A., Lakehal D. Perspectives in Modeling Film Cooling of Turbine Blades by Transcending Conventional Two-Equation Turbulence Models. *Journal of Turbomachinery*. Vol. 124
- [5] Bergman, O., 2010, "Numerical Investigation of the Flow in a Swirl Generator Using OpenFOAM," M.S. thesis, Chalmers University of Technology, Goeteborg, Sweden.
- [6] Berkooz, G., Holmes, P., and Lumley, J.L.: 1993 "The proper orthogonal decomposition in the analysis of turbulent flows. *Annual Rev. of Fluid Mechanics* 25, pp. 539-575
- [7] Bienkiewicz, B., Ham, H. J., Sun, Y. 1993 Proper orthogonal decomposition of roof pressure. *Journal of Wind Engineering and Industrial Aerodynamics*, Vol. 50. pp. 193-202.
- [8] Bosioc A, Susan-Resiga R. F., Muntean S, Tanasa C., (2012) Unsteady Pressure Analysis of a Swirling Flow with Vortex Rope and Axial Water Injection in a Discharge Cone. *Journal of Fluids Engineering*, vol. 134 / 081104 p. 1-11
- [9] Bosioc, A., Susan-Resiga, R. F., and Muntean, S.: Design and Manufacturing of a Convergent-Divergent Test Section for Swirling Flow Apparatus, in: *Proceedings of the 4th German – Romanian Workshop on Turbomachinery Hydrodynamics (GRoWTH)*, June 12-15, Stuttgart 2008, Germany.
- [10] Bosioc, A., Tanasa, C., Muntean, S., Susan-Resiga, R. F.: 2D LDV measurements and comparison with axisymmetric flow analysis of swirling flow in a simplified draft tube. In *Proceedings 3rd IAHR International Meeting of the Workgroup on Cavitation and Dynamic Problems in Hydraulic Machinery and Systems*, Brno, Czech Republic, October 14-16, 2009.
- [11] Brekke, H. (2010). A Review on Work on Oscillatory Problems in Francis Turbines, *New Trends in Technologies: Devices, Computer, Communication and Industrial Systems*, Meng Joo Er (Ed.), ISBN: 978-953-307-212-8
- [12] Brücker, C. (1993) Study of Vortex Breakdown by Particle Tracking Velocimetry (PTV) Part 2: Spiral-Type Vortex Breakdown, *Exp. in Fluids*, Vol. 14, pp. 133-139.
- [13] Ciocan T., Muntean S., Susan-Resiga R. F.: Self-Induced Unsteadiness of the GAMM Francis Turbine at Partial Discharge. *Conference on Modelling Fluid Flow (CMFF'12)*. Budapest, Hungary, September 4-7, 2012.

- [14] Ciocan, G.D. and Iliescu, M. S.: Vortex rope investigation by 3d-piv method 2007
- [15] Ciocan, G.D., Iliescu, M.S., Vu, T.C., Nennemann, B., Avellan, F.: Experimental study and numerical simulation of the FLINDT draft tube rotating vortex, *J. Fluids Eng.* 129 (2007) 146–158.
- [16] Ciocan, T., Susan-Resiga, R. F., Muntean, S.: Analysis of the swirling flow at GAMM Francis runner outlet for different values of the discharge (2011)
- [17] Citriniti, J.H., and George, W.K., 2000, “Reconstruction of the global velocity field in the axisymmetric mixing layer utilizing the proper orthogonal decomposition”, *Journal of Fluid Mechanics*, **418**, pp. 137-166
- [18] Dantec Dynamics, a Nova Instruments company: Laser Doppler Anemometry (LDA) <http://www.dantecdynamics.com/>
- [19] Davidson L.: An Introduction to Turbulence Models. Chalmers University of Technology, Göteborg, Sweden, February 24, 2011
- [20] Davidson L.: Large Eddy Simulation. MTF270 Turbulence Modelling. 2006
- [21] Dörfler, P.K., Keller, M., Braun, O.: 2010 Francis full-load surge mechanism identified by unsteady 2-phase CFD. *IOP Conf. Series: Earth and Environmental Science* 12.
- [22] Doerfler, P. K., Ruchonnet, N. A statistical method for draft tube pressure pulsation analysis. *IOP Conf. Series: Earth and Environmental Science* **15** (2012) 062002
- [23] Dörfler, P., Sick, M. and Coutu, A. *Flow-Induced Pulsations and Vibration in Hydraulic Machinery*, DOI: 10.1007/978-1-4471-4252-2_1, Springer-Verlag London 2013.
- [24] Escudier, M.: Confined vortices in flow machinery, *Annual Rev. Fluid Mech.* 19 (1987) 27–52.
- [25] Fanelli, M. The vortex rope in the draft tube of Francis turbines operating at partial load: a proposal for a mathematical model. *Journal of Hydraulic Research*. Vol. 27. No. 6. 1989
- [26] Fox R.W., McDonald A.T., Dewoestine R.W.: Effects of swirling inlet flow on pressure recovery in conical diffusers, *AIAA J.* 9 (1971) 2014–2018.
- [27] Frunzaverde, D., Muntean, S., Marginean, G., Campian, V., Marsavina, L., Terzi, R., and Serban, V., 2010, “Failure Analysis of a Francis Turbine Runner”, *IOP Conf. Series: Earth and Environ. Sci.*, **12**, 012115, pp. 1-10, doi: 10.1088/1755-1315/12/1/012115.
- [28] Gallaire, F., Ruith, M., Meiburg, E., Chomaz, J.-M., and Huerre, P., 2006, “Spiral Vortex Breakdown as a Global Mode,” *J. Fluid Mech.*, 549, pp. 71–80.
- [29] Grinberg, L., Yakhot, A., Karniadakis, G. E.: Analyzing Transient Turbulence in a Stenosed Carotid Artery by Proper Orthogonal Decomposition, *Annals of Biomedical Engineering*, Vol. 37, No. 11, (2009) pp. 2200–2217
- [30] Holmes, P., Lumley, J.L., Berkooz, G., Rowley, C.W. 2012 *Turbulence, Coherent Structures, Dynamical Systems and Symmetry*, Second Edition. Cambridge University Press.

[31] Iliescu, M. S., Ciocan, G. D., Avellan, F.: Analysis of the Cavitating Draft Tube Vortex in a Francis Turbine Using Particle Image Velocimetry Measurements in Two-Phase Flow. *Journal of Fluid Engineering* 2008, Vol. 130/021105-1

[32] Jawarneh, A. M., Vatistas, G. H. (2006) Reynolds Stress Model in the Prediction of Confined Turbulent Swirling Flows, in: *ASME Journal of Fluid Engineering*, Vol. 128, p.p.1377-1382.

[33] Jedelský, J., Lízal, F., Jícha, M. Power Spectra Density of Velocity Fluctuations Estimated from Phase Doppler Data. *EPJ Web of Conferences* **25**, 01034 (2012)

[34] Jerri, A.J., 1977, "The Shannon Sampling Theorem – Its Various Extensions and Applications. A Tutorial Review", *Proc. IEEE*, **65**(11), pp. 1565 – 1596.

[35] Jošt, D., Lipej, A. Numerical prediction of the vortex rope in the draft tube, in: *Proceeding of 3rd International Meeting of the Workgroup on Cavitation and Dynamic Problems in Hydraulic Machinery and Systems, 2009, Brno Czech Republic.*

[36] Kellnerová, R., Kukačka, L., Juračková, K., Uruba, V., Jaňour, Z.: PIV measurement of turbulent flow within a street canyon: Detection of coherent motion. *J. Wind Eng. Ind. Aerodyn.* 104–106 (2012) pp.302–313

[37] Kirschner, O. and Ruprecht, A.: Vortex rope measurement in a simplified draft tube, in: *Proceedings of the 2nd IAHR International Meeting of the Workgroup on Cavitation and Dynamic Problems in Hydraulic Machinery and Systems, Timisoara, Romania, 2007.*

[38] Kirschner, O., Schmidt, H., Ruprecht, A., Mader, R., and Meusburger, P., 2010, "Experimental Investigation of Vortex Control with an Axial Jet in the Draft Tube of a Model Pump-Turbine", *IOP Conf. Series: Earth and Environ. Sci.*, **12**, 012092, pp. 1-9, doi: 10.1088/1755-1315/12/1/012092.

[39] Kjeldsen, M., Olsen, K., Nielsen, T., and Dahlhaug, O., 2006, "Water Injection for the Mitigation of draft Tube Pressure Pulsations", *Proc. 1st IAHR International Meeting of Working Group on Cavitation and Dynamic Problems in Hydraulic Machinery and Systems, Barcelona, Spain.* pp. 1-11.

[40] Koutník J., Nicolet Ch., Scholn G. A., Avellan F. 2006 Overload Surge Event in Pumped-Storage Power Plant, *23rd IAHR Symposium, Yokohama*

[41] Koutník, J., Krüger, K., Pochylý, F., Rudolf, P., Habán, V., 2006, "On Cavitating Vortex Rope Form Stability During Francis Turbine Part Load Operation" *Proc. IAHR Int. Meeting of WG on Cavitation and Dynamic Problems in Hydraulic Machinery and Systems, Barcelona*

[42] Kuibin, P.A., Okulov, V.K., Susan-Resiga, R.F., Muntean, S.: Validation of mathematical models for predicting the swirling flow and the vortex rope in a Francis turbine operated at partial discharge. *IOP Conf. Ser.: Earth Environ. Sci.* 12 012051 (2010)

[43] Kurokawa, J., Kajigaya, A., Matusi, J., and Imamura, H., 2000, "Suppression of Swirl in a Conical Diffuser by Use of J-Groove", *Proc. 20th IAHR Symposium on Hydraulic Machinery and Systems, Charlotte, NC, USA, Paper No. DY-01*, pp. 1-10.

- [44] Kurokawa, J., Imamura, H., and Choi Y.-D., 2010, “Effect of J-Groove on the Suppression of Swirl Flow in a Conical Diffuser”, *Journal of Fluids Engineering – Transaction of ASME*, **132**(7), 071101, pp. 1-8, doi: 10.1115/1.4001899
- [45] Launder, B.E., and Spalding, D. B., 1974, “The numerical computation of turbulent flows”, *Int J. of Computations Methods in Applied Mechanics and Engineering*, Vol. 31 (8), pp. 1414-1421.
- [46] Lucca-Negro, O., O’Doherty, T. (2001) Vortex breakdown: a review, in: *Annual Review of Fluid Mechanics*, 10, 221-246, 1978.
- [47] Lumley JL 1967 The structure of inhomogeneous turbulence. In: *Yaglom AI Tatarski VI (eds) Atmospheric turbulence and wave propagation* (Moscow: Nauka)
- [48] Lumley, J.L. 1970 *Stochastic Tools in Turbulence*, Academic Press.
- [49] MathWorks Inc., 2010, MATLAB[®] 7.10 User’s Guide, Natick, Massachusetts, USA.
- [50] Mayer, K. E., Pedersen, J. M., Özcan, O.: A turbulent jet in crossflow analysed with proper orthogonal decomposition. *J. Fluid Mech.* (2007), vol. 583, pp. 199–227. (2007)
- [51] Menter, F.R., 1994, “Two-Equation Eddy-Viscosity Turbulence Models for Engineering Applications”, *AIAA Journal*, Vol. 32, No. 8, pp. 1598-1605.
- [52] Miyagawa, K., Sano, T., Kunimatsu, N., Aki, T., and Nishi, M., 2006, “Flow Instability With Auxiliary Parts in High Head Pump – Turbines”, Proc. 23rd IAHR Symposium on Hydraulic Machinery and Systems, Yokohama, Japan, Paper F307.
- [53] Muntean, S., Nilsson, H., and Susan-Resiga, R., 2009, “3D numerical analysis of the unsteady turbulent swirling flow in a conical diffuser using FLUENT and OpenFOAM”, Proc. 3rd IAHR International Meeting of the Workgroup on Cavitation and Dynamic Problems in Hydraulic Machinery and Systems, Brno, Czech Republic. Paper C4, pp. 1-10.
- [54] Muntean, S., Ruprecht, A., and Susan-Resiga, R., 2005, “A numerical investigation of the 3D swirling flow in a pipe with constant diameter. Part 1: Inviscid computation, Scientific Bulletin of the „Politehnica” University of Timisoara, Transactions on Mechanics, **50**(64), pp. 77-86
- [55] Muntean, S., Buntić, I., Ruprecht, A., and Susan-Resiga, R., 2005, “A numerical investigation of the 3D swirling flow in a pipe with constant diameter. Part 2: Turbulent computation”, Scientific Bulletin of the „Politehnica” University of Timisoara, Transactions on Mechanics, **50**(64), pp. 87-96
- [56] Muntean, S., Susan-Resiga, R., and Bosioc, A., 2009, “Numerical investigation of the jet control method for swirling flow with precessing vortex rope”, Proc. 3rd IAHR International Meeting of the Workgroup on Cavitation and Dynamic Problems in Hydraulic Machinery and Systems, Brno, Czech Republic. Paper B2, pp. 1-10.
- [57] Nishi, M., Matsunaga, S., Kubota, S., Senoo, Y. Surging characteristics of conical and elbow-type draft tubes. *IAHR Section Hydraulic Machinery, Equipment and Cavitation, 12th Symp. (Stirling, UK, 1984)*

- [58] Nishi, M., Kubota, T., Matsunaga, S., and Senoo, Y., 1980, “*Study on swirl flow and surge in an elbow type draft tube*”, Proc. 10th IAHR Symposium IAHR Section on Hydraulic Machinery, Equipment, and Cavitation, Tokyo, Japan, **1**, pp. 557–568.
- [59] Nishi, M., and Liu, S.H., 2013, “An Outlook on the Draft-Tube-Surge Study”, Int. J. Fluid Mach. Syst., **6**(1), pp. 33-48, doi: 10.5293/IJFMS.2013.6.1.033.
- [60] Nishi, M., Wang, X. M., Yoshida, K., Takahashi, T., and Tsukamoto, T., 1996, “An Experimental Study on Fins, Their Role in Control of the Draft Tube Surging,” Hydraulic Machinery and Cavitation, E. Cabrera, V. Espert, and F. Martinez (eds.), Kluwer Academic Publishers, Dordrecht, The Netherlands, pp. 905–914.
- [61] Nobach H.: A Global Concept of Autocorrelation and Power Spectral Density Estimation from LDA Data Sets, *Proc. of the 10th International Symposium on Applications of Laser Techniques to Fluid Mechanics*, July 10-13, 2000, Lisbon, Portugal.
- [62] Novak, F.G.: *An Experimental Investigation of Vortex Breakdown in Tubes at High Reynolds Numbers*. Dissertation thesis. Naval Postgraduate School. Monterey, California. 1998.
- [63] Oberleithner, K., Sieber, M., Nayeri, C. N., Paschereit, C. O., Petz, C., Hege, H.-C., Noack, B. R., Wygnanski I.: Three-dimensional coherent structures in a swirling jet undergoing vortex breakdown: stability analysis and empirical mode construction. *J. Fluid Mech.*, 32 pages. (2011)
- [64] Oberleithner, K., Sieber, M., Nayeri, C. N., Paschereit, C. O.: On the control of global modes in swirling jet experiments. *Journal of Physics: Conference Series* 318 (2011)
- [65] Oberleithner, K., Terhaar, S., Rukes, L., Paschereit, C. O. Why Non Uniform Density Suppresses the Precessing Vortex Core, *J. Eng. Gas Turbines Power*. Vol. 135, No. 12, 2013
- [66] Oudheusden, B. W., Scarano, F., Hinsberg, N. P., Watt, D. W.: Phase-resolved characterization of vortex shedding in the near wake of a square-section cylinder at incidence, *Experiments in Fluids* (2005) 39: 86–98 DOI 10.1007/s00348-005-0985-5
- [67] Ojima, A., and Kamemoto, K., 2010, “Vortex method simulation of three-dimensional and unsteady vortices in a swirling flow apparatus experimented in Politehnica University of Timisoara”, IOP Conf. Series: Earth and Environ. Sci., **12**, 012065, pp. 1-9, doi: 10.1088/1755-1315/12/1/012065.
- [68] OpenCFD Ltd. *OpenFOAM User Guide*, available from: <http://cfd.direct/openfoam/user-guide/>
- [69] Palde, U. J., 1972, “Influence of the Draft Tube Shape on Surging Characteristics”, *American Society of Civil Engineers National Water Resources Engineering Meeting*, Atlanta, GA.
- [70] Pappilon, B., Sabourin, M., Couston, M., and Deschenes, C., 2002, “Methods for Air Admission in Hydro Turbines,” *Proc. 21st IAHR Symposium on Hydraulic Machinery and Systems*, Lausanne, Switzerland, pp. 1–6.
- [71] Perrin, R., Braza, M., Cid, E., Cazin, S., Barthet, A., Servain, A., Mockett, C., Thiele, F.: Obtaining phase averaged turbulence properties in the near wake of circular cylinder at high Reynolds number using POD. *Exp Fluids* (2007) 43, pp.341–355.

[72] Petit, O., Bosioc A.I., Nilsson, H., Muntean, S., and Susan-Resiga, R., 2011, “Unsteady simulations of the flow in a swirl generator using OpenFOAM”, *International Journal of Fluid Machinery and Systems*, **4**(1), pp. 199-208, doi: 10.5293/IJFMS.2011.4.1.199

[73] Pochylý, F., Rudolf, P., Habán, V., Koutník, J., Krüger, K.: Stability of the Steady Flow in Rotationally Symmetrical Domain. *2nd IAHR International Meeting of the Workgroup on Cavitation and Dynamical Problems in Hydraulic Machinery and Systems Timisoara, Romania*. 2007.

[74] Půlpitel L., Koutník J., Skoták A.: Using Draft Tube Fins for Air Venting of a Pump-Turbine, *HRW* November 1999, pp. 22 – 25.

[75] Qian Z.D., Li W., Huai W.X., and Wu Y.L., 2012, “The effect of the runner cone design on pressure oscillation characteristics in a Francis hydraulic turbine”, *Proc. IMechE, Part A: J. Power and Energy*, **226**(1), pp. 137-150, doi: 10.1177/0957650911422865

[76] Rudman, M., Blackburn, H. M.: Large Eddy Simulation of Turbulent Pipe Flow. *Second International Conference on CFD in the Minerals and Process Industries CSIRO*, Melbourne, Australia, 1999.

[77] Rudolf P 2010 Eigenmode shapes of the swirling flow in a diffuser. *Proceedings of EUROMECH Fluid Mechanics Conference*, Bad Reichenhall

[78] Rudolf P and Jízdny M 2011 Decomposition of the swirling flow fields. *Proceedings of the 4th International Meeting on Cavitation and Dynamic Problems in Hydraulic Machinery and Systems*, Belgrade

[79] Rudolf P., Skoták A. – Unsteady flow in the draft tube with elbow. Part B – Numerical investigation, *WG on the behavior of hydraulic machinery under steady oscillatory conditions*, Trondheim 2001

[80] Rudolf, P. (2009) Connection between inlet velocity field and diffuser flow instability, in: *Applied and Computational Mechanics*, Vol. 3, No. 1, pp. 177 – 184.

[81] Rudolf, P., Hudec, M., Gríger, M. and Štefan, D. Characterization of cavitating flow in converging-diverging nozzle based on experimental investigations. *EPJ Web of Conferences* **67**, 02101 (2014)

[82] Rudolf, P., Pochyly, F., Hában, V., & Koutnik, J. (2007). Collapse of cylindrical cavitating region and conditions for existence of elliptical form on cavitating vortex rope. *IAHR WG (Cavitation and Dynamic Problems in Hydraulic Machinery and Systems) 2nd Meeting*, Timisoara Romania, October 24–26, 2007.

[83] Rudolf, P., Štefan, D.: 2012 Decomposition of the swirling flow field downstream of Francis turbine runner. *IOP Conf. Ser.: Earth Environ. Sci.* 15

[84] Rudolf, P., Štefan, D. Reduced order model of draft tube flow. *IOP Conference Series: Earth and Environmental Science*, 2014, Vol. 22, No. 1

[85] Rudolf, P., Štefan, D., Klas, R. 2015 Spatio-Temporal Description of the Swirling Flow in Hydraulic Turbine Draft Tube. *Wasserwirtschaft*, 2015,(13), pp. 18-22.

- [86] Rudolf, P., Uruba, V., Štefan, D., Hladík, O. 2013 Analysis of the Coherent Vortical Structures in a Diffuser. 5th International Workshop on Cavitation and Dynamic Problems in Hydraulic Machines, Lausanne, Switzerland
- [87] Ruprecht A, Helmrich T, Aschenbrenner T and Scherer 2002 Simulation of Vortex Rope in a Turbine Draft Tube. *In Proc. of the 21st IAHR Symp. on Hydr. Mach. and Syst.* vol 1 (Lausanne, Switzerland) pp 259-76
- [88] Shih T. H., Liou W. W., Shabbir A., Yang Z., and Zhu J. A New k- ϵ Eddy Viscosity Model for High Reynolds Number Turbulent Flows—Model Development and Validation. *Computers Fluids*. 24(3):227-238, 1995
- [89] Sirovich, L.: 1987 Turbulence and the dynamics of coherent structures. Part I: Coherent structures. *Quarterly of Applied Mathematics XLV*, pp. 561-571
- [90] Štefan, D., Rudolf P., Muntean, S., Susan-Resiga, R. 2014 Structure of Flow Fields Downstream of Two Different Swirl Generators. *Engineering Mechanics*, vol. 20, No. 5, pp. 339-353
- [91] Štefan, D., Rudolf, P. 2015 Proper Orthogonal Decomposition of Pressure Fields in a Draft Tube Cone of the Francis (Tokke) Turbine Model. *Journal of Physics: Conference Series*, Vol. 579, No. 1.
- [92] Štefan, D.; Rudolf, P. *Computational Fluid Dynamic Study of the Flow Downstream of the Swirl Generator Using Large Eddy Simulation*. HPC-EUROPA2. 2013. p. 1-2.
- [93] Štefan, D., Zubík, P., Hudec, M. and Habán, L. Numerical and experimental investigation of swirling flow in a conical diffuser. 2015. *EPJ Web of Conferences*. Vol. 92.
- [94] Stuparu, A., Susan-Resiga, R. The Origin of the Plunging Pressure Fluctuations for a Swirling Flow With Precessing Vortex Rope In a Straight Diffuser. *6th IAHR International Meeting of the Workgroup on cavitation and Dynamic Problems in Hydraulic Machinery and Systems*, Ljubljana, Slovenia. 2015
- [95] Susan-Resiga R., Ciocan G D, Anton I and Avellan F 2006 Analysis of the Swirling Flow Downstream a Francis Turbine Runner *J. Fluids Eng.*128 177-89
- [96] Susan-Resiga, R., Vu, T.C., Muntean, S., Ciocan, G.D., and Nennemann, B., 2006, “Jet Control of the Draft Tube in Francis Turbines at Partial Discharge”, Proc. 23rd IAHR Symposium on Hydraulic Machinery and Systems, Yokohama, Japan, Paper F192, pp. 1-14.
- [97] Susan-Resiga, R., Muntean, S., Avellan, F., Anton, I.: Mathematical Modelling of swirling Flow in Hydraulic Turbines for the Full Turbine Operating Range, *Journal of Applied Mathematical Modelling*, vol. 35 pp: 4759-4773, 2011.
- [98] Susan-Resiga, R., and Muntean, S., 2008, “Decelerated Swirling Flow Control in the Discharge Cone of Francis Turbines”, Proc. 4th International Symposium on Fluid Machinery and Fluid Mechanics, Beijing, China, Paper IL-18, pp. 89-96, doi: 10.1007/978-3-540-89749-1_12
- [99] Susan-Resiga R, Muntean S, Bosioc A, Stuparu A, Miloş T, Baya A, Bernad S and Anton L E 2007 Swirling Flow Apparatus and Test Rig for Flow Control in Hydraulic Turbines Discharge Cone 2nd IAHR Int. Meet. of the Workg. on Cavit. and Dyn. Probl. in

Hydr. Machin. and Syst. (Timisoara, Romania) *Scientific Bulletin of the "Politehnica" University of Timisoara, Transactions on Mechanics, Tom 52(66), Issue 6* 203-17

[100] Susan-Resiga, R.F., Muntean, S., Hasmatuchi, H., Anton, I., Avellan, F., Analysis and Prevention of Vortex Breakdown in the Simplified Discharge Cone of a Francis Turbine. *Journal of Fluids Engineering*, Vol. 132. (2010)

[101] Susan-Resiga, R. F., Muntean, S., Tanasa, C., Bosioc, A. (2008) Hydrodynamic Design and Analysis of a Swirling Flow Generator, in: *Proceedings of the 4th German – Romanian Workshop on Turbomachinery Hydrodynamics (GRoWTH)*, June 12-15, 2008, Stuttgart, Germany.

[102] Susan-Resiga R, Muntean S, Vu T C, Ciocan G D and Nennemann B 2006 Jet Control of the Draft Tube Vortex Rope in Francis Turbines at Partial Discharge *Proc. of the 23rd IAHR Symp. on Hydr. Machin. and Syst.* (Yokohama, Japan) p 192

[103] Tanasa C, Susan-Resiga R, Bosioc A and Muntean S 2010 Design, Numerical Analysis and Practical Implementation of a Flow-Feedback System for Conical Diffuser with Swirling Flow *Scientific Bulletin of the „Politehnica” University of Timisoara Transactions on Mechanics* ISSN 1224-6077

[104] Tanasa C, Susan-Resiga R, Bosioc A and Muntean S 2010 Mitigation of pressure fluctuations in the discharge cone of hydraulic turbines using Flow-Feedback IOP Conf. Series: *Earth and Environmental Science* 12

[105] Tanasa, C., Susan-Resiga, R., Muntean, S., and Bosioc, A.I., 2013, “Flow-Feedback Method for Mitigating the Vortex Rope in Decelerated Swirling Flows”, *Journal of Fluids Engineering – Transaction of ASME*, **135**(6), 061304, pp. 1-11, doi: 10.1115/1.4023946

[106] Thicke, R.H., 1981, “Practical Solutions for Draft Tube Instability”, *International Water Power and Dam Construction*, **33**(2), pp. 31-37.

[107] Tridon S, Barre S, Ciocan G. D and Tomas L 2010 Experimental analysis of the swirling flow in a Francis turbine draft tube: Focus on radial velocity component determination. *European J. of Mech. B/Fluids*

[108] Tutkun, M., Johansson, P.B.V, and George, W.K., 2008, “Three-component vectorial proper orthogonal decomposition of axisymmetric wake behind a disc”. *AIAA Journal* **46**, pp. 1118-1134

[109] Vevke, T., 2004, “An Experimental Investigation of Draft Tube Flow,” Ph.D thesis, Norwegian University of Science and Technology, Trondheim, Norway.

[110] Wilcox, D.C., 1988, “Reassessment of the Scale-Determining Equation for Advanced Turbulence Models”, *AIAA Journal*, Vol. 26, No. 11, pp. 1299-1310.

[111] Wright N.G., Easom G.J. Non-linear k- ϵ turbulence model results for flow over building at full-scale. *Applied Mathematical Modelling*. Vol. 27. No. 12.

[112] Wu Y.L., Li S.C., Liu S.H., Dou, H.-S., and Qian Z.D., 2013, *Vibration of Hydraulic Machinery*, Springer Verlag.

[113] Zhang, R.-K., Cai, Q.-D., Wu, J.-Z., Wu, Y.-L., Liu, S.-H., and Zhang, L., 2005, “The Physical Origin of Severe Low-Frequency Pressure Fluctuations in Giant Francis Turbines,” *Mod. Phys. Lett. B*, **19**(28–29), pp. 99–102.

[114] Zhang, Z. *LDA Application Methods: Laser Doppler Anemometry for Fluid Dynamics*. Springer 2010.

NOMENCLATURE

Acronym	Unit	Description
$a_k(t)$		k-th temporal mode
c_p	1	pressure recovery factor
D	m	diameter
g	$m.s^{-2}$	gravity acceleration
H	m	head
k	$m^2.s^{-2}$	turbulent kinetic energy
L	m	longitudinal direction
n	min^{-1}	revolution
n_{11}	min^{-1}	specific speed
p	Pa	pressure
p_v	Pa	vapor pressure
\hat{p}	Pa	reconstructed pressure
p^*	1	dimensionless pressure
p_d	Pa	dynamic pressure
p_s	Pa	static pressure
P	W	power
Q	$m^3.s^{-1}$	discharge
Q_{11}	$m^3.s^{-1}$	specific discharge
r	m	radial coordinate
R	m	turbine runner radius
Re	1	Reynolds number
\bar{S}_{ij}		rate-of-strain tensor
S_n	1	swirl number
t	s	time
u	$m.s^{-1}$	circumferential velocity
u_{RMS}	$m.s^{-1}$	random mean square velocity
v	$m.s^{-1}$	absolute velocity
\bar{v}	$m.s^{-1}$	time averaged (mean) velocity
v'_i	$m.s^{-1}$	fluctuating part of velocity vector
v_i	$m.s^{-1}$	3D velocity vector (i = 1,2,3)
v_{ax}	$m.s^{-1}$	axial velocity
v_m	$m.s^{-1}$	meridional velocity
v_n	$m.s^{-1}$	normal velocity
v_u	$m.s^{-1}$	circumferential component of absolute velocity
v_{tan}	$m.s^{-1}$	tangential velocity
v_{ref}	$m.s^{-1}$	reference velocity
V	m^3	volume
w	$m.s^{-1}$	relative velocity
x_i	m	coordinate (i = 1,2,3)
Y	$J.kg^{-1}$	specific energy

λ		eigenvalue
ρ	kg.m^{-3}	density
σ	1	cavitating number
Ω	rad.s^{-1}	angular velocity
$C(t, t')$		temporal correlation matrix
β	deg	relative velocity angle
\mathcal{D}	W	dissipation function
δ_{ij}	-	Kronecker delta ($\delta_{ij} = \begin{cases} 0 & \text{if } i \neq j \\ 1 & \text{if } i = j \end{cases}$)
η	1	efficiency
μ	Pa.s	dynamical viscosity
μ_t	Pa.s	turbulent dynamic viscosity
ν	$\text{m}^2.\text{s}^{-1}$	kinematic viscosity ($\nu = \mu/\rho$)
ν_t	$\text{m}^2.\text{s}^{-1}$	turbulent kinematic viscosity
ν_t	$\text{m}^2.\text{s}^{-1}$	kinematic turbulent viscosity
ξ	1	hydraulic loss coefficient
ω	s^{-1}	specific dissipation rate
ϵ	$\text{m}^2.\text{s}^{-3}$	turbulent dissipation rate
τ_{ij}	Pa	Reynolds stress tensor
Π_{ij}	Pa	stress tensor
$\phi_i^k(\mathbf{x})$		k-th spatial mode

ABBREVIATIONS

BEP	Best Efficiency Point
BUT	Brno University of Technology
CFD	Computational Fluid Dynamics
DNS	Direct Numerical Simulation
EPFL	École Polytechnique Fédérale de Lausanne
EXP	experiment-al
FFM	Flow-Feedback Method
FFT	Fast Fourier Transformation
FLINDT	Flow Investigation in Draft Tubes
HSC	High Speed Camera
LDA	Laser Doppler Anemometry
LDV	Laser Doppler Velocimetry
LES	Large Eddy Simulation
NCESCF	National Center for Engineering Systems with Complex Fluids
OF	OpenFOAM
OpenFOAM	Open Source Field Operation and Manipulation
PIV	Particle Image Velocimetry
PISO	Pressure-Implicit Split-Operator
POD	Proper Orthogonal Decomposition

PRESTO!	PREssure STagging Option
PSHPP	Pump Storage Hydropower Plant
RANS	Reynolds Averaged Navier-Stokes
ROM	Reduced Order Model
RSM	Reynolds Stress Model
SGS	Sub Grid Scale
SIMPLE	Semi-Implicit Method for Pressure-Linked Equations
TKE	Turbulent Kinetic Energy
UPT	“Politehnica” University of Timisoara
URANS	Unsteady Reynolds Averaged Navier-Stokes

LIST OF PUBLICATIONS

2015

Štefan, D., Rudolf, P., Hudec, M., Habán, L. Comprehensive Study of Unsteady Pressure Pulsations Induced by the Spiral Vortex Structure in a Conical Diffuser. *6th IAHR International Meeting of the Workgroup on Cavitation and Dynamic Problems in Hydraulic Machinery and Systems*. Ljubljana, Slovenia. 2015.

Rudolf, P., Štefan, D., Klas, R. 2015 Spatio-Temporal Description of the Swirling Flow in Hydraulic Turbine Draft Tube. *Wasserwirtschaft*, 2015,(13), pp. 18-22.

Štefan, D., Zubík, P., Hudec, M., Rudolf, P. Numerical and experimental investigation of swirling flow in a conical diffuser. *EPJ Web of Conferences*, 2015, Vol. 2015, No. 92, p. 1-5.

Štefan, D., Rudolf, P. 2015 Proper Orthogonal Decomposition of Pressure Fields in a Draft Tube Cone of the Francis (Tokke) Turbine Model. *Journal of Physics: Conference Series*, Vol. 579, No. 1.

2014

Štefan, D., Rudolf, P., Muntean, S., Susan-Resiga, R. Structure of Flow Fields Downstream of Two Different Swirl Generators. *Engineering Mechanics*, 2014, Vol. 20, No. 5, p. 339-353.

Rudolf, P., Štefan, D., Pochylý, F. Dynamics of swirling flows in industrial applications. In *Engineering Mechanics 2014: Book of Full Texts*. Brno: Brno University of Technology, 2014. p. 38-41.

RUDOLF, P.; HUDEC, M.; GRÍGER, M.; ŠTEFAN, D. Characterization of the cavitating flow in converging- diverging nozzle based on experimental investigations. *EPJ Web of Conferences*, 2014, Vol. 2014, No. 67, p. 1-6.

RUDOLF, P.; ŠTEFAN, D.; HUDEC, M.; KOZÁK, J. Cavitation in swirling flows. In *Proceedings of Kolloquium Kavitation und Kavitations Erosion*. Bochum: RUB Bochum, 2014. p. 1-15.

Rudolf, P., Štefan, D. Reduced order model of draft tube flow. *IOP Conference Series: Earth and Environmental Science*, 2014, Vol. 22, No. 1, p. 1-10.

2013

Štefan, D., Habán, V., Hudec, M., Veselý, J., Rudolf, P. Analysis of Pelton Turbine Jet Decay Using a Proper Orthogonal Decomposition of Experimentally Obtained Image Ensemble. *Book of Abstract, 5th International Workshop on Cavitation and Dynamic Problems in Hydraulic Machinery*. Lausanne, Switzerland, 2013.

Štefan, D.; RUDOLF, P. *Computational Fluid Dynamic Study of the Flow Downstream of the Swirl Generator Using Large Eddy Simulation*. 2013. s. 1-2.

2012

RUDOLF, P.; POCHYLÝ, F.; ČERMÁK, L.; ŠTEFAN, D. *Instability of the swirling flows with/ without cavitation*. Book of Extended Abstracts. 1. Praha: Czech Society for Mechanics, 2012. s. 1123-1124. ISBN: 978-80-86246-39- 0.

ŠTEFAN, D.; RUDOLF, P.; SKOTÁK, A.; MOTYČÁK, L. Energy transformation and flow topology in an elbow draft tube. *Applied and Computational Mechanics*, 2012, roč. 6, č. 1, s. 93-106. ISSN: 1802- 680X.

RUDOLF, P.; ŠTEFAN, D. Decomposition of the swirling flow field downstream of Francis turbine runner. *IOP Conference Series: Earth and Environmental Science*, 2012, roč. 15, č. 6, s. 1-8. ISSN: 1755- 1315.

RUDOLF, P.; HUDEC, M.; ZUBÍK, P.; ŠTEFAN, D. Experimental measurement and numerical modeling of cavitating flow in converging- diverging nozzle. *EPJ Web of Conferences*, 2012, roč. 25, č. 01081, s. 1-8. ISSN: 2100- 014X.

2011

ŠTEFAN, D.; RUDOLF, P.; SKOTÁK, A.; MOTYČÁK, L. Energy transformation and flow topology in an elbow draft tube. In *COMPUTATIONAL MECHANICS 2011, EXTENDED ABSTRACTS*. Plzeň: ZČU - Plzeň, 2011. s. 55-56. ISBN: 978-80-261-0027- 0.

2010

ŠTEFAN, D.; RUDOLF, P. Kritické posouzení vztahů pro určování součinitele tření. In *Sborník XXIX. ročníku mezinárodní konference Setkání kateder mechaniky tekutin a termomechaniky 2010*. Ostrava: VŠB- TUO Ostrava, 2010. s. 1-5. ISBN: 978-80-248-2244- 0.

AUTHOR'S CV

Name: David Štefan

Date of birth: 5. 2. 1987

Education:

- 2011 – 2015
Design and Process *Doctoral degree* - Brno University of Technology,
Faculty of mechanical engineering, specialization
Engineering
- 2009 – 2011
 Engineering degree - Brno University of Technology,
Faculty of mechanical engineering, specialization Fluid
Engineering
- 2006 – 2009
Mechanical engineering *Bachelor degree* - Brno University of Technology,
Faculty of mechanical engineering, specialization
- 2002 – 2006
 Secondary School and Vocational Technical School in
Brno, Sokolská 1, specialisation: Industries – 2D and 3D
drawings

Research visits and internships:

- August – September 2012 IHS, University Stuttgart, Germany, within
HPC-Europa2 programme
- October – December 2012 Department of Hydraulic Machinery,
Politehnica University of Timisoara,
Romania, within ERASMUS programme

APPENDIX 1

fvSchemes and fvSolution dictionaries of simpleFoam solver (presented dictionaries are for case of $Q = 7 \text{ l/s}$)

```
/*-----* C++ *-----*\
|=====|
|\ \ / F i e l d | OpenFOAM: The Open Source CFD Toolbox |
|\ \ / O p e r a t i o n | Version: 1.6 modified according to 2.1.0 |
|\ \ / A n d | Web: http://www.OpenFOAM.org |
|\ \ M a n i p u l a t i o n |
\*-----*/
FoamFile
{
    version 2.0;
    format ascii;
    class dictionary;
    location "system";
    object fvSchemes;
}
// ***** //

ddtSchemes
{
    default steadyState; //backward;
}

gradSchemes
{
    default Gauss linear;
    grad(p) Gauss linear;
    grad(U) Gauss linear;
}

divSchemes
{
    default Gauss linear;
    div(phi,U) bounded Gauss upwind;//Gauss limitedLinearV 1;
    div(phi,k) bounded Gauss upwind;//Gauss limitedLinear 1;
    div(phi,epsilon) bounded Gauss upwind;//Gauss limitedLinear 1;
    div(R) Gauss linear;
    div(phi,nuTilda) bounded Gauss upwind;//Gauss limitedLinear 1;
    div((nuEff*dev(T(grad(U)))) Gauss linear;
}

laplacianSchemes
{
    default none;
    laplacian(nuEff,U) Gauss linear corrected;
    laplacian((1|A(U)),p) Gauss linear corrected;
    laplacian(DkEff,k) Gauss linear corrected;
    laplacian(DomegaEff,omega) Gauss linear corrected;
    laplacian(DepsilonEff,epsilon) Gauss linear corrected;
    laplacian(DREff,R) Gauss linear corrected;
    laplacian(DnuTildaEff,nuTilda) Gauss linear corrected;
}

interpolationSchemes
{
```

```
    default    linear;
    interpolate(U) linear;
}
```

```
snGradSchemes
{
    default    corrected;
}
```

```
fluxRequired
{
    default    no;
    p;
}
```

```
// ***** //
```

```

/*-----* C++ *-----*\
|=====|
| \ / Field | OpenFOAM: The Open Source CFD Toolbox |
| \ / Operation | Version: 1.6 |
| \ / And | Web: http://www.OpenFOAM.org |
| \ Manipulation |
|-----*/
FoamFile
{
    version 2.0;
    format ascii;
    class dictionary;
    location "system";
    object fvSolution;
}
// ***** //

solvers
{
    p
    {
        solver PCG;
        preconditioner DIC;
        tolerance 1e-6;
        relTol 0.1;
    }

    pFinal
    {
        solver PCG;
        preconditioner DIC;
        tolerance 1e-7;
        relTol 0;
    }

    "(U|k|epsilon)"
    {
        solver PBiCG;
        preconditioner DILU;
        tolerance 1e-5;
        relTol 0.1;
    }

    "(U|k|epsilon)Final"
    {
        solver PBiCG;
        preconditioner DILU;
        tolerance 1e-6;
        relTol 0;
    }
}

SIMPLE //PIMPLE
{
    correctPhi no;
    nOuterCorrectors 2;
    nCorrectors 1;
    nNonOrthogonalCorrectors 1;
}

relaxationFactors

```

```
{
  p      0.3;
  U      0.7;
  "(k|omega|epsilon)"  0.7;
}
```

```
cache
{
  grad(U);
}
```

```
// ***** //
```

APPENDIX 2

fvSchemes and fvSolution dictionaries of pimpleFoam solver (presented dictionaries are for case of $Q = 7 \text{ l/s}$)

```
/*----- C++ -----*\
|=====|
|\ \ / Field | OpenFOAM: The Open Source CFD Toolbox |
|\ \ / Operation | Version: 1.6 modified according to 2.1.0 |
|\ \ / And | Web: http://www.OpenFOAM.org |
|\ \ Manipulation |
\*-----*/
FoamFile
{
    version 2.0;
    format ascii;
    class dictionary;
    location "system";
    object fvSchemes;
}
// *****

ddtSchemes
{
    default backward;
}

gradSchemes
{
    default Gauss linear;
    grad(p) Gauss linear;
    grad(U) Gauss linear;
}

divSchemes
{
    default Gauss linear;
    div(phi,U) Gauss limitedLinearV 1;
    div(phi,k) Gauss limitedLinear 1;
    div(phi,epsilon) Gauss limitedLinear 1;
    div(R) Gauss linear;
    div(phi,nuTilda) Gauss limitedLinear 1;
    div((nuEff*dev(T(grad(U)))) Gauss linear;
}

laplacianSchemes
{
    default none;
    laplacian(nuEff,U) Gauss linear corrected;
    laplacian((1|A(U)),p) Gauss linear corrected;
    laplacian(DkEff,k) Gauss linear corrected;
    laplacian(DomegaEff,omega) Gauss linear corrected;
    laplacian(DepsilonEff,epsilon) Gauss linear corrected;
    laplacian(DREff,R) Gauss linear corrected;
    laplacian(DnuTildaEff,nuTilda) Gauss linear corrected;
}

interpolationSchemes
```

```
{
  default    linear;
  interpolate(U) linear;
}
```

snGradSchemes

```
{
  default    corrected;
}
```

fluxRequired

```
{
  default    no;
  p;
}
```

```
// ***** //
```

```

/*-----*- C++ -*-----*\
|=====|
|\ \ / Field | OpenFOAM: The Open Source CFD Toolbox |
|\ \ / Operation | Version: 1.6 |
|\ \ / And | Web: http://www.OpenFOAM.org |
|\ \ Manipulation |
\*-----*/
FoamFile
{
    version 2.0;
    format ascii;
    class dictionary;
    location "system";
    object fvSolution;
}
// *****

solvers
{
    p
    {
        solver PCG;
        preconditioner DIC;
        tolerance 1e-6;
        relTol 0.1;
    }

    pFinal
    {
        solver PCG;
        preconditioner DIC;
        tolerance 1e-7;
        relTol 0;
    }

    "(U|k|epsilon)"
    {
        solver PBiCG;
        preconditioner DILU;
        tolerance 1e-5;
        relTol 0.1;
    }

    "(U|k|epsilon)Final"
    {
        solver PBiCG;
        preconditioner DILU;
        tolerance 1e-6;
        relTol 0;
    }
}

PIMPLE
{
    correctPhi no;
    nOuterCorrectors 3;
    nCorrectors 1;
    nNonOrthogonalCorrectors 1;
}

relaxationFactors

```



```
{
  p      0.3;
  U      0.7;
  "(k|omega|epsilon)"  0.7;
}
```

```
cache
{
  grad(U);
}
```

```
// ***** //
```